

TUNABLE FOCUSED X-RAYS FOR PATTERNING AND LITHOGRAPHY

TUNABLE FOCUSED X-RAYS FOR PATTERNING AND LITHOGRAPHY

By ADAM FRED GLENN LEONTOWICH, B.Sc. (Hons)

A Thesis Submitted to the School of Graduate Studies in Partial Fulfillment of the
Requirements for the Degree Doctor of Philosophy

McMaster University Copyright © 2012 Adam F.G. Leontowich

McMaster University DOCTOR OF PHILOSOPHY (2012)

Hamilton, Ontario, Canada (Chemistry)

TITLE: Tunable Focused X-rays for Patterning and Lithography

AUTHOR: Adam F.G. Leontowich, B.Sc. (Hons) (University of Saskatchewan)

SUPERVISOR: Professor Adam P. Hitchcock

NUMBER OF PAGES: xxiii, 190

ABSTRACT

Scanning transmission x-ray microscopes (STXM) focus monochromatic x-rays into an intense sub-30 nm diameter spot. Samples are then positioned at the focal plane and raster scanned through the spot while the transmitted x-rays are acquired to build up images at x-ray photon energies. In addition, x-ray absorption spectroscopy (XAS) can be performed by recording image sequences over a photon energy range of interest. STXMs excel at characterizing thin sections of inhomogeneous soft matter with their combination of high spatial (<30 nm) and photon energy (<0.1 eV) resolution. However, the overarching theme of this thesis is to apply the intense, tightly focused spot of x-rays to induce spatially resolved chemical and physical changes, and directly pattern materials, primarily thin polymer films. The irradiated areas are then investigated using several types of microscopy (scanning transmission x-ray, atomic force, scanning electron) and XAS. The experiments cover three broad areas: i) Nanofabrication; realization of the smallest possible feature sizes, and fabrication schemes unique to focused x-rays with applications including nanofluidics. ii) Radiation chemistry and physics; investigating the mechanisms of radiation-induced processes such as bond formation/loss, morphological change, carbon contamination, and temperature increase. iii) X-ray optics; the spatial distribution of x-rays at a focal plane can be recorded in a thin polymer film and later read out using an atomic force microscope. Applications include feedback for optics fabrication and enhanced image processing, the ultimate goal being increased spatial resolution.

ACKNOWLEDGEMENTS

I want to thank Prof. Matthew Paige for giving me my first opportunity to pursue real scientific research, and Prof. Robert Scott for preparing me for graduate school. I would not be on this path without those first steps.

I thank all of my labmates during my time at McMaster: Alexander Imbault, Anne Marie Smith, Dr. Bonnie Leung, Dr. Ebrahim Najafi, Dr. Glyn Cooper, Dr. Jian Li, Karen Lam, Katie Harding, Maryam Badv, Sahar Mokhtari, Samanbir Kalirai, Dr. Viatcheslav Berejnov, Victoria Ju, Dr. Vincent Lee, Zhisheng Qin, Dr. Zulima Martin, and especially Dr. Jian Wang who oriented me with the lab and left behind a strong foundation to build this thesis upon.

I thank Prof. Andrew Knights and Prof. Harald Stöver for serving on my Ph.D. committee and their interest in my progress, and Prof. Alan Michette for serving as my external examiner.

I am eternally grateful to Prof. Adam Hitchcock for accepting me as a graduate student. Adam provided many helpful suggestions and guidance towards designing experiments which really isolated the issues such that, no matter the outcome, a conclusive result(s) would be produced. He gave extensive feedback on my written reports and correspondence in a timely fashion, always within a few days and often within hours. But most of all, Adam gave me what felt like total freedom to pursue my own questions and choose the directions in which this thesis unfolded. This work was not at any point limited by funding, location or access to instrumentation, but by my mental and sometimes physical stamina,

especially in the case of synchrotron data collection. Looking back now, this was a unique and unbelievably fortunate situation. I hope I've made the best of it.

I am also thankful for financial support from McMaster University, the Advanced Light Source doctoral fellowship in residence program along with my exceptionally talented mentor Dr. Tolek Tyliszczak, and the Canadian Light Source graduate student travel support program.

I thank the McMaster Chemistry Graduate Student Society, the Mother Liquors, the Ball Blockers, Organometallica, the Phoenix, and all my friends for the welcome departures from research.

I want to thank all of my family, especially my parents Glenn and Shelley Leontowich. They inspire me to always do my best. I could not have accomplished what I have without their unconditional love and support.

Finally I thank Rachelle for her love, companionship, humour and patience. Thank you for understanding during those distant times I put towards this thesis.

TABLE OF CONTENTS

Descriptive note	ii
Abstract	iii
Acknowledgements	iv
List of figures	xii
List of tables	xix
List of abbreviations and symbols	xx
1. Introduction	1
1.1 Tunable focused x-rays	1
1.2 Patterning and lithography	6
1.2.1 Focused (direct write) x-ray patterning and lithography	10
1.3 Radiation chemistry	13
1.4 Thesis overview	16
2. Methods	19
2.1 Synchrotrons	19
2.1.1 Synchrotron radiation	21
2.1.2 Synchrotron light sources	22
2.1.3 Properties of synchrotron radiation from synchrotron light sources	24
2.1.4 Modes of operation	26
2.2 NEXAFS spectroscopy	27
2.2.1 Overview	27
2.2.2 X-ray absorption theory	29
2.2.3 Peak widths and assignment	30
2.2.4 Additional properties	33
2.3 Scanning transmission x-ray microscope	34
2.3.1 Fresnel zone plate lenses	36
2.3.1.1 Diffraction limited focusing	38
2.3.1.2 Zone plate equations	42
2.3.2 The order sorting aperture and higher order radiation	44
2.3.3 Current number of soft x-ray STXMs	48
2.3.4 ALS 5.3.2 type STXM	49
2.4 Atomic force microscope	53
2.5 Scanning electron microscope	56

3.	Experimental	58
3.1	Sample preparation	58
3.1.1	Materials, sources and purities	58
3.1.2	Preparation of thin polymer films on Si ₃ N ₄ windows	59
3.1.2.1	Preparing polymer solutions	59
3.1.2.2	Spin coating	60
3.1.2.3	Float transfer from mica to Si ₃ N ₄	60
3.1.2.4	Annealing	62
3.1.2.5	Thickness measurement	63
3.1.2.6	Optical microscopy	64
3.1.2.7	Alternative transfer/fabrication methods	65
3.1.3	Affixing/removing samples to/from sample holders	66
3.2	STXM data collection and analysis	66
3.2.1	STXM and beamline set up	66
3.2.2	Collecting optical density images	67
3.2.3	Collecting image stacks and NEXAFS spectra	69
3.2.4	Creating “OD1” spectra for quantitative analysis	70
3.2.5	Patterning	72
3.2.6	Determining absorbed dose	72
3.3	Development	73
3.4	Proper sequence of analysis to avoid artefacts	74

Part I: Nanofabrication with focused x-rays

4.	Zone plate focused soft x-ray lithography	76
4.1	Introduction	77
4.2	Experiment	78
4.2.1	Materials	78
4.2.2	Complementary characterization	78
4.2.3	Preparation of thin polymer films on Si ₃ N ₄ substrates	79
4.2.4	Scanning transmission x-ray microscope and patterning	79
4.2.5	Development of patterned polymer films	79
4.3	Results	80
4.3.1	Lithographic characteristics of PMMA and PMGI patterned with 300 eV soft x-rays	80
4.3.2	Minimum developed feature size	80
4.3.3	Exposure spreading phenomenon	80

4.4	Discussion	81
4.4.1	Focused soft X-ray lithography in PMMA and PMGI at 300 eV	81
4.4.1.1	Lithographic characteristics of PMMA and PMGI for 300 eV monochromatic x-rays	81
4.4.1.2	Minimum feature size	83
4.4.2	Exposure spreading mechanism for focused soft x-rays	83
4.4.3	Avenues toward reducing minimum feature size	85
4.4.3.1	Improving the resist and development	85
4.4.3.2	Improving the optics and exploring new energies	85
4.4.4	Outlook	85
4.5	Conclusion	86
5.	33 nm feature sizes via direct write x-ray lithography	88
5.1	Introduction	88
5.2	Experimental	90
5.3	Results	92
5.4	Discussion	94
5.5	Conclusion	95
6.	Zone plate focused soft x-ray lithography for fabrication of nanofluidic devices	96
6.1	Introduction	97
6.2	Methodology	98
6.2.1	Appropriate resists for chemically selective lithography	98
6.2.1.1	Controlling the location of energy absorption by chemically selective patterning	98
6.2.1.2	Added requirements for chemically selective lithography	98
6.2.2	Sample preparation	99
6.2.3	Scanning transmission x-ray microscope (STXM)	99
6.2.4	Development	99
6.2.5	Imaging	99
6.3	Results	100
6.3.1	Layered structure and NEXAFS spectra	100
6.3.2	Fabricating nanochannels	100
6.3.3	Characterization of the nanochannel	101

6.3.4	Optimizing doses and development times	102
6.3.5	Cross sectional area of the nanochannel in relation to its maximum length	103
6.4	Discussion	104
6.4.1	Maximum nanochannel length	104
6.4.2	Interfacing with conventional microfluidics	104
6.4.3	Outlook	105
6.5	Conclusion	106

Part II: Radiation chemistry of polymers

7.	Accurate dosimetry in scanning transmission x-ray microscopes via the cross-linking threshold dose of poly(methyl methacrylate)	108
7.1	Introduction	109
7.2	Methodology	110
7.2.1	Materials	110
7.2.2	Sample preparation	110
7.2.3	Development	110
7.2.4	Scanning transmission x-ray microscope	110
7.2.4.1	Imaging and spectroscopy	111
7.2.4.2	Patterning	111
7.2.4.3	Calculating dose	111
7.2.5	Other characterization techniques	112
7.3	Results	112
7.3.1	Thermal characterization of PMMA	112
7.3.2	Surface roughness of PMMA films	112
7.3.3	Patterning	113
7.3.4	Spectromicroscopy	113
7.3.5	Development	114
7.4	Discussion	115
7.4.1	Thickness decrease	115
7.4.2	Effect of annealing	116
7.4.3	Critical dose	116
7.4.4	Detector calibration in STXM with PMMA	117
7.4.5	Determination of detector efficiency using the onset of cross-linking dose	118
7.5	Conclusions	119
7.6	Supplemental material	121

7.6.1	Create *.xyt files for the PatternGen routine within STXM_Control	121
7.6.2	Execution of *.xyt files with the PatternGen routine within STXM_Control	121
7.6.3	Derivation of a convenient form of the photon absorption rate	122
8.	Secondary electron deposition mechanism of carbon contamination	125
8.1	Introduction	126
8.2	Experiment	126
8.3	Results and discussion	127
8.4	Summary and conclusions	128
9.	Utility of the G value and the critical dose to soft x-ray radiation damage of polyacrylonitrile	129
9.1	Introduction	131
9.2	Experimental	132
9.3	Results and discussion	133
9.4	Conclusion	139
Part III: Characterization of an x-ray focal point		
10.	Measurement of the point spread function of a soft x-ray microscope by single pixel exposure of photoresists	141
10.1	Introduction	142
10.2	Methodology	143
10.2.1	Sample preparation	143
10.2.2	Scanning transmission x-ray microscopes, resist exposure, development and visualization	143
10.3	Results	144
10.4	Discussion	145
10.5	Conclusion	148
11.	Experimental investigation of beam heating in a soft x-ray scanning transmission x-ray microscope	150
11.1	Introduction	151
11.2	Experimental	152

11.2.1	Variable temperature sample holder device	152
11.2.2	Sample preparation	152
11.2.3	Microscopy	152
11.3	Results	153
11.3.1	Device accuracy	153
11.3.2	Measurement of beam-induced heating in STXM	153
11.4	Discussion	154
11.5	Conclusion	155
12.	Summary and future work	157
12.1	Reflection	157
12.2	Original contributions of this thesis	158
12.3	Future work	160
12.3.1	Further reduction of minimum feature size	160
12.3.2	Patterning at wavelengths relevant to industry	161
12.3.3	Focused deep x-ray lithography	164
12.3.4	Towards a dedicated x-ray writer instrument	165
12.3.4.1	Auto-focusing: Large areas, opaque substrates	166
12.3.4.2	Throughput	167
12.3.4.3	Software	168
12.3.4.4	Is it practical?	170
12.3.5	Functional nanofluidic devices	171
12.3.6	Deconvolution of the PSF from STXM images	171
12.3.7	Variable temperature sample holder	172
References		175
Appendices		183
A.1	Publications	183
A.2	Presentations	184
B.1	Software packages used for this thesis	188

LIST OF FIGURES

Chapter 1

1.1	The electromagnetic spectrum (from [B58] Table 1-1, © 2012 John Wiley & Sons Inc., used with permission)	1
1.2	Various classes of focusing optics for x-rays (adapted from [SS00] Table 1, © 2012 American Institute of Physics, used with permission)	4
1.3	Flow chart of various patterning techniques used in nanofabrication	6
1.4	Side view schematic depicting the general steps of the radiation-based lithography process	8
1.5	Photograph depicting the hand drawing of original artwork for an integrated circuit at 200x to 1000x final size (from [CCM66], © Mass Media Publications, Inc.)	9

Chapter 2

2.1	Schematic depicting the essential components of a synchrotron (adapted from [WSK&93] Fig. 3, © 2012 IBM Corp., used with permission)	20
2.2	Schematic diagrams of (left) a bend magnet and (right) an insertion device (from [R12], images provided by RIKEN, used with permission)	22
2.3	C 1s NEXAFS spectra of PAN (red), PMGI (green) and PMMA (blue) normalized to 1 nm thickness, along with their chemical structures	28
2.4	(Left) Schematic orbital energy diagram for the C atoms of PAN. (Right) The C 1s NEXAFS spectrum of PAN (black) normalized to 1 nm thickness, overlapped with the spectrum for 1 nm PAN calculated from the weighted sum of the atomic photoabsorption cross sections [HGD93] (red). The spectra have been rotated 90° to depict the relationship between orbital energy diagrams and NEXAFS spectra	29
2.5	Schematic depicting the essential components of a STXM (adapted from [A99] Fig. 9.21, © 2012 Cambridge University Press, used with permission)	35
2.6	(Top left) Photograph of a typical CXRO zone plate used throughout this thesis. A pencil eraser is included for size reference. The zone plate itself is indicated by the arrow. (Top right) Scanning electron micrograph of a CXRO zone plate. (Bottom) Scanning electron micrograph of the area within the red rectangle at top right, revealing the innermost zones and the buttressing system. The continuous area at right is part of the central stop	38
2.7	Side view schematic depicting the spatial coherence condition described by Eqn. 2.4. The Fraunhofer diffraction pattern (top right) is that of a square aperture	40
2.8	Side view schematic depicting the geometry of the foci of a Fresnel ZP in combination with a central stop and OSA (bl = beamline)	46
2.9	(Top) Schematic depicting the general arrangement and stacking of the stages and components of an ALS 5.3.2 type STXM (from [KTS&03] Fig. 2, © 2012 International Union of Crystallography, used with permission). (Bottom) Three dimensional CAD rendering of X07DA (courtesy of Dr. Benjamin Watts and Dr. Jörg Raabe, PSI, used with permission)	50

2.10	(Left) Schematic depicting the laser interferometer system of ALS 5.3.2 type STXMs. (Right) Photograph of 10ID-1 depicting the orthogonal interferometers and mirrors. The sample mount has been removed for clarity .	51
2.11	(Top) Photograph of the X07DA chamber and a portion of the beamline which includes the exit slits and shutter. (Left) Photograph viewing inside the X07DA chamber. (Right) Side view close up photograph of the ZP, OSA, sample and detector of 5.3.2.2 set for measurements at the C 1s edge .	52
2.12	(Left) Schematic depicting the essential components of an atomic force microscope (adapted from [RW09] Fig. 1, © 2012 John Wiley & Sons Inc., used with permission). (Right) Photograph of the Quesant Q-Scope 350 atomic force microscope .	54
2.13	Photograph of the JEOL JSM-7000F scanning electron microscope .	57

Chapter 3

3.1	Photographs depicting the transfer of polymer film pieces from the scribed mica to the surface of water .	61
3.2	(Left) Photograph depicting the transfer of a polymer film piece (dashed rectangle) from the surface of water to a Si ₃ N ₄ window. (Right) Photograph of a polymer film piece on Si ₃ N ₄ , covering the bottom right corner of the 1 mm x 1 mm window area .	62
3.3	C 1s NEXAFS spectral changes induced by sputter coating 0 nm Au (red), 1 nm Au (green) and 5 nm Au (black) onto 50 nm PMMA films (acquired using 5.3.2.2). .	75

Chapter 4

4.1	(a) The pattern used to drive the sample positioning stages relative to the focal point consists of nine 600 x 600 nm areas. (b) Each square in (a) is composed of 10 x 10 individual exposures spaced 60 nm center to center. (c) AFM image of the pattern directly written in PMMA with focused 300 eV monochromatic x-rays after development. (d) Expanded three dimensional view of the eighth area in (c). The measured center to center spacing of the crosslinked PMMA mounds is 60 ± 5 nm .	79
4.2	AFM image of the pattern directly written in PMGI with focused 300 eV monochromatic x-rays after development (the resolution of this image is equal to Fig. 4.1c) .	80
4.3	Plot of residual thickness, as determined by AFM after development, as a function of dose for PMMA and PMGI exposed to 300 eV monochromatic x-rays. 1 corresponds to the initial spun cast thickness, 0 being full removal .	80
4.4	(a) The elbow pattern used to drive the sample positioning stages relative to the focal point. (b) AFM image of the pattern directly written in PMMA with focused 300 eV monochromatic x-rays after development. Dose: 1 MGy. (c) Line out from the <i>dashed vertical line</i> in (b). (d) SEM image of the region outlined by the <i>dashed rectangle</i> in (b) demonstrating 40 ± 5 nm 1:2 developed lines .	82

4.5	SEM images of identical elbow patterns directly written in PMMA with focused 300 eV monochromatic x-rays after development (all images are the same scale). (a) An optimum dose of 1 MGy produces the narrowest positive mode features. The developed linewidth increases with increasing dose (b), 3 MGy, (c) 4 MGy. (d) An extensive positive mode region extends beyond the high dose (100 MGy) negative mode regions. The crosslinked 1:1 lines of (d) are 90 ± 5 nm wide	82
4.6	(a) AFM image of a developed PMMA pattern consisting of two single pixel exposures, each at a dose of 370 MGy. The <i>dots</i> in the centers are crosslinked PMMA. (b) SEM image of the <i>top left</i> single pixel exposure of (a). (c) SEM image of a developed PMGI pattern consisting of two single pixel exposures, each at a dose of 900 MGy. The <i>dots</i> in the centers are crosslinked PMGI	83
Chapter 5		
5.1	Schematic of a zone doubled zone plate made of HSQ resist and Ir (from [VGF&11] Fig. 1, © 2012 Optical Society of America, used with permission).	90
5.2	Scanning electron micrographs of 1 μm long lines of cross-linked PMMA with a pitch of 160 nm, made with various doses. a) Continuous 33 ± 4 nm lines, dose: 25 ± 4 MGy. b) Discontinuous 26 nm lines, dose: 24 ± 4 MGy. c) At a dose of 23 ± 4 MGy the cross-linked lines hardly form	92
5.3	Averaged AFM line trace of lines presented in Fig. 5.2a, recorded before Pt coating and SEM imaging	93
Chapter 6		
6.1	a) Optical micrograph of a PMGI/PMMA/Si ₃ N ₄ sample. b) X-ray absorption (NEXAFS) spectra of PMGI and PMMA, normalized to 1 nm thickness	100
6.2	a) Pattern A; access hole pattern for the top PMGI layer. b) Pattern B; channel pattern for the bottom PMMA layer. c) Exploded view drawing of the desired nanofluidic structure. a) and b) are on the same positional scale	100
6.3	STXM OD images at 288.5 eV of developed PMGI/PMMA/Si ₃ N ₄ samples patterned with different exposure times for the channel (a = 2 ms, b = 3 ms, c = 4 ms, d = 5 ms, e = 5 ms). Exposure time for the access holes for a – d was 14 ms. Access holes were not patterned for e). With a sufficient dose (3 MGy), the channel is fully cleared by the developer, if access holes are present. All images are on the same positional and OD scale	101
6.4	Quantitative component maps of a) PMGI and b) PMMA derived from SVD analysis of NEXAFS spectromicroscopy data, on the same positional and thickness scales. c) Non rescaled two color composite map of a) in green, and b) in red. Yellow corresponds to the presence of both polymer layers. d) Scanning electron micrograph of the nanochannel structure. c) and d) are on the same positional scale	102
6.5	Scanning electron micrographs of nanochannels tilted at 45° fabricated by chemically selective lithography. a) Under optimal dose conditions (3 MGy), the channel is cleared yet the PMGI overlayer remains intact. b) Pinholes appear at channel doses >3.5 MGy, or c) the PMGI overlayer is fully removed. All images are on the same positional scale	102

6.6	STXM OD and AFM images of nanochannels created with the same dwell time (5 ms) but different width. STXM and AFM images are on the same OD and Z scale, respectively, and all are on the same positional scale	103
6.7	A double T injector device fabricated by chemically selective lithography. a) Optical micrograph (100x, reflection) of the entire device. b) Non rescaled two color composite map (PMGI in green, PMMA in red) derived from SVD analysis of NEXAFS spectromicroscopy data. c) Scanning electron micrograph of the device. Pinholes occurred at the intersections of channels	105
Chapter 7		
7.1	Thermogram of as-received powdered PMMA in air. Ramp rate: 5 K / min	112
7.2	(a) Optical micrograph (transmission, 100x) of an annealed PMMA sample after patterning with 300 eV x-rays. (b) Atomic force micrograph of PMMA after exposure [same area/doses for (a) and (b)]. (c) Plot of the height reduction of individual patterned areas versus dose. Results from different pre-exposure thermal treatments [as-spun, vacuum dried (343 K, 2×10^{-2} Torr, 24 h), and annealed (423 K, 1 h)] are compared	113
7.3	C 1s NEXAFS spectra of PMMA extracted from individual areas patterned with different doses of 300 eV x-rays (color online): 0 MGy (red), 21 MGy (green), 60 MGy (blue), 150 MGy (black). The spectral trends were observed to be independent of the pre-exposure thermal treatments noted and dose rate ($73 - 1230 \text{ MGy s}^{-1}$)	113
7.4	(a) STXM OD image (288.4 eV) of an annealed PMMA sample patterned with various doses of 300 eV x-rays. (b) Plot of the OD at 288.4 eV values of individual patterned areas versus dose for different dose rates ranging from 73 to 1230 MGy s^{-1} . In each case the OD at 288.4 eV exponentially decreases with a critical dose of $62 \pm 8 \text{ MGy}$ derived from the indicated fit (solid line) to the average of all data sets. The separate data sets all agree within measurement uncertainty	114
7.5	(a) Atomic force micrograph of developed annealed PMMA showing several 600 nm x 600 nm areas patterned with various doses of 300 eV x-rays. (b) Measured heights of several “cross-linked” PMMA areas plotted versus dose for as-spun, vacuum dried (343 K, 2×10^{-2} Torr, 24 h), and annealed (423 K, 1 h) samples	114
7.6	Optical micrographs (reflection, 100x) of developed a) as-spun and b) annealed (423 K, 1 h) samples, patterned with identical doses (20, 40, 59, 99, 198, 296, 395, 593, 790 MGy) and dose rates (620 MGy s^{-1}) of 300 eV x-rays [(a) and (b) are on the same spatial scale]. Atomic force micrographs of developed (c) as-spun, (d) annealed and (e) vacuum dried (343 K, 2×10^{-2} Torr, 24 h) samples which received the same dose [(c), (d), and (e) are on equal height and spatial scales]	115
7.S-1	(a) The input file used for all patterning experiments. The white numbering serves to identify the areas and is not a part of the file. The dimensions of each square are 600 nm x 600 nm. (b) Each square in a) consists of 10 x 10 individual exposures with a pitch of 60 nm	123

7.S-2	Atomic force micrograph of a patterned area that had been previously imaged by STXM. The imaging parameters were 50/25/25 slits, 288.4 eV, 2 ms dwell, 60 nm pixel size; the dose associated with collecting the image was 1 MGy. The nine area pattern was executed within the area that had been STXM imaged. The outline of the single STXM image is visible, and the dose associated with it caused a 2 nm reduction in height	124
7.S-3	a) Atomic force micrograph of as-spun PMMA, patterned with 10ID-1. The patterned areas initially decrease and then increase with increasing dose due to carbon contamination. b) STXM OD at 300 eV measurements of each area in a) plotted versus dose. The carbon signal rises with dose, even above the virgin PMMA film	124

Chapter 8

8.1	Images of a 600 nm x 600 nm carbon deposit created by focused 300 eV soft x rays of a scanning transmission x-ray microscope (STXM), recorded by (a) atomic force microscopy in tapping mode, and (b) STXM at 293 eV [transmission measurement converted to optical density (OD)]	127
8.2	Amount of carbonaceous material deposited at a single energy (300 eV) vs fluence, quantified by atomic force microscopy (circles) and STXM (OD at 293 eV, triangles)	127
8.3	C 1s x-ray absorption (NEXAFS) spectrum of a carbon deposit (dots) compared to the amount of carbonaceous material deposited at constant fluence ($395 \pm 13 \text{ mJ/cm}^2$) at several specific photon energies, quantified by atomic force microscopy (circles) and STXM (OD at 293 eV, triangles)	127

Chapter 9

9.1	C 1s NEXAFS spectrum of a 62 ± 3 nm PAN film. The prominent feature at 286.8 eV is the $\text{C } 1s(\text{C}\equiv\text{N}) \rightarrow \pi^*_{\text{C}\equiv\text{N}}$ core electron transition	134
9.2	(a) STXM optical density (OD) image of several irradiated areas of a PAN film. (b) C 1s NEXAFS spectral changes induced by 300 eV x-rays. The signal at 286.8 eV decreases while new signals appear at 285 eV and 287.6 eV, and increase with dose. (c) The change in OD at 286.8 eV of PAN measured from images like (a) as a function of dose	135
9.3	The data from Figure 9.2c replotted as $(\Delta\text{OD}_{286.8 \text{ eV}}/\text{energy absorbed})$	137

Chapter 10

10.1	AFM topography image of a developed 100 single pixel exposure pattern in PMMA, made with ALS 11.0.2. Four separate images have been combined	143
10.2	High magnification AFM phase image of the 5000 ms single pixel exposure from the top right corner of Figure 10.1	144
10.3	Extracting the full point spread function from the AFM images of developed single pixel exposures. (a) Threshold-ed AFM phase image of the 5000 ms exposure. (b) The procedure used to make the 3D object (c) 3D view, of the outer surface of the stacked AFM images (the z-axis is the image number) made using IDL Slicer3	144

10.4	Horizontal cross section of the point spread function. The direction and width of the cross section are indicated by the dashed line in figure 10.3c. b) Intensity on a log scale, showing the maxima and minima	145
10.5	(a) Avg* from ALS 11.0.2 (Avg* is the negative of the average of the 100 aligned threshold-ed AFM images). (b) Illumination of the ZP at ALS 11.0.2 when the 100 point exposure was made. This image was made by (x,y) scanning the 72 μm diameter order sorting aperture (OSA) through a plane between the ZP and its focal point. Parts of the left and upper portion of the x-ray distribution (black areas) were unfortunately not included in the scan. (c) Avg* from CLS 10ID-1. (d) OSA scan for CLS 10ID-1. (e) Avg* from ALS 5.3.2.2 (f) OSA scan for ALS 5.3.2.2	147

Chapter 11

11.1	a) Front view of the variable temperature sample holder device, assembled, with two samples affixed. b) Back view, assembled. c) Front view, disassembled. d) Side view, mounted in ALS STXM 5.3.2.2 with zone plate, order sorting aperture and detector distances tuned for O 1s edge measurements	152
11.2	Optical microscope image of stearic acid confined between two Si_3N_4 windows. b) STXM optical density (OD) image, 320 eV, of the area outlined by the dotted line in a). c) Polarized optical microscope image of the area outlined by the dotted line in a)	153
11.3	STXM OD images, 288.0 eV, of palmitic acid confined between two Si_3N_4 windows at various temperatures. a) Solid at 25 °C. b) On raising the temperature throughout the image acquisition from 58 to 65 °C, the heterogeneous contrast characteristic of the solid began to distort at 61 °C. Contrast became homogenous at 63 °C. c) Liquid at 65 °C. d) Rapid cooling during image acquisition. All images are same position and OD scale	154
11.4	NEXAFS spectrum of stearic acid at 25 °C, in the region of the O 1s edge	154
11.5	STXM OD images, 532.2 eV, of stearic acid confined between two Si_3N_4 windows at various temperatures. a) Solid at 25 °C. b) Solid at 59 °C. c) On raising the temperature throughout the image acquisition from 59 to 70 °C, the image began to distort at 67 °C. Contrast became homogenous at 70 °C. d) Slow cooling during image acquisition. e) New crystalline pattern which formed after solidifying, 25 °C. All images are same position and OD scale. The grey rectangle in each image covers an extremely dense speck of material which has been omitted so that the contrast of the sample is enhanced	155

Chapter 12

12.1	Plot depicting the stepwise decrease of the exposure wavelength used in industrial lithography systems over time, along with the decrease in device minimum feature size over the same period (from [WK09] Fig 1.3, © 2012 McGraw-Hill, used with permission)	162
12.2	Scanning electron micrograph of developed PMMA patterned at 185 eV using STXM 11.0.2	163

12.3	Scanning electron micrograph of 600 nm x 600 nm holes in a 600 nm layer of PMMA on Si ₃ N ₄ patterned at 1 keV using 10ID-1	165
12.4	Comparison of the C 1s NEXAFS spectra of stearic acid in solid (blue) and liquid (red) phase, acquired at 11.0.2. The right plot has been rescaled to highlight the carbonyl peak shift	173

LIST OF TABLES

Chapter 1

1.1	Published demonstrations of direct write x-ray (>100 eV) patterning and lithography	11
-----	---	----

Chapter 2

2.1	The STXMs used within this thesis	36
2.2	Exit slit to zone plate distances of several operational STXMs	40
2.3	Soft x-ray STXMs in existence at the time of submission	49

Chapter 3

3.1	Comprehensive list of all materials used within this thesis	59
3.2	Glass transition and degradation temperatures of the polymers used in this thesis	62
3.3	The conditions used to prepare the thin polymer film samples used in this thesis	64

Chapter 4

4.1	Lithographic characteristics of PMMA exposed to 300 eV soft x-rays	81
4.2	Lithographic characteristics of PMGI exposed to 300 eV soft x-rays	81
4.3	Minimum developed feature widths created in PMMA	81

Chapter 7

7.1	Effect of thermal treatments on the surface roughness of PMMA samples as measured from atomic force micrographs	113
7.2	Measured detector efficiency (K) at 300 eV for various STXMs (measurements made between October 2010 and December 2011)	118

LIST OF ABBREVIATIONS AND SYMBOLS

5.3.2.1	STXM beamline 5.3.2.1, ALS, LBNL, Berkeley, California, USA
5.3.2.2	STXM beamline 5.3.2.2, ALS, LBNL, Berkeley, California, USA
11.0.2	STXM beamline 11.0.2, ALS, LBNL, Berkeley, California, USA
10ID-1	STXM beamline 10ID-1 (SM), CLS, Saskatoon, Saskatchewan, Canada
α	angle of radiation incident on a grating
β	angle of radiation diffracted from a grating
Γ	representation
$\Delta\lambda$	photon energy bandwidth
ΔOD	change in optical density
Δr	zone plate outer most zone width
Δz	depth of focus
λ	wavelength
μ	mass absorption coefficient
π	orbital antisymmetric with respect to rotation about the bond axis
ρ	density
σ	orbital symmetric with respect to rotation about the bond axis
σ_a	atomic x-ray photoabsorption coefficient
$\sigma_x(E)$	molecular x-ray photoabsorption cross section
φ	orbital
ψ	wave function
A	atomic weight; intensity scale factor in Ch. 9
A_0	distance from the front of the order sorting aperture to the sample
A_1	experimentally determined change in focal length with photon energy
a	absorbed dose
a_c	critical dose
ABB	Arthur Bourns Building, McMaster University
ACS	American Chemical Society
AFM	atomic force microscope
ALS	Advanced Light Source
BESSY II	Berliner Elektronenspeicherring-Gesellschaft für Synchrotronstrahlung
bl	beamline
BM	bend magnet
BMBF	Bundesministerium für Bildung und Forschung
c	speed of light in a vacuum
CAD	computer-aided design
CCD	charge-coupled device
CFI	Canada Foundation for Innovation
Ch.	chapter
CIHR	Canadian Institutes of Health Research
CLS	Canadian Light Source
Corp.	corporation
CXRO	Center for X-ray Optics
D	zone plate diameter; absorbed dose in Ch. 7
d	exit slit width; density in Ch. 7

D_s	diameter of the central stop in a zone plate
DMF	<i>N,N</i> -dimethylformamide
DOI	digital object identifier
DUV	deep ultraviolet
E	(photon) energy
E_e	electron energy
\vec{E}	electric vector of the photon
EBID	electron beam induced deposition
EPU	elliptically polarizing undulator
EUV	extreme ultraviolet
EUVL	extreme ultraviolet lithography
F	photon absorption rate
f	zone plate focal length
Fg	fibrinogen
$F_{ph}(E)$	number of incident photons per unit time per unit area
FWHM	full width at half maximum
G	groove frequency
GmbH	Gesellschaft mit beschränkter Haftung (limited liability company)
h	Planck's constant
HOMO	highest occupied molecular orbital
HPLC	high performance liquid chromatography
HSQ	hydrogen silsesquioxane
I	transmitted photon flux; transition intensity in Ch. 2.2.2
I_0	incident radiation (single energy measurement or spectrum)
ID	insertion device
IDL	Interactive Data Language
Inc.	incorporated
IPA	2-propanol (isopropyl alcohol)
IR	infrared
K	detector efficiency
K type	chromel-alumel
KB	Kirkpatrick-Baez
l	exit slit to zone plate distance
LBNL	Lawrence Berkeley National Laboratory
linac	linear accelerator
LMN	Laboratory for Micro- and Nanotechnology
LUMO	lowest unoccupied molecular orbital
M	number of molecules chemically transformed; molecular weight in Ch. 3.2.4
M_n	number average molecular weight
M_w	weight average molecular weight
m	diffraction order; mass in Ch. 2.1
MIBK	4-methyl-2-pentanone (methyl isobutyl ketone)
mp	melting point
MPI-IS	Max Planck Institute for Intelligent Systems
N	number of zones in a zone plate; number of ions produced in Ch. 9
N_A	Avogadro constant

NA	numerical aperture
NEXAFS	near edge x-ray absorption fine structure
NMR	nuclear magnetic resonance
NRC	National Research Council Canada
NSERC	Natural Sciences and Engineering Research Council of Canada
NSLS	National Synchrotron Light Source
NSLS-II	National Synchrotron Light Source II
NSOM	scanning near-field optical microscope
OD	optical density
OD_0	initial optical density
OD_1	optical density normalized to 1 nm thickness
OD_∞	residual optical density
OSA	order sorting aperture
p	phase space parameter
$P_{if}(E)$	number of electrons excited per unit time from the initial core state to a final state
PAN	polyacrylonitrile
PDMS	polydimethylsiloxane
PEC	poly(ethylene carbonate)
PET	polyethylene terephthalate
PLS	Pohang Accelerator Laboratory
PMGI	poly(dimethyl glutarimide)
PMMA	poly(methyl methacrylate)
PMT	photomultiplier tube
PPC	poly(propylene carbonate)
PS	polystyrene
PSF	point spread function
PSI	Paul Scherrer Institute
R^2	coefficient of determination
r_n	radius of the n^{th} zone of a zone plate
\vec{r}	sum of the linear moment operators of the electrons
RF	radio frequency
RMS	root mean squared
rpm	revolutions per minute
s	source size
SE	secondary electron
SEM	scanning electron microscope
SLS	Swiss Light Source
SPEM	scanning photoelectron microscope
SSRF	Shanghai Synchrotron Radiation Facility
SSRL	Stanford Synchrotron Radiation Lightsource
STM	scanning tunneling microscope
STXM	scanning transmission x-ray microscope
SVD	singular value decomposition
T	transmission; temperature in Ch. 11
T_d	thermal degradation temperature
T_g	glass transition temperature

<i>t</i>	thickness; exposure time in Ch. 7
TEY	total electron yield
UE46	STXM beamline UE46 (MAXYMUS), BESSY II, Berlin, Germany
UHV	ultra high vacuum
Und-L	linear polarizing undulator
UV	ultraviolet
UVSOR-II	Ultraviolet Synchrotron Orbital Radiation Facility
<i>V</i>	volume
<i>v</i>	frequency
<i>v/v</i>	volume to volume
wt%	weight percent
X07DA	STXM beamline X07DA (PolLux), SLS, PSI, Villigen, Switzerland
XANES	x-ray absorption near edge structure
XAS	x-ray absorption spectroscopy
XFEL	x-ray free electron laser
XPS	x-ray photoelectron spectroscopy
YOLO	you only live once
<i>Z</i>	atomic number
ZP	zone plate
ZPAL	zone plate array lithography

Chapter 1

Introduction

This chapter sets the context of this thesis, and begins with a discussion of some relevant, fundamental properties of x-rays and examples of their applications in materials analysis and materials processing. This is followed by an introduction to patterning and lithography, featuring several important applications, leading to examples involving focused x-rays. A short introduction to radiation chemistry is provided, which highlights the capabilities of STXM for unique radiation chemistry experiments. An overview of the chapters that follow concludes this chapter.

1.1 Tunable focused x-rays

X-rays are photons which occupy the portion of the electromagnetic spectrum from approximately 10 – 0.01 nm, or 100 – 100 000 eV (Fig. 1.1).

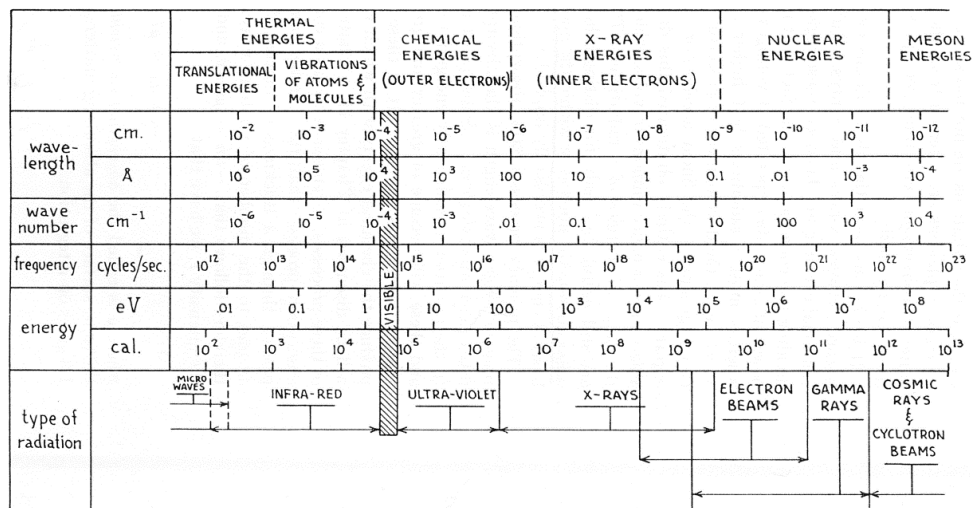


Figure 1.1: The electromagnetic spectrum (from [B58] Table 1-1, © 2012 John Wiley & Sons Inc., used with permission).

The absorption cross section for x-rays is low relative to visible or ultraviolet (UV) photons, therefore they penetrate deeply into matter. Röntgen was first to demonstrate this property by imaging the bones of a live human hand [R96]. In addition, their short wavelength allows them to resolve small features; the far field resolving power of a microscope, given by the Abbe criterion [A82] is,

$$resolution_{(x,y)} = \frac{\lambda}{2NA} \quad (1.1)$$

where λ is wavelength and NA is numerical aperture. The x-ray combination of high penetration and resolving power is well suited for microscopy. Micrographs of biological material with sub-10 nm resolution have been obtained by placing specimens between an unfocused x-ray source and an x-ray sensitive film [FST&77, KR85]. These are among the first and simplest demonstrations of x-ray microscopy.

Other properties of x-rays make them ideal for materials processing. X-rays have high energy due to their short wavelength, expressed by the Planck-Einstein relation [P01],

$$E = h\nu = \frac{hc}{\lambda} \quad (1.2)$$

where E is energy, h is Planck's constant, ν is frequency, and c is the speed of light in a vacuum. Expressing E in units of electron volts and λ in units of nanometres, we have,

$$E = \frac{1239.84}{\lambda} \quad (1.3)$$

Consequently, the majority of the possible interactions of x-rays with matter are ionizing processes which can induce chemical change. One of the largest materials processing applications of unfocused x-rays is sterilization (medical equipment, food, etc.) [I10]. Another application is deep x-ray lithography, where x-rays passed through patterned masks are used to machine micrometre scale metallic parts for micro-electrical/optical/mechanical systems [EM91]. The short wavelength of x-rays is also necessary for high resolution pattern transfer, and both applications utilize the penetration and ionization properties of x-rays. These examples fall within a larger field of research known as “radiation chemistry” which covers ionizing radiation-induced chemical changes in matter (Ch. 1.3).

Focusing x-rays was once thought to be impossible due to challenges which arise in optics fabrication, such as the almost negligible difference from unity in the refractive index of all materials at x-ray wavelengths, and the necessity to fabricate optical elements with accuracies comparable to the nanometre wavelengths of x-rays. The earliest demonstrations of x-ray focusing appeared in 1931 [J31] and 1933 [J33] involving bent crystals, and in 1947 involving a curved reflective surface [E47]. The field of x-ray optics research remains very active, perhaps more so now than at any other point in history. Several techniques have been developed and refined for focusing x-rays (Fig. 1.2).




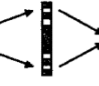
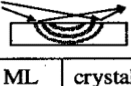

Bent mirror or crystal			Capillaries	Waveguides	Fresnel optics	Bragg-Fresnel Optics		Refractive optics
			Kreger 1948	Feng et al 1993	Baez 1952	Aristov et al, 1986 [2]		Snigirev et al, 1996 [9]
mirror	multilayer	crystal						
Kirkpatrick Baez, 1948	Underwood Barbee, 1986	Johann, Johansson, 1931-1933						

Figure 1.2: Various classes of focusing optics for x-rays (adapted from [SS00] Table 1, © 2012 American Institute of Physics, used with permission).

The condensed power of focused x-rays has vastly improved existing x-ray analysis techniques and enabled many new ones such as x-ray diffraction from samples inside diamond anvil cells to investigate matter at extreme pressures [IBP11]. Micro- and nano-focused x-ray beams have enabled the collection of high quality crystallographic data sets from very small crystals of difficult to crystallize molecules [H92]. Powerful materials analysis techniques such as x-ray micro-fluorescence have benefit from smaller spot sizes to resolve, identify and quantify ever smaller amounts of elements within ever smaller volumes [IBP11]. There are however few examples of focused x-rays in materials processing, beyond the millimetre scale beams used to treat certain types of cancer [HG06, EKL&09]. Micro- and nano-focused beams of ionizing radiation, namely electrons and ions, are used extensively for nanofabrication, especially the industrial scale manufacture of integrated circuits [B80]. The potential of focused x-rays for nanofabrication exists, but remains largely unexplored judging by the paucity of published examples (tabulated in the following section).

The first direct observation of synchrotron radiation occurred in 1947 [P83]. Synchrotrons were the first practical sources of broadly tunable x-rays. Tunable focused x-rays are especially powerful for materials analysis. Analysis at

specifically tuned wavelengths often presents advantages over other wavelengths. The electronic structure of materials can be explored through x-ray absorption spectroscopy (XAS) [S92]. Spatially resolved XAS can be used not only to locate and quantify the elements in a sample, but also to determine their chemical environment [AZC&92]. Techniques such as multi-wavelength anomalous diffraction in crystallography [H92] or resonant x-ray reflectivity [AH08] also exploit photon energy tunability.

Scanning transmission x-ray microscopes (STXM, described in Ch. 2.3) focus tunable, monochromatic x-rays into an intense spot – present generation instruments routinely achieve sub-30 nm Rayleigh criterion [A99] spot sizes. Samples are then positioned at the focal plane and raster scanned through the spot while the transmitted x-rays are acquired to build up images at x-ray photon energies. In addition, XAS can be performed by recording point spectra or image sequences over a photon energy range of interest. STXMs excel at characterizing thin sections of matter with a combination of high spatial (<30 nm) and photon energy (<0.1 eV) resolution. However, the novelty of this thesis lies in exploring the non-analysis possibilities of tunable focused x-rays using STXM. Tunable focused x-rays have been applied here to induce chemical and physical changes and directly pattern materials, primarily polymers. The irradiated areas were subsequently investigated using several types of microscopy including STXM, atomic force microscopy (AFM) and scanning electron microscopy

(SEM), as well as XAS. The research contained in this thesis falls within the general areas of nanofabrication via lithography, and radiation chemistry.

1.2 Patterning and lithography

Patterning involves exhibiting reproducible spatial control of a chemical or physical change on a surface or within a volume of material. There are many ways to pattern. A flow chart with some of the more prevalent patterning techniques is presented in Fig. 1.3.

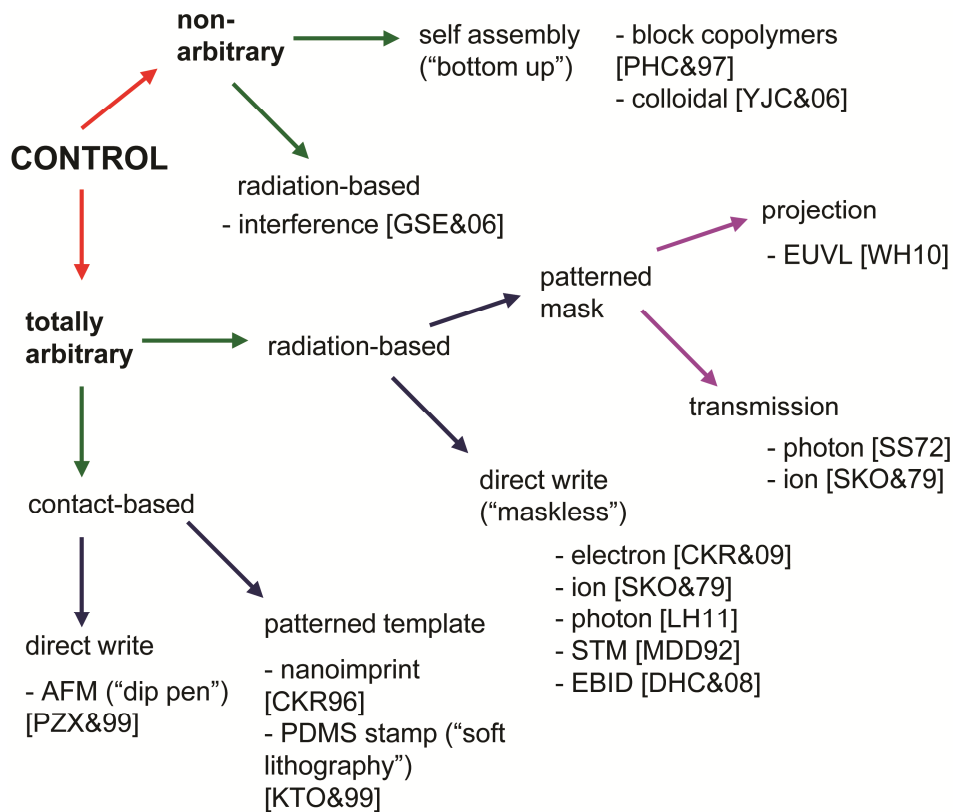


Figure 1.3: Flow chart of various patterning techniques used in nanofabrication.

Every technique has benefits and drawbacks. The choice of which technique to use depends on requirements such as desired degree of control, resolution,

instrument acquisition costs and patterning speed. The first step in lithography is the creation of a desired pattern in a sacrificial layer of material on a surface, followed by the subsequent transfer of that pattern onto or into the underlying substrate via a development process. The use of a post-exposure development step separates lithography from patterning in this thesis, however the terms patterning and lithography sometimes take on an overlapping meaning in the literature.

All patterning and lithography experiments in this thesis involve the radiation-based direct write method. To begin, a substrate is coated with a layer of radiation sensitive material termed the resist. Radiation is directed upon the resist in a controlled manner which causes changes to its chemical properties, patterning it into areas of irradiated and non-irradiated material. The sample then undergoes a development procedure, accomplished by immersing the entire sample in a suitable solvent. The chosen solvent may remove the irradiated resist, leaving behind the non-irradiated material (positive mode), or the solvent may remove the non-irradiated resist, leaving behind the irradiated material (negative mode). After development, the desired pattern exists as a mask of resist on the substrate. Development of the patterned resist is often a crucial step toward actual device fabrication. The radiation-based lithography process is outlined in Fig. 1.4.

This process was first disclosed in 1852 [T52]. While there has been much innovation with resists and developer formulations (for a historical review of resists see [D75]) and radiation sources over the last 150 years, the general steps

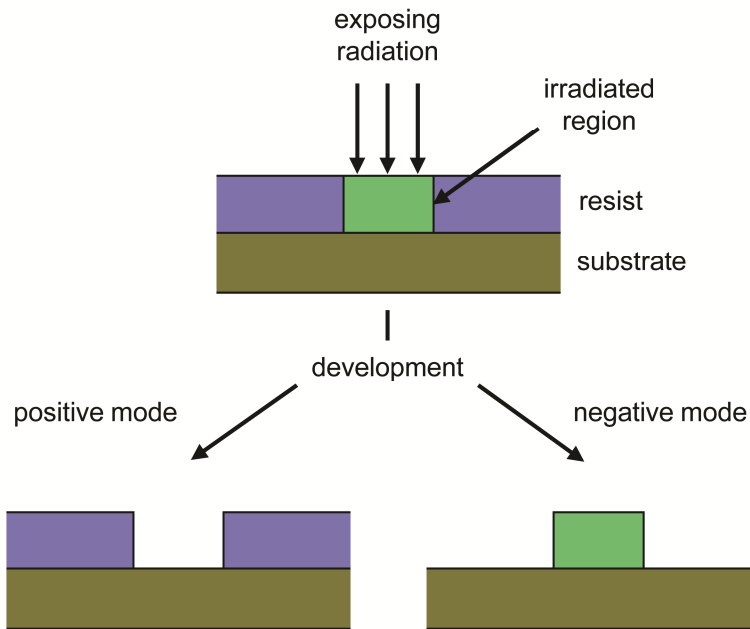


Figure 1.4: Side view schematic depicting the general steps of the radiation-based lithography process.

have not changed. Radiation-based lithography continues to be one of the most important methods for creating micrometre to nanometre scale structures for a wide variety of applications. It has enabled the fabrication of electronic devices on a massive scale with ever superior performance and reduced cost per function which society is increasing reliant upon. Arguably three of the most important steps that led to the information age in which we now live were enabled by lithography:

1) In the earliest electronic devices, the many individual components were connected together by point-to-point wiring. *Circuit boards*, fabricated by lithographic means (radiation-based patterned mask method), were revealed in a 1944 patent [E44]. Assembling devices by affixing the individual components to

assigned positions on a board immediately led to simpler, faster assembly and repair and more compact packaging.

2) In 1959 a patent was filed describing a *planar process* by which the individual electronic components themselves could be fabricated on inexpensive Si wafers [H59]. This process involves a series of lithographic steps again involving the radiation-based patterned mask method. The circuit designs were hand drawn on large boards (Fig. 1.5), and then reduced in scale by optical methods to create a set of patterned masks. Optical methods of scaling [GG70] provided a route to shrink the size of devices to micrometre dimensions, which made them faster simply via the shorter distance between components and also cheaper as many devices could be rapidly fabricated using less material.

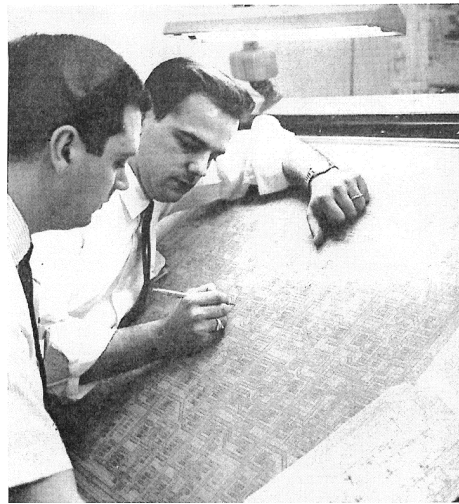


Figure 1.5: Photograph depicting the hand drawing of original artwork for an integrated circuit at 200x to 1000x final size (from [CCM66], © Mass Media Publications, Inc.).

3) In 1960, Möllenstedt and Speidel used the focused electron beam of an electron microscope to directly write sub-100 nm lines in a thin collodion film [MS60]. Eight years later a resist with a resolution comparable to the nanometre

focused beam was found [HHS68, H69]. Focused electron beam systems were then used to create *smaller patterned masks* for producing devices with sub-micrometre features. At present, the state-of-the-art in high volume integrated circuit manufacture involves focused electron beam lithography to create sets of patterned masks (up to 100 per integrated circuit at present) which are then illuminated with 193 nm photons from ArF lasers to produce devices with sub-30 nm features. Several books have covered the role of lithography in the electronics industry [TWB83, WK09].

By far the largest application of lithography is electronics production, however lithographic/patterning techniques have found hundreds of other applications. Lithographic techniques have been applied to record holograms [JHK&90], to produce microfluidic [DMS&98] and micromechanical devices [EM91], and to create advanced optics such as the zone plate lenses (described in Ch. 2.3.1) which enable STXM [OHV&04, JVP&07, CKR&09].

1.2.1 Focused (direct write) x-ray patterning and lithography

The introduction of the first published report of x-ray lithography reads, “X rays cannot be efficiently collimated or focused. As a result, X ray lithography is limited to shadow printing” [SS72]. This perspective has since been reinforced in the literature; at present, “x-ray lithography” is essentially synonymous with the patterned mask method and broadband synchrotron radiation. However there are indeed published examples of direct write patterning and lithography with

focused x-rays. The following is a comprehensive list of all examples in the peer reviewed scientific literature at present (Table 1.1).

Table 1.1: Published demonstrations of direct write x-ray (>100 eV) patterning and lithography.

Reference	Photon energy (eV)	Focusing method	Resist(s) used	Minimum feature size demonstrated
JWA&91	341	zone plate (STXM)	Not reported	300 nm
ZJL&95	317	zone plate (STXM)	PMMA	300 nm
PDC00	Broadband synchrotron	zone plate array	PMMA	500 nm
LGD&02	640	zone plate (SPEM)	LiF	500 nm
BJ03	525	zone plate (STXM)	PMMA	4 μ m
KHW&03	387	zone plate (SPEM)	thiol monolayers	10 μ m
AJZ&04	Not reported	zone plate	Shipley UV-III	67 nm
KHW&04	387	zone plate (SPEM)	thiol monolayers	10 μ m
KCH&05	380, 480	zone plate (SPEM)	thiol monolayers	10 μ m
MBD&05	450, 640	zone plate (SPEM)	LiF	200 nm
CHW&06	380, 480	zone plate (SPEM)	thiol monolayers	10 μ m
BAB&07	650	zone plate (SPEM)	LiF	340 nm
WSH07	288.4, 286.8, 290.4	zone plate (STXM)	PMMA, PAN, PPC, PEC	150 nm
WSH&07	288.4, 286.8	zone plate (STXM)	PMMA, PAN	150 nm
WBW&09	300, 528, 531.6, 534.1, 540.5	zone plate (STXM)	PET	600 nm
WML&09	300	zone plate (STXM)	PS, PMMA, Fg	600 nm
CKS&10	580	zone plate (STXM)	HSQ	90 \pm 14 nm
LH11	300	zone plate (STXM)	PMMA, PMGI	40 \pm 5 nm
LCK&11	7500	zone plate	ZEP520A-7	3 μ m
DGR&11	8000	zone plate	Au coated glass	190 nm
LH12c	282 – 300	zone plate (STXM)	C contamination	600 nm
LHT&12	300, 1000	zone plate (STXM)	PMMA	600 nm

Reports of direct write patterning and lithography with focused x-rays are scarce relative to those involving focused electrons or focused ions (both number in the thousands). There are several possible reasons for this. The first report of patterning with a focused electron beam (1960) demonstrated sub-100 nm features [MS60]. Electron beam writer systems were commercially available as early as

1970, and soon after sub-100 nm patterning was demonstrated with a focused ion beam [SKO&79]. In contrast x-ray optics capable of sub-100 nm focusing only became available in the mid to late 1980s, a development spurred by the founders of x-ray microscopy [KR85]. By that time electron beam lithography was a mature, established technology, while the raison d'être of the handful of instruments capable of sub-100 nm x-ray focusing throughout the 1980s and 1990s was advanced materials analysis. Perhaps it was not immediately clear that focused x-rays of any energy could provide advantages over a focused electron beam for sub-100 nm direct write patterning and lithography.

As outlined in Fig. 1.2, there are several methods by which x-rays can be focused to sub-micrometre spots. One dimensional focusing to 7 nm has recently been achieved in a long beam line with multiple Kirkpatrick-Baez (KB) focusing optics [MHK&10]. In principle, focused x-ray patterning and lithography could be accomplished with KB mirrors or other x-ray optics, yet all known examples (Table 1.1) involve a zone plate as the focusing element, almost always as part of an x-ray microscope (STXM, or a scanning photoemission microscope (SPEM)). Additionally, all examples except one involve a synchrotron as the x-ray source ([DGR&11] used an x-ray free electron laser (XFEL) [MT10]). There is more variety in sources and optics just outside the photon energy region defined here as x-ray (>100 eV). 82 nm features have been created in poly(methyl methacrylate) (PMMA) with zone plate focused 26 eV photons from a capillary discharge laser

[VBB&07], and 6 μm features have been created in PMMA with an off-axis parabolic mirror focusing 92 eV photons from an XFEL [BCN&09].

Aside from the examples in Table 1.1, there are comparably few examples of the use of zone plates in patterning and lithography. A zone plate has been used to demagnify a patterned mask using 589 nm photons [BBC87], and a similar system for use with 0.83 nm photons (1486 eV, Al K α line) has been patented [MI89]. A zone plate array lithography system (ZPAL) involving tens to hundreds of zone plates coupled to micromechanical shutters to control the parallel focused beams was proposed in the same publication [BBC87]. Prof. Henry I. Smith holds a patent on ZPAL [S97a] and has published at least 12 papers on such systems between 1996 and 2006 which operated at 193, 442, or 400 nm. The minimum feature size demonstrated was 115 nm in PFI-88 photoresist with 400 nm photons [CPB&05]. Prof. Smith is also the president of LumArray Inc. which markets ZPAL machines.

1.3 Radiation chemistry

Radiation chemistry is an area of chemistry concerned with the chemical effects of ionizing radiation on matter. The scope of systems in which radiation-induced effects have been observed is extremely broad, and many materials have been thoroughly studied. For example, there were more than 3000 scientific, technical, and review articles on the radiation chemistry of water as of 1971 [DD71]. The mechanisms of radiation induced chemical changes are often

complex, and the reaction pathways are not usually the elegant ones of organic and inorganic chemistry. Therefore, the scope of this thesis has been restricted to the effects of x-rays on synthetic polymers.

When ionizing radiation interacts with polymers the amount of energy absorbed often induces chemical (bond breakage and/or formation, cross-linking, main and/or side chain scission) and physical (mass loss, morphology, carbon contamination) changes. When the changes are perceived to be detrimental, they are usually referred to as “radiation damage”. For example, the imaging resolution attainable using ionizing radiation is ultimately limited by radiation damage [HBC&09]. The rapid degradation of some radiation sensitive polymers is undesirable for materials analysis using x-rays or other ionizing radiation as there is always a risk that the data collected may not be representative of the virgin sample. On the other hand, radiation-induced changes, such as the main chain scission of PMMA, are useful and relevant for patterning and lithography. There are many commercially available products/technologies that involve ionizing radiation and polymers, such as polymer-based radiation dosimeters [B82]. Heat shrinkable tubing (electron-irradiated polyethylene), used to tightly cover a variety of equipment for practical applications such as packaging and electrical work, was one of the first and most profitable radiation chemistry products [S73].

There is an enormous amount of literature on the radiation chemistry of polymers, with much of it dating from the late 1950s to the 1980s. Several books

have been written on the subject [B58, C60, D72]. PMMA is arguably the most studied of all the synthetic polymers, due in part to its important role in lithography for integrated circuit manufacture. No attempt will be made here to summarize the hundreds of works on the radiation chemistry of PMMA as there are already several extensive review articles on that topic which cover the effect of absorbed dose on molecular weight, the product molecules, the spectroscopic changes throughout the electromagnetic spectrum from nuclear magnetic resonance to inner shell ionization, proposed reaction mechanisms, and so on [H77, CMC&88, MC91].

The STXM was used throughout this thesis as a source of x-rays to perform radiation chemistry experiments. It is an attractive tool in this regard for several reasons. Accurate quantitation of radiation sensitivity (the absorbed dose required to produce a quantifiable change, following the Grotthuss-Draper law [KL84]) is essential in many technologies which involve ionizing radiation and polymers. Using STXM, x-ray flux can be precisely and reproducibly directed onto sub-100 nm sample areas. The shutter controlling the x-ray flux is both precise and fast; it can go from closed to fully open to closed in about 1 ms [KT04]. The x-rays are also monochromatic with an adjustable photon energy bandwidth that is routinely ≤ 0.1 eV and tunable over a range of several hundred electron volts. The mechanism of photoabsorption dominates over all other x-ray-matter interactions by orders of magnitude for most elements in the photon energy range explored in this thesis (over three orders of magnitude for carbon [HGØ80]).

Therefore any discrepancy between the rate of transmitted photons counted through a sample versus the rate measured through a blank at the same conditions can safely be assumed to have been photoabsorbed, depositing their total energy into a well defined sample volume. To summarize, absorbed dose can be administered reproducibly with high accuracy and spatial precision. In addition, the tunable photon energy available using STXM can be exploited for unique radiation chemistry and patterning/lithography studies. Finally, the STXM can be used to initiate radiation chemistry, and to analyse those areas by collecting images and spectra at x-ray wavelengths.

1.4 Thesis overview

The analysis methods which were used extensively throughout this thesis, including STXM, AFM and SEM are described in Ch. 2. The experimental details of sample preparation, patterning and lithography, STXM imaging and spectroscopy are covered in Ch. 3. The remaining chapters have been grouped into three parts.

The theme of **Part I** is nanofabrication with focused x-rays, beginning with Ch. 4 which builds upon the Ph.D. thesis work of Dr. Jian Wang [W08]. Before this thesis work began, the best minimum feature size demonstrated in our focused x-ray patterning experiments was about 150 nm, despite direct writing with a much smaller spot size (43 nm Rayleigh criterion). The incorporation of a post-exposure development step is described in this chapter which significantly

reduced the minimum feature size, ultimately leading to a new record of 40 ± 5 nm features in a thin film of PMMA [LH11]. Another important advance described in Ch. 4 is that a “radiation spreading” phenomenon, by which patterned features become wider with increasing dose, is shown to be related to the point spread function (PSF) of the optical system and not the polymeric resists [LH11]. The performance of focused x-rays relative to other direct write radiation-based lithography techniques is discussed and the potential for practical applications is addressed. The work in Ch. 5 describes our best effort to demonstrate the lowest possible feature size. 33 ± 4 nm features were achieved in PMMA using a special zone doubled zone plate in combination with a cold development procedure, surpassing our previous record. Finally, Ch. 6 describes a fabrication scheme that takes advantage of the photon energy tunability available using STXM. Sub-100 nm sealed nanofluidic channels were fabricated in carefully selected polymer bilayers by patterning at multiple wavelengths, which we have termed “chemically selective patterning”. The design rules for nanochannel formation were also investigated and are discussed in this chapter [LH12b].

Part II has a general theme of radiation chemistry of polymers. In Ch. 7 we took a deeper look at the radiation-induced changes that occur in PMMA, and their dependence on conditions such as dose rate and pre-exposure thermal treatments. A discrepancy found in the literature involving the radiation sensitivity of PMMA was explored in depth. From these experiments, a useful method to determine the detector efficiency of a STXM was developed, which

was then carried out at several STXM facilities [LHT&12]. Ch. 7 also outlines the problem of carbon contamination. In Ch. 8, the photon energy tunability of STXM was again exploited in an experiment designed to reveal the mechanism of carbon contamination [LH12c]. Ch. 9 presents our findings on x-ray induced changes to polyacrylonitrile (PAN), with a discussion that centres on identifying and correcting a misapplication of radiation damage sensitivity units in the literature.

The theme of **Part III** is characterizing the optical and thermal properties of the sub-100 nm focal spot of the STXM, beginning with Ch. 10 which returns to the issue of “radiation spreading” touched on in Ch. 4. A method is presented to extract the full PSF of the STXM from a series of single pixel exposures in a thin film of PMMA. This measurement was carried out at several STXMs with the important observation that the PSF was never found to be fully symmetric as diffraction theory predicts [LTH11]. The possible significance of beam-induced sample heating is addressed in Ch. 11. Though the temperature inside the STXMs when patterning was very stable at 25 ± 2 °C, it remained possible that the amount of energy involved in imaging and/or patterning could cause a local rise in temperature and play a role in the radiation-induced processes. A variable temperature sample holder was constructed to experimentally determine the rise in temperature, which was found to be negligible (<1 °C) [LH12a]. A summary of the original contributions contained in this thesis and a list of promising avenues of further study are provided in Ch. 12, followed by References and Appendices.

Chapter 2

Methods

The major analysis techniques, instrumentation and measurement conditions used throughout this thesis are described in this chapter. All of the works contained in this thesis involve a STXM, the operation of which is not considered to be common knowledge among chemists at this time. Therefore extensive descriptions of STXMs and their synchrotron x-ray sources are provided. Overviews of NEXAFS spectroscopy and AFM are also included with emphasis on those particular aspects which were exploited in this thesis. This chapter concludes with a brief description of SEM.

2.1 Synchrotrons

A synchrotron is a machine that circulates electrically charged particles at extremely high velocities. The essential components of a synchrotron are depicted in Fig. 2.1. Particle bunches from a linear accelerator (“linac”) are injected into a tube (the “ring”) which is under ultra high vacuum (UHV, generally $\leq 10^{-9}$ Torr) to minimize collisions with residual gas molecules [A99, W03]. Large dipole electromagnets (“bend magnets” (BM)) deflect the particles and keep them circulating in a closed orbit. Additional focusing and steering electromagnets (quadrupoles, hexapoles, octopoles) placed around the ring are used to control the trajectory and the transverse shape of the circulating particle bunches. The arrangement of these electromagnets is known as the “magnetic lattice”.

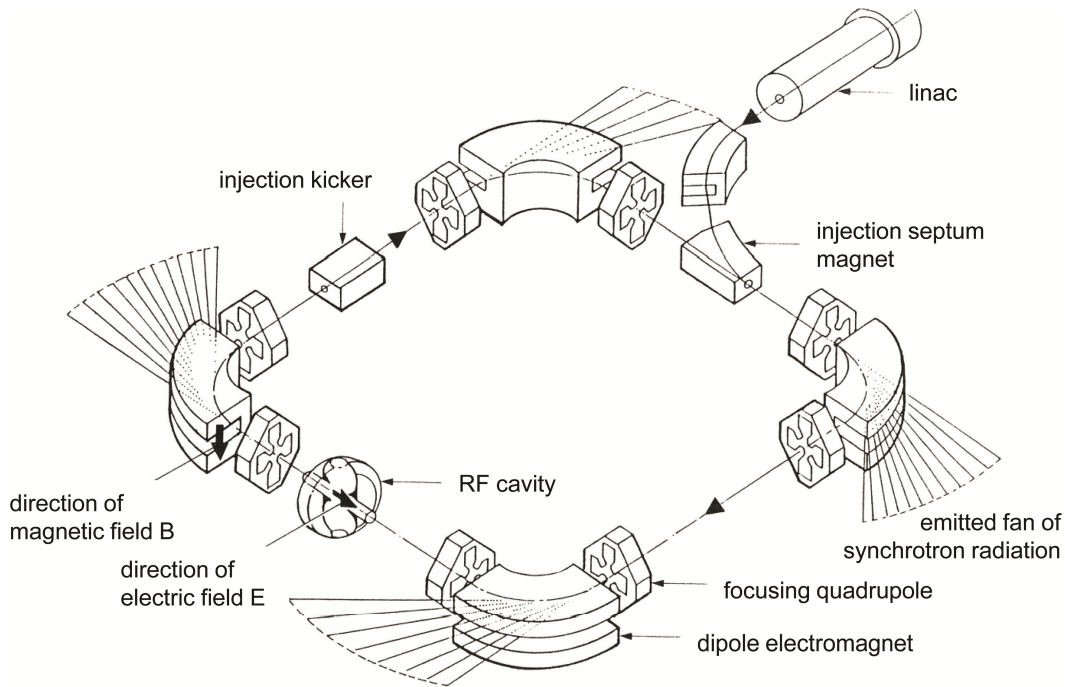


Figure 2.1: Schematic depicting the essential components of a synchrotron (adapted from [WSK&93] Fig. 3, © 2012 IBM Corp., used with permission).

The particle bunches make multiple passes through a radio frequency (RF) cavity which controls their velocity. The fields of the magnetic lattice are synchronized to the ramping of the frequency of the RF cavity, and this is the origin of the “synchro” in synchrotron. The particles commonly reach kinetic energies which are “relativistic”. A particle becomes relativistic when its kinetic energy is about equal to or greater than its rest mass (for electrons, $E = mc^2 = 0.511$ MeV). The kinetic energy of the electrons circulating in the Advanced Light Source (ALS) synchrotron at Lawrence Berkeley National Laboratory (LBNL) is 1.9 GeV. This works out to a velocity which is only about 11 m/s less than c ! Many different charged particles have been accelerated using synchrotrons. For example, the Large Hadron Collider near Geneva, Switzerland, is a

synchrotron which accelerates protons and Pb ions. The Advanced Photon Source near Chicago, USA is a synchrotron which uses positrons or electrons [RMF&97]. Synchrotrons are commonly used for high energy particle physics experiments and the production of synchrotron radiation.

2.1.1 Synchrotron radiation

Charged particles emit electromagnetic radiation when accelerated. This can be described using classical physics and is summarized in Maxwell's equations [GP75]. If the charged particles are moving at relativistic speeds when accelerated, the emitted radiation is highly collimated (narrow angular spread) in the forward direction, perpendicular to the acceleration vector, and the emission spectrum is shifted toward higher frequencies (higher photon energy i.e. into the x-ray and gamma ray region of the electromagnetic spectrum). This is known as synchrotron radiation, and was named as such because it was first directly observed (visually) emanating from a synchrotron in 1947. Synchrotron radiation is not exclusive to synchrotrons; it has since been observed as a product of astronomical phenomenon [WBH01, S10] and can be produced by other machines such as XFELs [MT10]. The pivotal events leading up to the visual discovery can be found elsewhere [B88a], and the personal recollections of those who witnessed this event have also been published [P83].

In a synchrotron, the acceleration necessary to produce synchrotron radiation is centripetal and induced by BMs (Lorentz force), and in addition,

insertion devices (ID) such as wigglers and undulators. These are periodic magnetic structures, consisting of two or more rows of magnets in which the relativistic particles undergo oscillatory motion (Fig. 2.2).

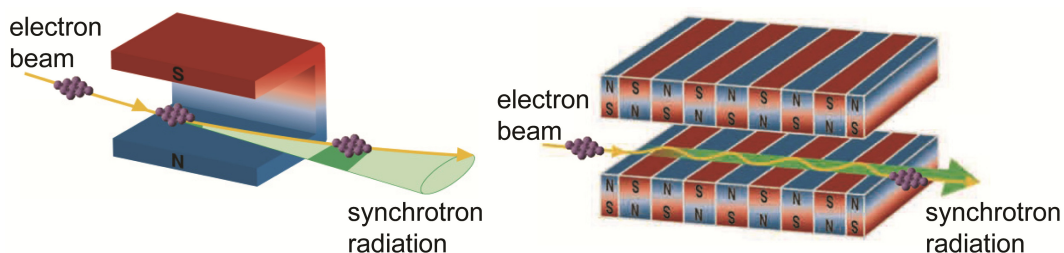


Figure 2.2: Schematic diagrams of (left) a bend magnet and (right) an insertion device (from [R12], images provided by RIKEN, used with permission).

They are called IDs because they are “inserted” into straight sections of the ring between BMs. Their only function is to produce synchrotron radiation, whereas BMs are an integral part of the machine and the radiation happens to be a desirable by-product of their primary function. Provisions can be made on synchrotrons so that the radiation emanating from BMs and IDs is allowed to travel down evacuated pipes called “beamlines”. Beamlines often contain mirrors, gratings, slits, intensity choppers, etc., and are meticulously designed to prepare the radiation for certain experiments while protecting the workers from radiation exposure. Experimental end stations which make use of the radiation (e.g. STXM) can be temporarily or permanently attached onto beamlines.

2.1.2 Synchrotron light sources

A synchrotron light source is a facility, often organized at a national level, which produces and utilizes synchrotron radiation. The first generation facilities

were designed and operated primarily as particle accelerators. The synchrotron radiation produced was essentially a by-product, and provisions were made to access it at the request of interested scientists. The earliest facilities were not optimum with respect to producing synchrotron radiation but still produced outstanding science. An example of a first generation facility still in operation today is the Cornell High Energy Synchrotron Source which is parasitic to an electron-positron collider. The success of first generation machines led to a wave of second generation synchrotrons in the late 1970s and the 1980s. These designs were dedicated solely to producing synchrotron radiation. A typical second generation facility is the National Synchrotron Light Source (NSLS, Brookhaven National Laboratory, Upton, USA). While these facilities greatly expanded the field of synchrotron science, they were designed primarily to exploit BM radiation. The first IDs were introduced in the early 1980s, after many of the second generation facilities had committed to their specific ring and magnetic lattice designs.

The first third generation synchrotrons were completed in the early 1990s (e.g. the ALS had its first operational beamline in 1994). These facilities are again fully dedicated to producing synchrotron radiation with a focus on increased brightness. This has been primarily accomplished primarily through decreased emittance¹ of the particle beam in the ring, especially in the horizontal direction,

¹ Emittance (nm-rad) is a measure of the phase space of the electron beam – the product of the angular divergence and lateral size. The brightness of a synchrotron is directly related to the ring emittance.

and the incorporation of long straight sections between the BMs for IDs. The maximum brightness of synchrotron sources has improved by 15 orders of magnitude from the first generation to present third generation machines [BBC&10]. Third generation synchrotron light sources actually consist of two synchrotrons with the same essential parts as shown in Fig. 2.1. The first synchrotron (the “booster ring”) accelerates particle bunches from the linac to the desired final speed. These are then transferred into another, larger diameter ring known as a “storage ring”. Storage rings are technically synchrotrons but their RF cavities only serve to maintain a constant particle velocity by replacing the energy lost through the synchrotron radiation process. All of the synchrotrons used in this thesis were third generation electron synchrotrons. These were the ALS, at LBNL, Berkeley, USA; the Canadian Light Source (CLS), Saskatoon, Canada; the Swiss Light Source (SLS), at the Paul Scherrer Institute (PSI), Villigen, Switzerland; and the Berliner Elektronenspeicherring-Gesellschaft für Synchrotronstrahlung (BESSY II), Berlin, Germany.

2.1.3 Properties of synchrotron radiation from synchrotron light sources

Synchrotron radiation has several distinguishing properties: 1) The radiation is *tunable*; BMs and wigglers emit a broad spectrum which can be tuned over almost the entire electromagnetic spectrum from THz and infrared (IR) to hard x-rays >100 000 eV. The spectrum of undulator emission is sharply peaked at periodic energies (a fundamental and many harmonics) but the peak positions

can be adjusted over a wide range by adjusting the undulator gap (the distance between the rows of magnets). 2) *Brightness*, the measure by which the properties of a radiation source are characterized, is the number of photons emitted per second, per bandwidth, per unit solid angle, and per unit area of the source (photons/s/0.1% bandwidth/mrad²/mm²) [MHK&05]. Brightness is an intrinsic property of the radiation source and cannot be improved with subsequent optics. Synchrotrons are the highest average brightness sources of radiation available today for extreme ultraviolet (EUV) and shorter wavelengths [R12]. 3) Synchrotron radiation is *extremely collimated* by nature. 4) The radiation is *polarized*; radiation from a BM in the plane of the synchrotron orbit is linearly horizontally polarized, while that above and below this plane is partly circularly polarized. Certain IDs such as elliptically polarizing undulators (EPU) can provide full control of the polarization from 0 – 180° linear, left or right circular, and any desired elliptical polarization via adjustable rows of magnets. 5) Finally, the radiation has a *pulsed* time structure; the RF cavity that maintains the particle energies also forms potential wells (“buckets” or “packets”) which cause the electrons to form into bunches. These bunches passing through BMs or IDs in turn create pulsed photon emission with pulse widths of 10 – 100 ps. The pulsed structure can be exploited to probe dynamic processes that take place on a similar temporal scale. The properties of the synchrotron radiation such its spectral, intensity, polarization, spatial and temporal distributions, can be predicted with high accuracy from the properties of the accelerator used [A99, W03].

2.1.4 Modes of operation

There are several modes of synchrotron light source operation. In multi-bunch mode, several hundred electron bunches circulate in the storage ring. Although the ring is under UHV, electrons are gradually lost over time through interactions with stray gas molecules and other processes, and these losses follow an exponential decay curve with lifetimes which can be anywhere from 30 min to 50 h. The photon flux also decays as it is directly proportional to the electron beam current. After several hours the electron beam is “dumped” and the storage ring is refilled to regain the lost flux. The CLS and BESSY II operated in multi-bunch mode for all experiments in this thesis.

In top-up mode, electrons are injected into the storage ring from the booster ring every 30 s or so to offset the losses described above. The photon flux is always high and effectively constant in this mode; the electron beam current can remain constant for days. In addition the stability of the storage ring and beamline optics generally improves due to the effectively constant thermal loads. The ALS and SLS operated in top-up mode for all experiments described in this thesis, which was the preferred mode for STXM experiments.

Another common operational mode is single- or few-bunch. This is essentially the same as multi-bunch, except there is one or just a few bunches circulating in the storage ring, resulting in increased time separation between photon pulses. This is advantageous for experiments which exploit the pulsed nature of synchrotron radiation at the cost of greatly decreased average photon

flux. None of the experiments described in this thesis were performed in few-bunch mode due to the low photon flux.

2.2 NEXAFS spectroscopy

2.2.1 Overview

Near edge x-ray absorption fine structure (NEXAFS), synonymous with x-ray absorption near edge structure (XANES), is a spectroscopy involving transitions of core (i.e. inner shell) electrons. To collect a NEXAFS spectrum, materials are placed in the path of a monochromatic x-ray beam which is then scanned in photon energy. While the NEXAFS spectra in this thesis were all recorded by measuring the photons transmitted through samples (and subsequently applying the Lambert-Beer law), spectra can also be recorded by measuring the emitted electrons (total electron yield, sample current, Auger) or emitted photons (x-ray fluorescence, optical). Core electron ionization edges are encountered as the photon energy is scanned which are observed as sharp increases in x-ray absorption. These “absorption edges” (or simply “edges”) occur at photon energies which are characteristic of specific elements and specific inner shell energy levels. For instance, the C 1s edge is always encountered between 284 – 290 eV, the O 1s between 530 – 536 eV, the Fe 2p between 704 – 710 eV, etc. Thus NEXAFS is an element specific spectroscopy. The approximate locations of core absorption edges for all but the highest atomic number elements have been tabulated [TAG&09]. Sharp absorption features (i.e. fine structure) are

often observed in the immediate vicinity of an absorption edge; a typical NEXAFS spectrum from low to high photon energy consists of a featureless pre-edge region, a few sharp peaks (often the most intense features), followed by a few broad ones and finally a featureless post-edge region. The C 1s NEXAFS spectra and chemical structures of three polymers used in this thesis, PAN, poly(dimethyl glutarimide) (PMGI) and PMMA, are presented in Fig. 2.3.

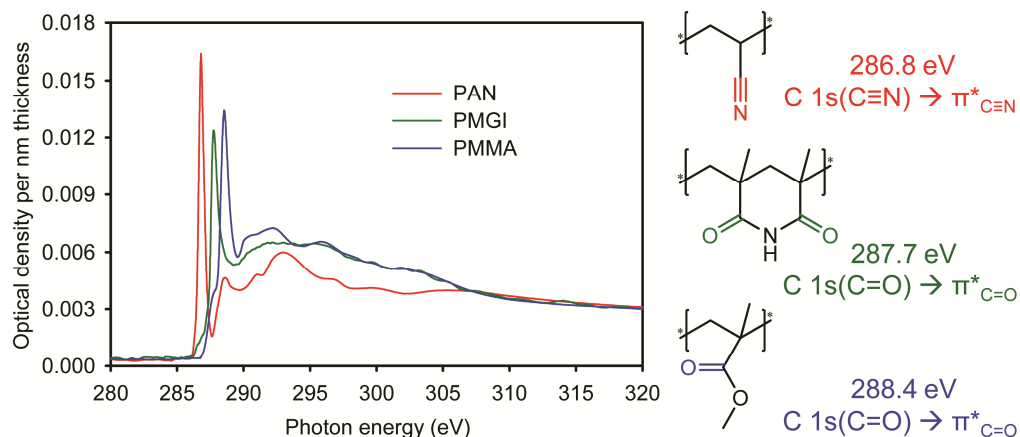


Figure 2.3: C 1s NEXAFS spectra of PAN (red), PMGI (green) and PMMA (blue) normalized to 1 nm thickness, along with their chemical structures.

The NEXAFS spectrum of a molecule can be loosely considered as a map of its unoccupied electronic structure and is related to its chemical composition; the fine structure is due to unoccupied or partly occupied electronic energy levels (orbitals, in the context of molecular spectroscopy, or empty bands in the context of extended solids) that lie near or just above the ionization potential. An electron from a core orbital (ground state) can be promoted into these unoccupied or partly occupied energy levels (excited state) via the energy obtained through resonant absorption of an x-ray photon i.e. photoabsorption. Conversely, there has to be an unoccupied state available for a core electron to go into if there is to be any

absorption event at the given photon energy. The relationship between schematic orbital energy diagrams and a typical NEXAFS spectrum (e.g. PAN) is presented in Fig. 2.4.

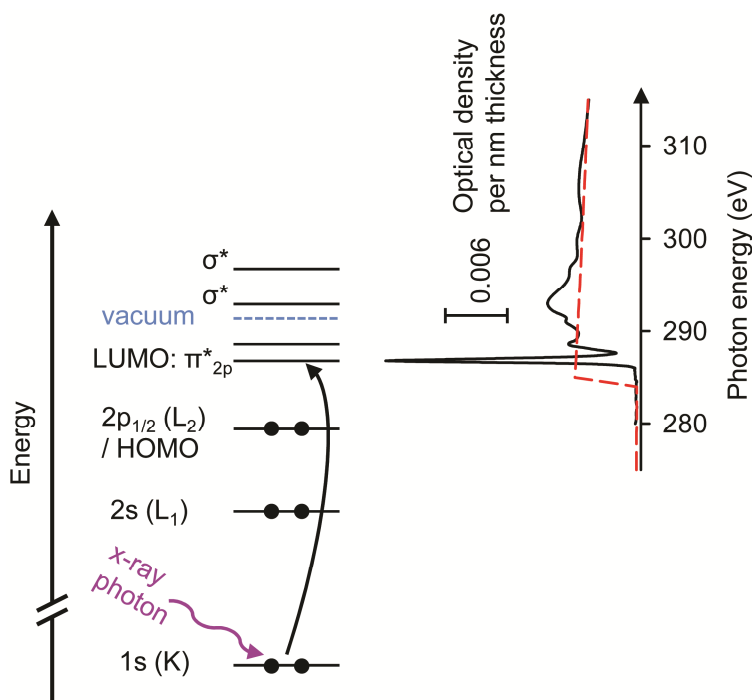


Figure 2.4: (Left) Schematic orbital energy diagram for the C atoms of PAN. (Right) The C 1s NEXAFS spectrum of PAN (black) normalized to 1 nm thickness, overlaid with the spectrum for 1 nm PAN calculated from the weighted sum of the atomic photoabsorption cross sections [HGD93] (red). The spectra have been rotated 90° to depict the relationship between orbital energy diagrams and NEXAFS spectra.

2.2.2 X-ray absorption theory

The probability for photoabsorption is described by the photon energy dependent x-ray absorption cross section $\sigma_x(E)$, which is the number of electrons excited per unit time from the initial core state to a final state $P_{if}(E)$, divided by the photon fluence, $F_{ph}(E)$, the number of incident photons per unit time per unit area,

$$\sigma_x(E) = \frac{P_{if}(E)}{F_{ph}(E)} \quad (2.1)$$

The intensity of a NEXAFS transition I is proportional to $P_{if}(E)$ and can be derived from a variation of Fermi's "Golden Rule" [F50],

$$I = P_{if}(E) \approx \left| \langle \psi_f | \vec{E} \cdot \vec{r} | \psi_i \rangle \right|^2 \cos^2 \theta \quad (2.2)$$

which describes a transition from an initial state $|\psi_i\rangle$ to a final state $\langle \psi_f |$ induced by a time-dependent perturbation, in our case, a resonant electromagnetic wave/photon, where \vec{E} is the electric vector of the photon, \vec{r} is the sum of the linear moment operators of the electrons, and θ is the angle between \vec{E} and \vec{r} . A full derivation of Eqn. 2.2 can be found in [S92].

2.2.3 Peak widths and assignment

The natural width of the absorption peaks is proportional to the lifetime of the excited states which can be derived from the Heisenberg uncertainty principle [S92]. Essentially, sharper absorption features are associated with long excited state lifetimes, which are on the order of $10^{-16} - 10^{-14}$ s. A photon energy resolution of ≤ 0.1 eV is required to realise all the subtleties in the NEXAFS spectra of polymers, while an energy resolution of ≤ 0.05 eV will most likely not reveal additional features [AU02]. All STXMs used to acquire the NEXAFS spectra in this thesis had energy resolutions ≤ 0.1 eV.

NEXAFS peaks are often assigned in terms of the symmetry of the final states, which are formally determined by a group theoretical analysis.

The probability of creating any specific final state is determined by the transition dipole moment, $\langle \psi_f | \vec{E} \cdot \vec{r} | \psi_i \rangle$. For molecules with a totally symmetric ground state ($|\psi_i\rangle \in \Gamma_{\text{TS}}$, all those investigated in this thesis), the electric dipole allowed transitions are those in which the final state is constructed from the core level and a ground-state-unoccupied level, where $|\psi_f\rangle = |(\varphi_{\text{core}}^{-1}, \varphi_{\text{unocc}})\rangle \in \Gamma_{\vec{E}\cdot\vec{r}}$. For spectra involving 1s core level excitation (all those studied in this thesis), where $\varphi_{1s} \in \Gamma_{\text{TS}}$, the requirement for a dipole allowed transition is that the unoccupied orbital belongs to the same irreducible representation as that of the dipole operator, $\varphi_{\text{unocc}} \in \Gamma_{x,y,z}$. The excitation features are typically labelled as either σ (with the un- or partly occupied orbital symmetric with respect to rotation about the bond axis), or π (with the un- or partly occupied orbital antisymmetric with respect to rotation about the bond axis). In addition to the formal group theory selection rules, among all possible allowed NEXAFS transitions the intense ones are those where the unoccupied orbital has a large density on the atom where the core level is excited. For 1s NEXAFS, this is equivalent to saying the spectra are dominated by unoccupied levels with a strong 2p contribution at the core-excitation site. An important factor in determining the energetics of NEXAFS transitions is the influence of the core hole. Typically the core hole stabilizes the final state; the valence electrons reorganize (relax) to the new core hole potential, thereby lowering the transition energy relative to that expected from a ground state frozen orbital/band approach (i.e. the sudden approximation,

which assumes that the transition energies are given simply by the difference between the unperturbed orbital energies). The core hole can also strongly distort the spatial distributions of the unoccupied levels [WRH92].

The assignment of the observed peaks to specific excited states can be complicated, and is often hotly debated [P99]. The accepted assignments for some molecules have changed multiple times [FU05] as the instrumentation, data collection and calculation methods, etc., have improved remarkably since the first NEXAFS measurements of the 1980s. Peak assignment can often be aided by comparing the spectrum of a material to those of chemically similar reference compounds i.e. compounds containing similar functional groups or other structural motifs. Online compendiums of core excitation spectra of gas phase small molecules, amino acids and other molecules, and polymers are maintained by the groups of Hitchcock, Jacobsen and Ade, respectively, and serve as an excellent starting point [HJA12].

The symmetry of the excited state giving rise to a spectral feature can sometimes be determined using a pure long range oriented sample and linearly polarized x-rays; I depends on θ , the angle between \vec{E} and the transition dipole moment (Eqn. 2.2). The peak intensities of final states of σ symmetry are maximized when the electric vector is aligned parallel with the bond axis, while those of π symmetry are maximized when the electric vector is perpendicular to the bond axis [RLR86, FU05].

The photon energy of NEXAFS features can be indicative of the bonding environment through correlation diagrams [UA02]. For example, the most intense feature in the C 1s NEXAFS spectrum of PMMA is the C 1s(C=O) \rightarrow $\pi^*_{\text{C=O}}$ peak at 288.4 eV (Fig. 2.3). The most intense peak of PMGI is also the C 1s(C=O) \rightarrow $\pi^*_{\text{C=O}}$, but it appears at 287.7 eV (Fig. 2.3). The bonding environment of the C atom of the carbonyl bond in PMMA is O–C=O, while in PMGI its N–C=O. The 0.7 eV energy difference is due to the different electronic environment of the carbonyl group. O is more electronegative than N, which reduces the electron density around the carbonyl C atom in PMMA relative to PMGI. In response, the carbonyl C atom of PMMA has a tighter hold on its electrons, thus requiring greater energy to promote one from PMMA. The same electronegativity dependent trends are evident in x-ray photoelectron spectroscopy (XPS) correlation diagrams [BG03].

2.2.4 Additional properties

The integrated intensities of NEXAFS spectral features have been demonstrated to be quantitative [AH08]. Thus, if a NEXAFS feature can be unambiguously assigned to a certain functional group, that signal is proportional to the quantity of that functional group present in the volume sampled. Likewise, the intensity of the continuum signal is proportional to the total amount of that element present in the volume sampled. In this thesis, the NEXAFS spectra of polymers were viewed as being indicative of radiation-

induced chemistry, and were monitored as a function of dose. NEXAFS was also used for chemical mapping [AZC&92] i.e. making x-ray images with the STXM at photon energies corresponding to absorption resonances which might be exclusive to one component/bond over others present in the sample. The vast majority of NEXAFS spectra contained in this thesis are at the C 1s edge, with some collected at the O 1s edge. Several review articles have covered the many other applications of NEXAFS [KJH95, HJW07, AH08].

2.3 Scanning transmission x-ray microscope

Scanning transmission x-ray microscopes (STXM) focus tunable, monochromatic x-rays into an intense spot – present generation instruments routinely achieve 30 nm spot size (Rayleigh criterion) using zone plate lenses. Samples are then positioned at the focal plane and raster scanned through the spot using piezo and/or mechanical stages while the transmitted x-rays are acquired to build up images at x-ray photon energies. In addition, NEXAFS spectra can be acquired by recording point spectra or image sequences over a photon energy range of interest. STXMs excel in characterizing thin sections of matter with a combination of high spatial (<30 nm) and photon energy (<0.1 eV) resolution, but they can also be used for direct write x-ray patterning and lithography as demonstrated in this thesis. The essential components of a STXM are presented in Fig. 2.5.

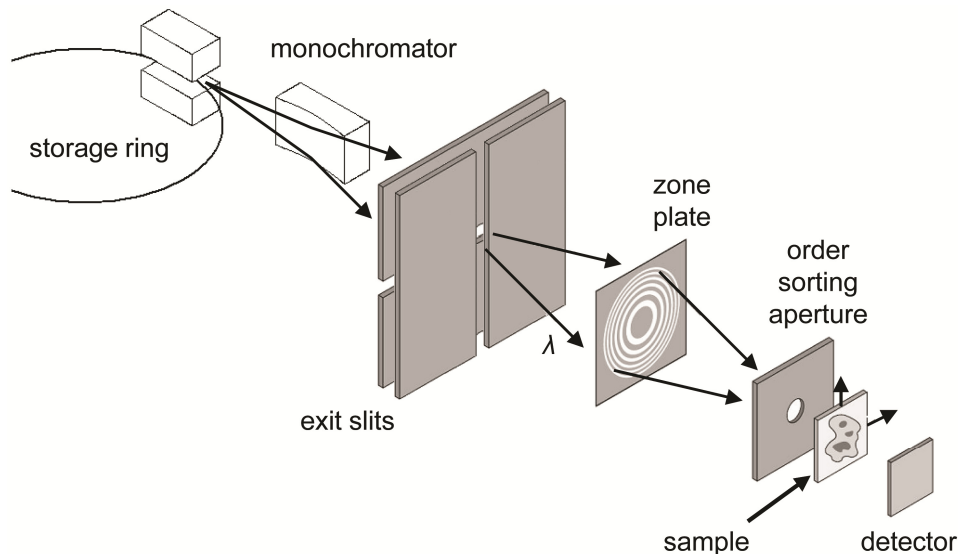


Figure 2.5: Schematic depicting the essential components of a STXM (adapted from [A99] Fig. 9.21, © 2012 Cambridge University Press, used with permission).

The first STXM to operate with this general layout (use of a zone plate and a monochromator) was built in 1982 at the NSLS [RKK&84]. The basic layout today remains unchanged, except that every subsystem has vastly improved over the past 30 years. All of the experiments in this thesis involved a STXM. Six different STXMs were used, which are summarized in Table 2.1. Henceforth the individual instruments will be referenced by the beamline at which they presently reside. While the beamlines differ, five of these STXMs are essentially based on the ALS 5.3.2.2 design [KTS&03] (formerly referred to as 5.3.2, now available through Bruker Advanced Supercon GmbH). 5.3.2.1 is a new enhanced design built at the ALS after ten years of experience with the 5.3.2 design, but they are similar in many ways. There are many excellent reviews of STXM technology, history, applications and x-ray microscopy in general [KR85, A99, H12]. The most technically thorough are [KJH95, KTS&03, HJW07].

Table 2.1: The STXMs used within this thesis.

Facility	Beamline (Name)	X-ray source	Instrument publication	Used in Ch. #
ALS	5.3.2.1	BM	Forthcoming	7
ALS	5.3.2.2	BM	[KTS&03]	3,4,6,7,8,10,11
ALS	11.0.2	EPU	[TWK&04]	7,10,12
BESSY II	UE46 (MAXYMUS)	EPU	[FSW&10]	7
CLS	10ID-1 (SM)	EPU	[KKL&07]	4,7,8,9,10,11,12
SLS	X07DA (PolLux)	BM	[RTF&08]	5,7

2.3.1 Fresnel zone plate lenses

Fresnel zone plates (ZP) are circular transmission gratings where the period (also called the pitch) of alternating transparent and opaque zones decreases with increasing zone radii. The period of the zones is arranged such that, when the ZP is fabricated within certain tolerances and sufficiently coherently illuminated (described in a forthcoming section), the physical path length difference between neighbouring transparent zones to the (first order) focal point differs by exactly one wavelength; the diffracted radiation from each transparent zone arrives in phase and interferes constructively at the (first order) focal point. If the NA of the ZP is $\ll 1$ (which is the case for all ZPs used in this thesis), this condition is expressed by the fundamental ZP relation,

$$r_n^2 = mn\lambda f_m \quad (2.3)$$

where r_n is the radius of the n^{th} zone, m is the focus order, λ is the wavelength of operation and f_m is the m^{th} order focal length. ZPs with >100 zones behave like conventional refractive lenses and can produce diffraction limited focal spots; the point spread function (PSF) is essentially the same as that of a

conventional refractive lens with equivalent parameters [M86]. A Fresnel ZP was the focusing element in all six STXMs used in this thesis.

The nanofabrication of high resolution ZPs for x-ray microscopy is currently a very active area of research. ZPs for x-ray microscopy have been fabricated by holographic [RS80] and sputter-slice methods [KTS&97], but since the mid 1980s the highest resolution ZPs have been fabricated by electron beam lithography. Except for those experiments reported in Ch. 5, ZPs with identical parameters obtained from the same supplier (Center for X-ray Optics (CXRO), LBNL) were installed in all of the separate STXMs for every experiment reported in this thesis: 240 μm diameter D , 25 nm outer most zone width Δr , 90 or 95 μm central stop diameter D_s . The opaque zones are 150 nm tall while the central stop and surrounding support are 2 μm thick, all made of Au on the flat side of a 100 nm thick Si_3N_4 window. Thus the transparent zones are only partly transparent (100 nm of Si_3N_4 with a density of 2.25 g/cm^3 is only about 63% transmissive at 300 eV) and the opaque zones are partly opaque (150 nm of Au with a density of 18 g/cm^3 is <2% transmissive at 300 eV, but about 23% transmissive at 1 keV) [HGD93]. A pseudo-random buttressing system is incorporated into the zone layout to prevent the opaque zones from collapsing due to their high aspect ratio of up to 6:1 [OHV&04]. These were fabricated by an electron beam lithography process described elsewhere [A99]. A photograph and scanning electron micrographs of one of these CXRO ZPs are presented in Fig. 2.6.

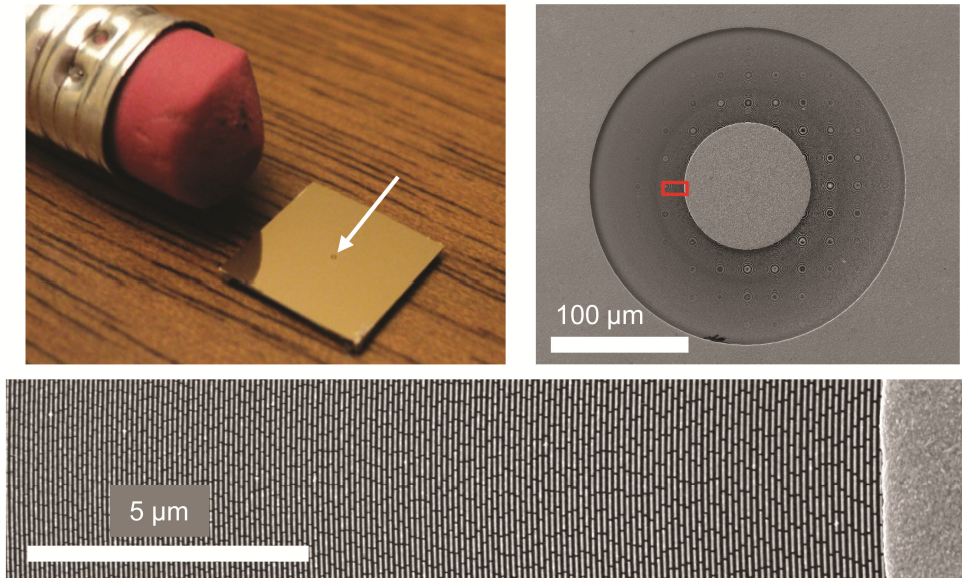


Figure 2.6: (Top left) Photograph of a typical CXRO zone plate used throughout this thesis. A pencil eraser is included for size reference. The zone plate itself is indicated by the arrow. (Top right) Scanning electron micrograph of a CXRO zone plate. (Bottom) Scanning electron micrograph of the area within the red rectangle at top right, revealing the innermost zones and the buttressing system. The continuous area at right is part of the central stop.

2.3.1.1 Diffraction limited focusing

ZPs produce the best possible (diffraction limited) focal spot when they are i) fabricated within certain tolerances and ii) sufficiently coherently illuminated. The major tolerance requirements are that the zones must be accurately placed to within about a third of their width (i.e. better than 8 nm positional accuracy was required to fabricate the CXRO ZPs), and the ellipticity must be less than 0.05% [M86, JWA&91].

Note that the description of ZP focusing in the previous section requires the wavefront incident on the ZP to be both spatially (transversely) and temporally (longitudinally) coherent. The incident radiation must be sufficiently

spatially coherent i.e. in phase across the ZP area, or the radiation emanating from all the transparent zones will not interfere constructively at the focal point and the quality of the focal spot will suffer. As ZP focusing is strongly chromatic (Eqns. 2.3, 2.7) the radiation must also be sufficiently longitudinally coherent i.e. monochromatic. If the photon energy resolution (spectral bandwidth) of the incident radiation is too large, the focal spot will be smeared along the optical axis and its quality will again suffer.

Spatial coherence is determined by the monochromator vertical and horizontal exit slits which are user-adjustable and form a square aperture. X-rays from the beamline impinge on one side of this aperture and diffract out the other [BW99]. To fulfil the spatial coherence requirement, the ZP must be positioned at least fully within the spatially coherent (Airy disk) fraction emanating from the exit slits. Assuming that the aperture is uniformly illuminated by the beamline and that the ZP is centred on the optical axis, the vertical and horizontal widths of the aperture d corresponding to this condition is,

$$d \leq \frac{\lambda}{\sin \theta} \quad (2.4)$$

where θ is the narrow angle of a right triangle formed by the exit slit to ZP distance (adjacent), and half of D (opposite). This condition is depicted in Fig. 2.7.

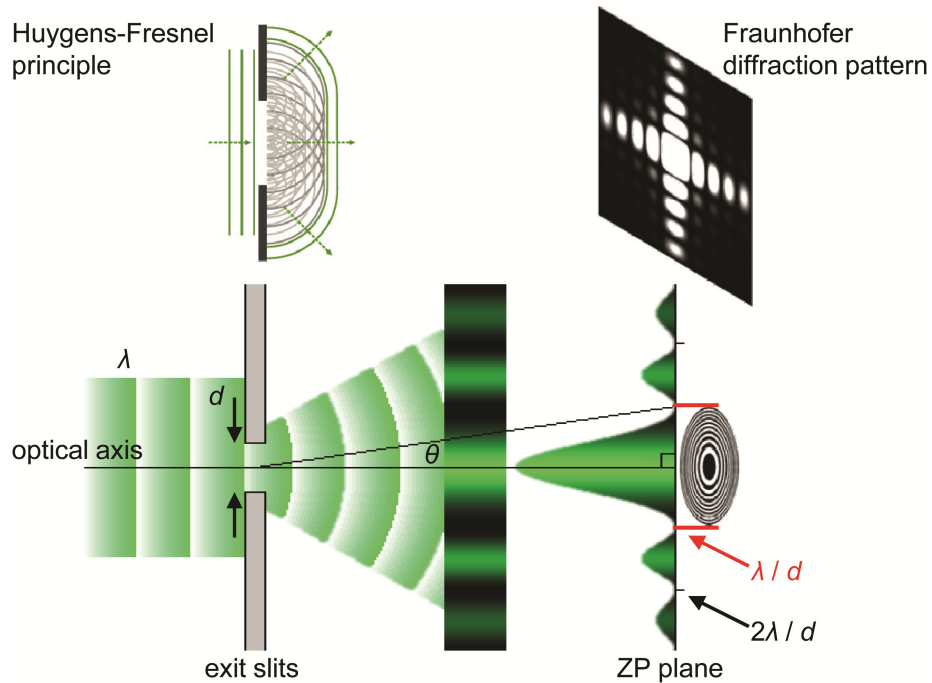


Figure 2.7: Side view schematic depicting the spatial coherence condition described by Eqn. 2.4. The Fraunhofer diffraction pattern (top right) is that of a square aperture.

The exits slit to ZP distances are sometimes not included in the STXM beamline papers (Table 2.1). Therefore, these distances were measured at all STXMs used within this thesis using a measuring tape and are tabulated below (Table 2.2).

Table 2.2: Exit slit to zone plate distances of several operational STXMs.

STXM	Exit slit to zone plate distance (m)
ALS 5.3.2.1	1.80
ALS 5.3.2.2	1.00
ALS 11.0.2	2.20
BESSY II UE46	3.00
CLS 10ID-1	3.30
SLS X07DA	1.07

Other groups have advocated for stricter spatial coherence using different terminology, describing spatial coherence by the phase space parameter, p/λ , where $p = 2s \sin\theta \approx sd/l$, and s is the width of the exit slits (i.e. source size), d is

the diameter of the illuminated area downstream of the exit slits with the calculated phase space parameter, l is the exit slit to ZP distance, and θ is the narrow angle of a right triangle formed by l (adjacent), and half of d (opposite). A larger phase space parameter indicates lower spatial coherence. [S97b] calculated a significant loss in spatial resolution when $p/\lambda > 0.5$, a value which corresponds to Rayleigh's quarter wavelength rule [R79]. At a phase space parameter of 0.5, the x-rays across the diameter of the ZP are up to 0.5π , or $\lambda/4$ out of phase. However the results of another calculation indicate that full spatial resolution is preserved for $p \leq 1$ [WAB&00]. The condition previously described by Eqn. 2.4 corresponds to a phase space parameter of 2, or λ out of phase at the edge of the ZP, depicted in Fig. 2.7. STXM beamlines are designed such that the spatially coherent fraction can overfill the ZP by selecting exit slit widths smaller than those calculated using Eqn. 2.4. This setting would be used when the highest spatial resolution is desired. In addition, overfilling the ZP improves stability by minimizing sensitivity to vibrations, but it also decreases the flux. No significant improvement in spatial resolution was found using exit slit widths 25% or 50% smaller than those calculated using Eqn. 2.4 (i.e. $p/\lambda = 1.5$ or 1.0 , respectively).

The longitudinal coherence requirement for diffraction limited focusing is [M86, T88],

$$\frac{\lambda}{\Delta\lambda} \geq Nm \tag{2.5}$$

where $\Delta\lambda$ is the photon energy bandwidth, N is the total number of zones of the ZP (both the opaque and the transparent), and m is the focus diffraction order.

$\frac{\lambda}{\Delta\lambda}$ is also known as the photon energy resolving power, and is controlled by

the properties of the monochromator and the width of the dispersive exit slit.

This equation (Eqn. 2.5) is essentially the same as the theoretical resolving power of a planar diffraction grating [PL05]. Most STXM beamlines are designed to attain a resolving power >3000 over the entire photon energy range with exit slit settings that provide reasonable flux [WAK&02], while N for the CXRO ZP, $90\ \mu\text{m}$ D_s , is 2062 (Eqn. 2.11).

2.3.1.2 Zone plate equations

Many of the optical properties of a given ZP can be calculated from a handful of physical values, namely, Δr , D , and the λ of operation. The Rayleigh criterion resolution of a ZP *without a central stop* is,

$$resolution_{x,y} = \frac{1.22\Delta r}{m} \quad (2.6)$$

The presence of a central stop (apodization) however, changes the PSF. As D_s increases relative to D , the relative intensity into the central Airy disk decreases, the central Airy disk becomes narrowed, and the intensity in the surrounding maxima increases [M86, T88, VGF&11]. The result is enhanced contrast for higher spatial frequencies but reduced contrast for lower spatial frequencies. The resolution of a ZP with a central stop operating in the first order focus

ranges from about $0.8\Delta r$ to $1.22\Delta r$, depending upon D_s relative to D [M86].

The resolution for the CXRO ZP, $90\ \mu\text{m}$ D_s , is about $1.05\Delta r$.

The m^{th} order focal length f_m in principle is,

$$f_m = \frac{D\Delta r}{\lambda m} \quad (2.7)$$

However, in practice f is determined by,

$$f = A_1 E + A_0 \quad (2.8)$$

where A_1 is the experimentally determined change in f with photon energy E , and A_0 is the distance from the front of the order sorting aperture (OSA) to the sample.

The depth of focus Δz at the first order focus is,

$$\Delta z = \pm \frac{2(\Delta r)^2}{\lambda} \quad (2.9)$$

Within the depth of focus, the on-axis intensity decrease is no more than 20%.

The numerical aperture at the first order focus is,

$$NA = \frac{\lambda}{2\Delta r} \quad (2.10)$$

The total number of zones (both opaque and transparent) in a ZP with or without a central stop is [VCJ&01],

$$N = \frac{D}{4\Delta r} \left[1 - \left(\frac{D_s}{D} \right)^2 \right] \quad (2.11)$$

The full derivations of these equations can be found elsewhere [K74, KJH95, A99, HJW07].

2.3.2 The order sorting aperture and higher order radiation

Sufficiently coherently illuminated Fresnel ZPs produce more than one focal point; at distances on the optical axis corresponding to *odd* whole number fractions of f ($f/3$, $f/5$...) the path length difference between neighbouring transparent zones happens to be integer multiples of λ (3λ , 5λ ...) resulting in a series of higher order foci (third, fifth...). The path length difference between neighbouring transparent zones to locations on the optical axis which are *even* whole number fractions of f ($f/2$, $f/4$...) are also integer multiples of λ (2λ , 4λ ...) but these foci are not observed when the widths of adjacent transparent and opaque zones are equal (as is the case for the CXRO ZPs used in this thesis) for reasons discussed in [M86, HJW07]. A significant second order focal spot has been calculated for the ZPs used in Ch. 5 [VGF&2011], as well as an interesting sub-harmonic focal spot at twice the first order focal length. The theoretical transmitted intensity in each of the foci can be calculated [HJW07] as well as the undiffracted intensity (zero order) which passes right through the transparent zones of the ZP.

A central stop incorporated in the ZP in combination with an OSA serves to prevent the intensity in the higher order fractions from reaching the sample plane, which would lead to unintended patterning and poor contrast when imaging. The central stop is made significantly thicker than the opaque zones so that it is non-transmissive in the photon energy range of the STXM beamlines. The OSA is a thin (tens of micrometres) metal strip with a small circular hole

often made by laser ablation. The diameter of the OSA used was almost always 50 μm , however some measurements used 40 or 70 μm OSAs. The diameter of the OSA is slightly smaller than D_s so that when the OSA is centered on the optical axis and positioned appropriately between the ZP first order focal plane and the ZP, the zeroth order and ZP higher order foci are blocked in principle and only the ZP first order focused component can pass and reach the sample plane (Fig. 2.8).

The situation becomes more complex when beamline higher order radiation is considered. STXMs use diffraction gratings i.e. monochromators to obtain the photon energy resolution necessary to acquire good quality NEXAFS spectra and to reach diffraction limited spatial resolution (Eqn. 2.5). The grating equation is,

$$Gm\lambda = \sin \alpha + \sin \beta \quad (2.12)$$

where G is the groove frequency (grooves/mm), m is the grating diffraction order, and α and β are the incident and diffracted angles of radiation of wavelength λ , respectively [PL05]. Integer multiples of λ (i.e. higher diffraction orders m) will satisfy the grating equation; x-rays with multiples of the first order diffracted wavelength exit the monochromator at exactly the same β as the desired first order radiation, assuming the incident radiation contains those wavelengths to begin with. Left unchecked, this higher order radiation can propagate down the beamline and eventually reach the sample plane and finally the detector. This is generally more of a problem with BM and wiggler beamlines because their

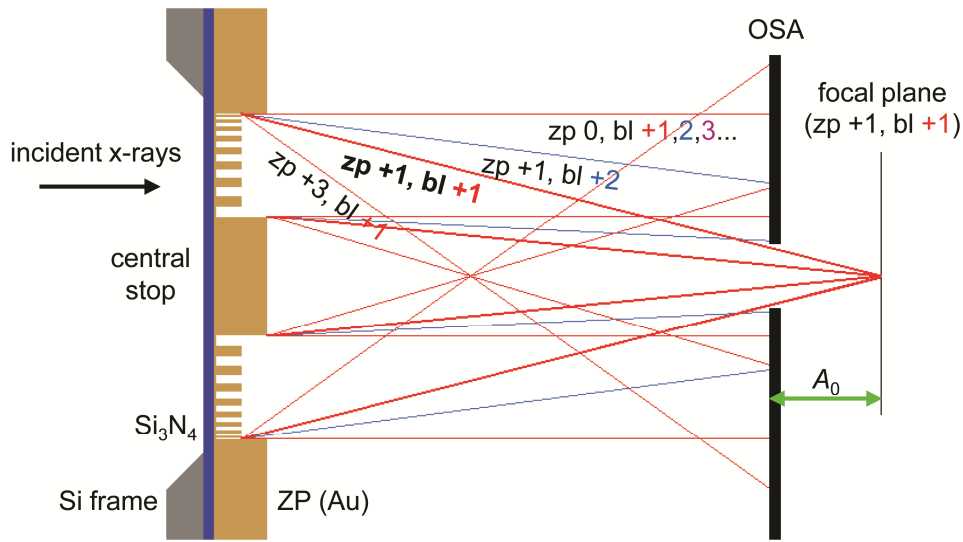


Figure 2.8: Side view schematic depicting the geometry of the foci of a Fresnel ZP in combination with a central stop and OSA (bl = beamline).

emission spectra are broad with significant intensity at higher energies, whereas undulators produce less intensity at wavelengths greater than the fundamental. Beamline higher order radiation is very undesirable; it reduces patterning/imaging contrast, and the maximum OD range measurable leading to distorted spectra. It results in a higher dose to the sample, and can introduce spectroscopic artefacts. STXM beamlines are designed to suppress higher order radiation to some extent by choosing the appropriate groove profile for the gratings [M86] along with certain coatings on optical surfaces [KTS&03]. Still, it can be especially problematic for experiments at the C 1s edge (270 – 330 eV) and below due to the cumulative suppression of the beamline first order radiation in this range. Carbon contamination (Ch. 8) on the beamline optics preferentially absorbs the first order radiation. The two 100 nm Si₃N₄ windows in the optical path (one separates the UHV beamline from the STXM chamber, the other supports the

ZP (Fig. 2.8)) happen to be much more transmissive at higher photon energy. Also, the STXM detectors in use were not energy-dispersive, and the efficiency of these detectors increases with increasing photon energy [KTS&03].

Some ZP focused beamline higher order x-rays are blocked by the OSA. For the CXRO ZPs, 90 μm D_s , operated at 300 eV, the focal length for the first order focused beamline second order radiation i.e. 600 eV is twice that of the first order focused beamline first order radiation (Eqn. 2.7). Simple trigonometry can be used calculate that this first order focused beamline second order radiation is an annulus at the OSA plane with an inner radius of 27 μm if A_0 is 280 μm (loosely depicted in Fig. 2.8). Thus in principle a 50 μm diameter OSA should prevent this radiation from reaching the detector if its position can be maintained on the optical axis within ± 2 μm . This assumes that the OSA hole is perpendicular to the optical axis, flat and circular (which can be measured by performing an OSA scan with the ZP in-focus). In practice, the OSA becomes distorted and/or polluted over time due to accidental contact with samples as the gap between the OSA and the sample is typically 200 – 250 μm , depending on the photon energy and sample flatness. Some of this radiation does pass the OSA and appears as an annulus at the first order focused beamline first order focal plane with an inner radius of 25 – 30 μm (often referred to as “halo” or simply “higher order”). The OSA is less effective at blocking the third order focused beamline second order radiation, and completely ineffective at blocking third order focused

beamline third order radiation which has the same focal length as the first order focused beamline first order radiation (Eqn. 2.7).

Higher order suppression systems have been installed on some STXM beamlines where this is a significant issue. These systems can be taken in or out of the beam path by the user as desired. Different approaches have been taken ranging from a simple 200 nm Ti foil at 10ID-1, to a 1.0 m long section of the beamline differentially pumped with N₂ at 600 mTorr at 5.3.2.2 [KTS&03], to a relatively elaborate MgF₂ coated three mirror system at X07DA [FRW&10]. A mirror system was also used on the now decommissioned NSLS STXM X1A [FCJ&98], and one will soon be installed at 5.3.2.1. These all effectively act as low-pass filters with varying ability to suppress higher orders relative to the desired beamline first order. If the STXM is on an EPU beamline, the amount of higher order radiation can be reduced by operating in circular polarized mode, as only the first order (fundamental) is emitted on axis and the other higher orders (undulator harmonics) are divergent, in principle [C04].

2.3.3 Current number of soft x-ray STXMs

All soft x-ray STXMs in the world which were operating, commissioning or under construction at the time of submission are summarized in Table 2.3 (Und-L: linearly polarizing undulator).

Table 2.3: Soft x-ray STXMs in existence at the time of submission.

Facility	Name	Location	Source	<i>E</i> range (eV)	Status
ALS	5.3.2.1	Berkeley, USA	BM	250 – 2600	Commissioning
ALS	5.3.2.2	Berkeley, USA	BM	250 – 750	Operating
ALS	11.0.2	Berkeley, USA	EPU	80 – 2100	Operating
BESSY II	MAXYMUS	Berlin, Germany	EPU	130 – 2000	Operating
CLS	10ID-1	Saskatoon, Canada	EPU	130 – 2500	Operating
Diamond	I08	Chilton, UK	EPU	250 – 2500	Construction
Elettra	Twin-mic	Trieste, Italy	Und-L	250 – 2200	Operating
PLS	Nanoscopy	Pohang, Korea	EPU	100 – 2000	Construction
SLS	PolLux	Villigen, Switzerland	BM	250 – 1600	Operating
SLS	NanoXAS	Villigen, Switzerland	BM	200 – 1400	Commissioning
SOLEIL	Hermes	Saint-Aubin, France	EPU	250 – 1500	Construction
SSRF	SXS	Shanghai, China	EPU	250 – 2000	Commissioning
SSRL	13-1	Stanford, USA	EPU	250 – 1000	Operating
UVSOR-II	BL4U	Okazaki, Japan	Und-L	50 – 800	Construction

The stated *E* ranges should be considered tentative as they often change with new optics and other improvements. STXMs are currently commercially available through two companies, Xradia Inc. (Pleasanton, USA) and Bruker Advanced Supercon GmbH (Bergisch Gladbach, Germany, formerly ACCEL).

2.3.4 ALS 5.3.2 type STXM

Five of the six STXMs used in this thesis (all except 5.3.2.1) are largely of the same design pioneered by the ALS 5.3.2 STXM. These STXMs offer control of the *z* position of the ZP (*x* and *y* control also available at UE46 and 5.3.2.1), the *x* and *y* position of the OSA, *x*, *y* and *z* control over the sample, and *x*, *y* and *z* control over the detector. The positioning is controlled using motorized stages, except for the sample (*x*, *y*) fine stage which is piezo-based. The arrangement and stacking of the stages is depicted in Fig. 2.9.

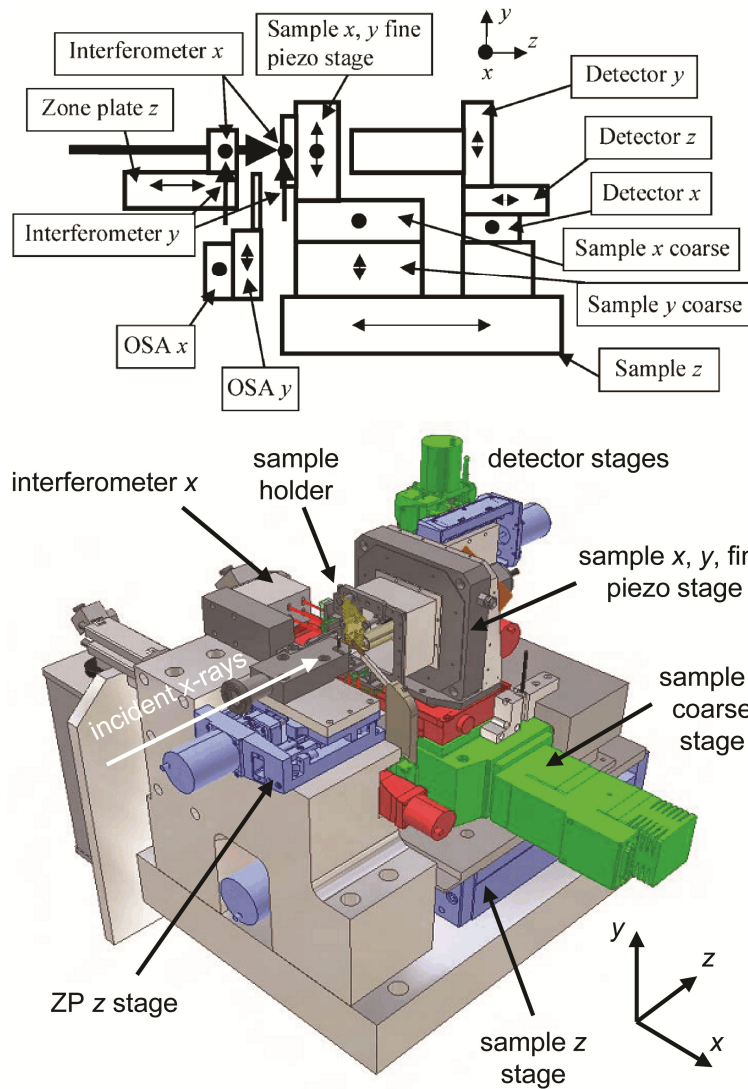


Figure 2.9: (Top) Schematic depicting the general arrangement and stacking of the stages and components of an ALS 5.3.2 type STXM (from [KTS&03] Fig. 2, © 2012 International Union of Crystallography, used with permission). (Bottom) Three dimensional CAD rendering of X07DA (courtesy of Dr. Benjamin Watts and Dr. Jörg Raabe, PSI, used with permission).

The positioning of the sample (x, y) piezo fine stage is maintained relative to the ZP to ≤ 10 nm via a laser interferometer feedback system (Fig. 2.10). The feedback system corrects for run-out (transverse motion) of the ZP z stage as the photon energy is scanned, and negates low frequency vibrations from the

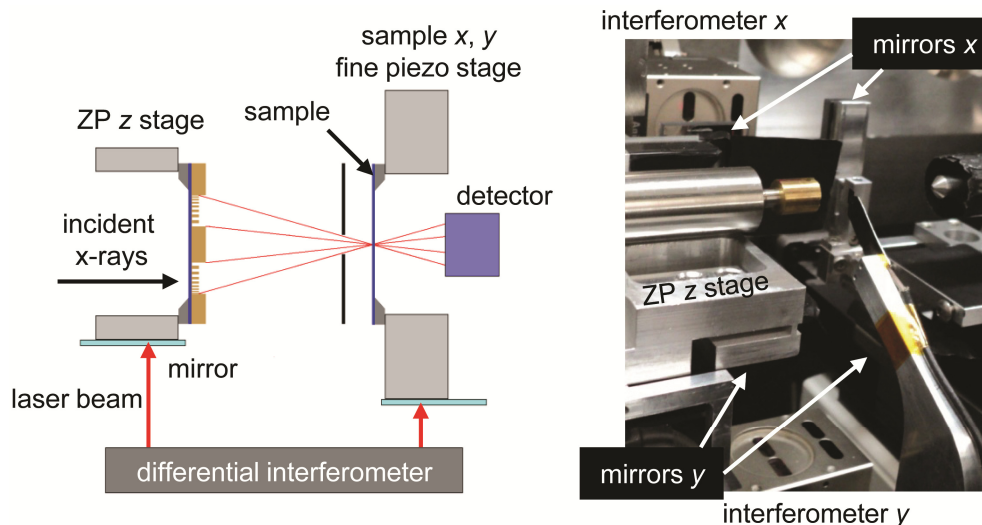


Figure 2.10: (Left) Schematic depicting the laser interferometer system of ALS 5.3.2 type STXMs. (Right) Photograph of 10ID-1 depicting the orthogonal interferometers and mirrors. The sample mount has been removed for clarity.

experimental floor. The feedback-control rate can be maintained indefinitely at about 100 Hz [KTS&03]. The performance of the feedback system in this family of STXMs is such that the minimum achievable patterning/imaging resolution is not limited by the microscope mechanics or vibrations but only by the properties and quality of the ZP used, though even this limitation is being overcome by ptycographic [TDM&08] and scanning probe [SRS&10] imaging modes (note however that these approaches achieve higher resolution based on novel detection schemes, not smaller focal spot sizes; these will not improve minimum patterning resolution). The feedback system was critical for high fidelity patterning experiments as well as imaging.

Except for UE46, the transmitted x-ray detectors consisted of a phosphor scintillator to convert x-rays to visible photons which were then counted by a high performance photomultiplier tube (PMT) [KTS&03, FKT04]. At UE46, the x-rays

were detected directly using an avalanche photodiode (S2382, Hamamatsu). The components, stages, interferometers, etc., are all mounted on a large Al block depicted in Fig. 2.9 (total weight of 150 – 250 kg) and housed inside a vacuum chamber. Photographs inside and outside of the X07DA chamber are presented in Fig. 2.11. The chambers can achieve a vacuum of about 10^{-6} Torr, except UE46 and 5.3.2.1 which were designed for UHV. A 100 nm Si_3N_4 window separates the UHV of the beamline from the chamber conditions.

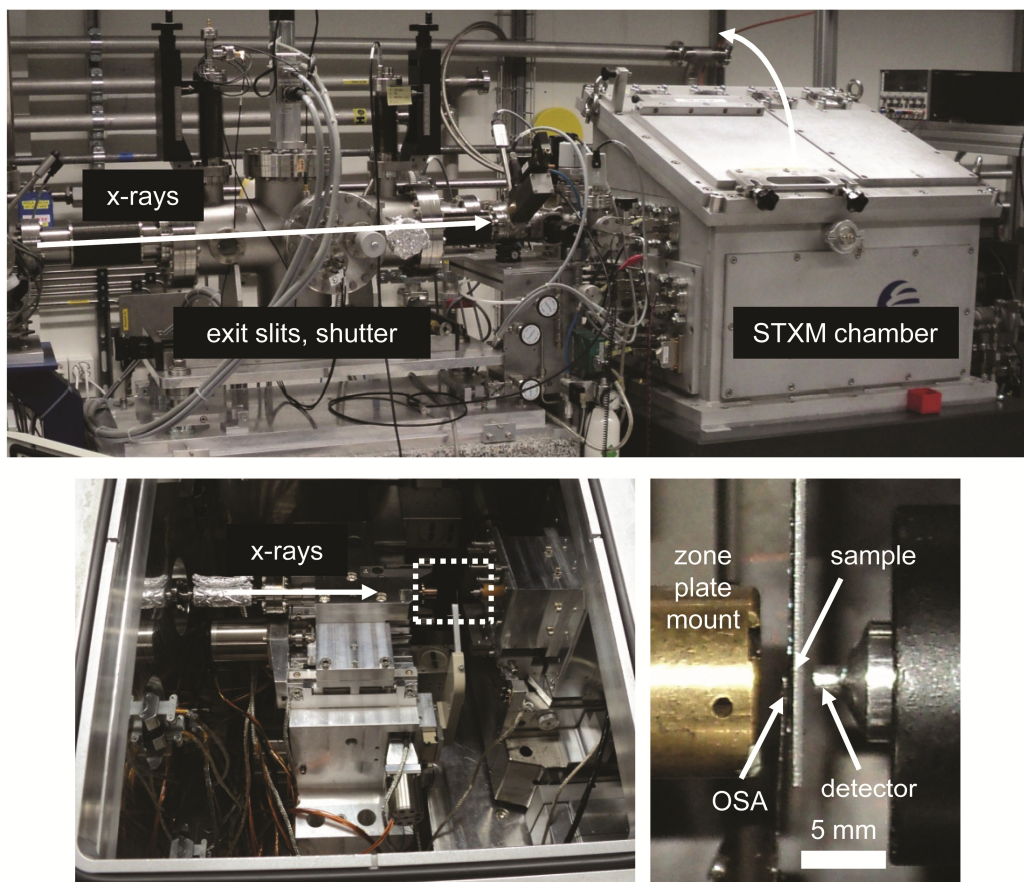


Figure 2.11: (Top) Photograph of the X07DA chamber and a portion of the beamline which includes the exit slits and shutter. (Left) Photograph viewing inside the X07DA chamber. (Right) Side view close up photograph of the ZP, OSA, sample and detector of 5.3.2.2 set for measurements at the C 1s edge.

All of the STXMs used the same operational software, STXM_Control [KTS&03], which controls the STXM and also controls many beamline components, depending on the beamline. All of the STXM beamlines were equipped with precise piezo x-ray shutter systems which can reliably go from closed to open to closed in 1 ms [KT04]. The shutters were positioned in vacuum between the exit slits and STXM chambers. Additional instrument details can be found in the instrument reports listed in Table 2.1 and in the chapters that follow.

2.4 Atomic force microscope

An atomic force microscope (AFM) was used to image and measure the topography of thin polymer film sample surfaces. This instrument involves a sharp tip with a radius of a few nanometres bonded to the end of a reflective cantilever, a laser beam focused onto the back of the cantilever, and a quadrant photodiode which measures the reflected laser light thereby monitoring the deflection of the cantilever in response to a surface. Images are built up from a series of scanned lines like in STXM. A diagram of the basic operation of an AFM along with a photograph of the Quesant Q-Scope 350 AFM instrument used for all AFM measurements is presented in Fig. 2.12. This microscope is currently located in room 332, ABB, McMaster University. Quesant was one of the earliest AFM manufacturers and was acquired by Ambios Technology Inc. in 2005. This company was acquired by KLA-Tencor in 2010 which does not appear to be marketing this AFM, and replacement parts are not readily available.

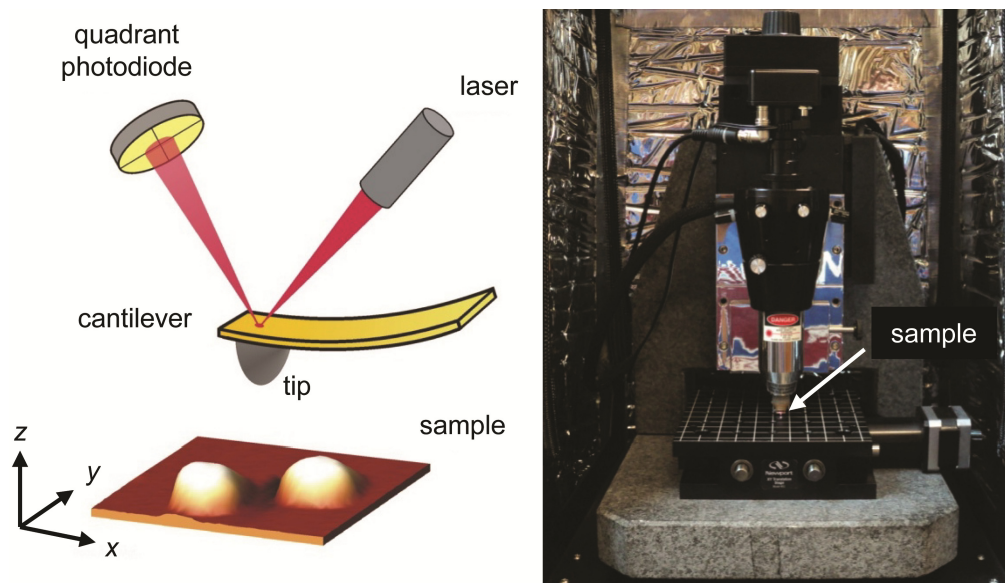


Figure 2.12: (Left) Schematic depicting the essential components of an atomic force microscope (adapted from [RW09] Fig. 1, © 2012 John Wiley & Sons Inc., used with permission). (Right) Photograph of the Quesant Q-Scope 350 atomic force microscope.

All atomic force micrographs were obtained in intermittent contact mode. In this mode, the cantilever/tip is driven into harmonic oscillation at its resonant frequency far away from the surface of the sample. The amplitude of oscillation with no surface influence is on the order of 100 nm. The oscillating tip is then brought close to the surface. At some point the tip will begin touching or “tapping” the surface, which dampens the oscillation. The closer it is brought toward the surface, the more its oscillation is dampened. The user then sets an oscillation dampening set point that essentially sets the force with which the tip presses on the surface. The oscillating tip is then raster scanned (x, y) across the surface with a piezo ceramic scanning tube under an adjustable feedback circuit. As the cantilever is scanned the feedback circuit applies a voltage to the piezo scanning tube in the z direction that attempts to maintain the oscillation

dampening set point during the scan. If the dampening increases while scanning (in response to some raised feature on the surface) the feedback system responds by decreasing the voltage on the piezo z height scan tube, causing it to contract moving the tip away from the surface until the oscillation dampening set point is re-established. Conversely, if the dampening decreases (in response to the tip encountering a depression on the surface) the feedback system increases the voltage on the piezo z height scan tube, causing it to extend moving the tip down so it tracks that feature. The voltage applied to the piezo z height scan tube for each pixel is proportional to the height of the surface and is used to build up a z height image.

Some images were also obtained in phase mode. In phase imaging, the tip is driven into harmonic motion, the oscillation dampening point is set, and the tip tracks the surface via a feedback loop in the same way as described in the previous paragraph. However the signals which are used to form the image are different. Contact between the tip and the sample surface while scanning can cause the phase of the tip oscillation to differ from the phase of the piezo oscillator driver. This phase lag of the tip oscillation relative to the driver oscillation is the basis of a phase image. Phase images can be sensitive to differences in friction and adhesion but do not contain height information. The Q-Scope 350 instrument acquires both phase and z height images simultaneously when operating in intermittent contact mode. Phase images sometimes revealed subtle details that were not resolved in the z height images.

Budget Sensors Multi75Al (force constant: 3 N/m, resonant frequency: 75 kHz) and Tap 150 Al-G (force constant: 5 N/m, resonant frequency: 150 kHz) cantilevers were used throughout this thesis. The tips share the same shape and dimensions (tip radius: <10 nm), however the higher resonant frequency Tap 150 Al-G cantilevers were found to be a much better match to the Q-Scope 350. Though the image quality for both probes was identical, the Tap 150 Al-G probes were easier to set up and were more stable during operation. The scan rate in any case was always 0.5 Hz. Higher scan rates led to resonant coupling of the tip oscillation with the thin (75 nm) Si₃N₄ windows and consequently poor images.

2.5 Scanning electron microscope

A scanning electron microscope (SEM) forms images by raster scanning (x, y) a nano-focused beam of electrons across a sample area using electric or magnetic fields. The inelastically scattered high energy electrons create secondary electrons (SEs) in the sample, which are collected to form SE images. All SEM images contained in this thesis were acquired using a SE detector, and are therefore SE images. A photograph of the JEOL JSM-7000F used throughout this thesis is presented in Fig. 2.13. This microscope is currently located in the Canadian Centre for Electron Microscopy, McMaster University.

Samples for SEM analysis were affixed to Al sample holder stubs with conductive Ag paint. A 5 ± 1 nm Pt layer was applied to all thin polymer film samples using a Gatan 682 Precision Etching Coating System, which was

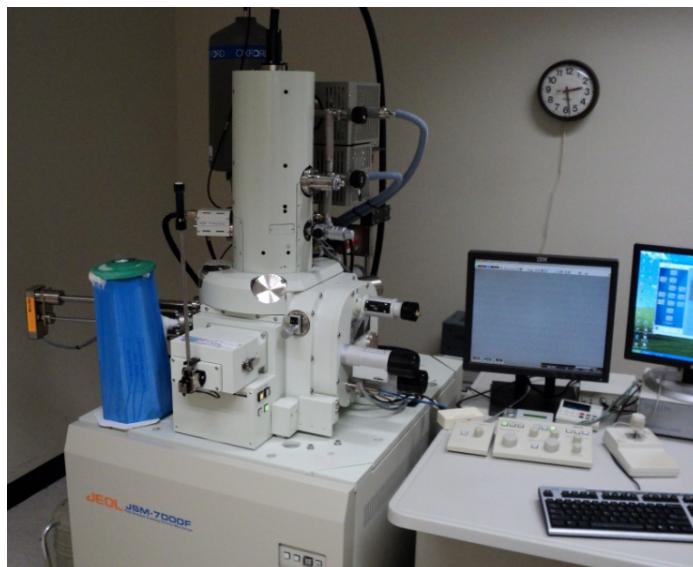


Figure 2.13: Photograph of the JEOL JSM-7000F scanning electron microscope.

necessary to reduce charging and improve image contrast. The SEM chamber vacuum was $10^{-5} - 10^{-4}$ Torr. Images were acquired with a voltage of 10 keV, a $60 \mu\text{A}$ beam current, and a typical working distance of 5 mm.

Chapter 3

Experimental

This chapter begins with an in-depth description of sample preparation and pre-STXM characterization procedures. The initial STXM set up procedure is described, followed by instructions for acquiring and processing x-ray images and spectra. Detailed instructions for STXM patterning and dose determination are also included. The development procedures are outlined, and finally the importance of the sequence in which the analysis techniques were carried out is explained.

3.1 Sample preparation

3.1.1 Materials, sources and purities

A comprehensive list of all materials used in the experiments described within this thesis is presented in Table 3.1. All materials were used as received, except stearic acid (described in Ch. 11.2.2).

Two types of samples were prepared within this thesis: 1) Thin polymer films on Si_3N_4 windows, and 2) thin fatty acid films sandwiched between two Si_3N_4 windows. The preparation of thin fatty acid film samples is fully described in Ch. 11.2.2.

Table 3.1: Comprehensive list of all materials used within this thesis.

Material	Acronym	Stated purity	Supplier	Additional information
2-propanol	IPA	99.5%	Caledon Laboratories	Common name: Isopropanol
4-methyl-2-pentanone	MIBK	>98.5% ACS reagent grade	Sigma-Aldrich	Common name: Methyl isobutyl ketone
5 minute epoxy			LePage®	
Double-sided tape			3M	
“Fast drying silver paint”			Ted Pella Inc.	
Hexatriacontane		99.9%	Supelco	
Mica			Ted Pella Inc.	
<i>N,N</i> -dimethylformamide	DMF	99.9% Chromasolv®	Sigma-Aldrich	
Parafilm® “M”			American National Can	
Palmitic acid		99%	Sigma-Aldrich	
Polyacrylonitrile	PAN		Sigma-Aldrich	$M_w = 150\ 000$
Poly(dimethyl glutarimide)	PMGI		MicroChem Corp.	A gift from Prof. Ash Parameswaran, Simon Fraser University
Poly(methyl methacrylate)	PMMA	Electronics grade	Polymer Source Inc.	$M_w = 315\ 000$ $M_w/M_n = 1.05$
Scotch® tape			3M	
Silicon nitride windows	Si ₃ N ₄		Norcada Inc.	75 nm x 1 mm x 1 mm window in a 200 μm x 5 mm x 5 mm Si frame
Stearic acid		99%	Sigma-Aldrich	
Toluene		99.9% Chromasolv®	Sigma-Aldrich	

3.1.2 Preparation of thin polymer films on Si₃N₄ windows

3.1.2.1 Preparing polymer solutions

Solutions of polymer in solvent were prepared at least one day before spin coating to ensure that the polymer had fully dissolved. The dissolution rates increased substantially upon gently heating the solutions to about 50 °C on a hot plate. Polymers should have a weight average molecular weight (M_w) of at least

10 000 g/mol to form strong, consistent films that can be transferred to Si_3N_4 windows without degrading. Solutions were stored in a laboratory refrigerator at 4 °C and wrapped with Parafilm® to suppress evaporation of the solvent when not in use.

3.1.2.2 Spin coating

The polymer solutions were allowed to warm up to room temperature (20 – 25 °C) before spin coating. Sheets of mica were cut with scissors into approximately 2 cm x 2 cm pieces. These mica pieces were cleaved using Scotch® tape immediately before being placed onto the vacuum chuck of the spin coater (P-6708D, Specialty Coating Systems, Inc.). As the successfully fabricated polymer films were transparent, a black marker was used to indicate the non-cleaved (i.e. bottom) side. Enough polymer solution was then pipetted dropwise onto the mica to fully cover the surface (usually 4 or 5 drops). The desired spin sequence was then initiated, and after completion the films on mica were inspected by eye. Films with a cloudy appearance often broke apart during the subsequent transfer step.

3.1.2.3 Float transfer from mica to Si_3N_4

The film on mica was then scribed into approximately 2 mm x 2 mm pieces using a scalpel and enough pressure to barely scratch the mica. The following steps were greatly aided by observation with a very low power

optical microscope: The scribed mica was held with tweezers, then very slowly dipped (polymer side up) in a Petri dish of distilled water at an approximate 45° angle. 2 mm x 2 mm pieces of polymer film then detach from the mica (sometimes readily, sometimes reluctantly) and float on the water's surface. The float process is depicted in Fig. 3.1.

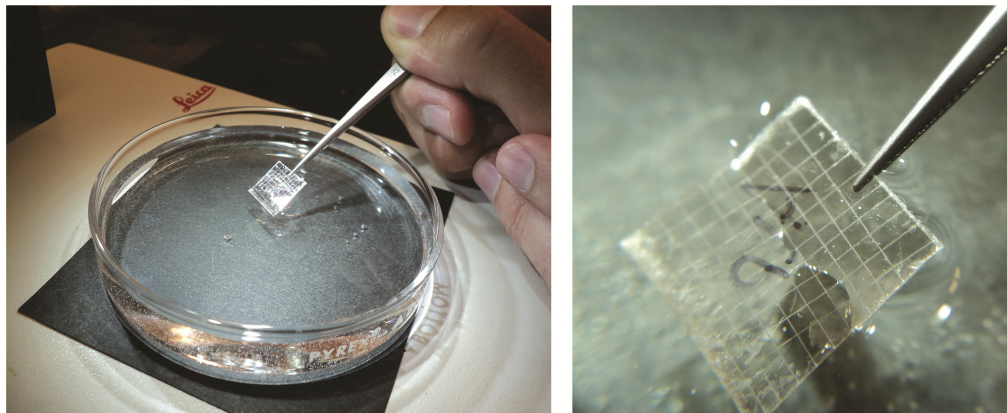


Figure 3.1: Photographs depicting the transfer of polymer film pieces from the scribed mica to the surface of water.

While floating, the film pieces were inspected for variations in thickness. The colour of the film can be used to estimate the thickness based on the interference of visible light [H70]. A piece of uniform thickness was then transferred onto a Si_3N_4 window by coaxing it over top of a submerged window held with tweezers, then slowly raising the window out of the water (Fig. 3.2). It is important to catch the film on the window in an orientation that only partially covers the window area to allow for measurements of the incident radiation I_0 during later STXM experiments. Usually several samples were made from one piece of mica. Occasionally, unscribed films on mica were prepared

in advance and stored in a laboratory drawer in labelled plastic dishes (polymer side up) for later use.

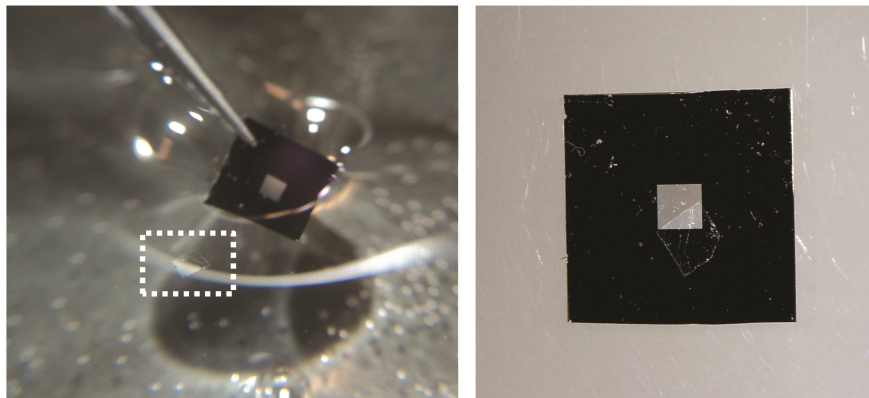


Figure 3.2: (Left) Photograph depicting the transfer of a polymer film piece (dashed rectangle) from the surface of water to a Si_3N_4 window. (Right) Photograph of a polymer film piece on Si_3N_4 , covering the bottom right corner of the 1 mm x 1 mm window area.

3.1.2.4 Annealing

After transferring onto Si_3N_4 , all thin polymer film samples were annealed, except for some specifically listed in Ch. 7. This was done to remove trapped solvent molecules, nano-voids, and to promote adhesion of the film to the window. To that end, the polymers were annealed at or above their glass transition temperature (T_g), but below their lowest thermal degradation temperature (T_d). The glass transition and degradation temperatures for the polymers used in this thesis in bulk form have been tabulated in Table 3.2.

Table 3.2: Glass transition and degradation temperatures of the polymers used in this thesis.

Polymer	T_g ($^{\circ}\text{C}$)	T_d ($^{\circ}\text{C}$)
PAN	85 [Aldrich]	311 [AGR&02]
PMGI	190 [MicroChem]	350 [MicroChem]
PMMA	103 [Ch. 7.3.1]	230 [Ch. 7.3.1]

Annealing was performed using a homebuilt vacuum annealer currently located in room 332, ABB, McMaster University. The temperature was monitored with a K type thermocouple and a glass thermometer (± 1 °C). Sometimes the annealing was performed under a low vacuum (2×10^{-2} Torr). The annealing conditions (temperatures, times, vacuum or no vacuum) varied between experiments. The exact conditions of each experiment are noted in the chapters that follow.

3.1.2.5 Thickness measurement

The thickness of the polymer films on Si_3N_4 was measured using AFM. A tweezer tip was used to scratch a line across the part of the film covering the Si_3N_4 window *frame*, and an atomic force micrograph was acquired over that line. The thickness of films produced by the spin coating process was found to be fairly consistent (± 10 nm) using constant conditions of polymer solution concentration, volume and final spin speed. Any changes in height due to annealing were less than the topographical resolution of the AFM (± 1 nm) for all polymers investigated. However, annealing was found to affect the surface roughness of polymer films (Ch. 7).

Though there are published works regarding spin coating theory [TWB83], obtaining a desired film thickness was a trial and error process. In general, the film thickness could be coarsely tuned by varying the concentration of the polymer solution, and fine tuned by varying the final spin speed. Polymer solutions within 1 – 5 wt% polymer, and final spin speeds

between 1500 – 4500 rpm produced 20 – 300 nm thick films acceptable for STXM measurements at photon energies spanning the C 1s edge. A comprehensive list of conditions used to prepare the various polymer films in this thesis has been compiled in Table 3.3.

Table 3.3: The conditions used to prepare the thin polymer film samples used in this thesis.

Polymer	Thickness (nm, ± 10)	Solvent	Concentration (wt%)	Final spin speed (rpm)	Used in (Ch. #)
PAN	60	DMF	1.5	3000	9
PMGI	50	DMF	2.8	2500	4, 6
PMMA	30	Toluene	1.0	4500	5, 12
PMMA	50	Toluene	1.5	4500	3, 4, 6, 7
PMMA	100	Toluene	1.5	2500	10
PMMA	300	Toluene	5.0	1900	12

3.1.2.6 Optical microscopy

Samples were inspected with an optical microscope after fabrication. They were checked for homogeneity, continuity, foreign material and other defects, using low and high power magnification in reflection and transmission modes. Small wrinkles and folds were common, as were micrometre-sized specimens of foreign material, suspected to be mica or dust. These were often sparsely distributed but more prevalent at the film edges. The bits of foreign material were in fact critical to the experiments; they were used to set and confirm the focus of the STXM. Samples that were obviously inhomogeneous, had too many specs of foreign material (>1 every $10 \mu\text{m} \times 10 \mu\text{m}$) or otherwise judged as defective were discarded. Optical micrographs were taken of the acceptable

samples, which aided in locating areas of interest in later STXM, AFM and SEM measurements.

3.1.2.7 Alternative transfer/fabrication methods

Some polymers investigated, but not used in this thesis, simply refused to separate from the mica during the float procedure. This problem could possibly be overcome by adjusting the pH of the water. If not, one option could be to spin cast the polymer solution directly onto the Si_3N_4 window, although films produced in this manner were often of non-uniform thickness possibly due to flexing of the thin window at high spin speeds. In addition this usually leads to complete coverage of the window with no area for an I_0 measurement. However, the thickness and purity of two windows cleaved side by side from a parent wafer were found to be practically identical by NEXAFS spectroscopy. Therefore, one window can be used for spin coating while the other can be dedicated to I_0 . Drop casting directly onto a portion of the window is another option, but again non-uniform thickness and also limited thickness reproducibility should be expected. Other interesting fabrication methods include spin casting on NaCl plates, which are then dissolved in water [MPK&05], drop casting onto liquid Hg, or microtoming sufficiently thin sections from a solid block of material [WBW&09].

3.1.3 Affixing/removing samples to/from STXM sample holders

Thin fatty acid samples (between two Si_3N_4 windows) were affixed to sample holders using 5 minute epoxy. Polymer film samples (on Si_3N_4 windows) were affixed using 2 mm strips of double-sided tape. Samples on double-sided tape can be successfully removed from the sample holder by carefully working a scalpel blade under the sides of the window while avoiding the corners. Great care must be taken (going slowly, only slight pressure, and working at multiple sides) as only a small amount of stress will crack the fragile windows.

3.2 STXM data collection and analysis

3.2.1 STXM and beamline set up

The following procedure was executed at the beginning of every STXM run. After loading the sample holder in the STXM, the chamber was evacuated to about 0.1 Torr by pumping for about 10 min, then backfilled with 250 Torr He. The evacuation step is important because O_2 has been shown to affect the rates of radiation chemistry process that occur in thin polymer layers [CUA02]. The OSA was carefully centered on the optical axis at the start of every run and about every 4 h after that. The OSA diameter and A_0 were chosen to select only the first order focused beamline first order component. Higher order suppression systems were used on beamlines that had such systems (Ch. 2.3.2) for all experiments carried out at the C 1s edge (270 – 330 eV). The monochromator exit slit widths were chosen to provide diffraction limited focus (Ch. 2.3.1.1).

Occasionally the calibration of the exit slits (and entrance slit, if present) was checked for accuracy, though they were never found to be miscalibrated by significant amounts. The detector was centered on the optical axis and positioned as close to the back of the sample holder as possible without touching it so that the active area (600 μm at 5.3.2.2) accepted the entire transmitted bright field signal. The detector-to-sample distance could differ by as much as 1.5 mm while still satisfying the above condition, however this has a negligible effect on its efficiency; the transmission of 300 eV x-rays through 1.5 mm of 250 Torr He used in these experiments is 97.7% [HGD93], which increases at higher photon energies [KTS&03]. The photon energy scale was calibrated to an accuracy of 0.05 eV using the known C 1s(C=O) \rightarrow $\pi^*_{\text{C=O}}$ peak of PMMA at 288.45 eV [WSH&07]. The photon energy scales at each beamline were almost always accurately calibrated upon arrival and shifts during a set of measurements over a few days at any given beamline were <0.1 eV.

3.2.2 Collecting optical density images

Transmission images were acquired after bringing an area of the sample into the focal plane. The user defines the image area, pixel size, dwell time, and the photon energy. The sample is then raster scanned (x, y) through the x-ray focal point while the transmitted photon flux is simultaneously recorded under computer control to build up a transmission image. These transmission images can then be converted to optical density (OD) images using the Lambert-Beer law,

$$OD = -\ln T = -\ln\left(\frac{I}{I_0}\right) = \mu\rho t \quad (3.1)$$

where OD is optical density (absorbance), T is transmission, I is the transmitted photon flux for each pixel in the image (photons/s), I_0 is the incident photon flux (photons/s), μ is the photon energy dependent mass absorption coefficient of the material (cm^2/g), ρ is the density of the material (g/cm^3), and t is the thickness of the material (cm). I_0 values were always recorded at the time of measurement for the most accurate OD scale possible. The conversion from transmission images to OD images was performed with the program aXis2000.

The importance of recording a relevant and accurate I_0 measurement (i.e. flux measured through a blank) to accompany each I measurement (i.e. flux measured through the sample and blank) for patterning, imaging, and spectroscopy experiments is paramount and cannot be understated. There must be a suitable area on the sample or some alternative area available to record I_0 . It should ideally be measured during, or immediately before or after recording I with exactly the same parameters as I . There should be no refocusing, changes to slit settings, or changes to the OSA or detector positions in the time between measuring I and I_0 , as backlash in some motorized stages, run-out and thermal drift lead to slightly different positions/alignment and a different I_0 . Even if STXM components could achieve, maintain and reproduce sub-angstrom level alignment, I_0 will still gradually change over time due to carbon contamination on the optics, sample and detector [LH12c], higher order radiation,

changes in the orbit in the storage ring, gradual degradation of the detector, and so on. It is almost never possible to go back later on (more than one day) and record I_0 , and without a relevant, timely and accurate I_0 measurement the results will be at least dubious, possibly meaningless and at worst misleading.

3.2.3 Collecting image stacks and NEXAFS spectra

NEXAFS spectra were obtained from image “stacks” [JWF&00]. An image stack is a series of successive monochromatic transmission images of the same area of the sample which span a photon energy range of interest, usually an x-ray absorption edge. The user can define the photon energy of the images (i.e. the photon energy sampling) and the dwell times. Stacks were often set up with a fine photon energy sampling (≤ 0.1 eV) in the regions of sharp absorption features and a coarser sampling (0.2 – 0.6 eV) in the pre-edge and ionization continuum regions. This decreases the possibility of introducing radiation damage artefacts (through decreased sample dose) and the stack acquisition time without sacrificing spectral quality. Stacks were collected with a slight defocus in situations where diffraction limited spatial resolution was not required which further reduces the dose associated with the stack acquisition. After acquiring the stack, each transmission image was converted to an OD image by applying the Lambert-Beer law (Eqn. 3.1) with an x-ray transmission spectrum of the incident radiation (I_0 spectrum). I_0 spectra were always recorded at the time of measurement for the most accurate OD scale possible, usually concurrently

within the stack area. If instrument drift was present, the images in the stack were spatially aligned using Fourier transform based cross-correlation procedures available in the program aXis2000. The aligned stack of images contains a NEXAFS spectrum for every pixel in the image.

3.2.4 Creating “OD1” spectra for quantitative analysis

The NEXAFS spectra acquired with STXM in transmission obey the Lambert-Beer law (Eqn. 3.1). For a single pure material, μ and ρ are intrinsic material properties whereas t varies with sample thickness; OD is linearly proportional to t (so long as absorption saturation is avoided). The thickness of a layer of known material can therefore be determined in units of nanometres by acquiring a NEXAFS spectrum with STXM (OD scale), and dividing this spectrum by a NEXAFS spectrum of the same material in which the OD scale has been normalized to the response for 1 nm of material (i.e. an “OD 1 nm”, or simply “OD1” spectrum). These thickness-normalized spectra can be used for quantitative microscopy of single or multi-component samples. OD images can also be converted to thickness images using information from an OD1 spectrum, so long as there are single component areas within the imaged area.

The creation of an OD1 spectrum begins with the acquisition of a NEXAFS spectrum with a generous pre- and post-edge photon energy range. This spectrum must be of the highest quality: i) The STXM photon energy scale must be accurately calibrated, ii) the material used to create the OD1 spectrum

must be identical to that in the real sample, iii) the maximum OD feature should be ≥ 0.2 but ≤ 1.0 to avoid absorption saturation, and iv) the spectrum should be free of radiation damage [WML&09]. A calculated OD spectrum is then created from a calculated μ value, the density of the material (e.g. PMMA, $C_5H_8O_2$, $\rho = 1.18 \text{ g/cm}^3$), and 1 nm thickness. Given the molecular formula of the material, μ can be calculated as the sum of the weighted atomic photoabsorption coefficients,

$$\mu = \frac{N_A}{M} \sum x_i \sigma_{ai} \quad (3.2)$$

where N_A is Avogadro's constant, M is the molecular weight of the compound containing x atoms of element i , and σ_{ai} is the atomic photoabsorption coefficient (cm^2/atom) of atoms of element i . Measured and/or calculated σ_a values for elements of atomic number $Z = 1 - 92$ and photon energies from 50 – 30 000 eV have been tabulated [HGD93] and are also available (and updated) on the CXRO website [C12]. These tabulated atomic photoabsorption coefficients are not accurate in the immediate vicinity of the absorption edge fine structure but are very accurate in the pre- and post-edge photon energy ranges. Calculated OD spectra were created with the program aXis2000 which contains the tabulated values list of the CXRO website. Finally, the OD scale of the high quality NEXAFS spectrum is normalized to the pre- and post-edge regions of the calculated absorption spectrum (between 275 – 282 eV and 340 – 360 eV respectively for the C 1s edge), resulting in an OD1 spectrum which is saved for later use. The OD1 spectra of PAN, PMGI and PMMA appear in Fig. 2.3.

Thickness values obtained by dividing acquired NEXAFS spectra by OD1 spectra agreed with those obtained by AFM within 10%, validating this approach.

3.2.5 Patterning

All patterning was performed using a scan option in STXM_Control called PatternGen. Patterning is fully described in Ch. 7.2.4.2. Instructions to create and execute patterns can be found in Ch. 7.6.1 and 7.6.2, respectively.

3.2.6 Determining absorbed dose

Calculation of absorbed dose (energy absorbed / mass) is fully described in Ch. 7.2.4.3. The Système International unit of dose, the gray (1 Gy = 1 J / kg), is used throughout this thesis. The doses used in this thesis range from 100 kGy – 1.5 GGy, while dose rates ranged from 10 MGy/s – 2.7 GGy/s. Some works cited in this thesis use the older unit of rads to quantify absorbed dose, where 100 rad = 1 Gy. In some of the works cited, the ionizing radiation used is electrons. Electron “dose” when patterning in an electron microscope is often reported in units of C/cm² (and is actually electron fluence). C/cm² can be converted to grays for electrons with energies less than about 200 keV by the following relationship [HHJ09],

$$(Gy) = (7.8 \times 10^{13}) \left(\frac{C}{cm^2} \right) \left(\frac{Z}{A} \right) \left(\frac{1}{E_e} \right) \ln \left(\frac{E_e}{13.5Z} \right) \quad (3.3)$$

where Z is the atomic number of the irradiated material, A is the atomic weight of the irradiated material, and E_e is electron energy in electron volts. Another equation to convert electron fluence to dose in grays can be found in [WBW&09, Eqn. 3], although two critical values in this equation are estimations, in contrast to the first principles approach of [HHJ09].

3.3 Development

The role of development in the general lithography process was discussed in Ch. 1.2. To develop, the sample was held with locking tweezers, then completely immersed and gently stirred in a 20 mL vial containing about 15 mL of a premixed developer solution for a precise length of time. This was sometimes immediately followed by immersing and stirring the sample in a rinse solution contained in another waiting vial. The development procedures used in this thesis are modified versions of those found in the lithography literature; the PMMA development procedure (3:1 v/v solution of IPA:MIBK, followed by a rinse in IPA) is essentially that discovered by [HHS68], with some additional inspiration from [GSE&06]. The PMGI development procedure (7:3 v/v IPA:H₂O) has been slightly modified from [JFP&08]. The exact immersion times, order, etc. are noted in the experimental section of each chapter which utilized a development step (Ch. 4 – 7, 10, 12). With the exception of Ch. 5, all development occurred at room temperature (20 – 25 °C). After development, all samples were allowed to dry in ambient air while held with locking tweezers. Developer solutions were

prepared in advance and stored in a laboratory refrigerator at 4 °C wrapped with Parafilm® to suppress evaporation of the solvent when not in use.

3.4 Proper sequence of analysis to avoid artefacts

As mentioned in Ch. 1.3, changes are often observed in polymers which have been exposed to ionizing radiation; polymers are radiation-sensitive. Two of the three major imaging techniques used throughout this thesis, STXM and SEM, probe the sample with ionizing radiation, which can induce mass loss, chemical change, and deposit carbon. The experiments in this thesis were conducted in an order which was cognisant of that. For example, imaging in STXM, however briefly, results in the sample receiving some quantity of absorbed dose. Special care was taken so that areas of the polymer film that were to be patterned using STXM were not previously imaged. AFM imaging did not noticeably alter the polymer films with the parameters used (Ch. 2.4), and was therefore always performed before STXM or SEM if images of the same area of the sample were desired. In some experiments STXM and SEM images of the same feature were desired. Here, identical duplicate structures were made on separate samples to obtain artefact free STXM and SEM images.

SEM imaging was always performed last as it was found to be the most destructive. Even the process of sputter coating a 5 nm or even a 1 nm metal film onto the polymer samples to enable SEM imaging was found to induce significant

chemical change observed in the NEXAFS spectra. These coating-induced changes to the C 1s NEXAFS spectrum of PMMA are presented in Fig. 3.3.

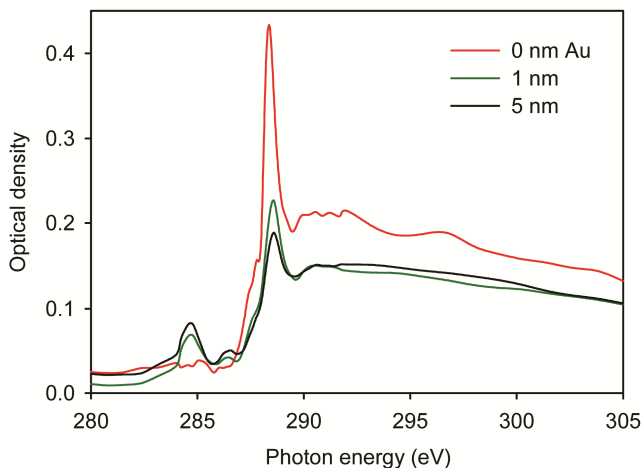


Figure 3.3: C 1s NEXAFS spectral changes induced by sputter coating 0 nm Au (red), 1 nm Au (green) and 5 nm Au (black) onto 50 nm PMMA films (acquired using 5.3.2.2).

1 nm of Au caused mass loss, judged by the decrease in the signal intensity at photon energies ≥ 305 eV, and loss of C=O bonds judged by the decrease in the prominent C 1s(C=O) $\rightarrow \pi^*_{\text{C=O}}$ signal at 288.4 eV. In addition, a new signal at 284.8 eV formed, indicative of C=C bonding. The thicker the coating, the greater the spectral change. These spectral changes of PMMA are similar to those induced by controlled x-ray exposure using STXM (Ch. 7, Fig. 7.3). After SEM imaging, the imaged sample was regarded as destroyed; once a polymer has been inside the SEM, it should be considered a changed material until proven otherwise, and not the other way around.

Chapter 4

Zone plate focused soft x-ray lithography

This chapter reports the fabrication of small features directly written in thin layers of PMMA using the zone plate focused x-rays of a STXM. The incorporation of a post-exposure development step is described in this chapter, and a minimum feature size of 40 ± 5 nm was achieved. A “radiation spreading” phenomenon by which patterned features become wider with increasing dose was found to be related to the PSF of the optical system and not the polymeric resists.

Reprinted with permission from Applied Physics A: Materials Science & Processing 2011, 103, 1-11, A.F.G. Leontowich, A.P. Hitchcock. DOI: 10.1007/s00339-010-6172-4, © 2012 Springer Science + Business Media.

A.P. Hitchcock and the author of this thesis conceived the experiments. The author of this thesis prepared all samples and developed them, performed all the experiments, analyzed the data and wrote the manuscript which was edited by A.P. Hitchcock.

Zone plate focused soft X-ray lithography

Adam F.G. Leontowich · Adam P. Hitchcock

Received: 6 December 2010 / Accepted: 9 December 2010 / Published online: 29 January 2011
© Springer-Verlag 2011

Abstract The zone plate focused soft X-rays of a scanning transmission X-ray microscope have been used to pattern poly(methyl methacrylate) and poly(dimethylglutarimide) films by a direct write method which is analogous to lithography with a focused electron beam. The lithographic characteristics of both polymers have been determined for 300 eV X-rays. With low doses (1 MGy), developed lines 40 ± 5 nm wide were created in poly(methyl methacrylate). At higher doses an exposure spreading phenomenon substantially increases the lateral dimensions of the developed patterns. The spreading mechanism has been identified as the point-spread function of the zone plate lens. The performance of focused soft X-ray lithography is compared to other direct write methods. The practicality of a dedicated focused soft X-ray writer instrument is discussed.

1 Introduction

The radiation based lithography process was first disclosed in 1852 [1]. Continuous improvement of radiation based lithography techniques has played a central role in facilitating the fabrication of ever shrinking devices (electronic [2], nanofluidic [3], photonic [4], mechanical [5], optical [6]) with ever superior performance which modern society is increasingly reliant upon. Yet after more than 150 years of innovation the fundamental steps have not changed: a substrate is coated with a layer of radiation sensitive material, termed

the resist. Radiation is directed upon the resist in a controlled manner which causes changes to its chemical properties, patterning it into areas of irradiated and non-irradiated material. The sample then undergoes a development procedure, often accomplished by immersing the sample in a suitable solvent. The chosen solvent may remove the irradiated resist, leaving behind the non-irradiated material (positive mode), or the solvent may remove the non-irradiated resist, leaving behind the irradiated material (negative mode). After development, the desired pattern exists as a mask of resist on substrate. Development of the patterned resist is a crucial step toward actual device fabrication.

There are at least three general methods to arbitrarily pattern resists via radiation.

- (1) Position a patterned mask with transparent and opaque areas between a radiation source and the resist, and flood the mask with radiation [7]. Current state of the art tools for mass production of electronic devices such as microprocessors employ the patterned mask method and use 193 nm photons to produce sub-50 nm features on an industrial scale [8].
- (2) Position a patterned reflecting surface between the radiation source and the resist, irradiate this surface, and allow only the reflected radiation to impinge upon the resist [9]. It is anticipated that this projection method with extreme ultraviolet photons (13.5 nm) will supersede the pattern mask method for industrial scale production at the 15 nm node.
- (3) Focus radiation with optics or electromagnetic fields to a small point, then scan either the beam above the resist, or the resist below the beam, in a controlled manner. This is the direct write method.

Both patterned mask and projection methods rely on the direct write method to create the arbitrarily patterned masks

A.F.G. Leontowich · A.P. Hitchcock (✉)
Brockhouse Institute for Materials Research, McMaster
University, Hamilton, L8S 4M1 ON, Canada
e-mail: aph@mcmaster.ca
Fax: +1-905-5212773

and surfaces for micron and sub-micron lithography. Focused beams are also generally used for low volume production when the cost of fabricating a mask is prohibitive, such as producing masters for microfluidic devices, prototyping, and in fabricating one-off devices.

Reports of sub-100 nm direct write patterning and lithography with focused photons are scarce relative to those involving focused electrons and ions. We hypothesize several reasons for this. The first report of patterning with a focused electron beam (1960) demonstrated sub-100 nm features [10]. For far field techniques, the Rayleigh criterion prevents focusing of photons at visible and UV wavelengths into sub-100 nm spots (though sub-100 nm direct write patterning with visible light and highly specific resists has been reported [11]). As one reaches beyond the deep ultraviolet in search of higher resolution, massive challenges arise in optics fabrication: almost negligible differences in refractive index from unity, relatively large absorption coefficients, and the necessity to fabricate optical elements with an accuracy comparable to the wavelength of X-rays [12]. Another early problem was the unavailability of bright X-ray sources. Meanwhile, very early in the history of electron beam lithography, electron beams could be focused into sub-10 nm Rayleigh resolution spots with adequate current to expose resist materials. By 1980 there were commercially available electron beam writer systems, and focused ion beams had demonstrated sub-100 nm patterning capability [13]. An early comparison of direct write electron and UV systems reported that focused electron beams had greater write speed and could produce narrower features [14]. In addition to the massive technological challenges that needed to be overcome at that time, it was not clear that a focused photon source of any energy could provide any advantages over a focused electron beam for sub-100 nm direct write patterning. At present, “X-ray lithography” is nearly synonymous with the patterned mask method and broadband synchrotron radiation, while direct write electron beam systems are the exposure tools of choice in terms of minimum feature size and flexibility.

Spurred by the developers of water window (2.5–4.5 nm) soft X-ray microscopy [15, 16] the technological barriers hindering sub-100 nm direct write patterning with focused X-rays have since been overcome. Modern scanning transmission X-ray microscopes (STXM) [17–19] routinely focus monochromatic soft X-rays into sub-40 nm Rayleigh resolution spots using Fresnel zone plates [20] (fabricated by electron beam lithography!) with the state of the art resolution being 10 nm [21]. Though the efficiencies of zone plates are quite low (often less than 10%) the performance of modern third generation synchrotrons and associated beamlines is so tremendous that instrument performance is rarely flux limited. The first example of direct write X-ray patterning was reported by Zhang et al. [22], who used focused

317 eV soft X-rays at the National Synchrotron Light Source (NSLS) to pattern poly(methyl methacrylate). Larciprete et al. [23] used focused 640 eV soft X-rays at ELETTRA to pattern LiF films. Wang et al. [24, 25] using Advanced Light Source STXM 5.3.2.2 (formerly referred to as 5.3.2) have pioneered direct write X-ray patterning at multiple wavelengths to pattern multi-layer polymer films with chemical selectivity.

However, in all reported direct write X-ray patterning experiments to date the best minimum feature size of either undeveloped or developed patterns is only 90 ± 14 nm in hydrogen silsesquioxane (HSQ) [26], despite writing with focused X-ray sources of much finer spot size. The resolution limitation is due to an exposure spreading phenomenon whose origin has not been understood until this work. Here we report the creation of patterns at 40 ± 5 nm feature size in thin layers of polymeric resists with focused soft X-rays, their development, and subsequent characterization. Feature broadening at higher doses is documented and the exposure-spread mechanism is shown to be due to the point-spread function of the zone plate lens. The performance relative to other radiation based lithography techniques is discussed and the potential for practical applications of focused soft X-ray lithography is addressed.

2 Experiment

2.1 Materials

Poly(methyl methacrylate) (PMMA) M_w : 315 000 M_w/M_n : 1.05 electronics grade was purchased from Polymer Source Inc. Toluene 99.9% Chromasolv®, 4-methyl-2-pentanone (MIBK) >98.5% ACS reagent grade, and *N,N*-dimethylformamide (DMF) 99.9% Chromasolv® were purchased from Sigma-Aldrich. 2-Propanol (IPA) 99.5% and water HPLC grade were purchased from Caledon. Mica was purchased from Ted Pella Inc. 75 nm Si_3N_4 windows (1×1 mm window area in a 5×5 mm Si wafer frame) were purchased from Norcada Inc. Poly(dimethylglutarimide) (PMGI) was a gift from Professor Ash Parameswaran, Simon Fraser University, British Columbia, Canada.

2.2 Complementary characterization

Atomic force microscopy (AFM) measurements were performed with a Quesant 350 microscope equipped with Budget Sensors Multi75A1 probes. All images were collected with the AFM operating in non-contact mode at a 0.5 Hz scan rate with 512×512 pixels. Scanning electron microscope (SEM) measurements were performed with a JEOL JSM-7000F microscope operating at 10 keV with a 60 μA beam current at a working distance of 5 mm. A Gatan model

682 Precision Etching Coating System was used to coat all samples with 5 nm Pt before analysis. AFM measurements were always performed before Pt coating and SEM measurement to avoid artifacts due to Pt deposition or electron beam damage.

2.3 Preparation of thin polymer films on Si₃N₄ substrates

Thin polymer films were fabricated by spin casting four drops of a 1.0% w/w PMMA/toluene solution, or a 2.8% w/w PMGI/DMF solution onto a 1.5 × 1.5 cm piece of freshly cleaved mica. The films remained in ambient air for 10 minutes and were then cut into 3 × 3 mm pieces with a scalpel. Upon slowly dipping the mica into a Petri dish filled with water, small pieces of the film release and float on the surface, which were then caught on Si₃N₄ windows. The pieces were positioned such that the polymer film only partially covered the window to allow for measurements of the spectrum of incident radiation (*I₀*). The samples were then annealed for 1 hour at 140°C (PMMA) or 230°C (PMGI) at reduced pressure ($\sim 2 \times 10^{-2}$ Torr). The annealed films were consistently 45 ± 5 nm (PMMA) and 65 ± 5 nm (PMGI) as measured by AFM and near edge X-ray absorption fine structure (NEXAFS) spectroscopy.

2.4 Scanning transmission X-ray microscope and patterning

An interferometrically controlled STXM [17] on bend magnet beamline 5.3.2.2 [27] at the Advanced Light Source (ALS) at Lawrence Berkeley National Lab (LBNL) was used to direct write the desired patterns. The zone plate lens (25 nm outer zone, 240 μm diameter, 90 μm central stop) was supplied by the Center for X-ray Optics (CXRO), LBNL. A N₂ gas filter (a differentially pumped 1 m long section of the beamline at a pressure of ~ 0.6 Torr) was used to eliminate higher order radiation. The patterning was carried out with the STXM tank backfilled with He to 1/3 atmospheric pressure, after evacuation of air. A uniform area of the film was located and a sharp focus was established at a point within 80 μm of the area to be patterned. Patterning was executed using the pattern generation capabilities of the STXM Control software, as described by Wang et al. [24]. Special care must be taken to ensure that the patterning is done on a pristine area of the film just beside the area of focusing, since even very brief (1 ms) exposures used while imaging are sufficient to cause unwanted patterning, especially to PMMA. The patterned areas were never imaged by STXM before or after patterning. For all experiments the exposure energy was fixed at 300 eV. The detector efficiency in the C K edge region [17], mass loss, and other instrumental parameters have been taken into account in computing the absorbed radiation doses presented, which are believed to be precise within 10%, using methods described in detail earlier [24, 25].

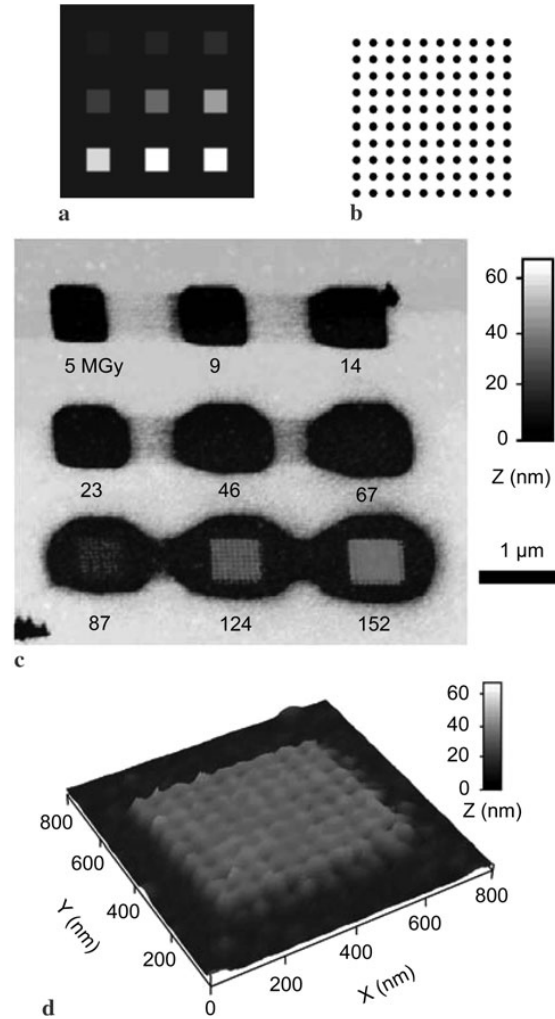


Fig. 1 (a) The pattern used to drive the sample positioning stages relative to the focal point consists of nine 600×600 nm areas. (b) Each square in (a) is composed of 10×10 individual exposures spaced 60 nm center to center. (c) AFM image of the pattern directly written in PMMA with focused 300 eV monochromatic X-rays after development. (d) Expanded three dimensional view of the eighth area in (c). The measured center to center spacing of the crosslinked PMMA mounds is 60 ± 5 nm

2.5 Development of patterned polymer films

Development of PMMA was accomplished by immersing the entire Si₃N₄ window in 3:1 IPA:MIBK for 30 s, then IPA for 15 s. PMGI was developed by immersing the entire Si₃N₄ window in 7:3 IPA:H₂O for 30 s, following the procedure of Johnstone et al. [28]. All development occurred at ambient temperature ($\sim 20^\circ\text{C}$).

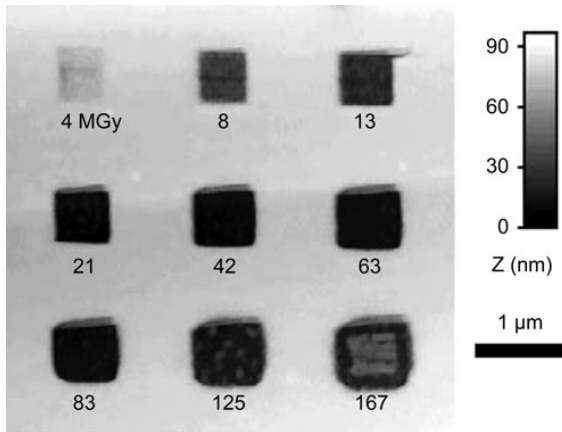


Fig. 2 AFM image of the pattern directly written in PMGI with focused 300 eV monochromatic X-rays after development (the resolution of this image is equal to Fig. 1c)

3 Results

3.1 Lithographic characteristics of PMMA and PMGI patterned with 300 eV soft X-rays

PMMA was exposed to a pattern consisting of nine 600×600 nm exposure areas (Fig. 1a) which was designed to efficiently characterize the lithographic transitions of PMMA. We define two lithographic transitions: (a) the dose/dose range required for complete removal of the resist from the exposure area after development (positive mode), and (b) the dose/dose range required to transition from positive mode to negative mode. Each square is composed of 10×10 pixels spaced 60 nm center to center (Fig. 1b). The pixel dwell time of the exposure areas increases from left to right and top to bottom such that each area receives a controlled dose that progressively increases from one area to the next. After patterning the sample was removed from the STXM and developed. The developed pattern was then imaged with AFM (Fig. 1c) and SEM (not shown). A high resolution AFM image of the eighth area (Fig. 1d) shows that all 10×10 exposed points are resolved as mounds of crosslinked (negative mode) PMMA with a center to center spacing of 60 ± 5 nm.

Many areas of the PMMA film were patterned covering a dose range from 0.1–300 MGy. The dose dependent lithographic transitions of PMMA were determined from analysis of AFM images of these features and the observations are summarized in Table 1.

The dose dependent lithographic transitions of PMGI were measured in the same fashion. Patterned areas were prepared by controlled exposure to 300 eV focused X-rays, developed and imaged with AFM (Fig. 2). The lithographic transitions of PMGI were determined from analysis of the

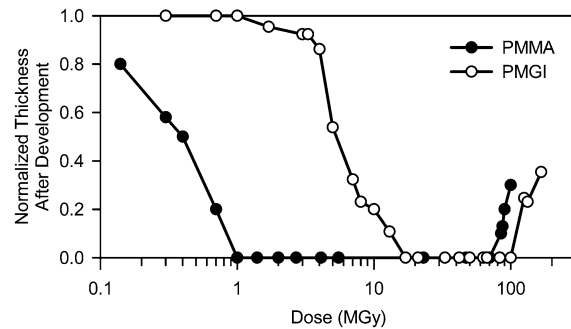


Fig. 3 Plot of residual thickness, as determined by AFM after development, as a function of dose for PMMA and PMGI exposed to 300 eV monochromatic X-rays. 1 corresponds to the initial spun cast thickness, 0 being full removal

AFM images and the observations are summarized in Table 2. The response of both polymers to dose after development was quantified by AFM and is presented graphically in Fig. 3.

3.2 Minimum developed feature size

An elbow pattern (Fig. 4a) was directly written in a PMMA film with a dose of 1 MGy. After patterning the sample was removed from the STXM, developed, and imaged with AFM (Fig. 4b). The developed lines were determined by AFM to be ~ 50 nm deep (Fig. 4c), indicating that these lines extend down to the substrate. The SEM image of the developed elbow pattern (Fig. 4d) reveals a different surface morphology at the center of the lines versus other areas of the film. The morphology at the center of the lines is identical to that of bare Si_3N_4 , again confirming complete removal of PMMA from the exposure area after development. We determined the width of the developed horizontal lines to be 40 ± 5 nm with a pitch of 120 nm (a 1:2 linewidth-to-spacewidth ratio) by analyzing the SEM image. The width of the vertical lines is somewhat larger and less regular which we suspect is due to incomplete closure of the shutter between pixels and the direction in which the patterns are written (horizontal line after horizontal line from bottom to top). The minimum 1:1 linewidth achievable, as well as the minimum negative mode linewidth, were determined by adjusting the size of the elbow pattern and were characterized in the same fashion. Minimum linewidth values for PMMA are presented in Table 3.

3.3 Exposure spreading phenomenon

While attempting to find the optimum doses for positive mode lithography it was readily apparent that the width of the developed features increased with increasing dose. To demonstrate, several identical elbow patterns were written

Table 1 Lithographic characteristics of PMMA exposed to 300 eV soft X-rays

Dose (MGy)	Observation
<1	Incomplete removal of irradiated material
1–85	Complete removal of irradiated material (positive mode)
85–95	Onset of crosslinking (negative mode)
95–150	Fine crosslinked features
>150	Extensive crosslinked features

Table 2 Lithographic characteristics of PMGI exposed to 300 eV soft X-rays

Dose (MGy)	Observation
<15	Incomplete removal of irradiated material
15–110	Complete removal of irradiated material (positive mode)
110–140	Onset of crosslinking (negative mode)
>150	Extensive crosslinked features

directly in PMMA differing only in dose. After patterning, the sample was removed from the STXM, developed, and imaged with SEM. The series of SEM images (Fig. 5) clearly shows that as dose increases, the width of developed features increases. Closely spaced features experience substantial distortion; at higher doses the exposure spread can cause closely spaced lines to merge together. In Fig. 5d the exposure areas received sufficient dose to be in the negative mode regime; the 1:1 lines of crosslinked PMMA are 90 ± 5 nm wide. Surprisingly, material was removed more than 300 nm away from the expected exposure area. It is this type of exposure-spread phenomenon that has limited the minimum achievable feature sizes for direct write X-ray patterning in the past [23–26]. Understanding the origin, which in turn could lead to strategies to minimize the spread, was a major goal of this research.

Two single pixel exposures were made in PMMA with relatively high doses (370 MGy) to investigate the exposure-spread phenomenon. After patterning the sample was removed from the STXM, developed, and imaged by AFM (Fig. 6a). This image shows that the spatial distribution of the exposure spread around a single pixel exposure is anisotropic and extends several hundred nm from the central exposure point. The second single pixel exposure made under identical conditions has an identical spatial distribution. The spatial distribution of the apparent exposure spread around multiple separated single pixel exposures is completely reproducible with fine detail in PMMA. The developed single pixel exposures were also imaged by SEM (Fig. 6b). The spatial distribution observed by SEM is identical to that measured by AFM (Fig. 6a), negating AFM tip convolution effects as the origin of the reproducible anisotropic pattern.

The same single pixel, high dose exposure experiment was performed in PMGI. The developed patterns were imaged with AFM (not shown) and SEM (Fig. 6c). AFM im-

Table 3 Minimum developed feature widths created in PMMA

Feature Classification	Width (nm)
Positive mode 1:2 lines	40 ± 5
Positive mode 1:1 lines	75 ± 5
Negative mode 1:1 lines	90 ± 5

ages were not included because the features observed were identical to those in the SEM images. The spatial distribution of the exposure spread around multiple separated single pixel exposures is anisotropic and reproducible with fine detail in PMGI. A comparison of Figs. 6b and 6c shows the overall shape of the anisotropic spatial distribution is independent of the resist.

4 Discussion

4.1 Focused soft X-ray lithography in PMMA and PMGI at 300 eV

4.1.1 Lithographic characteristics of PMMA and PMGI for 300 eV monochromatic X-rays

There are hundreds of reports of radiation based lithography involving PMMA but relatively few involving PMGI. Our measured dose value of 1 MGy to adequately expose PMMA for positive mode lithography (Table 1) is consistent with other reported values (0.85 MGy [5], 1.4 MGy [29], 0.42 MGy [30]). However, caution must be used when comparing this value, as well as all dose values compiled in Tables 1 and 2, to other studies involving PMMA and PMGI, as these values also depend critically upon certain development (composition, development and rinse time, temperature) and

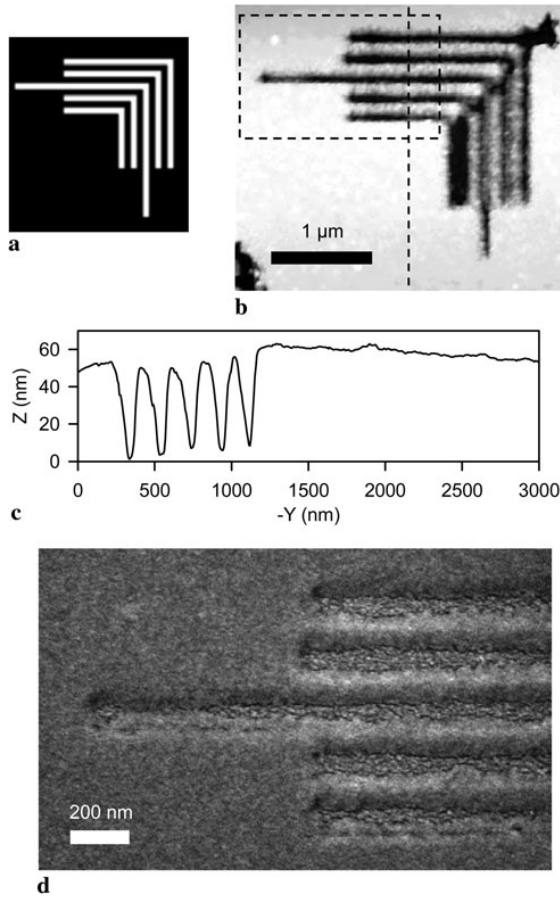


Fig. 4 (a) The elbow pattern used to drive the sample positioning stages relative to the focal point. (b) AFM image of the pattern directly written in PMMA with focused 300 eV monochromatic X-rays after development. Dose: 1 MGy. (c) Line out from the *dashed vertical line* in (b). (d) SEM image of the region outlined by the *dashed rectangle* in (b) demonstrating 40 ± 5 nm 1:2 developed lines

resist (M_w and M_n , casting solvent, thermal treatment) details [31, 32]. Still, we note that even though the wavelengths between these studies are very different (and thus primary radiation effects are different), a similar dose for full removal was determined, which suggests that secondary radiation damage processes dominate, and the overall process is mainly related to total energy deposited per unit of material (i.e. absorbed dose). We find it difficult to avoid causing a measurable change to the developed height of PMMA, even with the shortest possible dwell times (~ 1 ms due to the time needed to open and close an in-vacuum piezo shutter) and very narrow entrance and exit slit settings (thus minimizing the photon flux). The transition from non-irradiated height to full removal inside the exposure area is very rapid and occurs over a dose range of less than 1 MGy (Fig. 3) On the other hand the positive mode response of PMGI (Fig. 3)

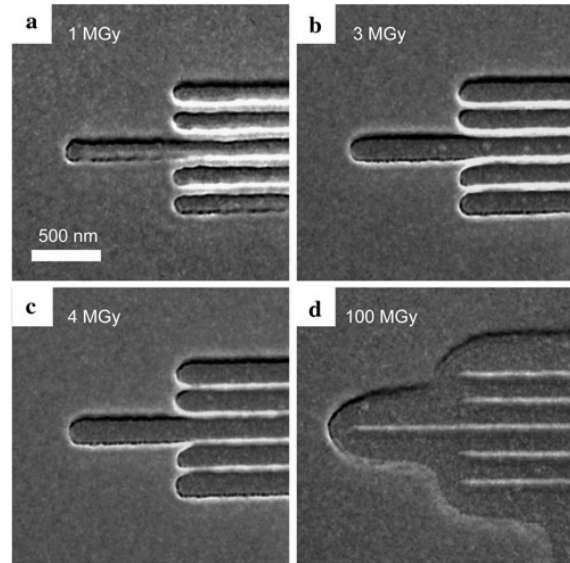


Fig. 5 SEM images of identical elbow patterns directly written in PMMA with focused 300 eV monochromatic X-rays after development (all images are the same scale). (a) An optimum dose of 1 MGy produces the narrowest positive mode features. The developed linewidth increases with increasing dose (b), 3 MGy, (c) 4 MGy. (d) An extensive positive mode region extends beyond the high dose (100 MGy) negative mode regions. The crosslinked 1:1 lines of (d) are 90 ± 5 nm wide

is much more gradual. It takes much more dose to cause a thickness change to PMGI as compared to PMMA, and the last few nm of PMGI are especially difficult to remove. More dose is required in order to fully remove all material down to the substrate. Consequently, the feature sizes broaden, and so the developed resolution of PMGI is not as high as PMMA.

PMMA and PMGI are somewhat unique in that they behave as positive resists at low doses and negative resists at high doses, as demonstrated in Figs. 1c and 2. This dose dependent transition from positive to negative mode has been known for some time for PMMA [2], but we are unaware of any reports of this behavior for PMGI. The onset of crosslinking for PMMA consistently occurred within a relatively narrow dose range (Table 1), and fine sub-100 nm features can be made with doses just beyond the onset, as demonstrated in Figs. 1d and 5d. Within the extensive crosslinking dose range the crosslinked material from individual pixels blurs together, such that the pixilation is smoothed and the thickness is even within ± 1 nm (Fig. 1c, area 9). In contrast, the onset of crosslinking in PMGI is not as well defined and occurs over a much larger dose range (Table 2). Within this dose range we observe random blobs of crosslinked PMGI with spotty coverage of the substrate (Fig. 2, area 8). The substrate could be fully covered with crosslinked PMGI using doses greater than 140 MGy,

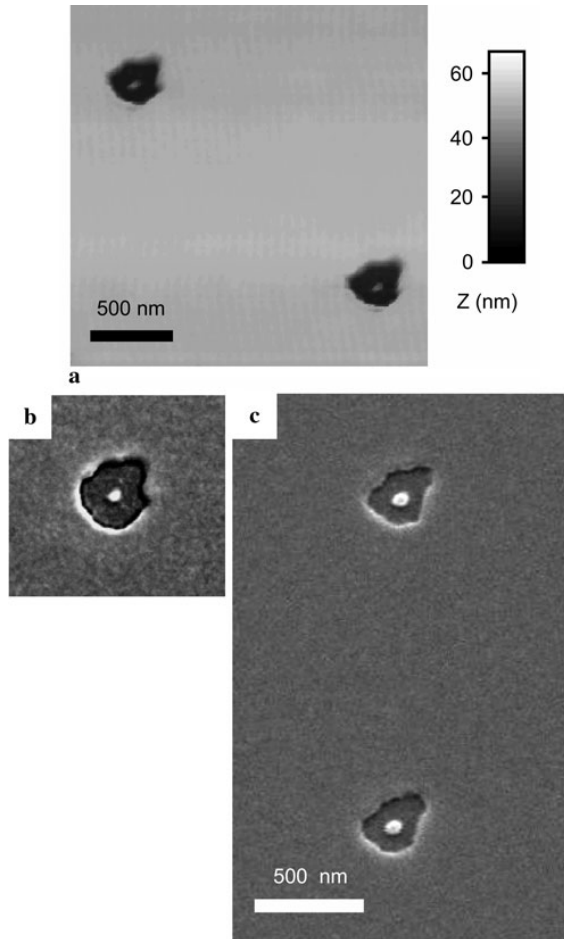


Fig. 6 (a) AFM image of a developed PMMA pattern consisting of two single pixel exposures, each at a dose of 370 MGy. The dots in the centers are crosslinked PMMA. (b) SEM image of the top left single pixel exposure of (a). (c) SEM image of a developed PMGI pattern consisting of two single pixel exposures, each at a dose of 900 MGy. The dots in the centers are crosslinked PMGI

though the thickness of this coverage was uneven at ± 5 nm (Fig. 2, area 9).

4.1.2 Minimum feature size

We have reduced the minimum feature sizes fabricated with focused soft X-rays by a factor of five from our earlier reports. In our previous work [24, 25, 33] films were patterned with high doses, and the patterned areas were then imaged at low doses with the STXM using photon energies sensitive to the damage chemistry (in PMMA and PMGI, C=O bond removal). The feature sizes were determined from analysis of the STXM images. In the case of PMMA, when imaging at 288.5 eV (the sensitive C 1s(C=O) \rightarrow $\pi_{C=O}^*$ transition) the contrast in each pixel of the image is proportional to the

number of carbonyl bonds. As the exposure area receives more dose, more carbonyl bonds are broken. Doses below 5 MGy show negligible change in contrast for PMMA [32], so the patterned areas must receive more than 5 MGy to just be observable above the background, which is five times that required for positive mode lithography.

The mechanism for development of PMMA is very well known [2, 34]. Briefly, PMMA experiences primarily main chain scission when exposed to ionizing radiation. Lower molecular weight (irradiated) PMMA is extremely soluble in the developer solution, whereas higher molecular weight (non irradiated) PMMA is only sparingly soluble. One main chain scission in the middle of a polymer chain will reduce its molecular weight in half, which has a very large effect on its solubility [31, 34]. Thus, without development, one bond scission has a negligible effect on contrast when visualizing the patterns by X-ray microscopy, whereas, with development, one bond break can produce a very large contrast change. Furthermore, in this work we have imaged the developed patterns by AFM and SEM which have significantly better spatial resolution, in the sub-5 nm range, as opposed to the 30 nm spatial resolution of the STXM with 25 nm zone plates. By incorporating a development step and employing imaging techniques with higher resolution we are able to visualize very low doses and avoid the large dose and thus exposure-spread regime, which has led to the significant improvement in minimum feature size.

We believe the 40 ± 5 nm features presented here are the smallest created with a zone plate lens at any wavelength in any orientation (including demagnifying a patterned mask [35]). The zone plates used in this study achieve 30 nm diffraction-limited resolution, thus we have demonstrated patterning at 1.3 times the diffraction limit. Still, many variables were not optimized. Avenues toward further reduction of minimum feature size are discussed in Sect. 4.3.

4.2 Exposure spreading mechanism for focused soft X-rays

Previous reports of STXM mapping of chemical changes caused by focused soft X-rays have observed signs of apparent exposure beyond the expected exposure area [24, 25]. Moving to development of patterns has reduced minimum achievable feature sizes dramatically but the exposure-spread phenomenon qualitatively depicted in Fig. 5 still exists. This spread is also apparent in Figs. 1 and 2—the squares become much wider than their defined 600×600 nm exposure areas with increasing dose. The features of this exposure spreading mechanism are quantifiable - the lateral extent of the spread depends on the polymer used and dose [24, 25]. Other direct write X-ray patterning studies have noted that this takes place not only in organic resists, but also inorganic resists [23, 26], and self assembled monolayers [36]. The radiation based lithography literature contains

numerous examples of effects which can cause the actual exposure area to be larger than intended (i.e. “proximity effects”) with very similar observable characteristics to this study, though the underlying mechanistic theories are very different. Several hypotheses have been put forward, but there is no consensus for focused soft X-rays.

Reports have shown that instability of a patterned mask or the radiation source can degrade the fidelity of patterning, blurring sharp features [37]. The possibility of unwanted movement of our focal point, which could cause the actual exposure area to be larger than anticipated, was considered but dismissed since the position of the focal point relative to the sample is stabilized by an interferometric feedback system to ± 10 nm in X, Y, and Z [17] with a feedback response in the 100 Hz range. The positional accuracy and stability of the STXM microscope is clearly demonstrated by the image presented in Fig. 1d where all 10 by 10 single pixel exposures are faithfully reproduced as dots of crosslinked PMMA spaced 60 ± 5 nm apart. The beam was positioned over each pixel for 225 ms, which is ~ 200 times longer than necessary for positive mode lithography in PMMA. This is a testament of the positional accuracy of ALS STXM 5.3.2.2, be it for patterning or imaging.

Observing the spread distribution surrounding single pixel exposures as revealed by development provides tremendous insight into the mechanism of exposure spread for the case of focused soft X-rays. Our PMMA and PMGI films are expected to be uniform since they were annealed above their respective T_g 's for one hour. Therefore, one expects an isotropic circular pattern for the case of a migrating damaging species spreading outward in a uniform medium. Instead, Fig. 6a shows that the spatial distribution of damage is not isotropic. Had this only been observed in one exposure, the source of the anisotropy could be rationalized as statistical variation in the migration of a damaging species, possibly due to a non uniform film. However we observe an identical anisotropic exposure-spread distribution in AFM and SEM images of identical repeated single pixel exposures. The migration of any damaging species produced by radiation, outward from the exposure area either through the sample or above it, is reasonably expected to be a random walk. Any suspected primary scattering processes [36] or possible radiation initiated propagating chemical reactions [38] would also be random. Since the spatial distribution of damage is not random, we deduce that the exposure-spread mechanism does not involve any process with a statistically random spatial distribution. Comparison of the SEM images of the spread distribution in PMMA (Fig. 6b) and PMGI (Fig. 6c) shows that the exposure spread is the same in two different polymers, when patterned under identical conditions. Ongoing work involving similar single pixel patterning experiments executed with the STXM at the Canadian Light Source (Saskatoon, SK) produced different, reproducible anisotropic spread patterns. Since the anisotropic

exposure-spread distribution is independent of the resist, it must involve something outside the sample.

The point-spread function of any given (zone plate) lens is expected to be the same for each single pixel exposure. In the best-case scenario, a perfectly fabricated lens, uniformly illuminated with coherent radiation will produce an intensity distribution that is an Airy disk in the focal plane. The focal point is not a “spot” of uniform intensity and finite diameter, but is in fact an intensity/dose distribution [39]. We have determined that a 1 MGy exposure is required to clear PMMA from the exposed area after development. When the exposure times are increased, the dose threshold of 1 MGy is exceeded further and further away from the central axis of the focal point, leading to the exposure-spread phenomenon. The relationship between the distance of exposure spread from the center of the focal point versus dwell time reflects the point-spread function. This approach has been used to characterize the point-spread function of zone plate lenses in two dimensions with non-ionizing radiation [40]. If the illumination or the lens itself deviates from perfection, the point-spread function will not be symmetric and the pattern developed after a single pixel exposure will mirror these deviations, leading to a non symmetric dose distribution and therefore a non symmetric exposure-spread distribution, independent of the resist.

We hypothesize that the anisotropy of the exposure-spread distribution for a single pixel exposure is due to some combination of aberrations in the zone plate and/or non uniform illumination of the zone plate. At this stage we can only say that the exposure-spread mechanism for the case of patterning with zone plate focused soft X-rays is related to the instrument properties, in particular, the point-spread function of the lens. Though the diffraction-limited value for resolution (the Rayleigh resolution) is often referred to as the “spot size”, this is a clear illustration of why that should not be taken literally. For example, the diameter of the first null of the Airy pattern for a zone plate with a 25 nm outermost zone at perfect focus is 61 nm, and 16.2% of the total intensity lies beyond that *in the best-case scenario* [39]. Acknowledgement of the point-spread function in STXM is clearly important for patterning but it is also critical for spectromicroscopy where spectral signals ascribed to a very small object do in fact contain contributions from X-ray absorption outside of that small object. While this is not important for majority signals, it could be important for minority components.

There is much debate concerning the radius over which a secondary electron (or any migrating damaging species for that matter) produced within the exposure area could migrate and spread damage, and it is this distance that is thought to be a fundamental limit of lithographic techniques which employ ionizing radiation [41, 42]. In solids the radius over which a liberated secondary electron could migrate

and cause damage can be predicted by the universal inelastic mean free path curve [43]. This distance is not likely to be more than 10 nm given that the maximum kinetic energy is the photon energy itself, and 300 eV soft X-rays are used. The observed damage spread distribution surrounding single pixel exposures provides an excellent opportunity to briefly comment. Under identical conditions, the anisotropic exposure-spread distribution is completely reproducible *in fine detail* within the resolution of the AFM and SEM images. Therefore, we infer that the radii of any damaging secondary processes initiated by 300 eV photons must be less than 10 nm, for, if this were not the case, these fine details would noticeably change from exposure to exposure.

4.3 Avenues toward reducing minimum feature size

4.3.1 Improving the resist and development

PMMA was chosen as a resist for this study because it is consistently found to be one of the highest resolution resists using many different radiation sources and patterning techniques. One avenue to higher resolution would be optimization of the development procedure. The 3:1 IPA:MIBK developer system was employed due to its popularity in the literature, which should facilitate a more valid direct comparison of our results to those of others. Ultrasonic agitation methods [44], cold development [45], as well as other solvent systems [44, 46] have been reported to reduce the width of developed features in PMMA. Thermal treatment methods have also led to reduced minimum feature sizes in PMMA [47]. Other resists such as HSQ [26] could offer higher resolution than PMMA. One can also envisage a resist and developer system designed specifically for focused soft X-ray lithography.

4.3.2 Improving the optics and exploring new energies

Perhaps the most obvious way to increase the resolution of any direct write technique would be to incorporate higher quality optics; patterning with improved zone plates should lead to a reduction in minimum feature size. Zone plates with 12 nm outer zone width, which have resolved 1:1 12 nm lines, have recently been fabricated [6]. Another possibility would be to use the third order rather than first order focus of a zone plate. This operational mode is difficult to establish but it provides three times smaller Rayleigh spot size [20, 48]. This approach has been used to resolve 1:1 14 nm lines with a zone plate having 25 nm outer zones [49]. In principle, patterning with focused X-rays could be accomplished with Kirkpatrick-Baez (KB) X-ray focusing mirrors instead of zone plates [20]. One dimensional resolution as small as 7 nm has recently been achieved in a long beam lines with multiple KB focusing optics [50]. KB focusing

has the added benefit of being achromatic. It may be possible to achieve lower minimum feature sizes by patterning at other soft X-ray energies. Patterning with lower energy electrons has been reported to decrease linewidths [51, 52] but to our knowledge this has not been explored for patterning with monochromatic X-rays. We note that lower electron beam energy is not intrinsically a recipe for higher resolution since the electron beam writers used to fabricate the smallest zone width zone plates, such as the LBNL Nanowriter [53], operate at 50–100 keV.

4.4 Outlook

Like the earliest reports of focused electron beam patterning [10], we and others have adapted existing X-ray microscopes to write patterns. Currently there are eight soft X-ray STXMs in the world and at least three more are under construction or are approved projects [54], all of which are technically capable of this type of work. Due to the requirement of strictly monochromatic X-rays for best focus with zone plates, at present STXMs are only found at high brightness third generation synchrotron light sources, for which there is high demand. These microscopes were not designed for patterning and so one faces certain instrumental limitations. For the STXM, fine focus is achieved by scanning the zone plate to sample distance and observing the transmitted images of a small opaque object. Soft X-ray absorption cross sections are relatively high, so STXM samples must be thin (~ 100 nm for illumination at the C 1s edge) and positioned free standing or on a soft X-ray transparent substrate such as Si_3N_4 or thin polymer materials such as polyimide or formvar. Consequently these thin substrates are extremely fragile. We are also limited to patterning relatively small areas. With the current instrument and relatively flat Si_3N_4 substrates the microscope stays in reliable focus over approximately $80 \times 80 \mu\text{m}$. Then there is the issue of write speed. It takes approximately 2–3 ms for the microscope to accurately position the stages based on interferometer feedback. The shortest period of time the shutter can open and close is about 1 ms. 1 ms in the current configuration provides enough dose to bring PMMA into the positive mode regime; thus the speed of patterning in positive mode is not limited by flux. This provides some estimate of the speed of patterning: 10% of a $20 \times 20 \mu\text{m}$ area with 30×30 nm pixels can be sufficiently exposed in about 3 minutes. It should be noted that PMMA is not considered to be a very sensitive resist and others are much more sensitive (though their sensitivity to soft X-rays remains to be measured). A faster acting shutter and more sensitive resist would provide some improvement. Many of these issues could be overcome by designing a dedicated X-ray writer instrument optimized for speed with autofocusing capability for patterning large areas (glass microscope slides, Si wafers, etc.).

Has the time come for such an instrument?

In our opinion, no. Even if the cost and access issues of third generation synchrotrons were addressed by compact, affordable, commercially available X-ray sources with similar performance, we feel it is unlikely that focused soft X-ray lithography will ever compete with electron beam lithography in terms of spatial resolution or throughput. Other groups have investigated zone plate arrays with multiple shutters for high throughput patterning [35, 55, 56]. After noting the difficulty in reproducibly fabricating a single high resolution zone plate, achieving and maintaining the sample to zone plate distance, keeping the order sorting aperture centered, etc., we feel that a large leap in technology will be required to fabricate and manage a zone plate array (tens to hundreds of beams) with parallel performance comparable to this study. Thus it seems that direct write lithography with focused soft X-rays offers negligible advantages *for applications currently well covered by electron beam lithography*. However one can envisage a number of special and possibly unique applications where focused soft X-ray lithography might be an attractive approach. In our view the biggest advantage is the ability to tune the photon energy. Chemically selective patterning in bilayer [24] and trilayer [25] systems has already been demonstrated. Exploitation of the chemical selectivity will likely drive applications of focused soft X-ray lithography.

5 Conclusion

A scanning transmission X-ray microscope has been used to pattern thin films of PMMA and PMGI with 300 eV monochromatic X-rays in a manner analogous to direct write lithography with a focused electron beam. The lithographic characteristics of both polymers were determined over a dose range from 0.1–300 MGy. With optimized doses, 40 ± 5 nm developed lines have been produced, which is approaching the diffraction-limited resolution of the zone plate lens used. We believe this to be the smallest feature size created with a zone plate lens at any wavelength in any orientation. The mechanism of the exposure spreading phenomenon was determined to be related to the point-spread function of the zone plate lens. We consider the development of a dedicated X-ray writer instrument to be premature at this point in time. Further investigation using present and future generation STXMs is adequate until there are specific examples which demonstrate unique advantages of focused soft X-ray lithography over existing direct write methods.

Acknowledgements This research was funded by NSERC, CFI and the Canada Research Chairs program. Most of the STXM was carried out at beamline 5.3.2.2 at the ALS, which is supported by the Director of the Office of Science, Department of Energy, under Contract No. DE-AC02-05CH11231. Some results were also obtained at

the Canadian Light Source which is supported by the Natural Sciences and Engineering Research Council of Canada, the National Research Council Canada, the Canadian Institutes of Health Research, the Province of Saskatchewan, Western Economic Diversification Canada, and the University of Saskatchewan. We thank Dr. David Kilcoyne and Dr. Tolek Tyliczszak for their expert support of the ALS STXMs and Dr. Jian Wang and Yingshen Lu for their support of the CLS STXM. We are especially grateful to Professor Ash Parameswaran for his generous gift of PMGI.

References

1. W.H.F. Talbot, British Patent 565 (1852)
2. M. Hatzakis, J. Electrochem. Soc. **116**, 1033 (1969)
3. S.-M. Park, Y.S. Huh, H.G. Craighead, D. Erickson, Proc. Natl. Acad. Sci. USA **106**, 15549 (2009)
4. A. Bingham, Y. Zhao, D. Grischkowsky, Appl. Phys. Lett. **87**, 051101 (2005)
5. E.W. Becker, W. Ehrfeld, D. Münchmeyer, H. Betz, A. Heuberger, S. Pongratz, W. Glashauser, H.J. Michel, R.V. Siemens, Naturwissenschaften **69**, 520 (1982)
6. W. Chao, J. Kim, S. Rekawa, P. Fischer, E.H. Anderson, Opt. Express **17**, 17669 (2009)
7. A.D. Wilson, IBM J. Res. Dev. **37**, 299 (1993)
8. D.P. Sanders, Chem. Rev. **110**, 321 (2010)
9. C.W. Gwyn, R. Stulen, D. Sweeney, D. Attwood, J. Vac. Sci. Technol. B **16**, 3142 (1998)
10. G. Möllenstedt, R. Speidel, Phys. Bl. **16**, 192 (1960)
11. L. Li, R.R. Gattass, E. Gershgoren, H. Hwang, J.T. Fourkas, Science **324**, 910 (2009)
12. V.V. Aristov, in *X-ray Microscopy II*, ed. by D. Sayre, M. Howells, J. Kirz, H. Rarback (Springer, Berlin, 1988)
13. R.L. Seliger, R.L. Kubena, R.D. Olney, J.W. Ward, V. Wang, J. Vac. Sci. Technol. **16**, 1610 (1979)
14. A.E. Brennemann, A.V. Brown, M. Hatzakis, A.J. Speth, R.F.M. Thornley, IBM J. Res. Dev. **11**, 520 (1967)
15. G. Schmahl, D. Rudolph, Optik **29**, 577 (1969)
16. B. Niemann, D. Rudolph, G. Schmahl, Appl. Opt. **15**, 1883 (1976)
17. A.L.D. Kilcoyne, T. Tyliczszak, W.F. Steele, S. Fakra, P. Hitchcock, K. Franck, E. Anderson, B. Harteneck, E.G. Rightor, G.E. Mitchell, A.P. Hitchcock, L. Yang, T. Warwick, H. Ade, J. Synchrotron Radiat. **10**, 125 (2003)
18. K.V. Kaznatcheev, Ch. Karunakaran, U.D. Lanke, S.G. Urquhart, M. Obst, A.P. Hitchcock, Nucl. Instrum. Methods Phys. Res., Sect. A, Accel. Spectrom. Detect. Assoc. Equip. **582**, 96 (2007)
19. J. Raabe, G. Tzvetkov, U. Flechsig, M. Böge, A. Jaggi, B. Sarafimov, M.G.C. Vernooij, T. Huthwelker, H. Ade, D. Kilcoyne, T. Tyliczszak, R.H. Fink, C. Quitmann, Rev. Sci. Instrum. **79**, 113704 (2008)
20. D. Attwood, *Soft X-rays and Extreme Ultraviolet Radiation Principles and Applications* (Cambridge University Press, Cambridge, 1999)
21. W. Chao, private communication
22. X. Zhang, C. Jacobsen, S. Lindaas, S. Williams, J. Vac. Sci. Technol. B **13**, 1477 (1995)
23. R. Larciprete, L. Gregoratti, M. Danailov, R.M. Monteverde, F. Bonfigli, M. Kiskinova, Appl. Phys. Lett. **80**, 3862 (2002)
24. J. Wang, H.D.H. Stöver, A.P. Hitchcock, T. Tyliczszak, J. Synchrotron Radiat. **14**, 181 (2007)
25. J. Wang, H.D.H. Stöver, A.P. Hitchcock, J. Phys. Chem. C **111**, 16330 (2007)
26. A.G. Caster, S. Kowarik, A.M. Schwartzberg, S.R. Leone, A. Tivanski, M.K. Gilles, J. Vac. Sci. Technol. B **28**, 1304 (2010)

27. T. Warwick, H. Ade, D. Kilcoyne, M. Kritscher, T. Tyliczszak, S. Fakra, A. Hitchcock, P. Hitchcock, H. Padmore, J. Synchrotron Radiat. **9**, 254 (2002)
28. R.W. Johnstone, I.G. Foulds, M.V. Pallapa, A.M. Parameswaran, J. Micro/Nanolithogr. MEMS MOEMS **7**, 043006 (2008)
29. A.C. Henry, R.L. McCarley, S. Das, C. Khan Malek, D.S. Poche, Microsyst. Technol. **4**, 104 (1998)
30. D.L. Spears, H.I. Smith, Electron. Lett. **8**, 102 (1972)
31. J.S. Greeneich, J. Electrochem. Soc. **122**, 970 (1975)
32. M. Hatzakis, J. Polym. Sci. **23**, 73 (1974)
33. J. Wang, C. Morin, L. Li, A.P. Hitchcock, A. Scholl, A. Doran, J. Electron Spectrosc. Relat. Phenom. **170**, 25 (2009)
34. J.S. Greeneich, J. Electrochem. Soc. **121**, 1669 (1974)
35. R.E. Burge, M.T. Browne, P. Charalambous, Microelectron. Eng. **6**, 227 (1987)
36. R. Klauser, I.-H. Hong, S.-C. Wang, M. Zharnikov, A. Paul, A. Götzhäuser, A. Terfort, T.J. Chuang, J. Phys. Chem. B **107**, 13133 (2003)
37. A.D. Dubner, A. Wagner, J.P. Levin, J. Mauer, J. Vac. Sci. Technol. B **10**, 3212 (1992)
38. G. Compagnini, G.G.N. Angilella, A. Raudino, O. Puglisi, Nucl. Instrum. Methods Phys. Res., Sect. B, Beam Interact. Mater. Atoms **175–177**, 559 (2001)
39. M. Born, E. Wolf, *Principles of Optics*, 7th edn. (Cambridge University Press, Cambridge, 1999)
40. M.D. Galus, E. Moon, H.I. Smith, R. Menon, J. Vac. Sci. Technol. B **24**, 2960 (2006)
41. A.N. Broers, IBM J. Res. Dev. **32**, 502 (1988)
42. A.N. Broers, A.C.F. Hoole, J.M. Ryan, Microelectron. Eng. **32**, 131 (1996)
43. M.P. Seah, W.A. Dench, Surf. Interface Anal. **1**, 2 (1979)
44. S. Yasin, D.G. Hasko, H. Ahmed, Appl. Phys. Lett. **78**, 2760 (2001)
45. W. Hu, K. Sarveswaran, M. Lieberman, G.H. Bernstein, J. Vac. Sci. Technol. B **22**, 1711 (2004)
46. E. Lavallée, J. Beauvais, J. Beerens, J. Vac. Sci. Technol. B **16**, 1255 (1998)
47. N. Arjmandi, L. Lagae, G. Borghs, J. Vac. Sci. Technol. B **27**, 1915 (2009)
48. G. Schmahl, D. Rudolph, D. Neimann, in *Proc. Eight Int. Conf. on X-ray Optics and Microanalysis*, Boston (1977), p. 60A
49. S. Heim Rehbein, P. Guttmann, S. Werner, G. Schneider, Phys. Rev. Lett. **103**, 110801 (2009)
50. H. Mimura, S. Matsuyama, H. Yumoto, Jpn. J. Appl. Phys. **44**, L539 (2005)
51. C.R.K. Marrian, E.A. Dobisz, J.A. Dagata, J. Vac. Sci. Technol. B **10**, 2877 (1992)
52. P.A. Peterson, Z.J. Radzimski, S.A. Schwalm, P.E. Russell, J. Vac. Sci. Technol. B **10**, 3088 (1992)
53. W. Chao, B.D. Harteneck, J.A. Liddle, E.H. Anderson, D.T. Attwood, Nature **435**, 1210 (2005)
54. A.P. Hitchcock, J.J. Dynes, G. Johansson, J. Wang, G. Botton, Micron **39**, 741 (2008)
55. H.I. Smith, J. Vac. Sci. Technol. B **14**, 4318 (1996)
56. A. Pépin, D. Decanini, Y. Chen, J. Vac. Sci. Technol. B **18**, 2981 (2000)

Chapter 5

33 nm feature sizes via direct write x-ray lithography

This chapter presents our best effort to create the smallest feature size possible with focused x-rays. Continuous and reproducible 33 ± 4 nm wide lines were created in a thin layer of PMMA using a STXM equipped with a 15 nm outer most zone width zone plate and a cold development procedure. These are among the smallest feature sizes demonstrated with the direct write method and photons of any wavelength.

5.1 Introduction

Prior to this report, the lowest feature size created with focused x-rays and the direct write method was 40 ± 5 nm in PMMA using a STXM operating at 300 eV [LH11, Ch. 4]. This result was not limited by the properties of the resist (the ability of PMMA to record sub-10 nm features has been demonstrated multiple times [FST&77, YHA01, CLB07]) but rather the x-ray optical system, specifically the zone plate lens used. Assuming that the zone plate is fabricated within certain tolerances and sufficiently coherently illuminated (Ch. 2.3.1.1), the diffraction limited x-ray spot size will be proportional to the outer most zone width of the zone plate, Δr (Eqn. 2.6). The result of [LH11, Ch. 4] was accomplished with a 25 nm Δr zone plate. Incorporating a zone plate with a reduced Δr should lead to smaller spot sizes and correspondingly smaller feature sizes. The fabrication of high resolution x-ray zone plates is technically

demanding and remains a very active area of research. Zone plates with 15 nm Δr have been achieved by novel fabrication schemes such as double patterning [CKR&09] and zone doubling [JVP&07]. Recently these high resolution zone plates have been made available to general users at some STXM beamlines.

Alternative resist development procedures have also been reported to benefit patterned features. Several groups have reported the effects of simply lowering the temperature of the development solution. Benefits include reduced number of defects [PAM98], increased contrast [RKV&02] and most importantly, decreased feature size. Development of PMMA in the pseudo-standard developer of 3:1 v/v IPA:MIBK at 4 – 10 °C has been reported to produce narrower features versus development at room temperature [HSL&04, CLB07]. Cold development decreases the feature sizes in patterned polymeric resists by reducing the molecular weight range between those values which are soluble enough to be removed during development and those which are not. This resolution enhancement has been found to peak at -15 °C for PMMA [CLB07]. Development aided by ultrasonic agitation has also been reported to reduce feature sizes [YHA01]. In a direct comparison, [HSL&04] found cold development produced smaller features than an ultrasonic method at room temperature.

In this chapter we seek to decrease the minimum feature size created with focused x-rays through patterning with higher resolution x-ray optics and implementing a cold development procedure.

5.2 Experimental

A PMMA film on a 75 nm thick Si_3N_4 window was fabricated following the procedures outlined in Ch. 3.1. Minimum feature size has not been found to depend upon the weight average molecular weight (M_w) of PMMA [B88b, KF96], therefore the same batch of PMMA from the same supplier with the same M_w was used as our last attempt [LH11, Ch. 4]. The sample was annealed under vacuum (2×10^{-2} Torr) at 150 °C for 1 h. After annealing the film thickness was found to be 37 ± 2 nm by AFM.

The STXM at beamline X07DA [RTF&08], at the SLS, PSI was used to pattern the sample. The zone plate used for these experiments was made by Dr. Joan Vila-Comamala at the Laboratory for Micro- and Nanotechnology (LMN), PSI. Briefly, an electron beam was used to directly write template zones in an HSQ film on a Si_3N_4 window. The irradiated areas become SiO_2 after development. A 15 nm layer of Ir was conformally deposited on the 120 – 150 nm high SiO_2 template zones by atomic layer deposition, which in effect produces 15 nm wide Ir zones with double the period of the SiO_2 template [JVP&07] (Fig. 5.1). The dimensions of the zone plate were 15 nm Δr , 150 μm D , 60 μm D_s .

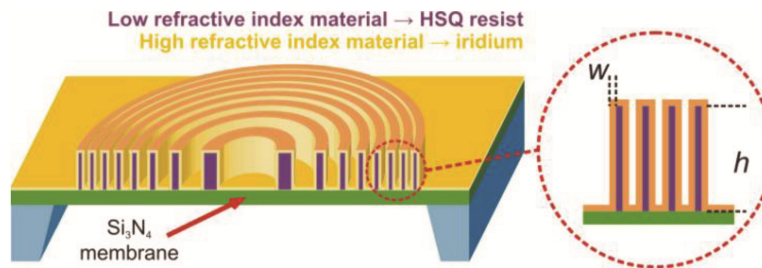


Figure 5.1: Schematic of a zone doubled zone plate made of HSQ resist and Ir (from [VGF&11] Fig. 1, © 2012 Optical Society of America, used with permission).

The 2 μm thick central stop was prepared by a second electron beam lithography exposure. Patterning was carried out at 1 keV, corresponding to the photon energy of maximum diffraction efficiency (first order focused) for this zone plate. The monochromator exit slit widths were set to 10 μm x 10 μm to exceed diffraction limited focusing conditions given the zone plate diameter, photon energy, and the 1.07 m exit slit to zone plate distance at X07DA (Ch. 2.3.1.1). The zone plate was centred on the optical axis by adjusting the position of the entire STXM chamber using a girder mover system [RTF&08]. A 40 μm OSA was used to suppress undiffracted zeroth order and higher order x-rays, in combination with the central stop incorporated in the zone plate. Otherwise, the STXM was set up as described in Ch. 3.2. Details of patterning and dose determination are described in Ch. 7.2.4.2 and 7.2.4.3, respectively. A pattern consisting of several 1 μm long lines with a pitch of 160 nm was created using the program aXis2000. Patterning was executed using the PatternGen routine in the STXM_Control software. Instructions to create and execute patterns can be found in Ch. 7.6.1 and 7.6.2, respectively. The patterned sample was developed for 60 s in a solution of 3:1 v/v IPA:MIBK cooled to -8 °C, mimicking the procedure of [CLB07]. The sample was then allowed to dry in ambient air (20 – 25 °C). The developed patterned areas were imaged by AFM first (Ch. 2.4, Tap 150 Al-G cantilevers), and then by SEM (Ch. 2.5) to avoid artefacts introduced by Pt coating and SEM imaging (Ch. 3.4). Feature widths were measured from the scanning electron micrographs.

5.3 Results

The absorption cross section of PMMA at 1 keV is very low relative to the C 1s edge; the thin PMMA film is practically invisible. However, sub-micrometre bits of mica or dust in or on the film from the sample preparation are conveniently opaque to 1 keV x-rays. These were used to set the final focus of the STXM. A defect-free area of the film was located by cross referencing the acquired STXM images to an optical micrograph of the sample. The pattern of lines was then executed over a range of dwell times corresponding to a range of absorbed doses. After patterning the sample was removed from the chamber, developed, and then imaged using AFM and SEM. Scanning electron micrographs of some of these developed patterns are presented in Fig. 5.2.

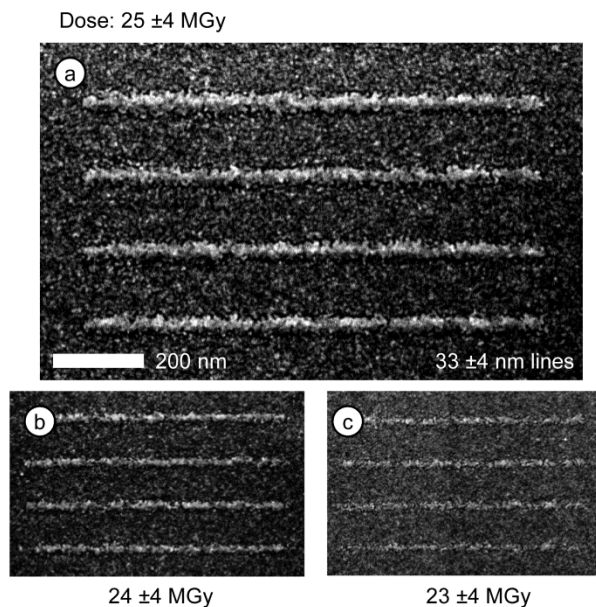


Figure 5.2: Scanning electron micrographs of 1 μm long lines of cross-linked PMMA with a pitch of 160 nm, made with various doses. a) Continuous 33 \pm 4 nm lines, dose: 25 \pm 4 MGy. b) Discontinuous 26 nm lines, dose: 24 \pm 4 MGy. c) At a dose of 23 \pm 4 MGy the cross-linked lines hardly form.

Continuous 33 ± 4 nm (full width) lines of cross-linked PMMA were produced at a dose of 25 ± 4 MGy (Fig. 5.2a). These line width measurements are pessimistic as they include the 5 ± 1 nm Pt coating. The average height of these lines was 17 ± 1 nm measured using AFM before Pt coating and SEM imaging (Fig. 5.3).

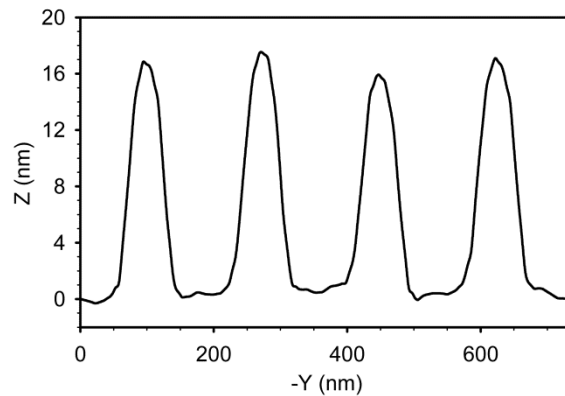


Figure 5.3: Averaged AFM line trace of lines presented in Fig. 5.2a, recorded before Pt coating and SEM imaging.

Doses greater than 25 MGy resulted in line widths >33 nm. This increase in feature size with dose, which is in many ways similar to the proximity effect known in electron beam lithography [C75], is in fact due to the point spread function (PSF) of the optical system [LTH11, LH11]. Lines made at a dose of 24 ± 4 MGy had an average width of 26 nm, and some were continuous over their 1 μm length (Fig. 5.2b). However, lines made with doses of ≤ 24 MGy were not reproducibly continuous. Lines just begin to form (i.e. onset of negative mode) at a dose of 23 ± 4 MGy (Fig. 5.2c). This is significantly lower than the 90 ± 5 MGy onset of negative mode for PMMA developed using the same developer but at 20 °C [LH11]. However, this reduction is consistent with the observations of others [CLB07].

5.4 Discussion

The lines demonstrated here are the smallest continuous features produced with focused x-rays and the direct write method, and the smallest produced involving a zone plate lens at any wavelength in any orientation. Furthermore, these may be the smallest *totally arbitrary, continuous, and reproducible* lines produced with the direct write method and photons. The minimum feature size attainable when patterning (and also imaging) in the far field with visible photons is usually limited to >100 nm due to diffraction [KPG09]. However, sub-100 nm direct write lithography with visible photons has been achieved through several innovative approaches [F10]. Advancements in the far-field technique of multi-photon absorption polymerization have led to examples of 80 nm lines with 800 nm laser light [LGG&09], and 65 ± 5 nm lines with 520 nm light [HCH&07]. Near-field patterning schemes have demonstrated 80 nm line width capability using wavelengths of 325 nm and 633 nm [ATM09]. Sub-100 nm features have also been directly written with scanning near-field optical microscopes (NSOM) [SCL02, TDH&02, SL04, MWK&08]. The smallest continuous line widths achieved appear to be between 20 nm and 40 nm [SL04, MWK&08].

There are still avenues available to improve minimum feature size and feature quality produced using STXM. -8 °C is a convenient temperature for development as it can be reached in any refrigerator-freezer, but [CLB07] found the greatest benefit from cold development occurred at -15 °C. The roughness

of the Si_3N_4 window, resolved in the scanning electron micrographs (Fig 5.2), is presumed to significantly contribute to the line width roughness. STXM patterning is currently limited to thin x-ray transmissive substrates such as Si_3N_4 as they enable accurate focusing. Patterning on atomically flat Si wafers as well as other opaque substrates will soon be possible with the incorporation of an auto-focusing system in STXM (Ch. 12.3.4.1). Finally, high resolution x-ray optics fabrication is a very active field of research, and sub-5 nm focusing is a goal of several current synchrotron beamlines. The goal is in fact 1 nm focusing at the National Synchrotron Light Source II (NSLS-II) which is under construction at the time of submission. It seems probable that this will be achieved by the end of the decade using multilayer Laue lenses [KMS&06].

5.5 Conclusion

A scanning transmission x-ray microscope equipped with a 15 nm outermost zone width zone plate was used to create totally arbitrary, continuous, and reproducible 33 ± 4 nm lines in a thin PMMA film with 1 keV x-rays. This represents the smallest feature size involving focused x-rays and the direct write method, and the smallest feature size created involving a zone plate at any wavelength in any orientation. Furthermore, this is among the smallest feature size created using the direct write method and photons of any wavelength.

Chapter 6

Zone plate focused soft x-ray lithography for fabrication of nanofluidic devices

This chapter reports the development of a method to fabricate sealed nanofluidic channels in polymer bilayers with tunable x-rays. The design rules for nanochannel formation are investigated and discussed.

*Reprinted with permission from the Proceedings of the SPIE **2012**, 8323, 83231D, A.F.G. Leontowich, A.P. Hitchcock. DOI: 10.1117/12.915803, © 2012 SPIE.*

The author of this thesis conceived the experiments, prepared all samples and developed them, performed all the experiments, analyzed the data and wrote the manuscript which was edited by A.P. Hitchcock.

Zone plate focused soft X-ray lithography for fabrication of nanofluidic devices

Adam F. G. Leontowich and Adam P. Hitchcock*

Brockhouse Institute for Materials Research,
McMaster University, Hamilton, ON, Canada L8S 4M1

ABSTRACT

Sealed nanofluidic channels with cross sections of sub-100 nm * 100 nm were created in a polymer bilayer using the focused soft X-rays of a scanning transmission X-ray microscope and the direct write method. The width of the nanochannels can be controlled by the area patterned in X and Y, while the height can be controlled by tuning the layer thicknesses. Formation of the desired structures has been confirmed by near edge X-ray absorption fine structure spectromicroscopy and scanning electron microscopy. The maximum length of the nanochannels fabricated by this method was found to be limited by the efficiency of excavation of patterned material out of the channel, as well as the stability of the polymer over-layer which seals it. Schemes toward interfacing these nanochannels with conventional microfluidics are discussed.

Keywords: nanofluidics, X-ray lithography, advanced lithography, zone plates, NEXAFS spectromicroscopy

*aph@mcmaster.ca; phone 1 905 525-9140 x24749; fax 1 905 521-2773

1. INTRODUCTION

Monochromatic zone plate focused X-rays offer the possibility of direct write lithography, analogous to lithography with a focused electron beam, using established electron beam resists and development procedures. Historically, the majority of this work has been performed using scanning transmission X-ray microscopes (STXM) operating at soft X-ray photon energies (100 – 2500 eV, 12 – 0.5 nm). The minimum feature size obtainable is steadily approaching that of focused ion or electron beams. Initial work by Zhang et al. (1995)¹ with the Stony Brook scanning transmission X-ray microscope at National Synchrotron Light Source (NSLS) reported feature sizes of 300 ± 20 nm in poly(methyl methacrylate) (PMMA), significantly worse than the quoted spot size of the instrument. Caster et al.² using hydrogen silsesquioxane (HSQ) as the resist, were able to achieve 90 ± 14 nm lines. Recently Leontowich et al.,³ working at 300 eV and much lower X-ray exposures, were able to achieve 40 ± 5 nm lines in PMMA. The demonstrated feature size here was quite close to the Rayleigh resolution limit dictated by the properties of the zone plate lens used.

Patterning with monochromatic soft X-rays with full control over the photon energy, and a band width better than 0.2 eV, has opened up a unique patterning technique for multilayer resists that we have termed “chemically selective patterning”. The concept is as follows: Different molecules containing different elements or chemical functional groups often display different X-ray absorption spectra. Most resist-type molecules (polymers) experience chemical changes when irradiated with X-rays which can then be probed by X-ray absorption spectroscopy.⁴⁻⁶ If the sufficiently monochromatic X-ray beam is tuned to a photon energy corresponding to an absorption resonance exclusive to one component, then one can induce a chemical change to that component nearly independently of the others at the same point on the sample by patterning at that energy. Modern STXMs on synchrotron beamlines exceed the system requirements necessary to realize this concept. Using the Advanced Light Source (ALS) STXM 5.3.2.2, Wang et al. demonstrated chemically selective patterning of bilayer⁷ and later trilayer⁸ samples.

In this report we have combined chemically selective patterning of polymer multilayer samples with a suitable development procedure in order to demonstrate in a proof of concept experiment fabrication of nanofluidic (sub-100 nm) channels with the tunable, focused soft X-rays of a STXM. The restrictions on materials, patterning, developers, etc. for

this technique, and the underlying mechanisms of nanochannel formation are discussed. A potentially functional nanofluidic device is presented, and schemes to interface such devices with conventional microfluidics to realize fully functional fluidic devices are described.

2. METHODOLOGY

2.1 Appropriate resists for chemically selective lithography

2.1.1 Controlling the location of energy absorption by chemically selective patterning

Only those samples which fit the criteria outlined in this report may be suitable for chemically selective patterning with a STXM. The foremost sample requirement is that it must contain at least two chemically different components, and each component must display a significantly different X-ray absorption spectrum over a chosen photon energy region. Ideally, the spectrum of each component molecule should have a large inner shell resonance at a chosen absorption edge, and these resonances should be separated in energy by more than their feature width, i.e. by 1 eV or more. The absorption edge must also be within the energy range achievable by the beamline (100 – 2500 eV for existing soft X-ray STXM beamlines; 270 – 580 eV for ALS STXM 5.3.2.2 where this work was performed). The photon energy is then tuned to those specific resonance energies of the sample when patterning, so that the rate of energy absorption by one component is significantly greater than the other and vice versa. In principle the components could be selected based on different elemental composition (i.e. one component could contain F but not N, while the other contains N but not F) but in practice patterning at one absorption edge is preferred as moving between absorption edges often requires re-optimization of the STXM and beamline which may compromise the spatial alignment of multiple patterns. In addition, higher energy edges such as the N 1s edge, have a significant underlying absorption from the C 1s ionization continuum which is common to all molecules containing C.

Wang et al.^{7,8} showed experimentally that differing X-ray absorption cross sections and a monochromatic beam are not sufficient to realize chemically selective patterning. The concept only succeeded when applied to vertically-segregated multilayer structures, rather than phase separated blends or homogeneous material with multiple chemical functional groups sharing the same polymer backbone, or within the monomeric repeat unit. The mechanism put forth by Wang to explain the success of the layered structure has since been proven incorrect by Leontowich,³ and a new mechanism to explain the successful patterning of only layered samples is proposed here: When one component is selectively irradiated with soft X-rays, it initiates a cascade of damaging secondary processes, the dominant process being generation of secondary electrons (photoelectrons, Auger, shake-off, shake-up, etc.). The initial photoabsorption of energy can be made specific by tuning the patterning photon energy to an absorption resonance exclusive to one component, however, the damaging secondary processes are not specific. The specificity is lost if both components are within the damaging radius of the secondary processes. In a layered sample, there can be sufficient spatial separation of the absorbing and non absorbing components of the sample if enough of the non-resonant layer lies outside the damaging radius of the secondary processes emitted by the resonant layer, which typically have a range of a few nm at soft X-ray photon energies.⁹ This distance sets a minimum layer thickness for which chemically selective patterning will succeed, which we estimate to be 20 nm. The maximum total thickness of all layered components can only be about 300 nm to avoid absorption saturation.

2.1.2 Added requirements for chemically selective lithography

A development step which often consists of dipping the sample in a suitable solvent to reveal the patterned areas is necessary to realize nanofluidic channels or other unique structures, and differentiates chemically selective patterning^{7,8} from the present approach of chemically selective lithography. The solubility of the components of the multilayer sample in the developer must be taken into consideration. If for example, a bilayer is made of two components which both act as positive resists (irradiated material is removed by developer, non-irradiated material is unaffected), then the developer for the top layer can not significantly attack/dissolve the non-irradiated portions of the bottom layer and vice versa, or the structure would be ruined. This is perhaps the most inflexible requirement of chemically selective lithography. As one uses more layers of different components (beyond two) it becomes increasingly difficult to find polymeric components with both the appropriate X-ray absorption properties and suitable orthogonal developers.

2.2 Sample preparation

The samples in this report consist of a 30 – 100 nm layer of poly(dimethylglutarimide) (PMGI, a gift from Prof. Ash Parameswaran, Simon Fraser University, British Columbia, Canada), on a 30 – 100 nm layer of poly(methyl methacrylate) (PMMA, electronics grade, 315,000 M_w , 1.05 M_w/M_n , Polymer Source Inc.), on a Si_3N_4 window (75 nm * 1 mm * 1 mm window area in a 200 μm * 5 mm * 5 mm Si frame, Norcada Inc.). PMMA layers were fabricated by spin casting 1.0 – 2.0% w/w solutions of PMMA in toluene (99.9% Chromasolv®, Sigma-Aldrich) onto freshly cleaved mica (Ted Pella Inc.). The layer on mica was scribed into 3 * 3 mm pieces with scalpel, and slowly dipped into a Petri dish of distilled water. Pieces of the film detach from the mica and float upon the water's surface, and one piece was then caught on a Si_3N_4 window in an orientation which partially covered the window to allow for measurements of the spectrum of incident radiation (I_0) later on. The sample was then annealed for 1 hour at 150 °C at reduced pressure ($\sim 2 * 10^{-2}$ Torr). Next, layers of PMGI were fabricated by spin casting 1.0 – 2.0% w/w solutions of PMGI in *N, N*-dimethylformamide (99.9% Chromasolv®, Sigma-Aldrich) onto freshly cleaved mica. The PMGI layer on mica was then annealed for 5 minutes at 230 °C. One 3 * 3 mm piece of PMGI was transferred onto the sample by the float method above in an orientation that partially covered the PMMA layer yet only partially covered the window. This multiple float procedure has opened up greater possibilities for samples than our previous multiple spin casting procedure.^{7,8} Finally, the sample was annealed for 15 minutes at 150 °C at reduced pressure ($\sim 2 * 10^{-2}$ Torr).

2.3 Scanning transmission X-ray microscope (STXM)

Patterning of samples, collection of near edge X-ray absorption fine structure (NEXAFS) spectra, and imaging was performed with the STXM¹⁰ at beamline 5.3.2.2¹¹ at the Advanced Light Source (ALS), Lawrence Berkeley National Laboratories (LBNL). Zone plate lenses were supplied by the Center for X-ray Optics (CXRO) with the following parameters: 25 nm outer most zone width, 240 μm diameter, 90 μm central stop. A 50 μm order sorting aperture was used to suppress higher order light, as well as a 1 m long section of beamline differentially pumped with 0.6 Torr of N_2 . Experiments were performed with the STXM chamber backfilled with 250 Torr He, after the evacuation of air. Entrance (50 μm) and exit (25 * 25 μm) slit settings were chosen so that focusing performance would be diffraction-limited, offering the smallest possible spot size.¹²⁻¹⁴ Details of the pattern generation program and the calculation of doses, which are believed to be precise within 10%, have been reported previously.^{3,7,8}

2.4 Development

A 7:3 2-propanol (IPA, 99.5%, Caledon) : H_2O solution was used as the developer for PMGI,¹⁵ while a 3:1 IPA : 4-methyl-2-pentanone (MIBK, >98.5% ACS reagent grade, Sigma-Aldrich) solution was used to develop the PMMA layer.¹⁶ The performance of both developer/resist systems for this application has been explored previously.³ To develop, a sample was held with locking tweezers, then fully immersed in a vial containing the PMGI developer solution and gently stirred for 10 s. The sample was then immediately immersed into a waiting vial containing the PMMA developer solution and stirred for 30 s. Afterward, the sample was allowed to dry in ambient air. All development occurred at ambient temperature (~ 20 °C). These specific development times and conditions were applied for all results presented in this report.

2.5 Imaging

Optical micrographs of samples were collected using an Olympus BX51 optical microscope equipped with a CCD camera. The nanofluidic structures were imaged by three techniques, atomic force microscopy (AFM, Quesant 350 microscope, Budget Sensors Tap150Al-G probes, tapping mode), NEXAFS spectromicroscopy (section 2.3), and scanning electron microscopy (SEM, JEOL JSM-7000F microscope, 10 keV, 60 μA beam current, working distance: 5 mm). A 5 ± 1 nm Pt layer was applied (682 Precision Etching Coating System, Gatan) prior to SEM imaging to reduce charging and improve contrast. It is imperative to image the structures in the proper order to avoid introducing artefacts. Both SEM and STXM involve ionizing radiation which can induce mass loss, chemical changes, and deposit carbon,¹⁷ permanently altering the sample.⁴⁻⁶ Tapping mode AFM imaging did not noticeably alter the sample and therefore was always performed before SEM or STXM imaging. Identical duplicate structures were made on separate samples to obtain artefact free SEM and STXM images of the same structure.

3. RESULTS

3.1 Layered structure and NEXAFS spectra

An optical micrograph of a PMGI/PMMA/Si₃N₄ sample is presented in Figure 1a. C 1s (K) NEXAFS spectra were collected from areas of this sample composed only of one of the layers. These spectra were normalized to 1 nm thickness of material using the elemental response for the formula repeat unit,¹⁸ and the known bulk densities. The normalized spectra are presented in Figure 1b. The spectrum of PMGI is dominated by the large C 1s(C=O) → π*_{C=O} absorption feature at 287.7 eV, while the spectrum of PMMA is dominated by a slightly larger C 1s(C=O) → π*_{C=O} absorption feature at 288.5 eV. The π*_{C=O} resonance of PMGI is red shifted by 0.7 eV relative to PMMA due to differences in the electronic environment surrounding the carbonyl bond.¹⁹

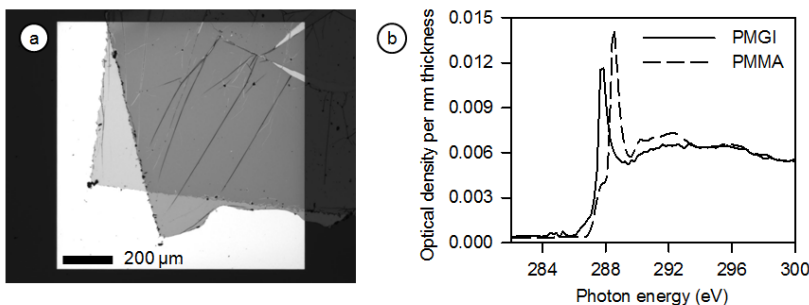


Figure 1: a) Optical micrograph of a PMGI/PMMA/Si₃N₄ sample. b) X-ray absorption (NEXAFS) spectra of PMGI and PMMA, normalized to 1 nm thickness.

3.2 Fabricating nanochannels

Two pattern generation files, each consisting of sets of discrete points on a 30 nm rectilinear grid, were created to fabricate nanochannels. Pattern A (Figure 2a) consisted of two parallel 570 * 570 nm square areas (i.e. 19 x 19 point exposures) separated by 4000 nm, while pattern B (Figure 2b) consisted of a 4680 nm long, 90 nm wide area. A graphical representation of the final desired structure and its orientation relative to the incident X-ray beam is presented in Figure 2c.

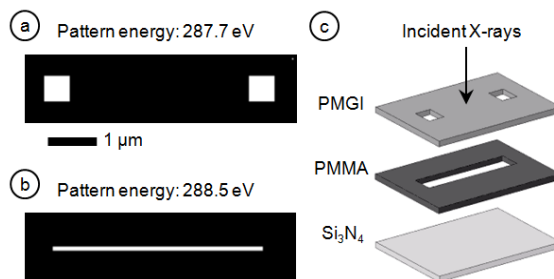


Figure 2: a) Pattern A; access hole pattern for the top PMGI layer. b) Pattern B; channel pattern for the bottom PMMA layer. c) Exploded view drawing of the desired nanofluidic structure. a) and b) are on the same positional scale.

A region of the PMGI/PMMA bilayer was then brought into sharp focus in the STXM, and was subsequently chemically selectively patterned in the following manner: The photon energy was tuned to 287.7 eV and pattern A was executed using the PatternGen routine³ in the STXM_control program with precise dwell time and sample position control (better than 10 nm by laser interferometry¹⁰). After completion, the photon energy was tuned to 288.5 eV and pattern B was executed over the exact same area as pattern A. Several combined A B patterns were made on the same sample covering

a range of dwell times. The sample was then removed from the STXM chamber and developed (section 2.4). The developed samples were loaded into the STXM chamber, and imaged at 288.5 eV (Figure 3). Figures 3a – e are STXM optical density (OD) images of developed patterns generated with successively increasing exposure times (2 – 5 ms) corresponding to increasing doses (1 – 3 MGy) for pattern B, while the exposure times for pattern A were held constant (14 ms, 10 MGy).

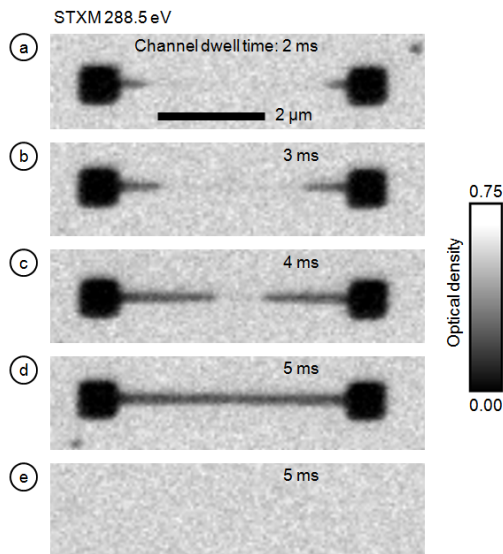


Figure 3: STXM OD images at 288.5 eV of developed PMGI/PMMA/Si₃N₄ samples patterned with different exposure times for the channel (a = 2 ms, b = 3 ms, c = 4 ms, d = 5 ms, e = 5 ms). Exposure time for the access holes for a – d was 14 ms. Access holes were not patterned for e). With a sufficient dose (3 MGy), the channel is fully cleared by the developer, if access holes are present. All images are on the same positional and OD scale.

The patterned PMMA material in the nanochannel is removed beginning from the square areas of pattern A (i.e. access holes) inward. As the dose received by the PMMA in the nanochannel area increases the nanochannel is developed further underneath the PMGI layer. The dose received by the patterned PMMA material in the nanochannel in Figure 3d was enough that it could be fully cleared during development. In Figure 3e, pattern B was executed with the same dwell time/dose as Figure 3d, but here pattern A was not executed; enough dose was given to clear the nanochannel, yet in this case the patterned material in the nanochannel was not removed during development.

3.3 Characterization of the nanochannel

A C 1s image sequence (or stack²⁰) of the nanochannel structure of Figure 3d was collected with the STXM. The stack, which consists of a C 1s NEXAFS spectrum for every pixel in an imaged area, was fit to the normalized PMGI and PMMA reference spectra (Figure 1b) using singular value decomposition (SVD) routines²¹ implemented in aXis2000.²² Figure 4 displays the resulting *quantitative* PMGI (Figure 4a) and PMMA (Figure 4b) component maps along with a color coded composite (Figure 4c). Since the NEXAFS spectra used for the fit procedure are normalized to 1 nm material, the component maps are literally thickness maps of each component in the system. As there are only two components here (PMGI and PMMA) the fit is very good and allows an accurate ($\pm 5\%$) determination of the thickness of each layer at every pixel. The total thickness of the bilayer derived from the individual component maps is consistent with data from an AFM image of the structure (not shown), within measurement uncertainties. The thickness of the PMMA layer within the nanochannel area is equal to that of the developed access hole areas, based on SVD analysis of the C 1s NEXAFS spectrum of the nanochannel. This indicates that the patterned PMMA in the nanochannel area has been practically fully removed by the developer. The thickness of the PMGI layer in the area of the nanochannel, which serves to seal it, is slightly different from elsewhere on the film; there was loss of $20 \pm 5\%$ of the PMGI top layer in the patterned nanochannel area. An SEM image was also taken of the nanochannel structure of Figure 3d and is presented in

Figure 4d. The morphology of the square areas is consistent with that of bare Si_3N_4 , and despite some loss of PMGI material the layer sealing the nanochannel appears intact and free of pinholes.

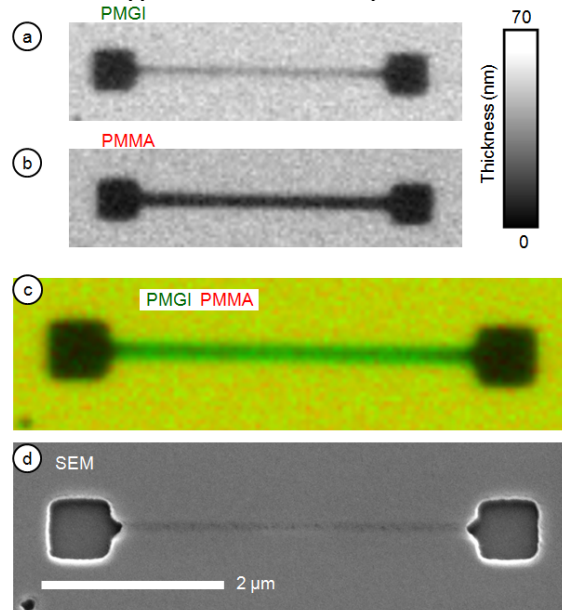


Figure 4: Quantitative component maps of a) PMGI and b) PMMA derived from SVD analysis of NEXAFS spectromicroscopy data, on the same positional and thickness scales. c) Non rescaled two color composite map of a) in green, and b) in red. Yellow corresponds to the presence of both polymer layers. d) Scanning electron micrograph of the nanochannel structure. c) and d) are on the same positional scale.

3.4 Optimizing doses and development times

SEM images collected at a 45° tilt of developed nanochannel structures are presented in Figure 5. The dwell time/dose to the channel in Figure 5a is the same as Figures 3d and 4. The entrance to the nanochannel is clearly observed, as well as the defect free PMGI top layer. SEM images of nanochannel structures fabricated with increased doses are presented in Figures 5b and 5c. As the dose is increased, pinhole defects in the PMGI top layer are observed, and eventually this covering layer is fully removed. Thus under the conditions presented, a “dose window” between 2.5 – 3.5 MGy exists in which the patterned PMMA in the nanochannel can be fully cleared while the top PMGI remains free of pinhole defects, sealing the channel.

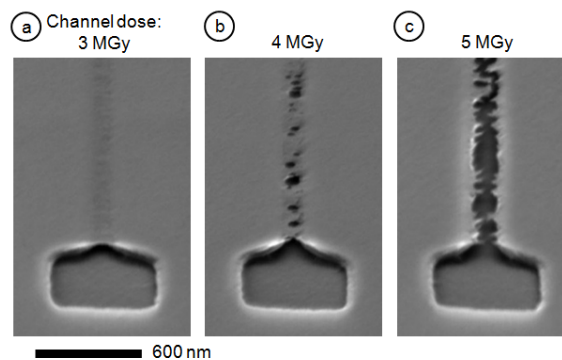


Figure 5: Scanning electron micrographs of nanochannels tilted at 45° fabricated by chemically selective lithography. a) Under optimal dose conditions (3 MGy), the channel is cleared yet the PMGI overlayer remains intact. b) Pinholes appear at channel doses >3.5 MGy, or c) the PMGI overlayer is fully removed. All images are on the same positional scale.

The development time for both PMGI and PMMA developers was also optimized. To reduce the removal of the PMGI layer sealing the nanochannel the amount of time the sample spends in PMGI developer should be as short as possible. It was found that the development time could be reduced to 10 s from the recommended time of 60 s¹⁵ if the dwell time for pattern A was increased. Here the increased dwell time was acceptable as both layers in the patterned area need to be fully removed to the substrate, although a larger increase in dwell time will result in rounded edges and expanded access holes (section 4.3). It is also conceivable that the amount of time the sample spends in PMMA developer should be as long as possible to increase the maximum nanochannel length. PMMA development times of 30 s, 60 s and 120 s were tested, but it was found that the 60 s and 120 s only increased the number and size of pinholes in the PMGI layer covering the nanochannel, therefore 30 s was optimal.

3.5 Cross sectional area of the nanochannel in relation to its maximum length

The pattern generation files were modified to explore the effect of a wider patterned channel area on its developed length. One 570 * 570 nm square was deleted from pattern A, and the length of pattern B was increased to 30 μm , while the width was varied (60, 90, 150, and 210 nm). Patterning of the sample was carried out as previously described. The dwell time/pixel (5 ms) was constant for all modified pattern B channel patterns, as well as the modified pattern A (14 ms), respectively. The patterned samples were then developed and imaged by STXM and AFM (Figure 6).

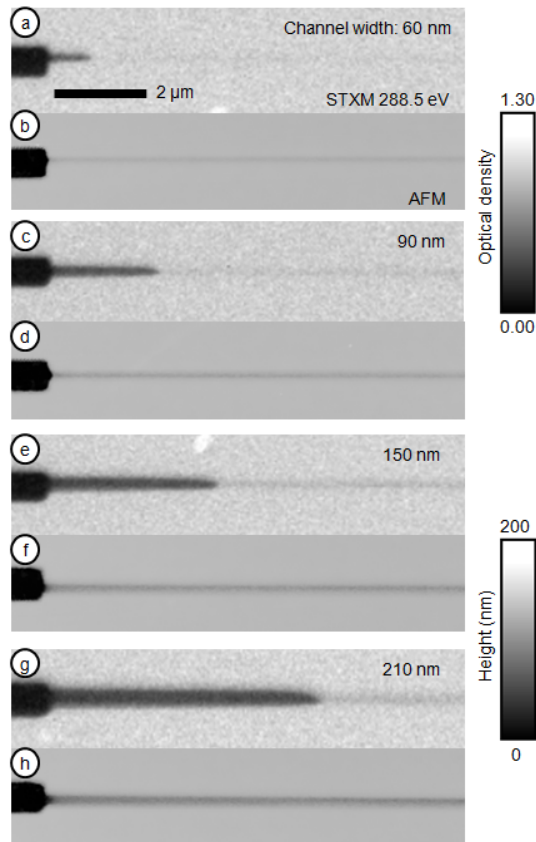


Figure 6: STXM OD and AFM images of nanochannels created with the same dwell time (5 ms) but different width. STXM and AFM images are on the same OD and Z scale, respectively, and all are on the same positional scale.

The STXM OD images show that as the width of the patterned nanochannel is increased, its developed length increases. AFM images reveal the entire nanochannel area patterned undergoes a decrease in height. A cross comparison with the STXM OD images reveals that the height reduction is the same whether the patterned PMMA material underneath is

removed or not. This result suggests that the thickness reduction is due to removal of PMGI during development, rather than the sagging of the PMGI top layer over the nanochannel, which is in agreement with the NEXAFS spectromicroscopy PMGI component map.

Although the same dwell times were used for all nanochannel patterns (pattern B) in Figure 6, the dose for the wider channels is not precisely the same as that of the narrower channels. The intense spot of focused X-rays at the focal plane is a distribution (often showing side lobes¹⁴, characteristics of being diffraction limited^{12,13}) rather than a finite circle, thus there is a cumulative dose overlap from adjacent exposures and as a result the material at the center of the channel receives a higher dose than that at the edges. However, a conceptually analogous experiment yielded an identical result. The height of the nanochannel is dependent upon the thickness of the bottom layer, which can be fine-tuned by adjusting the concentration of polymer solution before spin casting; increasing the thickness of the bottom PMMA layer increases the cross sectional area of the nanochannel. With a thin layer of PMMA (40 nm), the maximum length that a 90 nm wide nanochannel could be fully cleared yet free of pinholes is $5 \pm 1 \mu\text{m}$. With a thicker layer of PMMA (90 nm), this distance increased to $8 \pm 1 \mu\text{m}$.

4. DISCUSSION

4.1 Maximum nanochannel length

Patterning of the nanochannel was performed at 288.5 eV, corresponding to the maximum absorption cross section of PMMA at the C 1s edge. The energy absorption rate of PMMA at this photon energy is significantly greater than that of PMGI allowing its selective patterning. However, PMGI also absorbs energy, albeit at a lower rate, because the absorption cross section of PMGI at 288.5 eV is not zero (Figure 1b). This residual dose into the PMGI top layer during patterning of the nanochannel is enough to cause partial removal of the PMGI top layer, as observed by NEXAFS spectromicroscopy (Figure 4) and AFM (Figure 6). Within an experimentally determined dose window, this process is insignificant overall as PMGI remains continuous and seals the nanochannel. But at higher dwell times the residual dose induces significant pinhole formation, and eventually results in the full removal of the PMGI layer as well. This imposes an upper limit on the dwell time for patterning the nanochannel, even when done chemically selectively.

To realize the nanochannel, the PMMA developer solution must diffuse under the PMGI layer, into the nanochannel, dissolve the patterned PMMA material, and then diffuse out. When PMMA is exposed to ionizing radiation at low dose it primarily undergoes main chain scission which decreases the molecular weight and dramatically increases solubility in the PMMA developer solution.¹⁶ The development/excavation process of the patterned PMMA material in the nanochannel can therefore be facilitated by increasing the dose to the nanochannel, but only up to the limit imposed by the pinhole formation in the PMGI layer. The maximum length of the channel then becomes dependent upon the diffusion of developer into and out of the nanochannel. The longer the channel is, the more difficult excavating the patterned material inside the channel becomes. The diffusion limited excavation can be aided by increasing the cross sectional area of the nanochannel. When the cross sectional area is increased, conceivably better flow occurs, and longer nanochannels were realized. Consequently, this gets away from the uniqueness of our approach as the nanochannels take on larger dimensions. The maximum length that a $100 * 100 \text{ nm}$ nanochannel could be fabricated without pinholes was $10 \pm 1 \mu\text{m}$.

4.2 Interfacing with conventional microfluidics

The nanochannels fabricated here should be viable for working fluidic devices. The impermeability of the PMGI overlayer sealing the nanochannel is demonstrated in Figure 3e. Here only pattern B was carried out at the dose required to clear the nanochannel. Without defined “access holes”, either the developer could not reach the patterned PMMA or the solvated material could not escape (or a combination of these two effects) and the nanochannel was not realized. Work on functioning fluidic devices has begun. Images of a double T injector test structure fabricated with STXM 5.3.2.2 are presented in Figure 7. A major challenge now is plumbing this device so that the flow of liquid in and out can be controlled, and the velocity and flow rate measured, etc. We are attempting to interface this structure with more conventional microchannels by ‘bonding’ a poly(dimethylsiloxane) (PDMS) chip on top of the structure.²³ To that end, the access holes have been extended to a length of $50 \mu\text{m}$ to ease the alignment when mating the two structures.

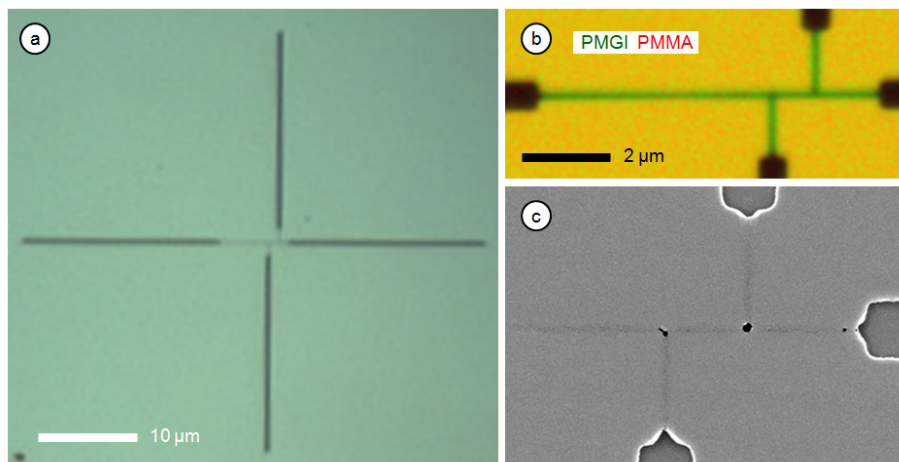


Figure 7: A double T injector device fabricated by chemically selective lithography. a) Optical micrograph (100x, reflection) of the entire device. b) Non rescaled two color composite map (PMGI in green, PMMA in red) derived from SVD analysis of NEXAFS spectromicroscopy data. c) Scanning electron micrograph of the device. Pinholes occurred at the intersections of channels.

4.3 Outlook

The survival of the top PMGI layer was a major challenge in this project. Here the absorption cross sections of the two components were just different enough to be viable but it would be beneficial if the difference in X-ray absorption was much larger. Furthermore the orthogonal developer requirement imposes limits which will probably make it difficult to evolve to completely three dimensional fluidic structures. Perhaps a better approach would be to use one resist with different initiator molecules such as photoacid generators²⁴ in layers which would bypass the need for orthogonal developers for each layer. Use of a self developing resist²⁵ would alleviate both the orthogonal developer and diffusion issues. Moving to higher X-ray photon energies may allow patterning and fabrication of thicker, more complex structures as photoabsorption cross sections decrease with increasing photon energy, reducing absorption saturation. However, the damaging radii of secondary processes increases; the inelastic mean free path, and the significance of fluorescence increase with higher photon energy. The soft X-ray region appears best suited to this type of approach.

This is a proof of concept demonstration for the formation of nanochannels by chemically selective lithography. For a functional nanofluidic device, the materials of the structure must ultimately be compatible with the solvent and analyte molecules. Although not yet tested, these PMGI/PMMA/Si₃N₄ nanochannels should be compatible with water and mild buffer solutions with a pH near 7.

Direct write patterning in STXM would benefit from a point spread function¹⁴ correction program, which would calculate the cumulative dose overlap from adjacent exposures and adjust the dwell time for each pixel to correct for it. For example, the holes seen only at the nexus of the nanochannels (Figure 7c) are likely due to overlap of point spread functions. Solutions to this problem exist for electron beam lithography²⁶ but have yet to be applied to patterning in STXM. Integrating a point spread function correction into the pattern generation program should increase the homogeneity of dose providing uniform exposure for complex patterns.

Finally, the concept of chemically selective lithography (section 2.1) is not exclusive to the direct write method, which is not well suited to the photolithographic mass production of devices. Multiple patterned masks, one for each layer/photon energy, could be fabricated and exposed with a suitable monochromatic beam for full wafer production. The exposures would need to be precisely aligned, but development of this technology is well underway within the deep X-ray lithography community.²⁷ The necessity of bright, tunable soft X-rays precludes a synchrotron source, therefore the experiment would essentially require mating an X-ray lithography scanner endstation with multiple patterning ability with a soft X-ray beamline at a synchrotron facility.

5. CONCLUSION

Sealed nanochannels with dimensions on the order of sub-100 nm were created in polymer bilayers with tunable focused soft X-rays and the direct write method. For a 100 x 100 nm channel, the maximum nanochannel length realized was $10 \pm 1 \mu\text{m}$. Excavation of the patterned channel material was found to be the largest impediment to the realization of even longer channels. If the cross sectional area is increased, a longer channel can be realised.

ACKNOWLEDGEMENTS

This research was supported by NSERC (Canada), the Canada Foundation for Innovation and the Canada Research Chair program. Adam Leontowich acknowledges receipt of an ALS Doctoral Fellowship in Residence. We thank Prof. Ash Parameswaran for the poly(dimethylglutarimide) and Prof. Dongqing Li for useful discussion of interfacing nanofluidics. We also thank Dr. David Kilcoyne and Dr. Tolek Tyliczszak for their support of the STXM facilities. The experiments were performed at the Advanced Light Source, beamline 5.3.2.2 (ALS, Berkeley, CA, USA). The Advanced Light Source is supported by the Director, Office of Energy Research, Office of Basic Energy Sciences, Materials Sciences Division of the U.S. Department of Energy, under Contract No. DE-AC03-76SF00098.

REFERENCES

- [1] Zhang, X., Jacobsen, C., Lindaas, S., and Williams, S., "Exposure strategies for polymethyl methacrylate from in situ x-ray absorption near edge structure spectroscopy," *J. Vac. Sci. Technol. B* 13, 1477-1483 (1995).
- [2] Caster, A. G., Kowarik, S., Schwartzberg, A. M., Leone, S. R., Tivanski, A., and Gilles, M. K. "Quantifying reaction spread and x-ray exposure sensitivity in hydrogen silsesquioxane latent resist patterns with x-ray spectromicroscopy," *J. Vac. Sci. Technol. B* 28, 1304-1313 (2010).
- [3] Leontowich, A. F. G., and Hitchcock, A. P., "Zone plate focused soft X-ray lithography," *Appl. Phys. A* 103, 1-11 (2011).
- [4] Coffey, T., Urquhart, S. G., and Ade, H., "Characterization of the effects of soft x-ray irradiation on polymers," *J. Elec. Spec. Relat. Phenom.* 122, 65-78 (2002).
- [5] Wang, J., Morin, C., Li, L., Hitchcock, A. P., Scholl, A., and Doran, A., "Radiation damage in soft x-ray microscopy," *J. Elec. Spec. Relat. Phenom.* 170, 25-36 (2009).
- [6] Wang, J., Botton, G. A., West, M. M., and Hitchcock, A. P., "Quantitative evaluation of radiation damage to polyethylene terephthalate by soft X-rays and high-energy electrons," *J. Phys. Chem. B* 113, 1869-1876 (2009).
- [7] Wang, J., Stöver, H. D. H., Hitchcock, A. P., and Tyliczszak, T., "Chemically selective soft X-ray patterning of polymers," *J. Synchrotron Rad.* 14, 181-190 (2007).
- [8] Wang, J., Stöver, H. D. H., and Hitchcock, A. P., "Chemically selective soft X-ray direct-write patterning of multilayer polymer films," *J. Phys. Chem. C* 111, 16330-16338 (2007).
- [9] Seah, M. P., and Dench, W. A., "Quantitative electron spectroscopy of surfaces: A standard data base for electron inelastic mean free paths in solids," *Surf. Interface Anal.* 1, 2-11 (1979).
- [10] Kilcoyne, A. L. D., Tyliczszak, T., Steele, W. F., Fakra, S., Hitchcock, P., Franck, K., Anderson, E., Harteneck, B., Rightor, E. G., Mitchell, G. E., Hitchcock, A. P., Yang, L., Warwick, T., and Ade, H., "Interferometer-controlled scanning transmission microscopes at the advanced light source," *J. Synchrotron Rad.* 10, 125-136 (2003).
- [11] Warwick, T., Ade, H., Kilcoyne, D., Kritscher, M., Tyliczszak, T., Fakra, S., Hitchcock, A., Hitchcock, P., and Padmore, H., "A new bend-magnet beamline for scanning transmission x-ray microscopy at the advanced light source," *J. Synchrotron Rad.* 9, 254-257 (2002).
- [12] Attwood, D., [Soft X-rays and Extreme Ultraviolet Radiation: Principles and Applications], Cambridge University Press, Cambridge (1999).
- [13] Hawkes, P. W., and Spence, J. C. H., [Science of Microscopy], Springer, New York, ch. 13 (2007).
- [14] Leontowich, A. F. G., Tyliczszak, T., and Hitchcock, A. P., "Measurement of the point spread function of a soft X-ray microscope by single pixel exposure of photoresists," *Proc. SPIE* 8077, 80770N-1 (2011).
- [15] Johnstone, R. W., Foulds, I. G., Pallapa, M. V., and Parameswaran, A. M., "Isopropanol/water as a developer for poly(dimethylglutarimide)," *J. Micro/Nanolithogr. MEMS MOEMS* 7, 043006 (2008).
- [16] Greeneich, J. S., "Developer characteristics of poly-(methyl methacrylate) electron resist," *J. Electrochem. Soc.* 122, 970-976 (1975).

- [17] Leontowich, A. F. G., and Hitchcock, A. P., "Secondary electron deposition mechanism of carbon contamination," *Appl. Phys. Lett.* submitted (2012).
- [18] Henke, B. L., Gullikson, E. M., and Davis, J. C., "X-ray interactions: Photoabsorption, scattering, transmission, and reflection at $E = 50\text{-}30,000$ eV, $Z = 1\text{-}92$," *Atom. Data Nucl. Data Tables* 54, 181-342 (1993).
- [19] Urquhart, S. G., and Ade, H., "Trends in the carbonyl core (C 1s, O 1s) $\rightarrow \pi^*_{\text{C=O}}$ transition in the near edge x-ray absorption fine structure spectra of organic molecules," *J. Phys. Chem. B* 106, 8531-8538 (2002).
- [20] Jacobsen, C., Wirick, S., Flynn, G., and Zimba, C., "Soft X-ray spectroscopy from image sequences with sub-100 nm spatial resolution," *J. Microscopy* 197, 173-184 (2000).
- [21] Ade, H., and Hitchcock, A. P., "NEXAFS microscopy and resonant scattering: Composition and orientation probed in real and reciprocal space," *Polymer* 49, 643-675 (2008).
- [22] aXis2000 is written in Interactive Data Language (IDL). It is available free for non-commercial use from <http://unicorn.mcmaster.ca/aXis2000.html>
- [23] McDonald, J. C., and Whitesides, G. M., "Poly(dimethylsiloxane) as a material for fabricating microfluidic devices," *Acc. Chem. Res.* 35, 491-499 (2002).
- [24] Pawloski, A. R., and Nealey, P. F., "Efficiency of photoacid generators in chemically amplified resists for 157nm lithography," *J. Photopolymer Sci. Tech.* 15, 731-740 (2002).
- [25] Ito, H., and Wilson, C. G., "Chemical amplification in the design of dry developing resist materials," *Polym. Eng. Sci.* 23, 1012-1018 (1983).
- [26] Pavkovich, J. M., "Proximity effect correction calculations by the integral equation approximate solution method," *J. Vac. Sci. Technol. B* 4, 159-163 (1986).
- [27] Schmidt, A., Ehrfeld, W., Lehr, H., Müller, L., Reuther, F., Schmidt, M., and Zetterer, Th., "Aligned double exposure in deep X-ray lithography," *Microelec. Eng.* 30, 235-238 (1996).

Chapter 7

Accurate dosimetry in scanning transmission x-ray microscopes via the cross-linking threshold dose of poly(methyl methacrylate)

This chapter presents several responses of PMMA to various doses of 300 eV x-rays, and explores their dependence on conditions such as dose rate, pre-exposure thermal treatments and x-ray polarization. A discrepancy found in the literature involving the radiation sensitivity of PMMA was explored in depth. A method to determine the efficiency of a STXM transmission detector was developed based on the onset of negative mode (cross-linking) dose and was carried out at several STXMs worldwide.

*Reprinted with permission from the Journal of Synchrotron Radiation, 2012, 19, forthcoming, A.F.G. Leontowich, A.P. Hitchcock, T. Tyliszczak, M. Weigand, J. Wang, C. Karunakaran. DOI: 10.1107/S0909049512034486
© 2012 International Union of Crystallography.*

A.P. Hitchcock and the author of this thesis conceived the experiments. A.P. Hitchcock conceived the idea to use the onset of negative mode as a dosimeter. The author of this thesis prepared all samples and developed them, performed all the experiments (except those noted here), analysed the data, wrote the manuscript which was edited by A.P. Hitchcock and served as corresponding author. Frank Gibbs performed the TGA measurement. M. Weigand and the author of this thesis performed the experiments at UE46. J. Wang performed the detector efficiency photodiode measurement at 5.3.2.2.

Accurate dosimetry in scanning transmission X-ray microscopes *via* the cross-linking threshold dose of poly(methyl methacrylate)

Adam F. G. Leontowich,^{a*} Adam P. Hitchcock,^a Tolek Tyliczszak,^b
Markus Weigand,^c Jian Wang^d and Chithra Karunakaran^d

^aBrockhouse Institute for Materials Research, McMaster University, 1280 Main Street West, Hamilton, Ontario, Canada L8S 4M1, ^bAdvanced Light Source, Lawrence Berkeley National Laboratory, One Cyclotron Road, MS 6R2100, Berkeley, CA 94720, USA, ^cMax Planck Institute for Intelligent Systems, Stuttgart, Baden-Württemberg 70569, Germany, and ^dCanadian Light Source Inc., 101 Perimeter Road, Saskatoon, Saskatchewan, Canada S7N 0X4.
E-mail: leontoai@mcmaster.ca

The sensitivity of various polymers to radiation damage by soft X-rays has been measured previously with scanning transmission X-ray microscopes. However, the critical dose values reported by different groups for the same material differ by more than 100%. Possible sources of this variability are investigated here for poly(methyl methacrylate) (PMMA) using controlled exposure to monochromatic soft X-rays at 300 eV. Radiation sensitivity, judged by several different criteria, was evaluated as a function of dose rate, pre-exposure thermal treatments and X-ray polarization. Both the measured critical dose and the dose required to initiate negative mode (cross-linking) were observed to depend only on dose, not the other factors explored. A method of determining detector efficiency from the dose required to initiate negative mode in PMMA is outlined. This method was applied to many of the soft X-ray STXMs presently operating to derive the efficiencies of their transmitted X-ray detectors in the C 1s absorption-edge region.

1. Introduction

Many advanced technologies use ionizing radiation as a processing tool. In these applications, knowledge of the radiation sensitivity [the absorbed dose required to produce a defined outcome, following the Grotthuss–Draper law (King & Laidler, 1984)] of materials is critical. For example, polymer thin films or resists are irradiated and used as sacrificial layers in the manufacture of integrated circuits. The sensitivity of a resist is an important characteristic when considering its suitability for a specific manufacturing process. Assuming all other processing properties are equal, a more sensitive resist, *i.e.* one which requires less dose to reach the same outcome, would increase productivity. The dose accuracy when measuring radiation sensitivity is therefore of critical importance. In proton therapy, beams of energetic protons are used to destroy cancerous tissues (Hall & Giaccia, 2006). The goal is to destroy the offensive tissue using the minimum dose possible to limit the destruction of the surrounding healthy tissue, therefore the accuracy of the radiation dose administered is of utmost importance. For dose-dependent applica-

tions of ionizing radiation, the precision and accuracy of dose determinations are critical to achieving reproducible outcomes across the field of radiation science.

Several studies involving radiation damage to polymer thin films have been carried out using scanning transmission X-ray microscopes (STXMs) (Zhang *et al.*, 1995; Coffey *et al.*, 2002; Beetz & Jacobsen, 2003; Wang *et al.*, 2007, 2009*a,b*). In these studies the sensitivity is often reported in terms of a critical dose, or the absorbed dose required to cause a decrease (or increase) in the intensity of a chosen spectroscopic feature to 1/e or 37% of its initial value. Although the methodology is seemingly quite similar, there is frequently relatively poor agreement among critical dose values derived for nominally the same material and spectral feature, with values in some cases differing by more than 100%. Reported critical dose values for the decrease of the C 1s(C=O) \rightarrow $\pi_{C=O}^*$ signal (288.4 eV) of poly(methyl methacrylate) (PMMA) measured by STXMs differ by more than 500% (Zhang *et al.*, 1995; Coffey *et al.*, 2002; Wang *et al.*, 2007, 2009*a*). It is puzzling why the goal of deriving what should be a fundamental property of a material has so far been elusive to STXM microscopists.

research papers

PMMA-based radiation dosimeters for the 0–100 kGy dose region are commercially available (Red 4034, Amber 3042, Harwell Dosimeters) and have been in use for several decades (Barrett, 1982). They are commonly used in industrial radiation processing applications such as the sterilization of medical devices and the processing of foods. Once critical control parameters are understood and protocols are established, dose can be measured very accurately. There are several possibilities that may explain the discrepancies in the literature. Dose rate has been shown to affect radiation sensitivity using electrons (Jiang & Spence, 2012), ions (Schrepel & Witthuhn, 1997) and high-energy photons (Plaček *et al.*, 2003; Leiros *et al.*, 2006). The possible influence of dose rate for the STXM studies cited above was acknowledged by some (Coffey *et al.*, 2002; Wang *et al.*, 2009a) but not further investigated. Pre-exposure thermal treatments could also play a role, as was suggested by Zhang *et al.* (1995).

In this report PMMA is used as an example of a radiation-sensitive material, and several factors which could explain why accurate radiation sensitivity quantitation has been a challenge for STXMs are examined. First, pre-exposure thermal treatments, dose rate and X-ray polarization were systematically varied while the effects on the radiation damage characteristics of PMMA as a function of dose were measured by a combination of lithographic techniques, atomic force microscopy (AFM) and near-edge X-ray absorption fine-structure (NEXAFS) spectroscopy. The dose for the onset of negative mode (cross-linking) was found to be very reproducible, and independent of the factors investigated. A facile method to determine the efficiency of a STXM X-ray detector involving the onset of negative mode is presented. This measurement was then carried out at most of the currently operational soft X-ray STXMs. Large differences were found among the detector efficiencies of different STXMs, which may account for much of the variation in critical dose values reported in previous studies.

2. Methodology

2.1. Materials

PMMA (electronics grade, $M_w = 315000$, $M_w/M_n = 1.05$, synthesized by living anionic polymerization, *sec*-butyllithium initiator) was purchased from Polymer Source. Toluene 99.9% Chromasolv and 4-methyl-2-pentanone (MIBK) >98.5% ACS reagent grade were purchased from Sigma-Aldrich. 2-Propanol (IPA) 99.5% was purchased from Caledon Laboratories. Mica was purchased from Ted Pella. Si_3N_4 windows (75 nm \times 1 mm \times 1 mm window in a 200 μm \times 5 mm \times 5 mm Si wafer frame) were purchased from Norcada. All materials were used as received.

2.2. Sample preparation

Thin films of PMMA were fabricated by spin casting four drops of a 1.5% *w/w* PMMA/toluene solution onto a 1.5 cm \times 1.5 cm piece of freshly cleaved mica. The films remained in ambient air for 10 min and were then cut into 3 mm \times 3 mm

pieces with a scalpel. Upon slowly dipping the mica into a Petri dish filled with distilled water, small pieces of the film release and float on the water's surface. These were then caught on Si_3N_4 windows in an orientation such that the film only partially covered the window to allow for measurements of the incident X-ray flux (I_0) in the bare regions. Samples labelled 'as-spun' underwent no further processing. Samples labelled 'vacuum dried' were placed in a vacuum oven (2×10^{-2} torr) at 343 K for 24 h. Samples labelled 'annealed' were placed on a hot plate at 423 K for 1 h. Temperatures were monitored using a K-type thermocouple and a glass thermometer (± 1 K). The film thicknesses were 50 ± 5 nm, measured by AFM across a scratch through the film, and by STXM by dividing the measured optical density (OD) in the C 1s region by the response of 1 nm of PMMA, established by matching the C 1s NEXAFS spectrum of PMMA between 275–282 eV and 340–360 eV to the absorption predicted from the literature elemental X-ray absorption coefficients (Henke *et al.*, 1993) for $\text{C}_5\text{H}_8\text{O}_2$, and the bulk density of PMMA (1.18 g cm^{-3}). Thickness values from both techniques were in agreement within 5%.

2.3. Development

The sample was held with locking tweezers and gently stirred in a vial containing a 3:1 *v/v* solution of IPA:MIBK for 30 s, then immediately stirred in a waiting vial of IPA for 15 s. The sample was then allowed to dry in air. Development and air drying occurred at ambient temperature (293–298 K).

2.4. Scanning transmission X-ray microscope

Five soft X-ray (80–2500 eV) STXMs were used to expose PMMA samples to 300 eV X-rays and to probe the irradiated material after exposure. The instruments used were located at the following beamlines: 5.3.2.2 (Kilcoyne *et al.*, 2003) and 11.0.2 (Tyliczszak *et al.*, 2004) at the Advanced Light Source [ALS; Lawrence Berkeley National Laboratory, Berkeley (LBNL), USA]; 10ID-1 (Kaznatcheev *et al.*, 2007) at the Canadian Light Source (CLS; Saskatoon, Canada); X07DA (Raabe *et al.*, 2008) at the Swiss Light Source (SLS; Paul Scherrer Institute, Villigen, Switzerland); and UE46 (Follath *et al.*, 2010) at Berliner Elektronenspeicherring-Gesellschaft für Synchrotronstrahlung (BESSY II; Berlin, Germany). Henceforth the individual instruments will be referenced by the beamline at which they presently reside. While the beamlines differ, all five of these STXMs are essentially based on the ALS 5.3.2.2 design (Kilcoyne *et al.*, 2003) which is now commercially available (Bruker Advanced Supercon GmbH, formerly Accel). All are equipped with precise in-vacuum piezo shutter systems which can reliably go from closed to open to closed in 1 ms (Kilcoyne & Tyliczszak, 2004). At present all of these STXMs use the same operational software, *STXM_Control* (Kilcoyne *et al.*, 2003). All maintain the sample position (x, y) relative to the zone plate lens to better than 10 nm by laser interferometer feedback systems. For these experiments all were equipped with zone plates with the same characteristics (25 nm outer most zone width, 240 μm

diameter, 90 μm central stop) from the Center for X-ray Optics, LBNL. Except for UE46, the transmitted X-ray detectors consist of a phosphor scintillator to convert soft X-rays to visible-wavelength photons which are then counted by a high-performance photomultiplier tube (PMT) (Kilcoyne *et al.*, 2003; Fakra *et al.*, 2004). At UE46 the X-rays were detected directly using an avalanche photodiode (S2382, Hamamatsu) gated to the arrival times of the 500 MHz flashes of synchrotron light to reduce background.

Samples were fixed to an aluminum sample plate and loaded into the STXM chamber. The chamber was evacuated to 0.1 torr by pumping for about 10 min, then backfilled with 250 torr He. The evacuation step is important because O_2 has been shown to affect the radiation damage chemistry of thin polymer layers (Coffey *et al.*, 2002). All possible efforts were taken to eliminate higher order radiation. Higher order X-rays were blocked geometrically by the sufficiently absorbing central stop incorporated in the zone plate, and an order-sorting aperture (OSA), carefully centered on the optical axis. The OSA diameter and OSA-to-sample distances were chosen to select only the zone plate first order component. In addition, higher order suppression systems were used on beamlines that currently have them [a 200 nm Ti foil at 10ID-1, a 1.0 m-long section of the beamline differentially pumped with N_2 at 600 mtorr at 5.3.2.2, and a MgF_2 -coated mirror system at X07DA (Frommherz *et al.*, 2010)]. The detector was positioned so that the active area accepted the entire transmitted bright field signal. The photon energy scales were calibrated to an accuracy of 0.05 eV using the known $\text{C } 1s(\text{C}=\text{O}) \rightarrow \pi_{\text{C}=\text{O}}^*$ peak of PMMA at 288.45 eV (Wang *et al.*, 2007). Photon energy scale shifts during a set of measurements over a few days at any given beamline were less than 0.1 eV.

2.4.1. Imaging and spectroscopy. STXMs focus monochromatic X-rays into an intense 30 nm-diameter spot [Rayleigh criterion for a 25 nm outer most zone width zone plate operated under diffraction-limited conditions (Howells *et al.*, 2007)]. Samples are then positioned at the focal plane and x - y raster scanned through the X-ray spot under computer control while the transmitted signal is acquired to form transmission images at X-ray photon energies. These transmission images can be converted to OD images by applying the Lambert–Beer law with an I_0 measurement through a suitable blank. In addition, NEXAFS spectra can be measured by recording image sequences, or ‘stacks’ (Jacobsen *et al.*, 2000), over a photon energy range of interest. If necessary, the images were aligned spatially using Fourier-transform-based cross-correlation procedures. The resulting data set (x, y, E) provides a NEXAFS spectrum at each pixel. The detailed procedures for imaging, spectroscopy and data analysis have been reviewed elsewhere (Jacobsen *et al.*, 2000; Ade & Hitchcock, 2008; Hitchcock, 2012). Image and spectroscopic data processing was performed using the program *aXis2000*.

2.4.2. Patterning. Samples were precisely patterned using PatternGen, a routine within *STXM_Control*. The pattern-generation input files (*.xyt) consist of a set of records, with

each record providing the x - y positional coordinates for each point exposure and the length of time the piezo shutter is to be opened. The input file used for all experiments here consisted of nine 600 nm \times 600 nm areas, each composed of 10×10 single point exposures with a pitch of 60 nm (see Fig. 1 of the supplementary material), and each area has a progressively increasing exposure time. This input file and instructions for creating such files are included as supplementary material.¹ In order to obtain reproducible results it is necessary to set the microscope to best focus before executing the pattern, which can be achieved using a micrometer or sub-micrometer specimen of radiation-insensitive material in/on the sample, which is typically a piece of mica from sample preparation. The focus must be set within a few tens of micrometers of the patterned area, as it is not currently possible to reliably have the sample perfectly orthogonal to the X-ray beam over much more than 80 μm . Care was taken during set-up so that the areas of the sample to be patterned were never imaged with the STXM, as even a single image with typical microscope settings can cause quantifiable radiation-induced effects (supplementary Fig. 2). When the pattern-generation scan is initiated, the program performs the following sequence: (i) with the shutter closed, move to the desired position (x, y) under interferometric feedback, (ii) open the shutter, (iii) close the shutter after the specified exposure time for that point. This sequence is repeated for each record in the input file until all points have been exposed. Patterning in this way is very accurate, precise and reproducible. The temperature of the aluminum sample plate during patterning was monitored with a K-type thermocouple bonded 2 mm from the sample, and was found to be 298 ± 2 K.

In order to determine dose, I_0 at the patterning photon energy must be measured immediately before and/or after patterning. It is critical to measure I_0 with exactly the same parameters used for patterning, *i.e.* no refocusing, no changes in slit settings, no changes to the OSA position, *etc.* The CLS (10ID-1) and BESSY II (UE46) synchrotrons were operating in multi-bunch mode when these experiments were performed. For those measurements, I_0 was measured before and after each pattern was executed, and the average value was used. As the total time to execute the nine area patterns is 5–10 min, the before–after difference was never more than 3%. The SLS (X07DA) and ALS (5.3.2.2, 11.0.2) operated in top-up mode so the storage ring current and thus the X-ray flux through the shutter was constant (to within 0.2%); only one I_0 measurement was necessary.

2.4.3. Calculating dose. Absorbed dose (amount of energy absorbed by the sample volume divided by the amount of mass irradiated) D was calculated using the following equation,

$$D = (F/K)tE/Vd \quad (1)$$

where D is the dose in Grays ($\text{Gy} = \text{J kg}^{-1}$); F is the photon absorption rate of the irradiated volume of material (photons

¹ Supplementary data for this paper are available from the IUCr electronic archives (Reference: HF5212). Services for accessing these data are described at the back of the journal.

research papers

s^{-1}) at the chosen patterning photon energy; K is the detector efficiency (unitless), which is the ratio of the number of single photon events per second counted, over the photons s^{-1} that impinge on the detector, and must be determined experimentally at the photon energy of exposure. At 5.3.2.2, K was determined by comparing the PMT signal with that from a calibrated Si photodiode (AXUV-HS1; International Radiation Detectors) and found to be $35 \pm 5\%$ at 300 eV; t is the exposure time (s); E is the energy per photon (J photon $^{-1}$) at the patterning photon energy (300 eV throughout this work); V is the volume of the material irradiated (cm 3), in this case the exposure area multiplied by the film thickness; d is the density of the material (1.18 g cm $^{-3}$ for PMMA).

If the X-ray absorption cross section at the patterning photon energy does not change significantly as a function of dose (which must be determined experimentally, but is often valid for very short exposures, highly radiation-resistant materials, and materials which do not undergo mass loss with increased dose) the photon absorption rate is simply the difference between I_0 and I , the photons s^{-1} transmitted through the sample,

$$F = I_0 - I. \quad (2)$$

This approach is valid in the photon energy region currently accessible with soft X-ray STXMs (80–2500 eV) where photoabsorption dominates over all other process by orders of magnitude for most elements [three orders of magnitude for carbon (Hubbell *et al.*, 1980)] and it can be safely assumed that F is due to photoabsorption alone. A convenient form of the photon absorption rate for STXMs is (derivation in the supplementary material),

$$F = I_0[1 - \exp(-OD)] \quad (3)$$

where OD is the optical density of the polymer film at the patterning photon energy, measured from an OD image recorded adjacent to the patterning area. These values depend on the individual beamlines and the response of the material at specific photon energies and must be determined experimentally.

It is often the case, however, that irradiation induces chemical change, mass loss, *etc.*, which results in changes to the X-ray absorption cross section of a material as a function of dose. F is then not constant, and the changes in F during exposure must be accommodated when determining the dose. For several polymers including PMMA, the change in absorption cross section as a function of dose has been experimentally determined to follow first-order rate laws (Zhang *et al.*, 1995; Coffey *et al.*, 2002; Beetz & Jacobsen, 2003; Wang *et al.*, 2007, 2009a,b). Specifically, when the X-ray absorption features decay exponentially to a residual value, the following applies,

$$OD = OD_\infty + a \exp(-bt) \quad (4)$$

where OD is the OD of the polymer film after exposure time t , OD_∞ is the residual OD value of the polymer film after receiving a very high dose, and a and b are found through a fit to the data points by plotting OD as a function of t . To

compute absorbed dose in cases where the X-ray absorption cross section at the patterning photon energy undergoes exponential decay in response to dose as the patterning proceeds, the OD term in (3) is replaced by the integrated OD at the patterning photon energy for a given exposure time,

$$\begin{aligned} OD &= \frac{\int_0^t [OD_\infty + a \exp(-bt)] dt}{t} \\ &= \frac{OD_\infty t + (a/b)[1 - \exp(-bt)]}{t}. \end{aligned} \quad (5)$$

As PMMA is irradiated, it undergoes mass loss, which results in the exponential decay of the X-ray absorption cross section at 300 eV. Therefore, the integrated OD [equation (5)] was used in this work. Doses were calculated using an Excel spreadsheet, which is available upon request.

2.5. Other characterization techniques

Thermogravimetric analysis was performed with a Netzsch STA 409 PC/PG thermal analyser. Optical micrographs were collected with an Olympus BX51 optical microscope equipped with a 100 \times objective and a CCD camera. AFM was performed using a Quesant Q-Scope 350 microscope with Budget Sensors Tap 150 Al-G probes in intermittent contact mode with a 0.5 Hz scan rate.

3. Results

3.1. Thermal characterization of PMMA

Thermogravimetric analysis was performed on PMMA in as-received powdered form measured in air with a temperature ramp of 5 K min $^{-1}$ (Fig. 1). The glass transition (T_g) occurred at 376 K while thermal degradation (T_d) took place at and above 503 K.

3.2. Surface roughness of PMMA films

Atomic force micrographs were taken of the as-spun, vacuum-dried and annealed samples. RMS roughness values were determined from these micrographs and are presented

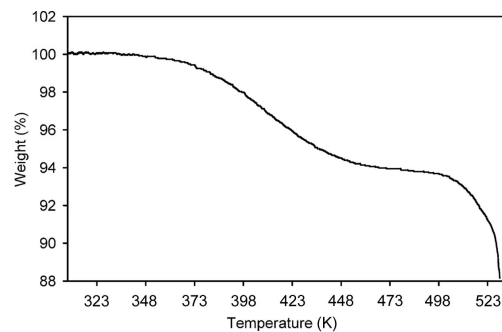


Figure 1
 Thermogram of as-received powdered PMMA in air. Ramp rate: 5 K min $^{-1}$.

research papers

Table 1
 Effect of thermal treatments on the surface roughness of PMMA as measured from atomic force micrographs.

Sample	RMS roughness (nm)
As-spun	0.78
Vacuum dried (343 K, 2×10^{-2} torr, 24 h)	1.08
Annealed (423 K, 1 h)	0.70

in Table 1. The annealed samples showed the lowest RMS roughness relative to the as-spun and vacuum-dried samples.

3.3. Patterning

As-spun, vacuum-dried and annealed samples were loaded into 5.3.2.2 and patterned using the input file described in §2.4.2. After patterning, the samples were removed from the STXM and inspected with an optical microscope (Fig. 2a). All nine patterned areas are resolved, and they become increasingly transmissive with increasing dose. An atomic force micrograph of the patterned areas is presented in Fig. 2(b). The individual exposures which make up each area are resolved in detail. The heights of individual patterned areas were measured and plotted *versus* dose (Fig. 2c). The height of the PMMA film decreased with increasing dose roughly linearly until 60 ± 15 MGy, at which point the film thickness was

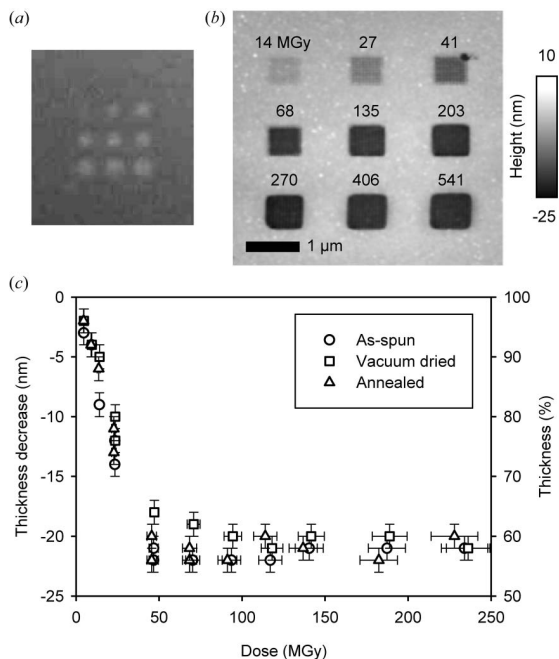


Figure 2
 (a) Optical micrograph (transmission, 100 \times) of an annealed PMMA sample after patterning with 300 eV X-rays. (b) Atomic force micrograph of PMMA after exposure [same area/doses for (a) and (b)]. (c) Plot of the height reduction of individual patterned areas *versus* dose. Results from different pre-exposure thermal treatments [as-spun, vacuum-dried (343 K, 2×10^{-2} torr, 24 h) and annealed (423 K, 1 h)] are compared.

reduced by 40%. No significant height changes were observed for doses beyond this point up to 900 MGy, as long as carbon contamination was not significant (§4.4). This behavior was found to be independent of the different pre-exposure thermal treatments and dose rate over the 73–1230 MGy s^{-1} range investigated, accomplished by adjusting the monochromator exit-slit widths (increasing/decreasing I_0) and t .

3.4. Spectromicroscopy

Spectroscopic changes within the patterned areas were investigated with 5.3.2.2. Stacks of the patterned areas were collected, and C 1s NEXAFS spectra of individual patterned areas were obtained by extracting the average spectrum of the central region of each area (roughly 400 nm \times 400 nm). The dose associated with the stack acquisition was 5–10 MGy. Spectra corresponding to four different doses are compared in Fig. 3. Several spectral changes were observed as the dose increases. A new feature at 285.1 eV attributed to C=C bond creation appears and increases with dose. The signal intensity at 288.4 eV, corresponding to the C 1s(C=O) $\rightarrow \pi_{C=O}^*$ decreases with dose, as does the C 1s continuum signal (≥ 305 eV). The signal at 305 eV was reduced by 30% relative to the virgin polymer after receiving 150 MGy. These observations are consistent with other NEXAFS investigations of PMMA (Zhang *et al.*, 1995; Coffey *et al.*, 2002; Wang *et al.*, 2007, 2009a). In this work the spectral trends *versus* dose were investigated for the different pre-exposure thermal treatments noted and several dose rates between 73 and 1230 MGy s^{-1} . The spectral behavior in all cases was found to be identical given identical dose.

The integrated area of the 288.4 eV peak (above a background estimated as the average of the spectral intensities at 288.0 eV and 289.5 eV) is proportional to the number of C=O bonds in the volume sampled. Thus, a decrease of this peak is proportional to the amount of C=O bond loss or chemical change. OD images of several areas of as-spun, vacuum-dried

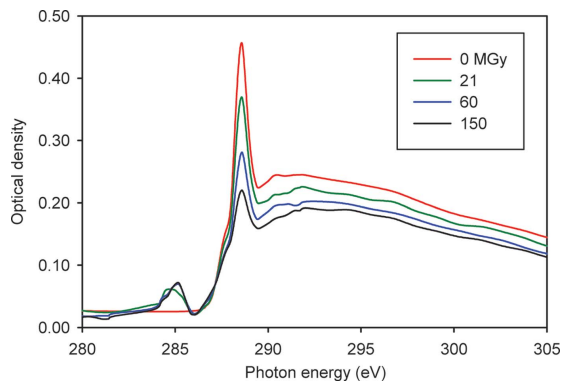


Figure 3
 C 1s NEXAFS spectra of PMMA extracted from individual areas patterned with different doses of 300 eV X-rays (color online): 0 MGy (red), 21 MGy (green), 60 MGy (blue), 150 MGy (black). The spectral trends were observed to be independent of the pre-exposure thermal treatments noted and dose rate (73–1230 MGy s^{-1}).

research papers

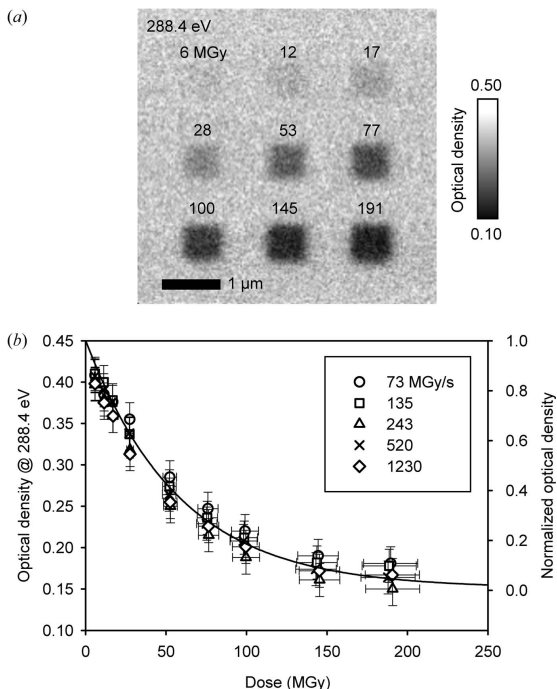


Figure 4
 (a) STXM OD image (288.4 eV) of an annealed PMMA sample patterned with various doses of 300 eV X-rays. (b) Plot of the OD at 288.4 eV values of individual patterned areas versus dose for different dose rates ranging from 73 to 1230 MGy s⁻¹. In each case the OD at 288.4 eV exponentially decreases with a critical dose of 62 ± 8 MGy derived from the indicated fit (solid line) to the average of all data sets. The separate data sets all agree within measurement uncertainty.

and annealed samples patterned with different doses were collected with STXM 5.3.2.2 at 288.4 eV [an example image is shown in Fig. 4(a)]. The dose associated with collecting these OD images was less than 1 MGy. Average OD values of the central regions of many individual patterned areas were determined, and then plotted versus dose (Fig. 4b). These data were used to calculate the critical dose for the C 1s(C=O) → π*_{C=O} decrease at 288.4 eV. The critical dose was found to be 62 ± 8 MGy (average of the critical doses derived independently for each measurement; the uncertainty is the standard deviation). This result was independent of the pre-exposure thermal treatments noted and also independent of dose rate over the 73–1230 MGy s⁻¹ range investigated.

3.5. Development

Some of the samples were subjected to development (§2.3) after patterning. An atomic force micrograph of developed annealed PMMA which was patterned at 5.3.2.2 is presented in Fig. 5(a). Doses greater than 1 MGy result in the full removal of the irradiated material by the developer, i.e. positive mode, while no measurable difference in the thickness of the non-patterned film away from the patterned areas was observed.

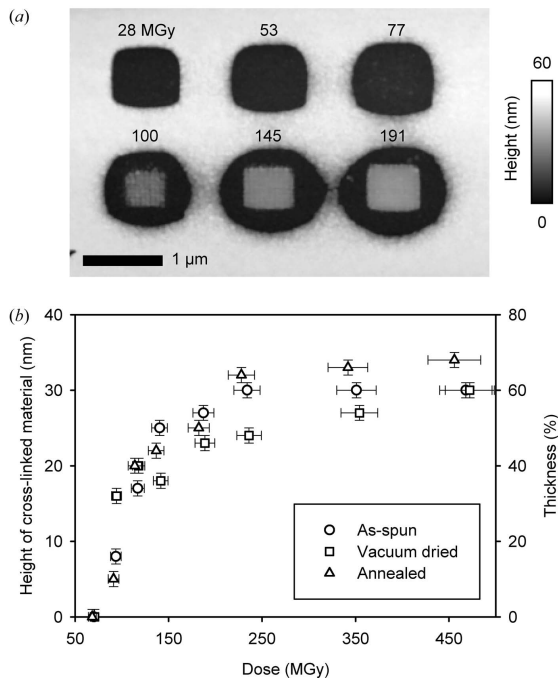


Figure 5
 (a) Atomic force micrograph of developed annealed PMMA showing several 600 nm × 600 nm areas patterned with various doses of 300 eV X-rays. (b) Measured heights of several 'cross-linked' PMMA areas plotted versus dose for as-spun, vacuum-dried (343 K, 2 × 10⁻² torr, 24 h) and annealed (423 K, 1 h) samples.

At a dose of 90 ± 4 MGy, PMMA switches from positive mode to negative mode, i.e. the irradiated material remains after development (Leontowich & Hitchcock, 2011). The height of this 'cross-linked' PMMA remaining in the patterned areas after development was measured for as-spun, vacuum-dried and annealed samples and the values were plotted versus dose (Fig. 5b). As the dose increases beyond the 90 ± 4 MGy onset of negative mode, the height of cross-linked PMMA increases and eventually reaches a maximum value near 350 MGy. The maximum height of the cross-linked PMMA corresponds to about 60% of the original film thickness. No further height changes were observed for doses from 350 to 900 MGy, as long as carbon contamination was not significant (§4.4). This behavior, and the onset of negative mode dose, was found to be independent of (i) pre-exposure thermal treatments; (ii) dose rate over the 73–1230 MGy s⁻¹ range investigated; and (iii) X-ray polarization [left circular, right circular, 80% linear (circular polarized experiments were performed with 11.0.2)]. The individual 600 nm × 600 nm areas of cross-linked PMMA are large and dense enough to be resolvable in an optical microscope with a 50× or greater magnification objective lens (Figs. 6a, 6b). Although the as-spun, vacuum-dried and annealed samples required the same dose for the onset of negative mode and exhibit the same dose-dependent cross-linked material growth behavior (Fig. 5b), differences were

research papers

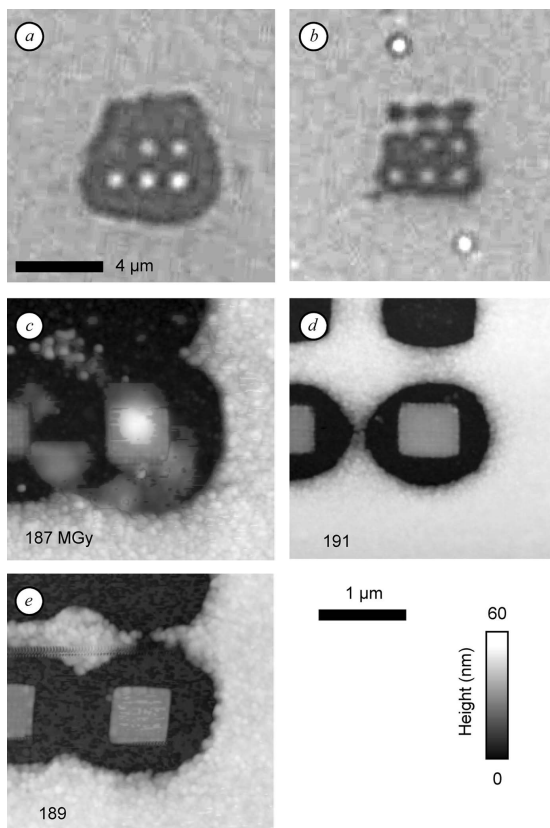


Figure 6
Optical micrographs (reflection, 100 \times) of developed (a) as-spun and (b) annealed (423 K, 1 h) samples, patterned with identical doses (20, 40, 59, 99, 198, 296, 395, 593, 790 MGy) and dose rates (620 MGy s⁻¹) of 300 eV X-rays [(a) and (b) are on the same spatial scale]. Atomic force micrographs of developed (c) as-spun, (d) annealed and (e) vacuum-dried (343 K, 2 \times 10⁻² torr, 24 h) samples which received the same dose [(c), (d) and (e) are on equal height and spatial scales].

observed in the area immediately surrounding the patterned areas. The mechanism of the increased lateral removal of resist beyond the presumed exposure area with increasing dose was previously identified as resulting from the point spread function of the optical system (Leontowich & Hitchcock, 2011; Leontowich *et al.*, 2011). However, given identical dose, the lateral distance beyond the patterned area over which material was removed by development was significantly greater for the as-spun and vacuum-dried samples (Fig. 6a) compared with annealed samples (Fig. 6b). Identically patterned areas were inspected by AFM (Figs. 6c–6e) for each of the sample types. The as-spun samples showed the most extensive lateral removal. The edges of the two non-annealed films are much rougher and seem to show the presence of spherical PMMA aggregates 80–100 nm in diameter. Similar PMMA aggregates or nodules have been observed previously using AFM (Dobisz *et al.*, 1997). The annealed film showed the lowest lateral

removal, smoother edges and smaller aggregates. These behaviors were independent of dose rate over the 73–1230 MGy s⁻¹ range investigated.

4. Discussion

4.1. Thickness decrease

Several reports have shown that PMMA undergoes a change in height in response to dose. Here, the height of PMMA was observed to decrease with increasing dose, but only until 60 ± 15 MGy where the rate of thinning drops to zero. A decrease in film height with dose has been reported previously with soft X-rays (Zhang *et al.*, 1995) and other radiation sources including electron (Dobisz *et al.*, 1997) and ion beams. Schrepel & Witthuhn (1997) reported a linear dependence of the thickness on ion (H⁺, He⁺) fluence. The samples used were 1.5 mm thick, and the maximum decrease in height observed was only 1 μ m, less than 1% of the virgin film height. Using ion (¹⁵N⁺) fluences two orders of magnitude larger than those of Schrepel & Witthuhn (1997), Kallweit *et al.* (1991) observed an initial linear height decrease with fluence, and no further decrease beyond a certain fluence. Schrepel *et al.* (2002) reported that irradiated areas of 1 mm-thick PMMA initially increased in height, before relaxing over 200 min to show a net decrease. An attempt was made to observe this process, and an increase in height of the patterned areas was observed in atomic force micrographs collected within 60 min of patterning at 10ID-1 (supplementary Fig. 3a). However, these patterned areas did not decrease in height after 36 days. The thickness increase observed here was later determined to be an artefact of carbon contamination.

The change in height in response to dose has been attributed to both loss of material and/or densification. When centimeter-sized blocks of PMMA were irradiated with neutrons and γ -rays, bubbles were observed in the interior, indicating trapped gaseous products, while the zone within approximately 1 mm from the surface did not show bubbling, which was ascribed to outgassing of the product molecules (Charlesby & Ross, 1953; Ross & Charlesby, 1953). Hiraoka (1977) identified many of the gas molecules given off by mass spectrometry. The thickness decrease could also involve a densification of the material. Rück *et al.* (1992) found that He⁺ ion-irradiated PMMA had an increased index of refraction and decreased thickness and attributed this to increased density, while Kallweit *et al.* (1991) concluded that the loss in height is entirely due to loss of material *via* outgassing as opposed to radiation-induced densification. Loss of material from an irradiated surface has been classified into desorption and ablation regimes (Haglund, 1996). The ablation threshold for PMMA occurs with power density levels which are at least three orders of magnitude greater than presently available at the STXMs used here (Makimura *et al.*, 2011). The desorption mechanism is most compatible with our observations; the observed reduction in thickness is likely due to the diffusion of gaseous product molecules out of the irradiated areas. This is supported by the observed decrease in the intensity of the C 1s

research papers

NEXAFS continuum signal with increasing dose (Fig. 3). The signal in the continuum region is proportional to the total amount of carbon, and eventually reaches a residual amount of approximately 70% of the virgin film. This decrease in continuum intensity has also been observed at room temperature in other STXM experiments (Coffey *et al.*, 2002; Wang *et al.*, 2007, 2009a) and transmission electron microscope electron energy-loss spectroscopy experiments (Egerton, 1980), and the same residual continuum signal value was observed by Coffey *et al.* (2002). Atomic force micrographs reveal a decrease in film height to a residual value of 60% (Fig. 2b), thus indicating the link between topography and spectroscopy. The same residual film height value was observed by Teh *et al.* (2003). The discrepancy between the larger height decrease relative to the amount of carbon lost could indicate a slight densification, but the contribution appears to be minor relative to outgassing of molecular fragments.

In passing, it is important to note that this height reduction of PMMA has been found by others to be temperature-dependent. This process of film thinning of PMMA (and other polymers) with dose has also been termed 'photo-etching'. There can be further removal of material, even full removal of the polymer film down to the substrate or 'self-development' if PMMA is heated during or following irradiation (Katoh & Zhang, 1998). Radiation-induced mass loss is often found to be temperature-dependent (Egerton, 1982; Beetz & Jacobsen, 2003). Here, the sample temperature was maintained at 298 ± 2 K throughout, and the temperature rise within the focal point has been experimentally determined to be <1 K for dose rates twice as high as the maximum used in this work (Leontowich & Hitchcock, 2012a).

4.2. Effect of annealing

Surface roughness was observed to decrease after annealing above T_g (Table 1), and the lateral extent of material removed around the patterned areas after development was found to depend upon the pre-exposure thermal treatment involved. Arjmandi *et al.* (2009) similarly reported that increased surface roughness was proportional to increased developed line-edge roughness for PMMA. Our measured value of T_g for powdered PMMA (376 K) is in agreement with other reported values [378 K (Rück *et al.*, 1997), 393 K (Kunz & Stamm, 1996)]. However, T_g has been shown to depend on film thickness, substrate and other effects (Fryer *et al.*, 2001); a value of 391 K has been reported for a film of similar thickness to the 50 ± 5 nm films used in this work (Keymeulen *et al.*, 2007). Our sample preparation temperatures were chosen with these values in mind. The temperature at which the vacuum-dried samples were heated was chosen so that the samples did not approach the lowest reported T_g that we are aware of for PMMA by tens of K. Likewise, the temperature at which the annealed samples were heated was tens of K higher than the highest literature T_g example that we are aware of, ensuring that the annealed samples passed through T_g . Furthermore, the amount of heat produced at the focal point of a STXM has

been shown experimentally to be <1 K with dose rates two times greater than those used in this work (Leontowich & Hitchcock, 2012a), negating unintended thermal processing during patterning.

In photolithography, polymer films are often baked above their T_g before being irradiated as this "promotes adhesion to the substrate" (Brewer, 1980), and also serves to remove residual solvent molecules trapped in the glassy polymer matrix during spin coating (Broers, 1981; Moreau, 1988). Ross & Charlesby (1953) and Hajimoto *et al.* (1965) have shown that small molecules trapped in a polymer 'glassy cage' can be released upon reaching or exceeding T_g . Residual solvent in the polymer layer has been shown to drastically increase the removal rate of PMMA during development (Greeneich, 1975). In addition, positron annihilation studies have shown that the size of physical voids within PMMA films decreases for films annealed at 423 K relative to non-annealed films (Puglisi *et al.*, 2001). Here, the combination of residual casting solvent and the greater permeation of the developer into the two non-annealed films owing to the increased void size increases the development rate, leading to greater lateral removal.

4.3. Critical dose

Several critical dose values for PMMA have been reported in the literature. Previous STXM measurements of the critical dose, specifically of the decrease in the $C 1s(C=O) \rightarrow \pi_{C=O}^*$ (288.4 eV) intensity, which are directly comparable with those measured in this report, include 69.4 MGy (Coffey *et al.*, 2002), 50.0 ± 3.0 MGy (Zhang *et al.*, 1995), 13.1 ± 0.2 MGy (Zhang *et al.*, 1995), 15.2 ± 1.4 MGy (Zhang *et al.*, 1995), 67 ± 10 MGy (Wang *et al.*, 2009a) and 60 ± 8 MGy (Wang *et al.*, 2007). A critical dose value for C=O loss measured at the O 1s absorption edge could be considered to be related (Beetz & Jacobsen, 2003). The possibility of a dose-rate dependence for the critical dose for PMMA has been discussed in prior STXM work (Coffey *et al.*, 2002; Wang *et al.*, 2009a) but never systematically investigated to our knowledge. Room-temperature measurements of mass-loss critical doses for PMMA in electron microscopes showed no evidence of dose-rate dependence (Egerton, 1980). The critical dose measured here (62 ± 8 MGy) was found to be independent of dose rate (Fig. 4), and the highest dose rate used here (1230 MGy s^{-1}) is significantly greater than those used in all previous STXM studies [three times higher than Wang *et al.* (2009a)]; therefore dose rate is not a significant cause of the variability in critical doses reported in the literature.

Zhang *et al.* (1995) reported that pre-exposure thermal treatments affect the critical dose of PMMA, and their three reported critical doses correspond to three different thermal treatments: 50 ± 3 MGy (as-spun), 13.1 ± 0.2 MGy (423 K, 2 h), 15.2 ± 1.4 MGy (473 K, 2 h). In contrast, we did not observe any change in the critical dose between our as-spun, vacuum-dried and annealed (423 K, 1 h) samples. The annealing temperature may be a factor. Reported T_d values vary from as low as 443 K for a 65 nm film (Hutchings *et al.*,

research papers

2001) to 523 K for a 1 μm film (Fragalà *et al.*, 1999). Like T_g , T_d depends on many factors, including the method of polymerization and the sample thickness (Manring, 1989). It would seem possible that the sample annealed at 473 K in the Zhang *et al.* (1995) report may have partly degraded during the annealing process as this temperature is above some reported values for T_d , and could explain why its critical dose was significantly lower. While this might explain that particular sample, there is more than a factor of four difference between the critical dose determined here and that reported by Zhang *et al.* (1995) for PMMA films annealed at 423 K. This temperature is well below the T_d measured for the as-received PMMA, and tens of K below the lowest reported T_d that we are aware of.

In the Zhang *et al.* (1995) study the critical dose for the as-spun sample was determined to be 50 MGy, yet the maximum dose administered appears to be only 30 MGy. The residual C=O bond concentration may not have been experimentally determined, and the extrapolated values may not be correct. An additional conflict is present in the data that Zhang *et al.* (1995) used to calculate the critical doses: mass loss, measured by the decrease in the C 1s NEXAFS continuum region (317 eV), was 80–100% of the original film thickness after receiving 30 MGy, indicating almost complete film loss. The C=O peak should have correspondingly decreased by an equal or greater amount, yet the C=O peak intensity decreased by only 30–40% for the same dose. Zhang *et al.* (1995) indicated that “baked PMMA will have less cross-linking than unbaked PMMA for a given dose”. However, this was only an extrapolation from the NEXAFS data and cross-linking was not directly observed. Here we have observed the cross-linked material *via* atomic force micrographs after development and found that the amount of cross-linked material depends on dose, independent of pre-exposure thermal treatments (Fig. 5).

Two highly probable and potentially significant contributions to the variation in critical dose are (i) differences in the data collection method between studies, and (ii) detector efficiency (§4.5). The STXM measurements of Coffey *et al.* (2002) and Zhang *et al.* (1995) involved an exposure–monitor sequence; alternatively exposing the same sample area to a high dose and then interrogating that area with a low dose. In those studies only the high-dose exposure was counted. In Coffey *et al.* (2002) the interrogation was single energy images, while for Zhang *et al.* (1995) it involved recording a defocused C 1s NEXAFS spectrum. In effect, the sample received a larger dose than reported, which would make the critical dose appear lower. In contrast, Wang *et al.* (2009a) patterned multiple virgin areas over a range of doses, and imaged them once at a single photon energy to collect the data necessary to determine the critical dose (Fig. 4).

4.4. Detector calibration in STXM with PMMA

The decrease in film height, the critical dose for C=O loss measured at 288.4 eV, and the onset of negative mode were all found to depend on dose, independent of dose rate and pre-

exposure thermal treatments. Thus it would seem that PMMA could be a robust platform for dosimetry in STXM. In fact, PMMA-based dosimeters have been commercially available for decades (Barrett, 1982). In this section the utility of these dose-dependent responses for dosimetry in STXM are outlined.

There are several drawbacks to monitoring dose by measuring a decrease in film height. Perhaps the largest is that the STXM chamber must be freshly cleaned. The chamber contains small partial pressures of carbonaceous molecules which decompose and build up on irradiated surfaces (Leontowich & Hitchcock, 2012b). The measurements for Fig. 2 were made using 5.3.2.2 days after it underwent a thorough cleaning process (disassemble, plasma clean, solvent rinse, reassemble, align). The rate of carbon contamination on the sample was below a measurable level for doses up to 900 MGy. However, when the nine area exposures were made at 10ID-1, the height of the patterned areas initially decreased with dose, and then increased, eventually exceeding the virgin film height (supplementary Fig. 3a). The growth in this case was due to carbon contamination on the sample. The carbon contamination layer could also prevent fragment molecules from escaping the patterned area, further increasing the height. Cleaning the chamber takes several days and unfortunately it does not take long for the STXM chamber to be re-polluted since the chamber is often vented to atmosphere, samples are mounted with double-sided tape and epoxy, and many samples containing volatile organics are studied. This approach also requires access to an AFM.

The radiation-induced decrease in the C 1s(C=O) $\rightarrow \pi_{\text{C=O}}^*$ transition (288.4 eV) of PMMA and the critical dose derived from that data could be used for dosimetry. Coffey *et al.* (2002) standardized the response of multiple copies of a gas proportional counter detector for STXM relative to the radiation-induced exponential decay of the intensity of the C 1s(C=O) $\rightarrow \pi_{\text{C=O}}^*$ peak of polycarbonate. The critical dose measurement requires identification of the residual bond concentration, and in practice this value must be decided by the observer which can be somewhat subjective. Carbon contamination, which over time causes the C 1s NEXAFS signal to increase (supplementary Fig. 3b), can mask the true residual bond concentration. This is problematic for critical dose measurements of radiation-resistant materials (Wang, 2008). To accurately measure the residual bond concentration for PMMA which we observe around 300 MGy, the chamber must be clean. The usefulness of critical dose as a monitor of radiation damage rates has been criticized (Cosslett, 1978). However, its application in STXM dosimetry does not require any additional equipment to measure, the data can be acquired rapidly, and the sample can remain in the chamber after the data are collected. In our view this is not the most accurate method, but it can serve as a ‘quick and dirty’ dosimeter to gain a fair estimate with relatively little effort.

Under the conditions used here, the dose for the onset of negative mode is exceptionally precise, within 5%. The onset occurs at 90 ± 4 MGy, which is below the point where significant carbon contamination occurred for all STXMs used

research papers

here. Identifying the onset of negative mode does require keeping the development chemicals on hand, but these are inexpensive, stable, of low hazard, and only small volumes (<10 ml) are needed per sample. The development procedure is simple, and the onset can be observed in an optical microscope equipped with a 50× or 100× objective, which most facilities have adjacent to the STXM for pre-characterization of samples.

4.5. Determination of detector efficiency using the onset of cross-linking dose

In order to compute dose, the detector efficiency must be known [equation (1)]. This value was recently measured at 5.3.2.2. However, at the other STXMs (except UE46) the detector efficiency was not known or had not been measured for some time. For most users this is not an issue as the primary use of STXMs is to collect images and X-ray absorption spectra; for these purposes it is not necessary to know the values of detector efficiency or dose. However, it is good practice to record an additional image at a damage-sensitive photon energy after any exposure-intensive measurement (*e.g.* a long stack) to check for excessive radiation damage. If the additional damage check image appears the same or only slightly different from an image recorded prior to the extensive analytical measurement, then the dose involved can be deemed acceptable (Wang *et al.*, 2009a). Such a check does not require that the dose be known, only that it did not significantly compromise the measurement.

The onset of negative mode at 300 eV was measured at 5.3.2.2, 11.0.2, 10ID-1, X07DA and UE46. Identical annealed samples and development procedures were used for these experiments. In each experiment the I_0 values were recorded, nine area patterns were executed with various dwell times, and the exposure time for the onset of negative mode was identified from an atomic force micrograph of the developed sample. The dose was then calculated with the assumption that the detector efficiencies at 300 eV at all STXMs were identical to that measured at 5.3.2.2. Under this assumption the dose values at which the onset of negative mode occurred differed among the various STXMs by more than an order of magnitude. Given the constant sample development conditions, dose rate and polarization independence, and that PMMA has been used as a stable and accurate dosimeter in other applications for over 40 years, an assumption was made that the dose for the onset of negative mode at 300 eV is an intrinsic value. Equation (1) was rearranged to solve for detector efficiency with 90 MGy as the value of D . The values for the detector efficiency at all the STXMs were then calculated based on this method (Table 2). In a separate and independent study, the efficiency of the avalanche photodiode detector at UE46 had been recently determined to be 4% at 300 eV by calibration against a GaAs photodiode [G1127-04, Hamamatsu (Weigand, 2012)]. With no prior knowledge of that measurement, the value obtained by our PMMA-based method matched the value determined by the photodiode method, confirming the validity of this approach.

Table 2

Measured detector efficiency (K) at 300 eV for various STXMs (measurements made between October 2010 and December 2011).

STXM	K (%)
5.3.2.2	35
11.0.2	10
10ID-1	74
X07DA	1.2
UE46	4.0

There could be several reasons why detector efficiency can differ between otherwise similar scintillator-PMT detectors. Different scintillator materials used in this application have different properties (Fakra *et al.*, 2004), and the length and face smoothness of the Lucite tubes may not be equal. Although the detectors were centered on the optical axis and the active area accepted the full bright-field signal, the detector-to-sample distance could differ by as much as 1.5 mm. However, this is expected to have a negligible effect on the detector efficiency measurements as the transmission of 300 eV X-rays through 1.5 mm of 250 torr He used in these experiments is 97.7% (Henke *et al.*, 1993). The detector, like the sample, experiences carbon contamination which degrades its performance over time. The scintillator can be contaminated and/or physically damaged by accidental contact while mounting samples. At 5.3.2.2 the scintillator is changed on a regular basis (~annually). However, the detector efficiency at 5.3.2.2 has been measured several times by our onset of negative mode method over the last three years and at 11.0.2 over the last year. The detector efficiency at each STXM had not changed significantly during those periods even though the scintillator coatings had been replaced numerous times and there were significant changes in the beamline intensity for otherwise standard slit settings, owing to changes in the storage ring and beamline optics. Nevertheless, detector efficiency values are likely to be subject to change over time. Uncertainty in the measurement of the detector efficiency is a likely reason why the critical doses for the same polymer measured in different STXMs do not match.

The common method of determining the detector efficiency of a STXM is by comparing the response of an uncharacterized detector with that of a calibrated photodiode. With current STXM designs this requires exchanging detectors which is disruptive and time-consuming; therefore the onset of the negative mode method could be an attractive complement. PMMA films are easy to make, cheap and stable for long periods of time: a time delay as long as two months between dosing and development did not affect the results, and two-year-old samples stored in a laboratory drawer in gelatin capsules gave consistent results. PMMA is insensitive to visible light [$\lambda \geq 260$ nm (Lin, 1975)]. Although M_w and M_n have not been found to affect the radiation sensitivity of PMMA (Broers, 1988), variations in M_w and M_n do affect the development characteristics. M_w values of less than 5×10^5 but greater than 5×10^4 g mol⁻¹ show ideal overall performance (Dobisz *et al.*, 2000). Ideally, annealed samples with the same M_w as that used in this work should be used.

research papers

In this report several factors which were thought to affect the sensitivity of PMMA were investigated, but we cannot rule out the possible existence of other factors. A photon energy dependence has been discussed in the literature (Coffey *et al.*, 2002; Beetz & Jacobsen, 2003). Radiation sensitivity may be different below the first core ionization level (where the decay of the primary electronic excited states is *via* direct processes) relative to above the core edge, where the two-electron Auger process dominates the core hole decay (Egerton *et al.*, 2004). However, Fujii & Yokoya (2009) irradiated DNA thin films at photon energies of 395, 408, 528 and 538 eV and found no effect on the damage yields. Some of the published critical doses for PMMA were measured at damage energies different than the 300 eV chosen here. Experiments are currently underway to determine the effect of photon energy variation on the radiation sensitivity of polymers.

5. Conclusions

Several factors which were thought to affect critical dose for radiation damage to PMMA at 300 eV were tested including pre-exposure thermal treatments, dose rate and X-ray polarization. None affected quantitative aspects (increase or decrease in spectral signals and chemical change for a given dose). Some qualitative effects did depend on pre-exposure thermal treatments. The most significant sources of dose quantitation error in prior work appear to be the method in which the doses are measured and inadequate characterization of detector efficiency. The onset of negative mode (cross-linking) was found to be very reproducible and easily measured. Measurement of the exposure needed to initiate negative mode is proposed as a simple and accurate means to calibrate detector efficiency and thus establish reliable dose and dose-rates scales in STXMs.

Note added in proof. PMMA also has a positive mode (*i.e.* full removal of PMMA from the irradiated area after development) threshold dose, which was previously determined to be 1 MGy (Leontowich & Hitchcock, 2011). Very recently, we performed a detector efficiency measurement at the ALS STXM 5.3.2.1 using the positive mode threshold dose and the method described in §4.5. The efficiency of the 5.3.2.1 scintillator-PMT detector was found to be 100% at 1 keV. The positive mode threshold dose was not as precise (within 10–15%) as the negative mode threshold dose (within 5%).

This research was supported by the Natural Sciences and Engineering Research Council (NSERC, Canada), the Canadian Foundation for Innovation (CFI) and the Canada Research Chairs program. We thank all the staff scientists at the various facilities for their expert support and assistance, including Benjamin Watts and Jörg Raabe (SLS), Yingshen Lu and James Dynes (CLS), and David Kilcoyne (ALS). Frank Gibbs is thanked for performing the TGA measurement. The ALS is supported by the Director, Office of Energy Research, Office of Basic Energy Sciences, Materials Sciences Division of the US Department of Energy, under Contract No. DE-AC02-05CH11231. The CLS is supported by NSERC, CIHR,

NRC and the University of Saskatchewan. The PolLux end-station was financed by the German Minister für Bildung und Forschung (BMBF), contract 05 KS4We1/6. This report contains data created at the MAXYMUS STXM of the Department Schütz, MPI-IS Stuttgart at BESSY II, Berlin. AFGL acknowledges support from an ALS doctoral fellowship in residence and the CLS graduate student travel support program.

References

- Ade, H. & Hitchcock, A. P. (2008). *Polymer*, **49**, 643–675.
- Arjmandi, N., Lagae, L. & Borghs, G. (2009). *J. Vac. Sci. Technol. B*, **27**, 1915–1918.
- Barrett, J. H. (1982). *Int. J. Appl. Radiat. Isot.* **33**, 1177–1187.
- Beetz, T. & Jacobsen, C. (2003). *J. Synchrotron Rad.* **10**, 280–283.
- Brewer, G. R. (1980). *Electron-Beam Technology in Microelectronic Fabrication*, p. 219. New York: Academic Press.
- Broers, A. N. (1981). *J. Electrochem. Soc.* **128**, 166–170.
- Broers, A. N. (1988). *IBM J. Res. Dev.* **32**, 502–513.
- Charlesby, A. & Ross, M. (1953). *Nature (London)*, **171**, 1153.
- Coffey, T., Urquhart, S. G. & Ade, H. (2002). *J. Electron Spectrosc. Relat. Phenom.* **122**, 65–78.
- Cosslett, V. E. (1978). *J. Microsc.* **113**, 113–129.
- Dobisz, E. A., Brandow, S. L., Bass, R. & Mitterender, J. (2000). *J. Vac. Sci. Technol. B*, **18**, 107–111.
- Dobisz, E. A., Brandow, S. L., Snow, E. & Bass, R. (1997). *J. Vac. Sci. Technol. B*, **15**, 2318–2322.
- Egerton, R. F. (1980). *Ultramicroscopy*, **5**, 521–523.
- Egerton, R. F. (1982). *J. Microsc.* **126**, 95–100.
- Egerton, R. F., Li, P. & Malac, M. (2004). *Micron*, **35**, 399–409.
- Fakra, S., Kilcoyne, A. L. D. & Tyliszczak, T. (2004). *AIP Conf. Proc.* **705**, 973–976.
- Follath, R., Schmidt, J. S., Weigand, M. & Fauth, K. (2010). *AIP Conf. Proc.* **1234**, 323–326.
- Fragalà, M. E., Compagnini, G. & Puglisi, O. (1999). *J. Mater. Res.* **14**, 228–231.
- Frommherz, U., Raabe, J., Watts, B., Stefani, R. & Ellenberger, U. (2010). *AIP Conf. Proc.* **1234**, 429–432.
- Fryer, D. S., Peters, R. D., Kim, E. J., Tomaszewski, J. E., Pablo, J. J., Nealey, P. F., White, C. C. & Wu, W. (2001). *Macromolecules*, **34**, 5627–5634.
- Fujii, K. & Yokoya, A. (2009). *Radiat. Phys. Chem.* **78**, 1188–1191.
- Greeneich, J. S. (1975). *J. Electrochem. Soc.* **122**, 970–976.
- Haglund, R. F. Jr (1996). *Appl. Surf. Sci.* **96–98**, 1–13.
- Hajimoto, Y., Tamura, N. & Okamoto, S. (1965). *J. Polym. Sci. A*, **3**, 255–263.
- Hall, E. J. & Giaccia, A. J. (2006). *Radiobiology for the Radiobiologist*, 6th ed. Philadelphia: Lippincott Williams and Wilkins.
- Henke, B. L., Gullikson, E. M. & Davis, J. C. (1993). *At. Data Nucl. Data Tables*, **54**, 181–342.
- Hiraoka, H. (1977). *IBM J. Res. Dev.* **21**, 121–130.
- Hitchcock, A. P. (2012). *Handbook of Nanoscopy*, Vol. 2, edited by G. V. Tendeloo, D. V. Dyck and S. J. Pennycook, ch. 22. New York: Wiley.
- Howells, M., Jacobsen, C. & Warwick, T. (2007). *Science of Microscopy*, Vol. 2, ch. 13, edited by P. W. Hawkes and J. C. H. Spence. New York: Springer Science + Business Media.
- Hubbell, J. H., Gimmi, H. A. & Øverbø, I. (1980). *J. Phys. Chem. Ref. Data*, **9**, 1023–1147.
- Hutchings, I. R., Richards, R. W., Thompson, R. L., Clough, A. S. & Langridge, S. (2001). *J. Polym. Sci. B*, **39**, 2351–2362.
- Jacobsen, C., Wirick, S., Flynn, G. & Zimba, C. (2000). *J. Microsc.* **197**, 173–184.
- Jiang, N. & Spence, J. C. H. (2012). *Ultramicroscopy*, **113**, 77–82.

research papers

- Kallweit, R., Baur, M., Eichinger, P. & Strack, H. (1991). *Nucl. Instrum. Methods Phys. Res. B*, **59/60**, 1288–1291.
- Katoh, T. & Zhang, Y. (1998). *J. Synchrotron Rad.* **5**, 1153–1156.
- Kaznatcheev, K. V., Karunakaran, Ch., Lanke, U. D., Urquhart, S. G., Obst, M. & Hitchcock, A. P. (2007). *Nucl. Instrum. Methods Phys. Res. A*, **582**, 96–99.
- Keymeulen, H. R., Diaz, A., Solak, H. H., David, C., Pfeiffer, F., Patterson, B. D., Veen, J. F., Stoykovich, M. P. & Nealey, P. F. (2007). *J. Appl. Phys.* **102**, 013528.
- Kilcoyne, A. L. D. & Tylliszczak, T. (2004). *AIP Conf. Proc.* **705**, 605–607.
- Kilcoyne, A. L. D., Tylliszczak, T., Steele, W. F., Fakra, S., Hitchcock, P., Franck, K., Anderson, E., Harteneck, B., Rightor, E. G., Mitchell, G. E., Hitchcock, A. P., Yang, L., Warwick, T. & Ade, H. (2003). *J. Synchrotron Rad.* **10**, 125–136.
- King, M. C. & Laidler, K. J. (1984). *Arch. Hist. Exact Sci.* **30**, 45–86.
- Kunz, K. & Stamm, M. (1996). *Macromolecules*, **29**, 2548–2554.
- Leiros, H.-K. S., Timmins, J., Ravelli, R. B. G. & McSweeney, S. M. (2006). *Acta Cryst.* **D62**, 125–132.
- Leontowich, A. F. G. & Hitchcock, A. P. (2011). *Appl. Phys. A*, **103**, 1–11.
- Leontowich, A. F. G. & Hitchcock, A. P. (2012a). *Analyst*, **137**, 370–375.
- Leontowich, A. F. G. & Hitchcock, A. P. (2012b). *J. Vac. Sci. Technol. B*, **30**, 030601.
- Leontowich, A. F. G., Tylliszczak, T. & Hitchcock, A. P. (2011). *Proc. SPIE*, **8077**, 80770N.
- Lin, B. J. (1975). *J. Vac. Sci. Technol.* **12**, 1317–1320.
- Makimura, T., Torii, S., Okazaki, K., Nakamura, D., Takahashi, A., Niino, H., Okada, T. & Murakami, K. (2011). *Proc. SPIE*, **8077**, 80770F.
- Manring, L. E. (1989). *Macromolecules*, **22**, 2673–2677.
- Moreau, W. M. (1988). *Semiconductor Lithography: Principles, Practices and Materials*, ch. 7. New York: Plenum Press.
- Plaček, V., Bartonček, B., Hnát, V. & Otáhal, B. (2003). *Nucl. Instrum. Methods Phys. Res. B*, **208**, 448–453.
- Puglisi, O., Fragalà, M. E., Lynn, K. G., Petkov, M., Weber, M., Somoza, A., Dupasquier, A. & Quasso, F. (2001). *Nucl. Instrum. Methods Phys. Res. B*, **175–177**, 605–609.
- Raabe, J., Tzvetkov, G., Flechsig, U., Böge, M., Jaggi, A., Sarafimov, B., Vernooij, M. G., Huthwelker, T., Ade, H., Kilcoyne, D., Tylliszczak, T., Fink, R. H. & Quitmann, C. (2008). *Rev. Sci. Instrum.* **79**, 113704.
- Ross, M. & Charlesby, A. (1953). *Atom. Atom. Tech.* **4**, 189–194.
- Rück, D. M., Brunner, S., Frank, W., Kulisch, J. & Franke, H. (1992). *Surf. Coatings Tech.* **51**, 318–323.
- Rück, D. M., Schulz, J. & Deusch, N. (1997). *Nucl. Instrum. Methods Phys. Res. B*, **131**, 149–158.
- Schrempel, F., Kim, Y. & Witthuhn, W. (2002). *Appl. Surf. Sci.* **189**, 102–112.
- Schrempel, F. & Witthuhn, W. (1997). *Nucl. Instrum. Methods Phys. Res. B*, **132**, 430–438.
- Teh, W. H., Liang, C., Graham, M. & Smith, C. G. (2003). *J. Microelectromech. Sys.* **12**, 641–648.
- Tylliszczak, T., Warwick, T., Kilcoyne, A. L. D., Fakra, S., Shuh, D. K., Yoon, T. H., Brown, G. E. Jr, Andrews, S., Chembrolu, V., Strachan, J. & Acremann, Y. (2004). *AIP Conf. Proc.* **705**, 1356–1359.
- Wang, J. (2008). *Radiation Chemistry by Soft X-ray Spectromicroscopy*, Appendix A. Hamilton: McMaster University.
- Wang, J., Botton, G. A., West, M. M. & Hitchcock, A. P. (2009b). *J. Phys. Chem. B*, **113**, 1869–1876.
- Wang, J., Morin, C., Li, L., Hitchcock, A. P., Scholl, A. & Doran, A. (2009a). *J. Electron Spectrosc. Relat. Phenom.* **170**, 25–36.
- Wang, J., Stöver, H. D. H., Hitchcock, A. P. & Tylliszczak, T. (2007). *J. Synchrotron Rad.* **14**, 181–190.
- Weigand, M. (2012). In preparation.
- Zhang, X., Jacobsen, C., Lindaas, S. & Williams, S. (1995). *J. Vac. Sci. Technol. B*, **13**, 1477–1483.

Supplemental material for
Accurate dosimetry in scanning transmission X-ray microscopes via
the cross-linking threshold dose of poly(methyl methacrylate)

Adam F. G. Leontowich^{a*}, Adam P. Hitchcock^a, Tolek Tyliszczak^b, Markus Weigand^c, Jian Wang^d and Chithra Karunakaran^d

^aBrockhouse Institute for Materials Research, McMaster University, 1280 Main Street West, Hamilton, Ontario, L8S 4M1, Canada, ^bAdvanced Light Source, Lawrence Berkeley National Laboratory, One Cyclotron Road MS 6R2100, Berkeley, California, 94720, USA, ^cMax Planck Institute for Intelligent Systems, Stuttgart, Baden-Württemberg, 70569, Germany, and ^dCanadian Light Source Inc., 101 Perimeter Road, Saskatoon, Saskatchewan, S7N 0X4, Canada

Correspondence email: leontoaf@mcmaster.ca

1. Create *.xyt files for the PatternGen routine within STXM_Control

- Using a graphics program such as Microsoft Paint, create a black and white *.gif file. With the current version of STXM_Control, an uncontrolled exposure is made at the bottom left and top right of patterns. Intentionally adding an extra single pixel at the bottom left and top right of the *.gif image keeps these unintended exposures away from the desired pattern.
- Read the *.gif file into the program aXis2000 (Read → Images → Graphics → GIF → Data).
- Resize the image (Images → Set XY scale).
- Set the pixel size by remeshing (Utilities → Change mesh).
- Threshold mask the image so the pixel values fall between 0 and 1 (Images → Generate mask → Threshold, or Images → Multiply/divide).
- Write out the *.xyt file (Write → ALS-xyt).

Note that there is a limit to number of records in *.xyt files (i.e. points in the pattern). STXM_Control will crash if an *.xyt file with greater than 20000 records is executed. Individual pixel exposure times and positions can also be manually adjusted by opening the *.xyt file in a program such as Microsoft Notepad.

2. Execution of *.xyt files with the PatternGen routine within STXM_Control

- With the shutter set to AUTO, initiate a PatternGen scan in STXM_Control.
- Select the desired *.xyt file.

- Manually select the pattern origin point. The sample will be patterned beginning at this point from left to right and bottom to top.
- Choose a time multiplier value. For example, if all pixel values in the *.xyt file are between 0 or 1, and a time multiplier value of 300 is entered, the pixel exposure times will be between 0 and 300 ms. 10000 ms is the maximum multiplier value. In addition, the minimum time the shutter can go from closed to open to closed is about 1 ms.
- Estimate the time it will take to complete the pattern before executing by multiplying the number of pixels by the dwell time per pixel.

3. Derivation of a convenient form of the photon absorption rate

The photon absorption rate F is,

$$F = I_0 - I \quad (\text{Eqn. 2})$$

Transmission T is,

$$T = \frac{I}{I_0} \quad (\text{Eqn. 6})$$

Rearranging,

$$I = T(I_0) \quad (\text{Eqn. 7})$$

Subbing Eqn. 7 into Eqn. 2,

$$F = I_0 - T(I_0) \quad (\text{Eqn. 8})$$

Rearranging,

$$F = I_0(1 - T) \quad (\text{Eqn. 9})$$

Optical density OD is,

$$OD = -\ln \frac{I}{I_0} \quad (\text{Eqn. 10})$$

It follows that,

$$e^{-OD} = \frac{I}{I_0} = T \quad (\text{Eqn. 11})$$

Eqn. 3 is the result of subbing Eqn. 11 into eqn. 9.

$$F = I_0(1 - e^{-OD}) \quad (\text{Eqn. 3})$$

Supplemental figures

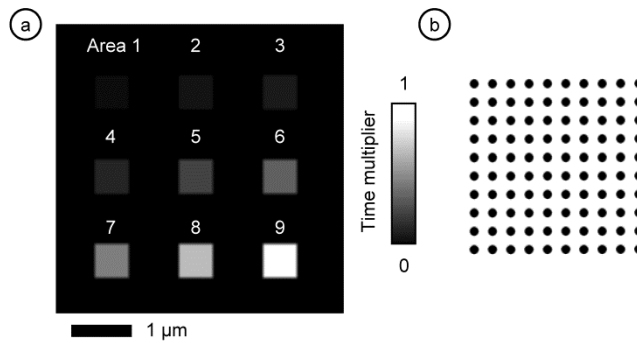


Figure S-1: a) The input file used for all patterning experiments. The white numbering serves to identify the areas and is not a part of the file. The dimensions of each square are 600 nm x 600 nm. b) Each square in a) consists of 10 x 10 individual exposures with a pitch of 60 nm.

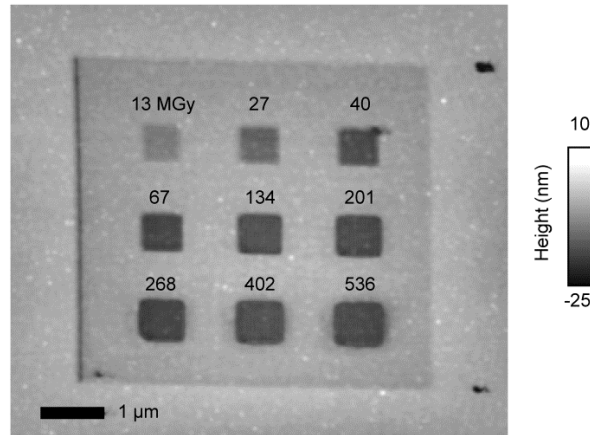


Figure S-2: Atomic force micrograph of a patterned area that had been previously imaged by STXM. The image parameters were 50/25/25 slits, 288.4 eV, 2 ms dwell time, 60 nm pixel size; the dose associated with collecting the image was 1 MGy. The nine area pattern was executed within the area that had been STXM imaged. The outline of the single STXM image is visible, and the dose associated with it caused a 2 nm reduction in height.

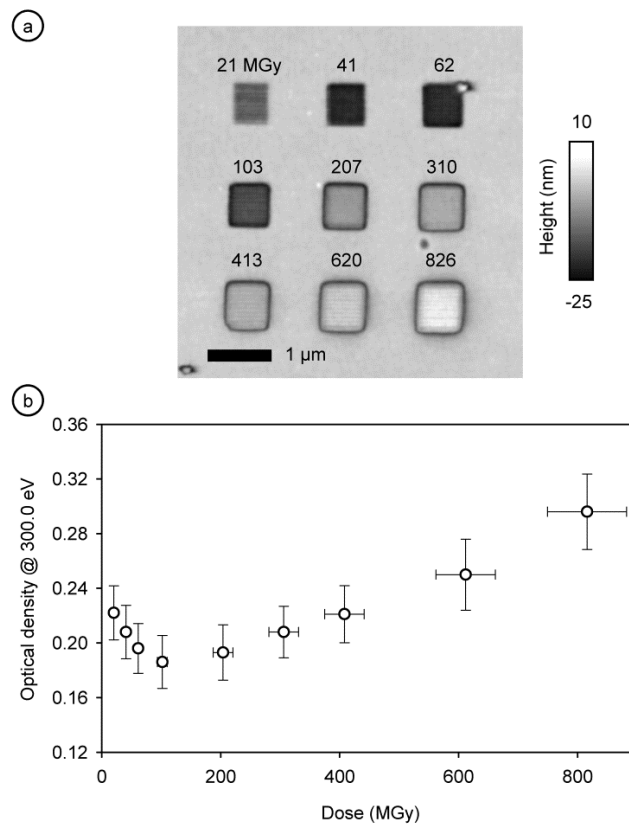


Figure S-3: a) Atomic force micrograph of as-spun PMMA, patterned with 10ID-1. The patterned areas initially decrease and then increase with increasing dose due to carbon contamination. b) STXM OD at 300 eV measurements of each area in a) plotted versus dose. The carbon signal rises with dose, even above the virgin PMMA film.

Chapter 8

Secondary electron deposition mechanism of carbon contamination

Signs of carbon contamination were observed in some STXM experiments performed in this thesis. Some of these observations were reported in Chapter 7. This chapter presents results of experiments which were expressly designed to illuminate the mechanism of carbon contamination.

Reprinted with permission from the Journal of Vacuum Science and Technology B, Microelectronics and Nanometer Structures: Processing, Measurement, and Phenomena 2012, 30, 030601, A.F.G. Leontowich, A.P. Hitchcock. DOI: 10.1116/1.3698602, © 2012 American Vacuum Society.

The author of this thesis conceived the experiments, prepared all samples, performed all the experiments, analyzed the data, wrote the manuscript which was edited by A.P. Hitchcock and served as corresponding author.

LETTERS

Secondary electron deposition mechanism of carbon contamination

Adam F. G. Leontowich^{a)} and Adam P. Hitchcock

Brockhouse Institute for Materials Research, McMaster University, Hamilton, Ontario L8S 4M1, Canada

(Received 30 January 2012; accepted 13 March 2012; published 30 March 2012)

Deposition of a carbonaceous contaminant layer on surfaces exposed to radiation exceeding 7–10 eV is ubiquitous in many fields of research. The mechanism of this deposition process is still debated. A scanning transmission x-ray microscope has been used to create and interrogate carbonaceous deposits with photon energies spanning the C 1s ionization edge. For equal fluence, the rate of carbon deposition is proportional to the x-ray absorption spectrum of the deposited material. The results are consistent with a deposition mechanism involving secondary electrons. Implications of this measurement with regard to future generations of high volume photolithography are discussed. © 2012 American Vacuum Society. [<http://dx.doi.org/10.1116/1.3698602>]

I. INTRODUCTION

The step from the generally non-ionizing or only weakly ionizing light sources of 193 nm (6.4 eV) presently used in photolithographic tools for high volume integrated circuit production, to strongly ionizing light sources of 13.5 nm (92 eV) being introduced for extreme ultraviolet (EUV) lithography has the potential to introduce serious contamination issues due to radiation-induced cracking and deposition of carbonaceous molecules.^{1,2} The precursor molecules for such contamination originate from a wide variety of sources (lubricants, outgassing, atmosphere, etc.), and become fixed to surfaces as a carbonaceous layer when irradiated with ionizing radiation. This phenomenon is common to diverse technologies that involve high energy radiation (electron microscopy,^{3–5} x-ray photoelectron spectroscopy,⁶ synchrotron and free electron laser beamlines,^{7–9} space-based telescopes^{10–13}). The carbonaceous deposits are often highly undesirable as they can degrade the transmissive or reflective properties of optics, introduce spectroscopic artifacts, and/or decrease the efficiency of detectors. With regards to EUV lithography, the carbonaceous layer has been observed to decrease reflected intensity, distort the wavefront,¹⁴ and change the optical path length,⁹ all conceivably capable of introducing defects in the devices produced and reducing throughput. Several methods of cleaning carbonaceous deposits from delicate optics exist.^{2,5,8,11,12,15–17} The results are sometimes mixed,^{8,9,12} but in certain cases the reflectance can be fully recovered,¹⁵ and an optic can survive multiple cleaning cycles.¹⁷ In practice, the contamination processes can be mitigated,^{5,7,18} but often cannot be totally eliminated, and cleaning processes entail some instrument downtime, which ultimately reduces productivity. The precise mechanism of deposition is a matter of debate. A mechanism based on secondary electrons (SEs) produced by the irradiated surface is the most established.⁷ However,

Hollenshead and Klebanoff concluded that the dominant mechanism of deposition is direct photoabsorption by the adsorbed precursor molecules, and that the SE mechanism plays an insignificant role.¹⁹ In this Letter, the relationship between the rate of carbon deposition and photon energy is probed in the vicinity of the C 1s (*K*) ionization edge to illuminate the mechanism of deposition.

II. EXPERIMENT

Scanning transmission x-ray microscopes (STXMs)^{20,21} routinely focus monochromatic soft x-ray photons (60–2500 eV) into an intense, sub-30 nm full width half maximum spot at the focal plane. Carbon deposits tens of nanometers thick can be created on surfaces within seconds to minutes. The Advanced Light Source (ALS) STXM 5.3.2.2²⁰ at Lawrence Berkeley National Laboratories was used to create carbon deposits on an initially clean 75 nm thick Si₃N₄ surface. With a STXM, one can accurately control and rapidly vary the conditions of deposition, such as photon energy (with a bandwidth as low as 0.05 eV), area irradiated, fluence [photons/s (s⁻¹) × dwell time (s) × photon energy (J)/area (nm²)] and fluence rate. The STXM 5.3.2.2 chamber is a low vacuum environment, capable of only 10⁻⁶ Torr. For these experiments, the chamber was evacuated then backfilled with 250 Torr He. Areas of 600 nm × 600 nm consisting of 10 × 10 single pixel exposures were irradiated to form the deposits. The thickness of the deposited material was quantified by two techniques; measuring the maximum height of the deposit by atomic force microscopy [(AFM) ± 1 nm], and measuring the average optical density [(OD) ± 0.02] at 293 eV of the center of the deposit with the STXM. The precursor molecules for the deposits created here probably include those which originate partly within the STXM chamber (lubricants from mechanical stages, outgassing, or ablated organics from previous samples), and partly outside the chamber (fingerprints, venting the chamber to atmosphere, double-sided tape and epoxy used to mount samples).

^{a)}Electronic mail: leontoaf@mcmaster.ca

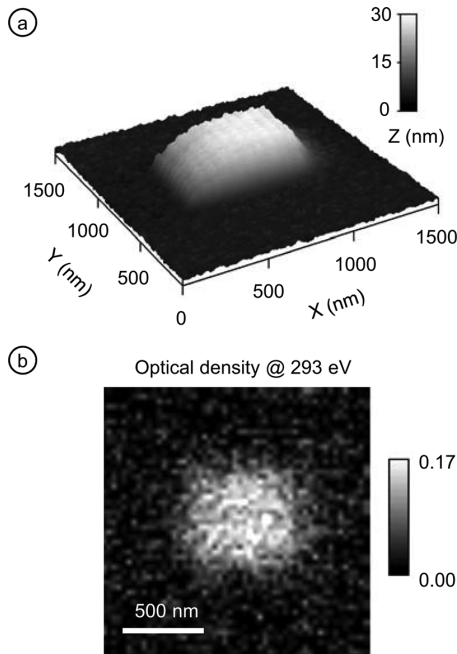


Fig. 1. Images of a 600 nm \times 600 nm carbon deposit created by focused 300 eV soft x rays of a scanning transmission x-ray microscope (STXM), recorded by (a) atomic force microscopy in tapping mode, and (b) STXM at 293 eV [transmission measurement converted to optical density (OD)].

III. RESULTS AND DISCUSSION

Several carbon deposits were made at the specific photon energy of 300 eV with increasing fluence. These deposits were imaged and quantified by AFM and STXM (Fig. 1). The rate of deposition observed was directly proportional to fluence (Fig. 2), which is consistent with the observations of others.^{7,15,18,19} The fluence involved in collecting single images for OD measurements was 0.5 ± 0.1 mJ/cm².

A near edge x-ray absorption fine structure (NEXAFS) spectrum of the carbon deposit material in the C 1s NEXAFS region (Fig. 3) was collected with the STXM in a second mode of operation where the sharp focus was maintained on

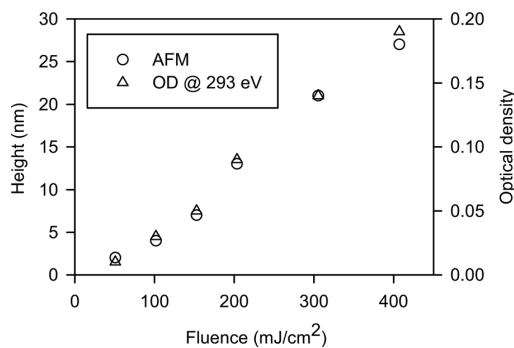


Fig. 2. Amount of carbonaceous material deposited at a single energy (300 eV) vs fluence, quantified by atomic force microscopy (circles) and STXM (OD at 293 eV, triangles).

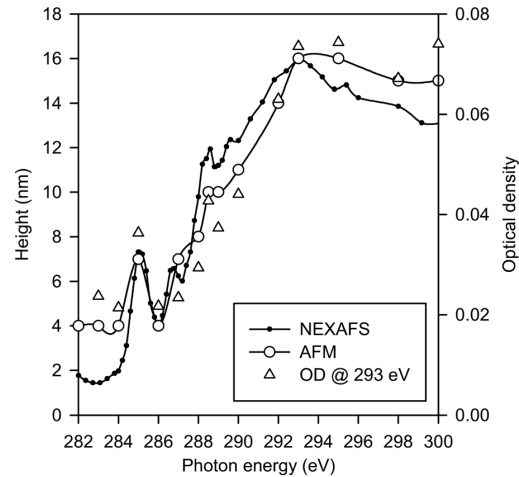


Fig. 3. C 1s x-ray absorption (NEXAFS) spectrum of a carbon deposit (dots) compared to the amount of carbonaceous material deposited at constant fluence (395 ± 13 mJ/cm²) at several specific photon energies, quantified by atomic force microscopy (circles) and STXM (OD at 293 eV, triangles).

the carbon deposit while the monochromator energy was scanned. The fluence involved in collecting this spectrum was 24 ± 5 mJ/cm². The spectrum shows a sharp feature at 285 eV, indicative of C=C bonds, a feature at 288.5 eV potentially indicative of C=O bonds, and a broad absorption maximum near 293 eV. NEXAFS spectra of carbon deposits made by the same method using another STXM [Canadian Light Source (CLS) beamline 10ID-1] under the same conditions were identical. The spectra of the carbon deposits at both the ALS and CLS are similar to a reported C 1s NEXAFS spectrum of carbon deposited in a system expressly designed to evaluate contamination rates and phenomena for EUV optics.²² It appears that beam-deposited carbonaceous material tends to have the same chemistry and thus a similar spectrum, independent of the precursor material.

Areas were then irradiated at specific photon energies spanning the C 1s NEXAFS region, forming carbon deposits as a function of photon energy (Fig. 3). Each area irradiated received the same fluence of 395 ± 13 mJ/cm². The fluence rate available at each energy differed between 74 and 388 mJ/cm²/s due to carbon contamination on the beamline and STXM optics; therefore the dwell times were varied to establish the desired fixed total fluence condition. In a separate experiment, the thickness of deposits made at specific photon energies at the same total fluence was observed to be independent of fluence rate over the same 74–388 mJ/cm²/s range. Figure 3 shows that, for constant fluence, the rate of carbon deposition is strikingly proportional to the C 1s NEXAFS spectrum of the carbon deposit material. Most notably, the prominent spectral feature at 285 eV is reflected in the quantity of material deposited; the deposition rate at 285 eV is significantly greater than at 284 or 286 eV, in accord with the spectrum. The maximum deposition rate occurred at 293 eV, coinciding with the maximum absorption cross section of the carbon deposit material.

IV. SUMMARY AND CONCLUSIONS

The number of SEs emitted by a substance irradiated with x-rays is proportional to its x-ray absorption spectrum, which is the basis of the total electron yield (TEY) acquisition mode.²³ Note that this approximation is widely accepted to be valid over short photon energy ranges, such as that in Fig. 3, but careful examination over large energy spans indicates that it is necessary to take into account other factors, in particular photon energy variations in the number of primary electrons produced, in order to have a fully quantitative agreement.²⁴ The results are consistent with a deposition mechanism primarily involving SEs. The rate of carbon deposition follows the spectrum of the carbon deposit material because the deposition process is driven by SEs emitted by the surface, and the surface rapidly becomes deposited carbon once the deposition is initiated. For an equal fluence, the number of SEs emitted by the carbon deposit when irradiated at 285 eV is significantly higher than at 284 or 286 eV, which leads to the higher deposition rate at that particular photon energy. For deposits less than about 4 nm thick (less than the escape depth), the SE emission of the underlying surface (Si₃N₄ in this case) should play a greater role, which may be why the data points in the pre-edge region of Fig. 3 are higher than the NEXAFS spectrum. If the mechanism of deposition was primarily direct photoabsorption by the adsorbed precursor molecules, the rate of deposition should be closely linked to the C 1s NEXAFS spectra of saturated hydrocarbons^{23,25} which do not contain features at 285 eV and have very prominent absorption features between 287 and 289 eV. This is not what was observed.

This result suggests a possible contamination mitigation strategy: For a given photon energy, the irradiated surface with the lowest TEY should display the lowest deposition rate. Ru, widely used as a capping layer for 13.5 nm EUV optics, conveniently approaches a minimum electron yield value around 13.5 nm. This minimum in TEY has been hypothesized as a reason why Ru performs so well in this role.¹⁸ However, this mitigation strategy would only be effective until a carbon contamination layer of a few nanometers forms.

What are the implications of these results for high volume photolithography? The industry standard photon energy (wavelength) used for the critical layers has increased (decreased) stepwise over time,²⁶ which has been a major reason why the size of integrated circuits and the devices that employ them have steadily decreased while performance has increased. This “wavelength scaling” is expected by some to continue²⁷ beyond the expected to be state-of-the-industry of 13.5 nm; research and development is already under way on a second generation of sources and optics for sub-10 nm “beyond EUV” systems. Early candidate wavelengths include 6.7, 3.37, and 2.48 nm.²⁷ The first two of these wavelengths approach the C 1s ionization edge, while the third exceeds it. We have shown that for equal fluence, the rate of carbon deposition is roughly four times higher above the edge than below it. This work indicates that, if future high volume photolithography tools operate at a

wavelength at or above the C 1s edge, the rate of carbon deposition on the optics will increase substantially. Perhaps the increase in deposition rate might be offset by an increase in resist sensitivity, if C-based photoresists continue to be used, as the x-ray absorption cross section will increase above the C 1s edge for all C-based materials. The composition of the resists remains an open question, even for 13.5 nm. Early identification of challenges in wavelength scaling will narrow the choices, and ultimately decrease the time necessary to develop and implement new technology.

ACKNOWLEDGMENTS

This research was funded by NSERC, CFI, and the Canada Research Chairs program and carried out at ALS beamline 5.3.2.2 and CLS beamline 10ID-1. The authors thank David Kilcoyne and Tolek Tyliczszak for support at the ALS and Jian Wang, Yingshen Lu, and Chithra Karunakaran for support at the CLS. The ALS is supported by the Director, Office of Science, Office of Basic Energy Sciences, of the U.S. Department of Energy under Contract No. DE-AC02-05CH11231. The CLS is supported by NSERC, CIHR, NRC, and the University of Saskatchewan. A.F.G.L. acknowledges the support of an ALS doctoral fellowship in residence.

- ¹R. L. Stewart, *Phys. Rev.* **45**, 488 (1933).
- ²S. Bajt, in *EUV Lithography*, edited by V. Bakshi (SPIE, Bellingham, WA, 2009), pp. 227–259.
- ³J. Hillier, *J. Appl. Phys.* **19**, 226 (1948).
- ⁴P. Roediger, H. D. Wanzenboeck, G. Hochleitner, and E. Bertagnolli, *J. Vac. Sci. Technol. B* **27**, 2711 (2009).
- ⁵A. E. Vladár, K. P. Purushotham, and M. T. Postek, *Proc. SPIE* **6922**, 692217 (2008).
- ⁶D. R. Cousens, B. J. Wood, J. Q. Wang, and A. Atrens, *Surf. Interface Anal.* **29**, 23 (2000).
- ⁷K. Boller, R.-P. Haelbich, H. Hogrefe, W. Jark, and C. Kunz, *Nucl. Instrum. Methods Phys. Res.* **208**, 273 (1983).
- ⁸R. A. Rosenberg, J. A. Smith, and D. J. Wallace, *Rev. Sci. Instrum.* **63**, 1486 (1992).
- ⁹S. Bajt *et al.*, *Proc. SPIE* **7361**, 73610J (2009).
- ¹⁰E. M. Wooldridge, NASA Technical Report No. 19980237489 (1998).
- ¹¹J. L. Tveekrem, D. B. Leviton, C. M. Fleetwood, and L. D. Feinberg, *Proc. SPIE* **2864**, 246 (1996).
- ¹²R. B. Gillette and B. A. Kenyon, *Appl. Opt.* **10**, 545 (1971).
- ¹³H. L. Marshall, A. Tennant, C. E. Grant, A. P. Hitchcock, S. L. O’Dell, and P. P. Plucinsky, *Proc. SPIE* **5165**, 497 (2004).
- ¹⁴A. Barty and K. A. Goldberg, *Proc. SPIE* **5037**, 450 (2003).
- ¹⁵K. Hamamoto *et al.*, *J. Vac. Sci. Technol. B* **23**, 247 (2005).
- ¹⁶R. W. C. Hansen, M. Bissen, D. Wallace, J. Wolske, and T. Miller, *Appl. Opt.* **32**, 4114 (1993).
- ¹⁷S. A. George, L. M. Baclea-an, P. P. Naulleau, R. J. Chen, and T. Liang, *J. Vac. Sci. Technol. B* **28**, C6E31 (2010).
- ¹⁸B. V. Yakshinsky, R. Wasielewski, E. Loginova, and T. E. Madey, *Proc. SPIE* **6517**, 65172Z (2007).
- ¹⁹J. Hollenshead and L. Klebanoff, *J. Vac. Sci. Technol. B* **24**, 64 (2006).
- ²⁰A. L. D. Kilcoyne *et al.*, *J. Synchrotron Radiat.* **10**, 125 (2003).
- ²¹M. Howells, C. Jacobsen, and T. Warwick, in *Science of Microscopy*, edited by P. W. Hawkes and J. C. H. Spence (Springer, Berlin, 2006), pp. 835–926.
- ²²M. Niibe *et al.*, *J. Vac. Sci. Technol. B* **25**, 2118 (2007).
- ²³J. Stöhr, *NEXAFS Spectroscopy* (Springer, Berlin, 1992).
- ²⁴H. Henneken, F. Scholze, and G. Ulm, *J. Appl. Phys.* **87**, 257 (2000).
- ²⁵A. Schöll, R. Fink, E. Umbach, G. E. Mitchell, S. G. Urquhart, and H. Ade, *Chem. Phys. Lett.* **370**, 834 (2003).
- ²⁶C. Wagner and N. Harned, *Nature Photon.* **4**, 24 (2010).
- ²⁷G. Tallents, E. Wagenaars, and G. Pert, *Nature Photon.* **4**, 809 (2010).

Chapter 9

Utility of the G value and the critical dose to soft x-ray radiation damage of polyacrylonitrile

This chapter presents our observations of radiation induced chemical changes of PAN and their kinetics. A misapplication of radiation damage sensitivity units in the literature was noted. PAN is used as an example to demonstrate this discrepancy and clarify the current situation. This work was submitted to the Journal of Physical Chemistry B on June 1, 2012. It is presented here in manuscript form.

The author of this thesis conceived the experiments, prepared all samples, performed all the experiments, analysed the data, wrote the manuscript with minor input from A.P. Hitchcock and served as corresponding author.

**Utility of the G value and the critical dose to soft x-ray radiation damage of
polyacrylonitrile**

*Adam F. G. Leontowich**

Department of Chemistry and Chemical Biology, McMaster University,

1280 Main Street West, Hamilton, ON, Canada L8S 4M1

(*) corresponding author: leontoaf@mcmaster.ca, v: +1.905.525.9140 x24864,

f: +1.905.521.2773

ABSTRACT: The sensitivity of organic matter to ionizing radiation is often reported in terms of a G value, and/or a critical dose value. Several reports exist where both a G value and a critical dose value have been derived from the same data set for a material when the behaviour of the signal chosen to represent its response to absorbed dose is described by first-order kinetics. In this report, the response of an x-ray absorption spectral feature of polyacrylonitrile to increasing doses of 300 eV soft x-rays is measured using a scanning transmission x-ray microscope and shown to undergo exponential decay. Both a G value and a critical dose value are derived, and the usefulness of each descriptor is discussed. The utility of G values was found to be greatly diminished in cases such as this and only a critical dose should be assigned.

KEYWORDS: STXM, NEXAFS, radiation sensitivity, damage rates

INTRODUCTION

When ionizing radiation interacts with soft condensed matter the amount of energy absorbed often induces chemical (bond formation and/or bond breakage) and physical (mass loss, morphology, carbon contamination) changes in the material.¹⁻⁴ The rapid degradation of radiation sensitive materials is undesirable for microscopic and/or spectroscopic investigations as the data collected may not be representative of the virgin sample. On the other hand, radiation-induced changes such as the main chain scission of poly(methyl methacrylate), are useful and relevant for patterning and lithography.^{5,6} Quantitation of radiation sensitivity (the absorbed dose required to produce a quantifiable change, following the Grotthuss–Draper law) is essential in many technologies which involve ionizing radiation and organic matter, such as medical device and food sterilization, macromolecular crystallography, and lithography.

At present there are two common single number descriptors of radiation sensitivity: The “critical dose”, and the “G value”. If the signal chosen to represent the response of the material diminishes exponentially as a function of dose (i.e. first-order kinetics), the rate can be described by the critical dose, which is the dose at which the signal is reduced to $1/e$ or 37% of its original value. Exponential decay of a signal with increasing dose is common to many fields, including radiobiology (where the concept of critical dose originated⁷), crystallography,^{8,9} electron¹⁰ and x-ray spectroscopy.^{4,10,11} This descriptor has also been termed the 37% dose (radiobiology) and the characteristic dose

(electron energy loss spectroscopy). The other descriptor of sensitivity, the G value, was introduced by Burton.¹² A G value is,

$$G = \frac{\text{yield}}{100 \text{ eV absorbed}} \quad (\text{Eqn. 1})$$

where yield is essentially the change in a signal chosen to represent the response of the material, normalized to 100 eV of energy absorbed. This unit was put forth to replace an even earlier and long since abandoned sensitivity descriptor “ M/N ”, where M is the number of molecules chemically transformed and N is the number of ions produced in the system.^{12,13} There are several reports where both a G value and a critical dose have been derived from the same data set for the same material when it is clear that the damage-sensitive signal displays first-order kinetics.⁹⁻¹¹ This paper reports quantitative measurement of the radiation-induced decrease of an x-ray absorption signal of polyacrylonitrile (PAN) using a scanning transmission x-ray microscope (STXM). The critical dose and G value are derived from the same data set and compared.

EXPERIMENTAL

A PAN ($M_w = 150\,000$, Sigma-Aldrich) film was fabricated by spin casting four drops of a 1.5% w/w PAN/ N,N -dimethylformamide (99.9% Chromasolv®, Sigma-Aldrich) solution onto a 1.5 cm x 1.5 cm piece of freshly cleaved mica (Ted Pella, Inc.), and then transferred onto a 75 nm thick Si_3N_4 window (Norcada Inc.) by the float method.¹⁴ The sample was then annealed at 80 °C

(above the glass transition temperature for thin PAN films but well below that of nitrile cyclization or degradation¹⁵) for 30 min at reduced pressure (2×10^{-2} Torr). The film thickness was determined to be 62 ± 3 nm by atomic force microscopy and NEXAFS spectroscopy using STXM.

The interferometrically controlled STXM 10ID-1¹⁶ at the Canadian Light Source (CLS, Saskatoon, Canada) was used to expose the film to 300 eV x-rays with dose accuracy and precision of better than 10%. Patterning was carried out with the STXM chamber filled with 250 Torr He, after evacuation of air. A 200 nm thick Ti strip, as well as a carefully selected and aligned order sorting aperture in combination with the central stop in the zone plate were used to suppress higher order radiation to negligible levels. Areas of the film were exposed using the PatternGen routine in the STXM_Control software. Details of STXM operation, patterning, dose calculation, determination of the detector efficiency, image and near edge x-ray absorption fine structure (NEXAFS) spectra acquisition are covered in greater depth elsewhere.^{17,18}

RESULTS AND DISCUSSION

A C 1s NEXAFS spectrum of a 62 ± 3 nm thick PAN film was collected using the STXM and is presented in Figure 1.

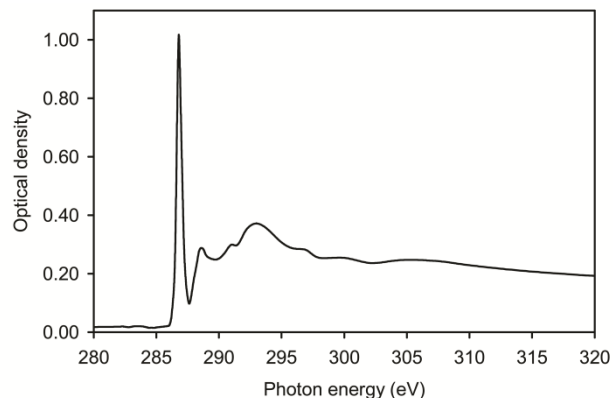


Figure 1: C 1s NEXAFS spectrum of a 62 ±3 nm PAN film. The prominent feature at 286.8 eV is the C 1s(C≡N) → π*_{C=N} core electron transition.

The spectrum is dominated by a large absorption feature at 286.8 eV which corresponds to the C 1s(C≡N) → π*_{C=N} core electron transition. Several 600 nm x 600 nm areas of the film were then exposed to 300 eV x-rays over a range of dwell times, corresponding to a range of absorbed doses from 8 – 700 MGy. An optical density (OD) image of several irradiated areas was collected using the STXM at 286.8 eV and is presented in Figure 2a. The irradiated areas display decreased contrast relative to non-irradiated areas. C 1s NEXAFS spectra of irradiated areas were obtained by collecting an image stack¹⁷ and averaging the signal from the central (60%) regions of these areas. Several of these spectra are overplotted in Figure 2b and depict the spectral changes of PAN with dose. As dose increases, the feature at 286.8 eV decreases while a new signal appears and grows at 285 eV. This C 1s → π*_{C=C} transition is indicative of the concomitant formation of C=C bonds. A shoulder at 287.6 eV, attributed to C 1s → π*_{C=N} transitions, also grows with dose. No significant trends were observed in the remaining photon energy region from 288 – 320 eV with dose up

to 700 MGy, indicating that PAN does not experience significant mass loss within this dose range. In addition, these processes and trends were found to be independent of dose rate over the range 54 – 952 MGy/s.

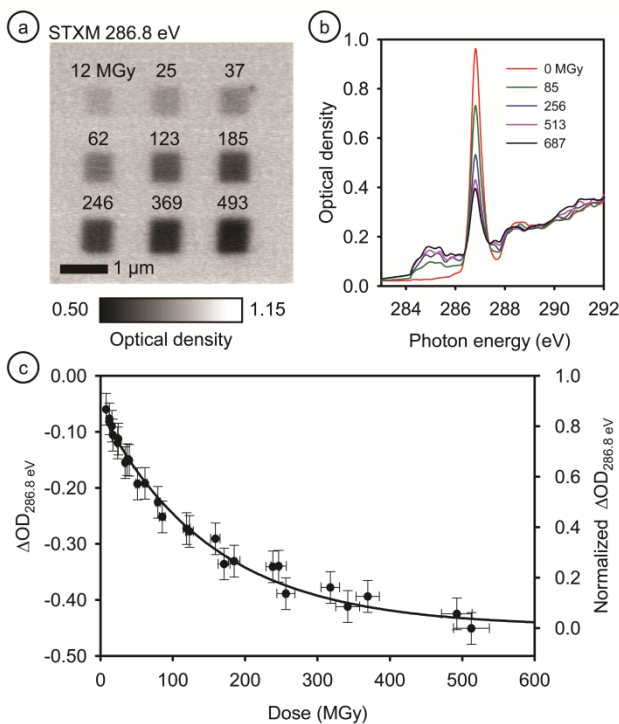


Figure 2: (a) STXM optical density (OD) image of several irradiated areas of a PAN film. (b) C 1s NEXAFS spectral changes induced by 300 eV x-rays. The signal at 286.8 eV decreases while new signals appear at 285 eV and 287.6 eV, and increase with dose. (c) The change in OD at 286.8 eV of PAN measured from images like (a) as a function of dose.

The prominent absorption feature at 286.8 eV was chosen to be the signal that represents the response of PAN to 300 eV x-rays. This feature is directly proportional to the number of nitrile bonds within the area of the film investigated, therefore changes in its magnitude are proportional to the number of nitrile bonds lost or gained as a result of absorbed dose. Averaged values of OD at 286.8 eV of the central regions of irradiated areas as well as a virgin area were measured from images like Figure 2a. Values of $\Delta\text{OD}_{286.8 \text{ eV}}$ ($\Delta\text{OD}_{286.8 \text{ eV}} =$

$OD_{286.8 \text{ eV irradiated area}} - OD_{286.8 \text{ eV virgin area}}$) were determined for several irradiated areas, and plotted versus dose (Figure 2c). The least squares fit of an exponential decay curve to the data points in Figure 2c is quite good ($R^2 = 0.98$), thus it is reasonable to conclude that the $OD_{286.8 \text{ eV}}$ of PAN displays exponential decay over the dose range investigated. A similar response has been found for several other polymers.^{4,10,11,14} The critical dose value can be determined from this data set using the following equation,

$$OD = OD_{\infty} + A \exp\left(-\frac{a}{a_c}\right) \quad (\text{Eqn. 2})$$

where OD is the OD of the PAN film after receiving an absorbed dose a , OD_{∞} is the residual OD value of the PAN film after receiving a very high dose (saturation of damage) on the same scale, A is an intensity scale factor and a_c is the critical dose. If the damage process follows first-order kinetics, a plot of $\ln(OD - OD_{\infty})$ versus a should be linear with a slope of $-1/a_c$, which was deduced by ordinary least squares (linear) regression. By this method, the critical dose of PAN measured at 286.8 eV was found to be 130 ± 10 MGy. Another simple method to determine the critical dose is to plot normalized OD values as a function of dose (Figure 2c) by determining the residual OD value, subtracting it from each OD measurement, then setting the OD of the virgin area to be 1 (normalized ΔOD). The dose where the normalized ΔOD decreases to 37% is then the critical dose.

The data points of Figure 2c have been replotted as ($\Delta\text{OD}_{286.8}$ eV/energy absorbed) versus dose in Figure 3. The quantity “energy absorbed” is a value which is already known as dose is (energy absorbed/mass), and does not involve any additional measurements. The left scale of Figure 3 is ($\Delta\text{OD}_{286.8}$ eV/J absorbed), while the right scale is ($\Delta\text{OD}_{286.8}$ eV/100 eV absorbed). Each data point is a G value. The $G(\Delta\text{OD}_{286.8}$ eV) value is highest for lightly irradiated PAN. A relatively small amount of energy absorbed produces the largest $\Delta\text{OD}_{286.8}$ eV. As the polymer absorbs more energy i.e. as dose increases, less of it is translated into further nitrile bond loss. Since the x-ray absorption cross section of PAN at 300 eV did not change as a function of dose over the range investigated here, the material continues to absorb energy at the same rate, but there are fewer and fewer nitrile bonds to break. The $G(\Delta\text{OD}_{286.8}$ eV) of PAN begins to saturate after receiving about 300 MGy; there very few $\text{C}\equiv\text{N}$ bonds left in the material that remains, resulting in almost no change with further increase in dose.

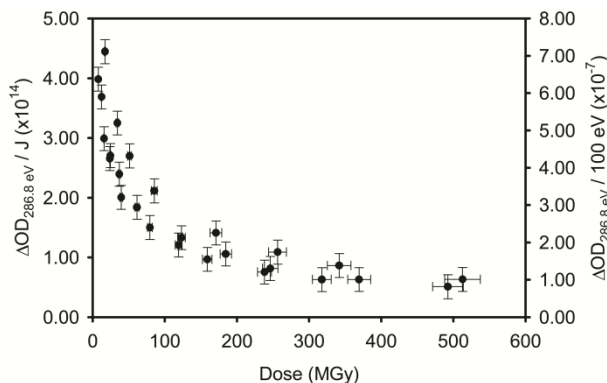


Figure 3: The data from Figure 2c replotted as ($\Delta\text{OD}_{286.8}$ eV/energy absorbed).

Thus, for a signal which undergoes exponential decay as a function of dose, such as the $\text{C } 1s(\text{C}\equiv\text{N}) \rightarrow \pi^*_{\text{C}\equiv\text{N}}$ feature of PAN at 286.8 eV, the G value will be

dependent on the dose received. To achieve a cross-comparable measure of material sensitivity using a G value in this case, the measurements for all materials compared would have to be performed to the same dose. A dose value should then accompany the G value, and comparison to other studies would not be valid unless those also measured the G value at the same dose. This could be complicated as x-ray absorption cross sections are material and energy dependent, and may also be subject to change in response to dose. Still, this dose dependent G value would be sensitive to the initial state of the material; if the material was unknowingly degraded before the measurement, the comparisons might not be valid. Whereas in principle if the kinetics are truly exponential, one critical dose number describes the sensitivity of a material for all doses, and the same value will be obtained regardless of the amount of damage of the initial state.

It is unclear how measuring a single G value for a *first-order* radiation-induced process would be useful. However, if the response is directly proportional to dose i.e. a zeroth-order processes, a single G value can be determined which is independent of dose and the amount of damage of the initial state. A G value is essentially a zeroth-order rate constant, yet several studies have derived a single G value and a critical dose from the same data set when it is clear that the damage-sensitive signal displays first-order kinetics.⁹⁻¹¹ Some materials display different reaction kinetics depending on the dose range or signal probed. For example, the $\Delta OD_{314 \text{ nm}}$ for poly(methyl methacrylate) displays zeroth-order kinetics over the dose region 5 – 45 kGy¹⁹ whereas the $\Delta OD_{288.5 \text{ eV}}$ of

nominally the same material displays first-order kinetics over the dose range 1 – 300 MGy.^{4,14}

CONCLUSION

The kinetics of radiation-induced reactions should always be determined before deriving radiation sensitivity values. If zeroth-order kinetics are discovered, G values are appropriate. If the process displays first-order kinetics, the critical dose should be used. The use of G values for first-order radiation-induced processes should be discontinued, except perhaps for the special circumstance where the materials being compared receive the same dose and have not been pre-irradiated, with that information accompanying the measurement.

ACKNOWLEDGEMENTS

Prof. Adam P. Hitchcock is thanked for reviewing the manuscript. Dr. Chithra Karunakaran, Dr. Jian Wang, and Yingshen Lu are thanked for expert maintenance and support of the CLS 10ID-1 STXM. The CLS is supported by NSERC, CIHR, NRC and the University of Saskatchewan. A.F.G.L. acknowledges support from the CLS graduate student travel support program and an Advanced Light Source doctoral fellowship in residence.

REFERENCES

1. Grubb, D. T. Radiation damage and electron microscopy of organic polymers. *J. Mater. Sci.* **1974**, *9*, 1715-1736.
2. Egerton, R. F.; Li, P.; Malac, M. Radiation damage in the TEM and SEM. *Micron* **2004**, *35*, 399-409.

3. Ravelli, R. B. G.; Garman, E. F. Radiation damage in macromolecular cryocrystallography. *Current Opinion Struct. Bio.* **2006**, *16*, 624-629.
4. Wang, J.; Morin, C.; Hitchcock, A. P.; Scholl, A.; Doran, A. Radiation damage in soft X-ray microscopy. *J. Electron Spectrosc. Relat. Phenom.* **2009**, *170*, 25-36.
5. Hatzakis, M. Electron resists for microcircuit and mask production. *J. Electrochem. Soc.* **1969**, *116*, 1033-1037.
6. Leontowich, A. F. G.; Hitchcock, A. P. Zone plate focused soft X-ray lithography. *Appl. Phys. A* **2011**, *103*, 1-11.
7. Lea, D. E. *Actions of Radiations on Living Cells* 2nd ed.; The University Press: Cambridge, England, 1955. pp. 60-64.
8. Clark, W. R. K.; Chapman, J. N.; Macleod, A. M.; Ferrier, R. P. Radiation damage mechanisms in copper phthalocyanine and its chlorinated derivatives. *Ultramicroscopy* **1980**, *5*, 195-208.
9. Reimer, L.; Spruth, J. Interpretation of the fading of diffraction patterns from organic substances irradiated with 100 keV electrons at 10-300 K. *Ultramicroscopy* **1982**, *10*, 199-210.
10. Rightor, E. G.; Hitchcock, A. P.; Ade, H.; Leapman, R. D.; Urquhart, S. G.; Smith, A. P.; Mitchell, G.; Fischer, D.; Shin, H. J.; Warwick, T. Spectromicroscopy of poly(ethylene terephthalate): Comparison of spectra and radiation damage rates in X-ray absorption and electron energy loss. *J. Phys. Chem. B* **1997**, *101*, 1950-1960.
11. Coffey, T.; Urquhart, S. G.; Ade, H. Characterization of the effects of soft X-ray irradiation on polymers. *J. Electron Spectrosc. Relat. Phenom.* **2002**, *122*, 65-78.
12. Burton, M. General discussion. *Discuss. Faraday Soc.* **1952**, *12*, 312-318.
13. Chapiro, A. *Radiation Chemistry of Polymeric Systems*; Interscience: New York, 1962. pp. 62.
14. Leontowich, A. F. G.; Hitchcock, A. P. Accurate dosimetry in scanning transmission X-ray microscopes via the cross-linking threshold dose of poly(methyl methacrylate). *J. Synchrotron Rad.* **2012**, submitted.
15. Hsu, H.-L.; Yang, W.-C.; Lee, Y.-L.; Yew, T.-R. Polyacrylonitrile as a gate dielectric material. *Appl. Phys. Lett.* **2007**, *91*, 023501.
16. Kaznatcheev, K. V.; Karunakaran, Ch.; Lanke, U. D.; Urquhart, S. G.; Obst, M.; Hitchcock, A. P. Soft X-ray spectromicroscopy beamline at the CLS: Commissioning results. *Nucl. Instrum. Methods A* **2007**, *582*, 96-99.
17. Jacobsen, C.; Wirick, S.; Flynn, G.; Zimba, C. Soft X-ray spectroscopy from image sequences with sub-100nm spatial resolution. *J. Microscopy* **2000**, *197*, 173-184.
18. Ade, H.; Hitchcock, A. P. NEXAFS microscopy and resonant scattering: Composition and orientation probed in real and reciprocal space. *Polymer* **2008**, *49*, 643-675.
19. Khan, H. M.; Ahmad, G.; Sattar, A.; Durrani, S. K. Radiation dosimetry using clear PMMA and PVC in the range of 5-45 kGy. *J. Radioanal. Nucl. Chem.* **1988**, *125*, 127.

Chapter 10

Measurement of the point spread function of a soft x-ray microscope by single pixel exposure of photoresists

This chapter reports the development of a method to extract the full PSF of a STXM from a series of single pixel exposures in a thin PMMA film. This measurement was carried out at several STXMs, with the important observation that the PSF was never found to be fully symmetric as diffraction theory predicts.

Reprinted with permission from the Proceedings of the SPIE 2011, 8077, 80770N, A.F.G. Leontowich, T. Tyliczszak, A.P. Hitchcock. DOI: 10.1117/12.887553, © 2012 SPIE.

A.P. Hitchcock and the author of this thesis conceived the experiments. The author of this thesis prepared all samples and developed them, performed all the experiments, analyzed the data with input and assistance from A.P. Hitchcock and T. Tyliczszak and wrote the manuscript which was edited by A.P. Hitchcock.

Measurement of the point spread function of a soft X-ray microscope by single pixel exposure of photoresists

Adam F. G. Leontowich,^a Tolek Tyliczszak^b and Adam P. Hitchcock^{*a}

^aBrockhouse Institute for Materials Research,

McMaster University, Hamilton, ON, Canada L8S 4M1

^bAdvanced Light Source, Lawrence Berkeley National Laboratory,
1 Cyclotron Road, Berkeley, CA, USA, 94720

ABSTRACT

The monochromatic zone plate focused soft X-rays of scanning transmission X-ray microscopes (STXM) can be used to directly write patterns in common photoresists, analogous to lithography with a focused electron or ion beam. A radiation damage spreading phenomenon when patterning with high doses was recently determined to be due to the point spread function of the optical system (Leontowich et al., *Applied Physics A: Materials Science and Processing* 103, 1 (2011)). We have used this phenomenon to measure the point spread function of three different STXMs by making a series of single pixel exposures in a photoresist at focus over a controlled dose range. Our results suggest this measurement is sensitive to zone plate aberrations; thus, it could be valuable feedback for optimizing zone plate fabrication schemes and STXM performance.

Keywords: Zone plate, point spread function, X-ray lithography, radiation damage, aberrations

*aph@mcmaster.ca; phone 1 905 525-9140 x24749; fax 1 905 521-2773

1. INTRODUCTION

The current generation of soft X-ray (60 – 2500 eV) scanning transmission X-ray microscopes (STXM) employ Fresnel zone plate (ZP) lenses^{1,2} to focus sufficiently coherent soft X-rays into a tightly focused probe. The sample is then positioned at the focal point and x-y raster scanned while the transmitted signal is acquired to form images at specific photon energies.¹⁻³ In addition, near edge X-ray absorption fine structure (NEXAFS) spectra can be measured by recording image sequences over the energy range of interest.²⁻⁵ STXM is an excellent instrument for NEXAFS spectromicroscopy and has been used extensively to characterize many diverse types of samples with high spatial and spectral resolution.^{4,5}

Advancements in ZP fabrication via electron beam lithography^{6,7} have steadily improved the spatial resolution of STXMs. The state-of-the-art is now 10 nm, and routine spot sizes (as defined by the Rayleigh criterion^{1,8}) are ~30 nm. Soft X-ray STXMs can provide an intensity of $10^7 - 10^8$ photons/sec in the focal spot; typical absorbed dose rates are in the 100 - 1000 MGy/s range, assuming an optical density of 1. The absorbed dose can be large enough to induce a variety of changes to the sample,⁹ and fundamentally limits useful spatial resolution.¹⁰ For sensitive samples, this can result in a race to capture spectroscopic information before it is modified by the effects of radiation.

Intense tightly focused probes of ionizing radiation (most commonly electrons or ions) are used extensively to direct write pattern materials for micro and nanofabrication. Zhang et al.¹¹ were the first to demonstrate sub-micron direct write patterning with focused X-rays by operating a STXM in a manner analogous to an electron beam writer. Since that initial work, several groups have investigated ZP focused X-rays for direct write patterning and lithography.¹²⁻¹⁵ A common observation in these experiments is that the minimum feature sizes created when patterning with ZP focused soft X-rays were always larger than the Rayleigh resolution predicted from the ZP properties and measured by imaging high contrast resolution test patterns. Further experiments revealed that feature sizes were dose dependent, implying the existence of an exposure spread mechanism which is in many ways similar to the proximity effect observed in electron beam lithography.¹⁶ We have recently shown¹⁷ that the exposure spread mechanism is caused by instrument properties, namely, the point spread function (PSF) of the optical system, i.e. the distribution of radiation intensity about the focal axis. This was experimentally determined by making repeated, long dwell time, single point exposures in photoresists

positioned at the focal plane of the ZP, and observing asymmetric yet fully reproducible patterns which delineate the spatial extent of the PSF.

In this report, we use thin films of poly(methyl methacrylate) (PMMA) positioned in the focal plane of the ZP to record precisely where X-rays impinge, analogous to photographic film. Soft X-rays cause primarily main chain scission in PMMA at low dose, and crosslinking at high dose. The lower molecular weight areas are then revealed by a wet chemical development step. We have previously determined that PMMA is fully removed from the substrate if it receives a dose of 1 MGy, but even a dose of 0.1 MGy will result in partial removal of material.¹⁷ The developed films are then read out using an atomic force microscope (AFM). Here, we explore more fully the relationship between developed pattern features, properties of the ZP, and its illumination. We have extracted full PSFs from a series of single pixel exposures in PMMA, at focus, over a controlled dose range. We have observed partial Airy patterns with three different STXMs. We have not yet observed the fully symmetric Airy pattern that theory predicts should be formed with a high quality zone plate and optimal illumination. We hypothesize some reasons for this, and discuss planned experiments intended to isolate the source(s) of the asymmetry.

2. METHODOLOGY

2.1 Sample preparation

Thin films (~100 nm) of poly(methyl methacrylate) (PMMA) (M_w : 315 000 M_w/M_n : 1.05 electronics grade, Polymer Source Inc.) were produced by spin casting a 1.5% w/w solution of PMMA in toluene (99.9% Chromasolv®, Sigma Aldrich) onto freshly cleaved mica (Ted Pella Inc.). The film on mica was scribed into 2 mm x 2 mm pieces with a scalpel. Upon slowly dipping this mica into a Petri dish of water (HPLC grade, Caledon), the film pieces release and float on the surface. These were then caught on Si_3N_4 substrates (1 mm x 1 mm x 75 nm window in a 5 mm x 5 mm Si wafer frame, Norcada Inc.) and annealed at 140°C for one hour at reduced pressure ($\sim 2 \times 10^{-2}$ Torr).

2.2 Scanning transmission X-ray microscopes, resist exposure, development and visualization

Three interferometrically controlled STXMs were employed to pattern the films: STXM 5.3.2.2,¹⁸ and STXM 11.0.2¹⁹ at the Advanced Light Source (ALS), Lawrence Berkeley National Labs (LBNL), and the STXM at beamline 10ID-1²⁰ at the Canadian Light Source (CLS). The methods of STXM operation are described elsewhere.²⁻⁵ Each STXM's zone plate had the same parameters (25 nm outermost zone width, 90 μm central stop, 240 μm diameter) and were fabricated by the Center for X-ray Optics (CXRO) at LBNL. The PMMA samples were affixed to an Al sample plate and loaded into the STXM, which was then evacuated and backfilled with 250 Torr He. Patterning was carried out with 300 eV photons using a pattern generation program in the STXM control software.¹⁸

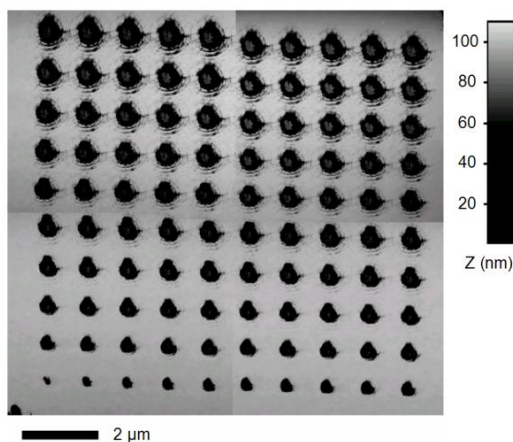


Figure 1. AFM topography image of a developed 100 single pixel exposure pattern in PMMA, made with ALS 11.0.2. Four separate images have been combined.



Figure 2. High magnification AFM phase image of the 5000 ms single pixel exposure from the top right corner of figure 1.

We note that it is imperative that the area which is to be patterned not be STXM imaged, either before or after patterning, as even brief imaging (about 1 ms) is enough to cause unintended patterning. The patterned sample is removed from the sample plate, and developed at ambient temperature ($\sim 20^{\circ}\text{C}$) by gently stirring it in a 3:1 solution of 2-propanol ((IPA) 99.5%, Sigma Aldrich) : 4-methyl-2-pentanone (>98.5% ACS reagent grade, Sigma Aldrich) for 30 s, followed immediately by stirring in IPA for 15 s, then drying in ambient air. The developed patterns were then imaged with a Quesant 350 atomic force microscope (AFM) equipped with Budget Sensors Multi75Al probes, operating in non-contact mode at a 0.5 Hz scan rate. For large areas, it was necessary to make several smaller images and combine them to achieve high spatial sampling and to reduce skew.

3. RESULTS

The pattern designed to record the PSF consisted of 100 single pixel exposures, in a 10×10 array, spaced $1 \mu\text{m}$ apart. The dwell time for each exposure increases in 50 ms steps from left to right and bottom to top, from 50 ms in the lower left, up to 5000 ms in the top right. **Figure 1** shows an AFM image of the developed 100 single pixel pattern, made using ALS 11.0.2. As pixel dwell times increase the diameter of the fully removed material becomes larger and larger. Insoluble crosslinked PMMA remains in the central part of the pattern, beginning around the tenth exposure. Many rings appear and expand around the central axis as the exposure time increases. A high resolution AFM phase image of the 5000 ms developed point exposure is shown in **Figure 2** to highlight these details. Clearly the rings tend to be circular but are incomplete. The performance of all three STXMs is diffraction limited (see discussion), therefore one expects an intensity distribution of an Airy pattern⁸ at the focal plane. We have thus recorded a partial Airy pattern.

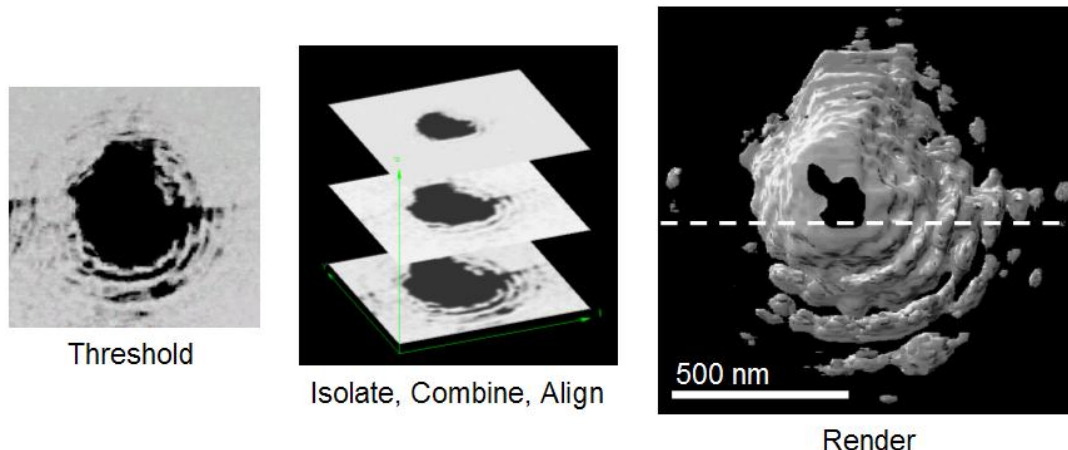


Figure 3. Extracting the full point spread function from the AFM images of developed single pixel exposures. (a) Threshold-ed AFM phase image of the 5000 ms exposure. (b) The procedure used to make the 3D object (c) 3D view, of the outer surface of the stacked AFM images (the z-axis is the image number) made using IDL Slicer²³.

The full PSF was extracted from the AFM images of the developed single pixel patterns in the following way. A threshold was applied to the AFM phase images such that areas with a height less than 80% of the film thickness were made black. One hundred threshold-ed image files were created, one for each single pixel exposure. There is some unintended overlap from adjacent exposures so that, while 1 μm was used in this work, the spacing should be somewhat larger. The subsequent data processing was carried out using aXis2000.²¹ The set of 100 images was converted into an image sequence (stack) and the individual images were then aligned (translational in x and y only) using Fourier transform cross-correlation procedures. The aligned images were then combined into a three dimensional object using IDL Slicer3²² within aXis2000, displayed in **Figure 3**. This surface represents the full PSF of the optical system.

Arbitrary cross sections of the PSF derived from this 3D object yield information equivalent to the common knife edge method, if one performed it over 180 degrees. A horizontal cross section is shown in **Figure 4**. It is difficult to assign the maxima we have recorded. Theoretically the separation between two neighboring rings of an Airy pattern approaches the value $\lambda / 2\text{NA}$.⁸ For our ZP this value is ~ 25 nm. The strongest recorded rings are regularly spaced, but the spacing is 60

10 nm (Figure 4b). The relative intensity of the maxima are also given by theory,⁸ but again we find no definitive agreement. There may be several reasons for this discrepancy (see discussion).

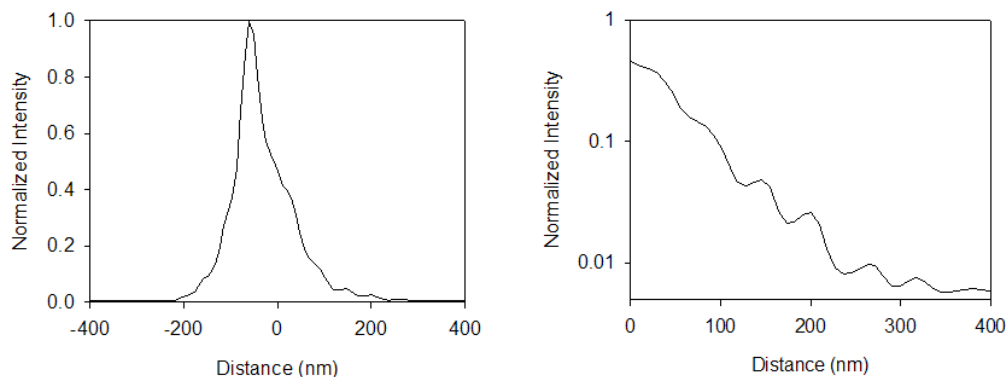


Figure 4. a) Horizontal cross section of the point spread function. The direction and width of the cross section are indicated by the dashed line in figure 3c. b) Intensity on a log scale, showing the maxima and minima.

4. DISCUSSION

A similar method for extracting the PSF of a ZP operating in the visible region has been described by Menon et al.²³, which is also similar to Chang's experimental measurement of the radial exposure intensity distribution introduced by a point source of electrons.¹⁶ In both methods the radial exposure intensity distribution (i.e. PSF) was extracted by plotting normalized intensity (constant/dwell time) versus the radius of the area of removed material. Using our dataset of 100 threshold-ed images, we have found that these methods can not model intensity minima, such as those present in the Airy pattern. In these methods, the presence of a minima would imply that the radius of removed material was observed to decrease with increased dwell time. This is impossible; the radius will only increase or remain the same with increasing dwell time. Our method can measure a minima (figure 4b), making it more accurate than the previous methods. Both prior methods extrapolate the full PSF from data in only one direction, and assume that the PSF is radially symmetric. However, we have shown that this assumption is not always true,¹⁷ and it is certainly not the case for each of the three STXM systems we have investigated. Knife edge measurements are also commonly radially extrapolated. They are challenging at soft X-ray wavelengths because the edge absorber thickness is typically larger than the depth of focus. Our method is not without its own pitfalls. We find it difficult to record the Airy disk (the most intense central spot of the Airy pattern, bordered by the first minima) by our method due to limitations of operating the instrument at full focus and very low exposure doses. The method is also susceptible to artifacts arising from skewed AFM images, and slight misalignment of the threshold-ed images. Despite these challenges we believe the novel method presented here provides unique information about the spatial distribution of radiation intensity in a focal plane with applications extending beyond ZP focused soft X-rays. We are still refining our method, and the findings will be presented in a future paper.

Our efforts are now directed towards understanding why the pattern is not radially symmetric. It was this asymmetry that allowed identification of the exposure spread phenomenon observed in ZP focused soft X-ray patterning as the PSF. The asymmetry is not due to the resist because it is completely reproducible¹⁷ when performed in different photoresists or different regions of the same film. Thus, this pattern must be created by something outside the film, in particular the mechanism of generating the focused spot by the combination of the properties of the ZP and how it is illuminated.

The criteria for diffraction limited focusing of soft X-rays by ZPs such as those used in this work have been given by Jacobsen.²⁴ Assuming the ZP is perfectly fabricated, the ZP is centered relative to the exit slits, and that the ZP and sample are perpendicular to the beam, the basic requirements are that the illumination has sufficient temporal and spatial coherence. For a ZP with n zones the energy resolving power ($\lambda / \Delta\lambda$) necessary to exceed the temporal coherence requirement (sufficient monochromaticity) at a given diffraction order m should be²⁵

$$\frac{\lambda}{\Delta\lambda} \geq n * m \quad (1)$$

The ZPs used in these microscopes have 800 zones, and thus a resolving power of 1000 is more than sufficient to achieve adequate temporal coherence at the first order focal point used to pattern. The ALS 11.0.2 and CLS 10ID-1 undulator based beamlines are routinely operated at a resolving power greater than 3000, while the ALS 5.3.2.2 bend magnet beamline is typically operated with a resolving power of 1500. Thus, the temporal coherence requirement is met by all three STXM beamlines. Spatial coherence is determined by the exit slits, which in each microscope are independently adjustable in x and y , forming an aperture. This aperture diffracts, and the ZP must be fully within the Airy disk emanating from the slits. The exit slit width d corresponding to this limiting condition is

$$d \leq \frac{\lambda}{\sin \theta} \quad (2)$$

where λ is the wavelength (300 eV = 4.13 nm) and θ is the narrow angle of a right triangle formed by the distance from the exit slits to the ZP (1 m for both ALS microscopes, 4 m for CLS 10ID-1) (adjacent), and half the diameter of the ZP (opposite). For our 240 μm ZPs both slits should be $\leq 34 \mu\text{m}$. In all experiments the exit slit widths are set significantly smaller. For the exposures performed at ALS 11.0.2 (figures 1-4) the exit slit sizes were 25 μm x 25 μm , therefore performance should be diffraction limited. As a result the focused intensity of the ZP should produce a symmetric Airy pattern in the focal plane. However we only observe a partial Airy pattern, with significant distortions in specific directions. Even if the ZP and sample were not perpendicular to the beam, that would not explain the roughness of the pattern, since, regardless of such misalignment, the wavefront should be smooth.

We can not yet rule out possible contributions to the PSF asymmetry from non-uniform ZP illumination or other unforeseen instrument problems. The illumination of the zone plate differs considerably among the three STXM microscopes we have examined with this methodology, and depends on the degree of overfill (which is related to the basic design of the beamline optics), and the position and directionality of the electron beam at the source point for the beamline. In the case of ALS 11.0.2, the ZP is uniformly illuminated, as evidenced by the uniformity of the annulus of light in an order sorting aperture scan (**Figure 5**), yet the PSF is not radially symmetric. The ZP illumination of CLS 10ID-1 appears equally uniform, but the PSF is farther away from the expected symmetric Airy pattern. At ALS 5.3.2.2, the illumination was observed to be non-uniform; the PSF here is also farther away from theory. The shape of the PSF of each instrument is unique and very reproducible. In the case of ALS 5.3.2.2 the 100 single pixel exposure measurement was performed several times over a six month period. Although large changes in the illumination of the ZP were observed over this period of time, the overall pattern remained essentially the same, suggesting that the source of the asymmetry lies somewhere after the exit slits and before the sample.

We turn our attention towards the ZP itself. Fabrication of soft X-ray ZPs is at the frontier of electron beam lithography and subsequent plating processes; it is a real challenge to create sub-30 nm ZPs. It may be that the ZPs have aberrations in the placement of zones, out of round, partial collapse of zones in certain regions, etc. These ZPs also have a pseudo-random buttressing system²⁶ to support the zones from collapse during electroplating. The buttressing could modify the ZP focusing from its ideal. There may also be minor contributions from insufficient uniformity in two Si_3N_4 membranes, one which supports the ZP, and another which lies between the exit slits and the ZP that separates the STXM chamber from the ultrahigh vacuum of the beamline.

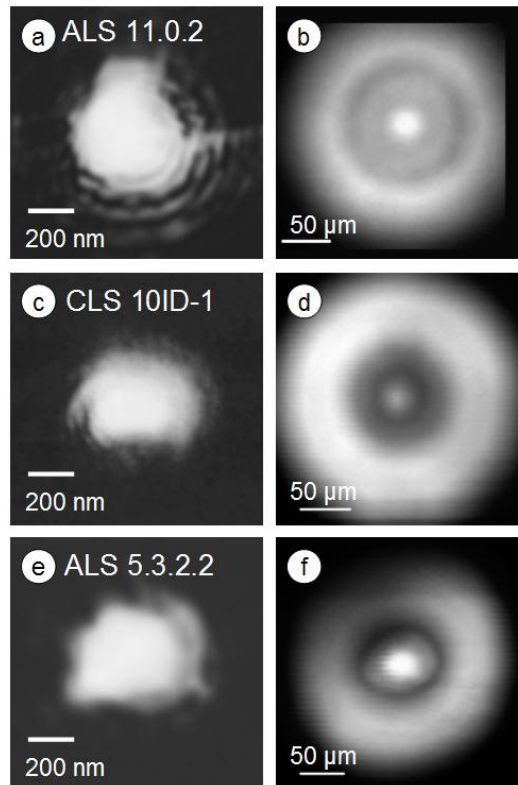


Figure 5. (a) Avg* from ALS 11.0.2 (Avg* is the negative of the average of the 100 aligned threshold-ed AFM images). (b) Illumination of the ZP at ALS 11.0.2 when the 100 point exposure was made. This image was made by (x,y) scanning the 72 μm diameter order sorting aperture (OSA) through a plane between the ZP and its focal point. Parts of the left and upper portion of the X-ray distribution (black areas) were unfortunately not included in the scan. (c) Avg* from CLS 10ID-1. (d) OSA scan for CLS 10ID-1. (e) Avg* from ALS 5.3.2.2. (f) OSA scan for ALS 5.3.2.2.

In order to separate possible effects of non-uniform illumination from those of ZP aberrations, we plan to make single pixel exposure measurements before and after rotating the ZP, with all other factors the same. If the asymmetric pattern is rotated by the same angle as the ZP was rotated, one can conclude that the origin of the asymmetry is the ZP. One difficulty with the three STXMs explored so far is that, once the ZP is rotated, it is possible that it will not be in the same position relative to the illumination, which is problematic because the position of the ZP is not easily adjustable. However, there are other STXMs which are more flexible in this regard, such as PolLux at the Swiss Light Source²⁷, which has a girder mover system that can be used to re-position the ZP in the light path. Also, a new STXM at the ALS (on beamline 5.3.2.1, currently being commissioned) incorporates additional motorized stages for scanning the ZP in the upstream beam. The recently commissioned MAXYMUS STXM at BESSY II has both a girder mover system and the ability to scan the ZP. We propose to carry out the ZP rotation experiment with one or more of these STXMs, in order to re-position the rotated ZP in the same spot relative to the illumination and thus ensure a clean separation of the effects of illumination from those of ZP aberrations on the PSF asymmetry.

Assuming that the asymmetry of the PSF is dominated by ZP aberrations (or that conditions can be adjusted to that end), we will then have developed a tool to characterize the full PSF of ZPs. This could be extremely useful in a number of ways. It could be used to evaluate the quality of different ZPs for soft X-ray focusing. Currently this is done only by examining images of high contrast resolution test patterns such as Siemens star or elbow patterns. Our method could be used to help improve ZP fabrication, by correlating different aspects of the distorted patterns with various process variables. It could also be used to remove image artifacts associated with ZP aberrations, by deconvoluting the PSF. This

approach was used many years ago by Chapman et al.²⁸ to significantly extend the spatial resolution in STXMs and is currently part of the signal processing of ptychography data.²⁹

5. CONCLUSION

We have previously shown that the exposure spread phenomenon observed when patterning with zone plate focused soft X-rays is due to the point spread function of the optical system. In this work we were able to record partial Airy patterns, further strengthening our hypothesis. A method was developed to extract the full point spread function of a sufficiently coherently illuminated zone plate from AFM images of developed single pixel exposures in a photoresist over a range of dwell times. Experiments are underway to separate the effect of illumination from zone plate aberrations, in order to determine precisely the extent to which the recorded pattern reflects the properties of the zone plate.

ACKNOWLEDGEMENTS

This research was supported by NSERC (Canada), the Canada Foundation for Innovation and the Canada Research Chair program. Studies were performed at the Advanced Light Source, beamlines 5.3.2.2 and 11.0.2 (ALS, Berkeley, CA, USA) and the Canadian Light Source, beamline 10ID-1 (CLS, Saskatoon, SK, Canada). We thank Dr. David Kilcoyne (ALS 5.3.2.2), Dr. Jian Wang and Yingshen Lu (CLS 10ID-1) for their support of the STXM facilities. The Advanced Light Source is supported by the Director, Office of Energy Research, Office of Basic Energy Sciences, Materials Sciences Division of the U.S. Department of Energy, under Contract No. DE-AC03-76SF00098. The CLS is supported by NSERC, CIHR, NRC and the University of Saskatchewan.

REFERENCES

- [1] Attwood, D., [Soft X-rays and Extreme Ultraviolet Radiation: Principles and Applications], Cambridge University Press, Cambridge (1999).
- [2] Hawkes, P.W., Spence, J.C.H., [Science of Microscopy], Springer, New York. Chapter 13 (2007)
- [3] Kirz, J., Jacobsen, C., Howells, M., "Soft X-ray microscopes and their biological applications," *Q. Rev. Biophys.* 28, 33-130 (1995).
- [4] Ade, H., Hitchcock, A.P., "NEXAFS microscopy and resonant scattering: Composition and orientation probed in real and reciprocal space," *Polymer* 49, 643-675 (2008).
- [5] Hitchcock, A.P. [Handbook on Nanoscopy], Wiley-VCH, Verlag Gmb-H. Volume I, Chapter XX (in press) (2011)
- [6] Chao, W., Harteneck, B.D., Liddle, J.A., Anderson, E.H., Attwood, D.T., "Soft X-ray microscopy at a spatial resolution better than 15 nm," *Nature* 435, 1210-1213 (2005).
- [7] Chao, W., Kim, J., Rekawa, S., Fischer, P., Anderson, E.H., "Demonstration of 12 nm resolution fresnel zone plate lens based soft X-ray microscopy," *Opt. Express* 17, 17669-17677 (2009).
- [8] Born, M., Wolf, E., [Principles of Optics], Cambridge University Press, Cambridge. pg 436ff (1999)
- [9] Beetz, T., Jacobsen, C., "Soft X-ray radiation-damage studies in PMMA using a cryo-STXM," *J. Synchrotron Rad.* 10, 280-283 (2003).
- [10] Howells, M.R., Beetz, T., Chapman, H.N., Cui, C., Holton, J.M., Jacobsen, C.J., Kirz, J., Lima, E., Marchesini, S., Miao, H., Sayre, D., Shapiro, D.A., Spence, J.C.H., Starodub, D., "An assessment of the resolution limitation due to radiation-damage in X-ray diffraction microscopy," *J. El. Spec. Rel. Phenom.* 170, 4-12 (2009).
- [11] Zhang, X., Jacobsen, C., Lindaas, S., Williams, S., "Exposure strategies for polymethyl methacrylate from in situ x-ray absorption near edge structure spectroscopy," *J. Vac. Sci. Technol. B* 13, 1477-1483 (1995).
- [12] Larciprete, R., Gregoratti, L., Danailov, M., Montecali, R.M., Bonfigli, F., Kiskinova, M., "Direct writing of fluorescent patterns on LiF films by x-ray microprobe," *Appl. Phys. Lett.* 80, 3862-3863 (2002).
- [13] Wang, J., Stöver, H.D.H., Hitchcock, A.P., Tyliczszak, T., "Chemically selective soft X-ray patterning of polymers," *J. Synchrotron Rad.* 14, 181-190 (2007).
- [14] Wang, J., Stöver, H.D.H., Hitchcock, A.P., "Chemically selective soft X-ray direct-write patterning of multilayer polymer films," *J. Phys. Chem. C* 111, 16330-16338 (2007).

- [15] Caster, A.G., Kowarik, S., Schwartzberg, A.M., Leone, S.R., Tivanski, A., Gilles, M.K., "Quantifying reaction spread and x-ray exposure sensitivity in hydrogen silsesquioxane latent resist patterns with x-ray spectromicroscopy," *J. Vac. Sci. Technol. B* 28, 1304-1313 (2010).
- [16] Chang, T.H.P., "Proximity effect in electron-beam lithography," *J. Vac. Sci. Technol.* 12, 1271-1275 (1975).
- [17] Leontowich, A.F.G., Hitchcock, A.P., "Zone plate focused soft X-ray lithography," *Appl. Phys. A* 103, 1-11 (2011).
- [18] Kilcoyne, A.L.D., Tyliczszak, T., Steele, W.F., Fakra, S., Hitchcock, P., Franck, K., Anderson, E., Harteneck, B., Rightor, E.G., Mitchell, G.E., Hitchcock, A.P., Yang, L., Warwick, T., Ade, H., "Interferometer-controlled scanning transmission microscopes at the Advanced Light Source," *J. Synchrotron Rad.* 10, 125-136 (2003).
- [19] Tyliczszak, T., Warwick, T., Kilcoyne, A.L.D., Fakra, S., Shuh, D.K., Yoon, T.H., Brown, G.E.Jr., Andrews, S., Chembrolu, V., Strachan, J., Acremann, Y., "Soft X-ray scanning transmission microscope working in an extended energy range at the Advanced Light Source," *AIP Conf. Proc.* 705, 1356-1359 (2004).
- [20] Kaznatcheev, K.V., Karunakaran, Ch., Lanke, U.D., Urquhart, S.G., Obst, M., Hitchcock, A.P., "Soft X-ray spectromicroscopy beamline at the CLS: Commissioning results," *Nucl. Inst. Meth. A* 582, 96-99 (2007).
- [21] aXis2000 is written in Interactive Data Language (IDL). It is available free for non-commercial use from <http://unicorn.mcmaster.ca/aXis2000.html>
- [22] Carr, D. "Slicer3.pro," in IDL, available from ITT Visual Information Solutions
- [23] Menon, R., Gil, D., Smith, H.I., "Experimental characterization of focusing by high-numerical-aperture zone plates," *J. Opt. Soc. Am. A* 23, 567-571 (2006).
- [24] Jacobsen, C., Williams, S., Anderson, E., Browne, M.T., Buckley, C.J., Kern, D., Kirz, J., Rivers, M., Zhang, X., "Diffraction-limited imaging in a scanning transmission x-ray microscope," *Opt. Comm.* 86, 351-364 (1991).
- [25] Sayre, D., Howells, M., Kirz, J., Rarback, H., [X-Ray Microscopy II], Springer-Verlag, Berlin. 74-78, (1988)
- [26] Olynick, D.L., Harteneck, B.D., Veklerov, E., Tendulkar, M., Liddle, J.A., Kilcoyne, A.L.D., Tyliczszak, T., "25 nm mechanically buttressed high aspect ratio zone plates: Fabrication and performance," *J. Vac. Sci. Technol. B* 22, 3186-3190 (2004).
- [27] Raabe, J., Tzvetkov, G., Flechsig, U., Böge, M., Jaggi, A., Sarafimov, B., Vernooij, M.G.C., Huthwelker, T., Ade, H., Kilcoyne, D., Tyliczszak, T., Fink, R.H., Quitmann, C., "PolLux: A new facility for soft x-ray spectromicroscopy at the Swiss Light Source," *Rev. Sci. Instrum.* 79, 113704 (2008).
- [28] Chapman, H.N., Jacobsen, C., Williams, S., "Applications of a CCD detector in scanning transmission x-ray microscope," *Rev. Sci. Instrum.* 66, 1332-1334 (1995).
- [29] Thibault, P., Dierolf, M., Menzel, A., Bunk, O., David, C., Pfeiffer, F., "High-resolution scanning X-ray diffraction microscopy," *Science* 321, 379-382 (2008).

Chapter 11

Experimental investigation of beam heating in a soft x-ray scanning transmission x-ray microscope

This chapter presents results of experiments which were expressly designed to measure beam heating of samples in a STXM at typical and extreme conditions. A variable temperature sample holder device fabricated to enable these experiments is also described in this chapter.

Reprinted with permission from Analyst 2012, 137, 370-375, A.F.G. Leontowich, A.P. Hitchcock. DOI: 10.1039/c1an15688h, © 2012 The Royal Society of Chemistry.

A.P. Hitchcock and the author of this thesis conceived the experiments. The author of this thesis fabricated the variable temperature sample holder device, prepared all samples, performed the optical microscope experiments and the majority of the STXM experiments (in collaboration with A.P. Hitchcock), analyzed the data, wrote the manuscript which was edited by A.P. Hitchcock and served as corresponding author.

Cite this: *Analyst*, 2012, **137**, 370

www.rsc.org/analyst

PAPER

Experimental investigation of beam heating in a soft X-ray scanning transmission X-ray microscope

Adam F. G. Leontowich* and Adam P. Hitchcock

Received 7th July 2011, Accepted 29th October 2011

DOI: 10.1039/c1an15688h

A variable temperature sample holder with an operational range of 15 to 200 °C and an accuracy of ± 1 °C has been fabricated for scanning transmission X-ray microscopes (STXM). Here we describe the device, and use it to image the polycrystalline morphology of solid stearic acid and palmitic acid at temperatures near their respective melting points as a means of checking for possible sample heating caused by the focused X-ray beam. The melting points observed in STXM were identical to those observed by conventional methods within measurement uncertainty, even under the most extreme, high dose rate imaging conditions investigated. The beam-induced temperature rise in the sample is inferred to be below 1 °C for dose rates of up to 2.7 GGy/s.

Introduction

Improvements in the manufacture of Fresnel zone plate lenses^{1,2} enable the current generation of soft X-ray (60–2500 eV) scanning transmission X-ray microscopes (STXM) to focus as much as 10^8 photons/s into a spot of continuously decreasing diameter. The size of the spot produced at the focal plane of a zone plate is proportional to the width of its outermost zone,³ which for this study is 25 nm. Assuming that the zone plate is manufactured within certain tolerances,⁴ free of aberrations (which may not always be the case⁵), and the beamline and STXM are tuned to produce the conditions necessary for diffraction-limited focusing^{4–6} (routine with current designs and components^{7–12}) 83.8% of the radiation diffracted into the first order focal point ends up inside a circle (the Airy disk) with a diameter of 61 nm at the focal plane.¹³ The net result is that, with typical microscope settings, the sample will absorb energy at a rate on the order of 0.1–1 GGy/s. By opening the monochromator entrance and/or exit slits, it is possible to exceed 3 GGy/s. However, this is accompanied by a reduction in spatial and energy resolution, and could exceed the limit of linearity of the detector.

The amount of energy absorbed by the sample during STXM investigation has been hypothesized to induce a rise in sample temperature (T), which could affect the outcomes of experiments in a variety of ways. (i) The heat generated could directly alter the sample. Braun *et al.*¹⁴ observed alteration of polymer and soot extract samples exposed to the focused X-ray beam and attributed it to heat dissipation in the sample, though no data to support this claim appears in their report and it is not clear how this effect was separated from other radiation-induced damage

mechanisms.^{15–17} (ii) Fu *et al.*¹⁸ entertained the possibility that a beam-induced rise in T could be large enough to cause reorientation of ordered alkane chains, introducing uncertainty in quantifying polarization dependent signals. (iii) Beam-induced heating could indirectly alter the sample. X-rays can create reactive molecular fragments such as radicals or ions in the sample,^{19–21} and migration of such molecular fragments is known to be T dependent.²² Wang *et al.*²³ considered the possibility of beam-induced heating affecting the migration distance of radicals/ions in thin polymer layers, but then negated it by calculating the rise in T to be less than 1 °C under their conditions. (iv) A rise in T could affect the quality of spectroscopic data. Certain X-ray absorption spectral features change shape for T changes in the range of tens of °C. Such changes have been shown to be reversible and not due to radiation damage.²⁴ An experimental determination of beam-induced sample heating deconvoluted from other radiation-induced effects would be a welcome compliment to the calculation of Wang *et al.*²³ However it is not a trivial task to accurately measure a T change within a sub-100 nm diameter area. To our knowledge there has not been an experimental study of beam-induced sample heating in STXM.

In the work reported here we sought to determine *via* experiment whether or not significant beam-induced sample heating occurs over STXM imaging conditions ranging from typical to extreme, using an indirect method inspired by reports from the early days of electron microscopy (reviewed by Reimer and Christenhusz²⁵). The polycrystalline morphology of thin films (30–200 nm) of fatty acids was imaged by STXM as a function of T. To perform this experiment a variable T sample holder device which employs a Peltier element was constructed. Here the device is described and the accuracy of the control of sample T is evaluated. The T values at which the fatty acids undergo a solid to liquid phase transition were recorded while being imaged at soft X-ray photon energies in STXM, and compared to values

Brockhouse Institute for Materials Research, McMaster University, 1280 Main St. W. L8S 4M1, Hamilton, Canada. E-mail: leontoaf@mcmaster.ca; Fax: +1 905.521.2773; Tel: +1 905.525.9140 x24864

obtained by a conventional melting point (mp) apparatus. Under the most extreme STXM imaging conditions noted, beam-induced sample heating is shown to be practically negligible – an upper limit of 1 °C is estimated.

Experimental

Variable temperature sample holder device

The device fabricated to enable this experiment is presented in Fig. 1. It was designed to fit the existing three pin kinematic sample mount of Advanced Light Source (ALS) STXM 5.3.2.2⁸ (formerly referred to as 5.3.2), at Lawrence Berkeley National Labs (LBNL) without modification so as to minimize installation time. The device fits the sample mounts of all operational STXMs to date which are based on the ALS 5.3.2.2 design (ALS 11.0.2,⁹ Canadian Light Source (CLS) 10ID-1,¹⁰ Swiss Light Source X07DA,¹¹ BESSY II UE46¹²) without additional modification. The device holds samples in X, Y and Z positions that are within tens of μm of a standard sample holder, which was not a trivial feat considering the spatial constraints. When operated in focus at 280 eV the distances from the sample to the zone plate, order sorting aperture and detector are 1355 μm , 280 μm and ~ 2 mm, respectively. The bottom part of the device, which holds up to three samples, is thermally isolated from the rest of the device. Its T is monitored by a K type thermocouple, read to 1 °C (DM6802B, Sampo). Heating and cooling is enabled by a Peltier thermoelectric element (TE-65-0.6-0.8, TE Technology, Inc.) controlled with a variable DC power supply (GPS-1850D, GW Instek). In this configuration, the bottom part of the device has a T range of 15 to 200 °C.

Sample preparation

Stearic acid (99%, Sigma-Aldrich) was purified by multiple recrystallizations from hot 4-methyl-2-pentanone (>98.5% ACS

reagent grade, Sigma-Aldrich), and was pure by ¹H NMR (600 MHz, AV 600, Bruker), mp 69.8 °C. Palmitic acid (99%, Sigma-Aldrich) was used as received, mp 62.7 °C. These mp values were determined using a conventional mp apparatus (MF370, Gallenkamp). 75 nm Si₃N₄ windows (1 mm × 1 mm window area in a 5 mm × 5 mm Si wafer frame) were purchased from Norcada Inc.

All samples investigated were prepared in the following manner: A very small (sub-mg) amount of stearic acid or palmitic acid was deposited onto the flat side of a Si₃N₄ window, which rested on the device. The T was raised until the solid melted, forming a small drop. With the T held above the mp, a second Si₃N₄ window was overlaid (flat side down) onto the drop, confining it between the two windows. The T was then slowly reduced to room T, and the thin liquid film solidified, a process readily observable if the sample is prepared under an optical microscope. Finally, the sample was affixed to the device with two small dabs of epoxy. Fatty acid film thicknesses, which were determined to be 30–200 nm by near edge X-ray absorption fine structure (NEXAFS) spectroscopy, are typical of most STXM samples and within the range acceptable for soft X-ray NEXAFS measurements free of absorption saturation.

Microscopy

In STXM, monochromatic X-rays are focused down to a small focal point. Samples are positioned at the focal plane and X-Y raster scanned through this focused probe while the transmitted photon flux is simultaneously recorded to form transmission images at X-ray photon energies. These transmission images can then be converted to optical density (OD) images using the Lambert-Beer law,

$$OD = -\ln(I/I_0) = \mu \cdot \rho \cdot t \quad (1)$$

where I_0 is the incident photon flux, I is the transmitted photon flux for each pixel of the image, μ is the mass absorption coefficient, ρ is density, and t is sample thickness. In a second mode of operation, X-ray transmission spectra can be acquired by positioning the sample at or near the focal plane and scanning the monochromator across a photon energy range of interest while recording I . The X-ray transmission spectra can be converted to X-ray absorption spectra by collecting an I_0 spectrum and applying the above relationship. Several excellent descriptions of STXM exist elsewhere.^{15,26}

STXM measurements at C 1s (K) edge photon energies were performed using ALS STXM 5.3.2.2,⁸ while those at the O 1s edge were performed using CLS STXM 10ID-1.¹⁰ Both microscopes use zone plate lenses with identical parameters (25 nm outermost zonewidth, 240 μm diameter, 90 μm central stop) supplied by the Center for X-ray Optics (CXRO), LBNL. All measurements were carried out with the STXM enclosure backfilled with He to 250 Torr, after evacuation of air. A N₂ gas filter (1 m path at a pressure of 0.6 Torr) was used to suppress second order radiation from the monochromator for measurements performed at the C 1s edge. The efficiency of the scintillation-photo multiplier tube (PMT) detector at the C and O 1s edge regions,⁸ and other instrumental parameters have been taken into account in computing the absorbed dose rates

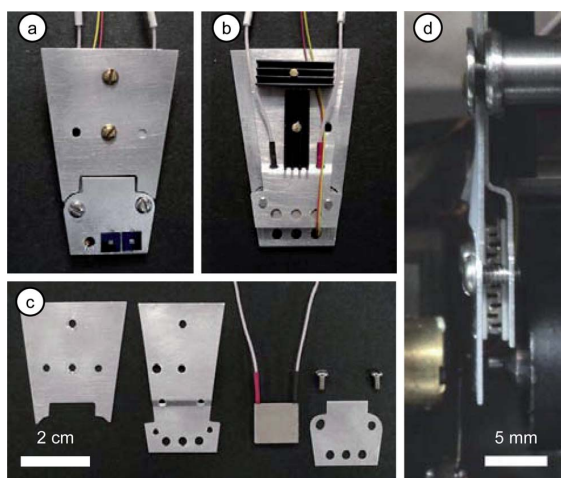


Fig. 1 a) Front view of the variable temperature sample holder device, assembled, with two samples affixed. b) Back view, assembled. c) Front view, disassembled. d) Side view, mounted in ALS STXM 5.3.2.2 with zone plate, order sorting aperture and detector distances tuned for O 1s edge measurements.

presented, which are believed to be precise within 10% using methods described in detail earlier.^{17,23} Optical microscope images were obtained with an Olympus BX51 optical microscope equipped with a polarizer-analyzer set and a CCD camera, operating in transmission mode.

Results

Device accuracy

Optical microscope and STXM OD images of a stearic acid sample at 25 °C are presented in Fig. 2. Fig. 2a is an optical microscope image of the entire sample. Fig. 2b is an OD image at 320 eV of a select area. At 320 eV, away from the fine structure of the absorption edge, C 1s X-ray absorption cross sections become atomic-like;²⁷ for a pure material, a change in contrast in an OD image at this energy indicates a change in thickness and/or density (eqn. (1)). Overall there is a significant increase in absorption going from the top of the OD image to the bottom. In addition, the contrast is not uniform; fine heterogeneous contrast fluctuations ($\pm 5\%$ variations in OD) are observed. Fig. 2c is a polarized (analyser orthogonal to polarizer) optical microscope image of the same area. A heterogeneous contrast pattern is observed, identical to that observed by STXM. The contrast in Fig. 2c is due to birefringence; areas which show increased contrast are ordered along certain directions. Polarized optical

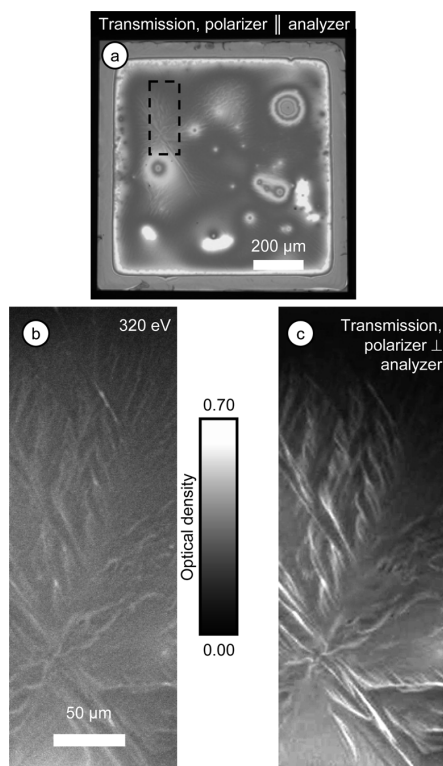


Fig. 2 a) Optical microscope image of stearic acid confined between two Si_3N_4 windows. b) STXM optical density (OD) image, 320 eV, of the area outlined by the dotted line in a). c) Polarized optical microscope image of the area outlined by the dotted line in a).

microscope images of fatty acid samples in the liquid state showed zero contrast. Therefore, since identical heterogeneous contrast patterns are observed by STXM and polarized optical microscopy, we ascribe the heterogeneous contrast patterns observed in the STXM OD images of the solid fatty acid samples to be primarily due to fatty acid film thickness variations arising from the way crystal domains of different orientation are organized spatially.

To determine the accuracy of T-control and T-measurement of the device, a stearic acid sample was affixed to the device and observed under the optical microscope while heating. The polarized optical microscope image was continuously monitored while T was raised at a rate of approximately $4\text{ }^\circ\text{C min}^{-1}$. Some signs of melting, notably movement of the solid material and some disappearance of contrast in the image, were observed at 67 °C. This low onset may be due to possible impurities on the Si_3N_4 windows. The contrast in the image completely and rapidly disappeared when $T = 70\text{ }^\circ\text{C}$ and was consistent across the whole $1\text{ mm} \times 1\text{ mm}$ sample. In summary, the stearic acid sample mounted on the device melted at the identical T (within measurement uncertainty) determined earlier for the same material by a mp apparatus. Therefore the control system and temperature measurement of the device are accurate within $\pm 1\text{ }^\circ\text{C}$. Note that T is measured at the bottom part of the device to which the samples are affixed, not the samples themselves. We therefore infer that the thin fatty acid films and the Si_3N_4 windows conduct heat sufficiently well and evenly enough that the samples are in thermal equilibrium with the device, at these conditions.

Measurement of beam-induced heating in STXM

A palmitic acid sample was affixed to the device and mounted in ALS STXM 5.3.2.2. The sample was imaged at 288.0 eV with an entrance slit setting of $50\text{ }\mu\text{m}$, exit slit settings of $25\text{ }\mu\text{m} \times 25\text{ }\mu\text{m}$, and a pixel dwell time of 2 ms. These settings are typical for diffraction-limited imaging at the C 1s edge. The dose rate was calculated to be $360 \pm 40\text{ MGy/s}$. A series of OD images of the same area of this sample at various T's are presented in Fig. 3. In Fig. 3a, acquired at a constant T of 25 °C, solid palmitic acid fills the majority of the imaged area, except for the area along the right side of the image which is free of material (OD = 0.00). The solid shows heterogeneous contrast as discussed previously. After this image was acquired sample T was elevated to 58 °C. T was gradually increased from 58 to 65 °C as the next image (Fig. 3b) was acquired (STXM images are acquired one line at a time; the acquisition/scan direction was always from bottom to top). Compared to the image acquired at constant T = 25 °C (Fig. 3a), details in the image began to change when $T = 61\text{ }^\circ\text{C}$. As the scan progressed further, the areas that previously showed heterogeneous contrast took on a smooth, homogeneous appearance when $T = 63\text{ }^\circ\text{C}$ and above. This suggests that for the remainder of the image acquisition the palmitic acid was in the liquid state, which would be expected at this T. $T = 65\text{ }^\circ\text{C}$ was maintained after this image (Fig. 3b) had been acquired, and another image of the same area was recorded at constant T = 65 °C (Fig. 3c). The palmitic acid in this smooth featureless image is unambiguously in the liquid state. The area on the right of this image, which in the solid state (Fig. 3a) had an OD = 0.00, now

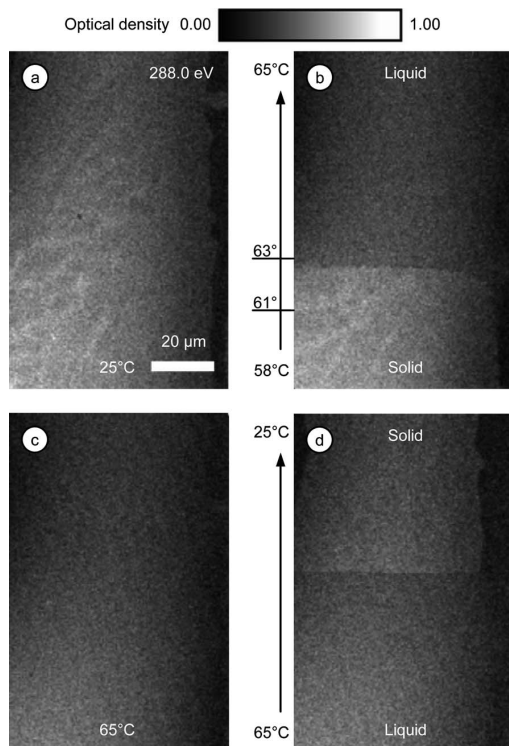


Fig. 3 STXM OD images, 288.0 eV, of palmitic acid confined between two Si_3N_4 windows at various temperatures. a) Solid at 25 °C. b) On raising the temperature throughout the image acquisition from 58 to 65 °C, the heterogeneous contrast characteristic of the solid began to distort at 61 °C. Contrast became homogenous at 63 °C. c) Liquid at 65 °C. d) Rapid cooling during image acquisition. All images are same position and OD scale.

has an OD of ~ 0.05 , indicating movement of material *i.e.* flow into this area. Comparing Fig. 3a and 3c, a change in thickness of the material occurred, which is ascribed to the flow of liquid between the confines of the two Si_3N_4 windows. Sample T was rapidly decreased from 65 to 25 °C as a final image was acquired (Fig. 3d). Midway through this image acquisition defined features reappeared, which we infer as the point at which the liquid palmitic acid had solidified. At this point the edge observed in Fig. 3a also reappeared as the material contracts upon solidifying. The palmitic acid is in the solid state for the remainder of the image acquisition.

In a second experiment, a stearic acid sample was affixed to the device and mounted in CLS STXM 10ID-1. An O 1s NEXAFS spectrum was recorded at 25 °C and is presented in Fig. 4. Based on this spectrum, we chose to perform our T-dependent imaging experiment at 532.2 eV as it is the photon energy of maximum absorption at the O 1s edge for this molecule. The exit slit settings ($15 \mu\text{m} \times 15 \mu\text{m}$) were chosen such that the photon flux (I_0) was just below the ~ 20 MHz limit of linearity of the scintillation-PMT detector.⁸ The dose rate was calculated to be 2670 ± 160 MGy/s. These conditions, which are rarely used due to the high dose rate, represent our attempt to create the most extreme imaging conditions which might be encountered in a STXM (see

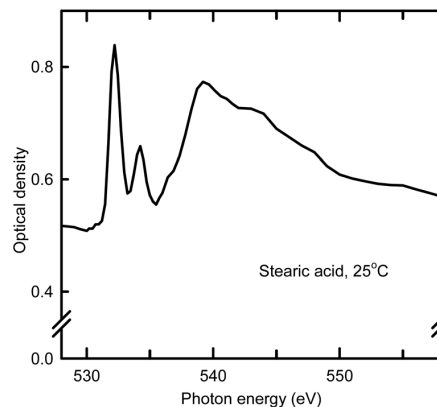


Fig. 4 NEXAFS spectrum of stearic acid at 25 °C, in the region of the O 1s edge.

further comments in the discussion). A series of OD images of the same area of this sample at various T's are presented in Fig. 5. The image in Fig. 5a was acquired with the stearic acid in the solid phase at a constant $T = 25$ °C. After this image was acquired sample T was elevated to 59 °C (10 °C below the mp). The next image (Fig. 5b) was acquired at a constant $T = 59$ °C. The heterogeneous contrast pattern in Fig. 5a and 5b is clearly identical. T was gradually increased from 59 to 70 °C as another image of the same area (Fig. 5c) was acquired. The heterogeneous contrast pattern showed signs of distortion at 67 °C, and by 70 °C the contrast in the image became homogenous. T was reduced from 70 to 50 °C as another image (Fig. 5d) was acquired of the same area. Heterogeneous contrast returned as the stearic acid solidified. The solid material took on a new heterogeneous contrast pattern, different from that of the same area before the melt-freeze cycle. The image presented in Fig. 5e was acquired at a constant $T = 25$ °C to record the new contrast pattern.

Discussion

All observations regarding the effects of T on the polycrystalline morphology of thin fatty acid films noted in the results section can also be made under the polarized optical microscope on the lab bench, and should not come as a surprise. However, these observations when made with a STXM reveal useful information about beam-induced sample heating. The fatty acid samples absorbed energy from the soft X-ray imaging process while the T was raised through their respective melting points using a variable temperature sample holder device. If this additional energy induced a significant rise in sample T, one would expect melting to occur at a T below the conventionally determined mps. This was not observed. Both palmitic acid and stearic acid were observed to melt at T values identical to those obtained with a conventional mp apparatus within measurement uncertainty while simultaneously being imaged with STXM (which could now be considered as a very expensive mp apparatus!). Upon transitioning from solid to liquid to solid, the heterogeneous contrast patterns of solid fatty acid films change randomly (Fig. 5). If, during imaging, the beam had induced a rise in T sufficient to melt the sample, the heterogeneous contrast pattern

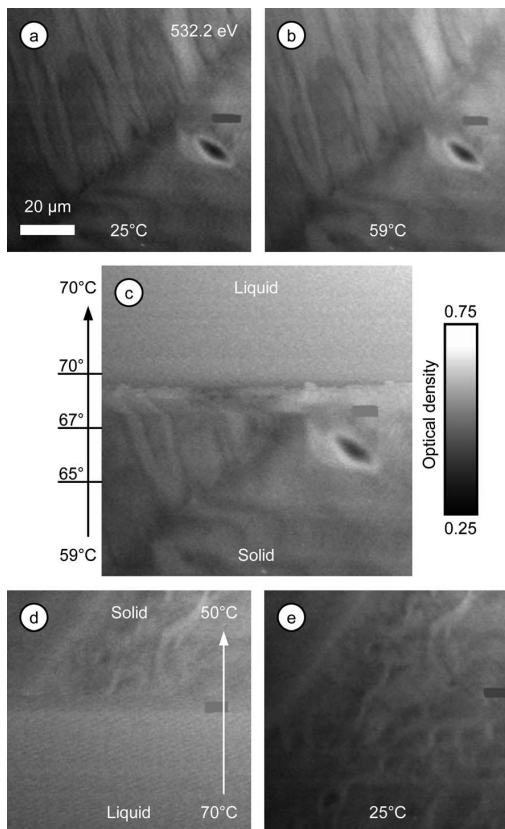


Fig. 5 STXM OD images, 532.2 eV, of stearic acid confined between two Si_3N_4 windows at various temperatures. a) Solid at 25 °C. b) Solid at 59 °C. c) On raising the temperature throughout the image acquisition from 59 to 70 °C, the image began to distort at 67 °C. Contrast became homogenous at 70 °C. d) Slow cooling during image acquisition. e) New crystalline pattern which formed after solidifying, 25 °C. All images are same position and OD scale. The grey rectangle in each image covers an extremely dense speck of material which has been omitted so that the contrast of the sample is enhanced.

of the imaged area would change upon successive imaging. However, successive images of the same area of the sample made at 25 °C and at a few °C below the mp were identical, again negating a significant beam-induced rise in sample T. Note that in our analysis we have ignored possible additional thermal contributions from X-ray absorption by the two 75 nm Si_3N_4 windows which encapsulate the fatty acids. Although they are sufficiently transparent for imaging with soft X-rays, each attenuates the flux by 30–35% throughout the C 1s edge region, and 40–45% throughout the O 1s edge region. The heat generated at the focal spot within these windows is also conducted to the sample, yet the T rise of the material within the focal spot is negligible.

Photon flux rates above 20 MHz, greater than the limit of linearity of the scintillation-PMT detector, can be achieved by further opening the monochromator entrance and/or exit slits, especially for those STXMs on undulator beamlines such as CLS

10ID-1. Flux rates above 20 MHz can be quantified. However, it would be unusual for a STXM equipped with a scintillation-PMT detector (at present, the most commonly used detector) to be operated in the non-linear high dose rate range for making images and collecting NEXAFS spectra. Other detectors/methods of detection have been used for this high photon flux regime, such as photodiodes,²⁸ avalanche photodiodes,¹² channeltrons,²⁹ monitoring sample current (conductive samples only),³⁰ or fluorescence.³¹ One must also consider that if the slits are opened too wide, the zone plate focusing may no longer be diffraction-limited, causing the spot diameter to increase *i.e.* the dose rate will no longer be linearly proportional to the flux rate. In this investigation we have restricted our determination of the beam-induced rise in sample T to those conditions encountered in the vast majority of STXM investigations past and present, which we define as collecting images and NEXAFS spectra with the microscope set for diffraction-limited focusing conditions, in transmission mode with a scintillation-PMT detector, operating within the limit of linearity of the detector. The O 1s experiments were performed at an absorbed dose rate of 2670 ± 160 MGy/s, the maximum possible under linear photon counting conditions using the scintillation-PMT detector. No sign of beam-induced sample heating was found. Therefore it is inferred that any beam-induced rise in sample T was less than the 1 °C accuracy of our T measurements.

Conclusion

The solid-liquid phase transitions of stearic acid and palmitic acid were unambiguously observed by STXM with the aid of a variable temperature sample holder device. While being imaged at soft X-ray photon energies, these phase transitions occurred within ± 1 °C of their conventionally determined values, even under high dose rate conditions. Therefore, it is inferred that for the conditions investigated, beam-induced heating within the focused spot of the STXM is less than 1 °C. This conclusion does not rely on a direct temperature measurement, but rather is deduced from observations of an equilibrium phase transition which acts as an absolute, sample-dependent thermometer. This indirect method gets around the challenges of directly measuring the temperature of the sample itself within the focal point of the X-ray beam, and separates the issue of beam-induced heating from other effects such as X-ray beam-induced radiation damage.

Acknowledgements

We thank Yosh Kitamura of the McMaster University Engineering Machine Shop for his assistance in fabricating the variable temperature sample holder device, and Dave McLeod for performing the NMR measurement. This research was funded by NSERC, CFI and the Canada Research Chairs program and carried out at beamline 10ID-1 at the CLS and 5.3.2.2 at the ALS. The CLS is supported by NSERC, CIHR, NRC and the University of Saskatchewan. The Advanced Light Source is supported by the Director, Office of Science, Office of Basic Energy Sciences, of the U.S. Department of Energy under Contract No. DE-AC02-05CH11231.

References

- 1 W. Chao, J. Kim, S. Rekawa, P. Fischer and E. H. Anderson, *Opt. Express*, 2009, **17**, 17669–17677.
- 2 D. L. Olynick, B. D. Harteneck, E. Veklerov, M. Tendulkar, J. A. Liddle, A. L. D. Kilcoyne and T. Tyliczszak, *J. Vac. Sci. Technol., B*, 2004, **22**, 3186–3190.
- 3 D. Attwood, in *Soft X-rays and Extreme Ultraviolet Radiation: Principles and Applications*, Cambridge University Press, Cambridge, 1999, ch. 9.
- 4 C. Jacobsen, S. Williams, E. Anderson, M. T. Browne, C. J. Buckley, D. Kern, J. Kirz, M. Rivers and X. Zhang, *Opt. Commun.*, 1991, **86**, 351–364.
- 5 A. F. G. Leontowich, T. Tyliczszak and A. P. Hitchcock, *Proc. SPIE*, 2011, **8077**, 80770N-1.
- 6 J. Thieme, in *X-Ray Microscopy II*, ed. D. Sayre, M. Howells, J. Kirz and H. Rarback, Springer-Verlag, Berlin, 1988, pp. 70–79.
- 7 T. Warwick, H. Ade, D. Kilcoyne, M. Kritscher, T. Tyliczszak, S. Fakra, A. Hitchcock, P. Hitchcock and H. Padmore, *J. Synchrotron Radiat.*, 2002, **9**, 254–257.
- 8 A. L. D. Kilcoyne, T. Tyliczszak, W. F. Steele, S. Fakra, P. Hitchcock, K. Franck, E. Anderson, B. Harteneck, E. G. Rightor, G. E. Mitchell, A. P. Hitchcock, L. Yang, T. Warwick and H. Ade, *J. Synchrotron Radiat.*, 2003, **10**, 125–136.
- 9 T. Tyliczszak, T. Warwick, A. L. D. Kilcoyne, S. Fakra, D. K. Shuh, T. H. Yoon, G. E. Brown, Jr., S. Andrews, V. Chembrolu, J. Strachan and Y. Acremann, *AIP Conf. Proc.*, 2004, **705**, 1356–1359.
- 10 K. V. Kaznatcheev, Ch. Karunakaran, U. D. Lanke, S. G. Urquhart, M. Obst and A. P. Hitchcock, *Nucl. Instrum. Methods Phys. Res., Sect. A*, 2007, **582**, 96–99.
- 11 J. Raabe, G. Tzvetkov, U. Flechsig, M. Böge, A. Jaggi, B. Sarafimov, M. G. C. Vernooij, T. Huthwelker, H. Ade, D. Kilcoyne, T. Tyliczszak, R. H. Fink and C. Quitmann, *Rev. Sci. Instrum.*, 2008, **79**, 113704.
- 12 R. Follath, J. S. Schmidt, M. Weigand and K. Fauth, *AIP Conf. Proc.*, 2010, **1234**, 323–326.
- 13 M. Born and E. Wolf, in *Principles of Optics*, Cambridge University Press, Cambridge, 7th edn, 1999, pp. 436–446.
- 14 A. Braun, F. E. Huggins, N. Shah, Y. Chen, S. Wirick, S. B. Mun, C. Jacobsen and G. P. Huffman, *Carbon*, 2005, **43**, 117–124.
- 15 H. Ade and A. P. Hitchcock, *Polymer*, 2008, **49**, 643–675.
- 16 A. F. G. Leontowich and A. P. Hitchcock, *Appl. Phys. A: Mater. Sci. Process.*, 2011, **103**, 1–11.
- 17 J. Wang, C. Morin, L. Li, A. P. Hitchcock, A. Scholl and A. Doran, *J. Electron Spectrosc. Relat. Phenom.*, 2009, **170**, 25–36.
- 18 J. Fu and S. G. Urquhart, *J. Phys. Chem. A*, 2005, **109**, 11724–11732.
- 19 H. Hiraoka, *IBM J. Res. Dev.*, 1977, **21**, 121–130.
- 20 M. C. K. Tinone, K. Tanaka and N. Ueno, *J. Vac. Sci. Technol., A*, 1995, **13**, 1885–1892.
- 21 A. Cheng and M. Caffrey, *Biophys. J.*, 1996, **70**, 2212–2222.
- 22 S. V. Postnikov, M. D. Stewart, H. V. Tran, M. A. Nierode, D. R. Medeiros, T. Cao, J. Byers, S. E. Webber and C. G. Wilson, *J. Vac. Sci. Technol., B*, 1999, **17**, 3335–3338.
- 23 J. Wang, H. D. H. Stöver, A. P. Hitchcock and T. Tyliczszak, *J. Synchrotron Radiat.*, 2007, **14**, 181–190.
- 24 A. Schöll, R. Fink, E. Umbach, G. E. Mitchell, S. G. Urquhart and H. Ade, *Chem. Phys. Lett.*, 2003, **370**, 834–841.
- 25 L. Reimer and R. Christenhusz, *Lab. Invest.*, 1965, **14**, 1158–1168.
- 26 M. Howells, C. Jacobsen and T. Warwick, in *Science of Microscopy*, ed. P. W. Hawkes and J. C. H. Spence, Springer Science + Business Media, New York, 2007, vol. 2, ch. 13.
- 27 R. C. Moffet, A. V. Tivanski and M. K. Gilles, in *Fundamentals and Aspects of Aerosol Spectroscopy*, ed. R. Signorell and J. P. Reid, CRC Press Taylor & Francis Group, Boca Raton, 2010, ch. 17, pp. 436.
- 28 R. Dähn, M. Vespa, T. Tyliczszak, E. Wieland and D. K. Shuh, *Environ. Sci. Technol.*, 2011, **45**, 2021–2027.
- 29 C. Hub, S. Wenzel, J. Raabe, H. Ade and R. H. Fink, *Rev. Sci. Instrum.*, 2010, **81**, 033704.
- 30 H. Shin, K. Jeong, D. C. Johnson, S. D. Kevan, M. Noh and T. Warwick, *J. Korean Phys. Soc.*, 1997, **30**, 575–579.
- 31 R. Alberti, A. Longoni, T. Klatka, C. Guazzoni, A. Gianoncelli, D. Bacescu and B. Kaulich, *IEEE Nuclear Science Symposium Conference record*, 2008, **N14-3**, 1564–1566.

Chapter 12

Summary and future work

This chapter begins with a reflection on certain events that led to breakthroughs in this research, followed by a summary of the original contributions contained in this thesis. Promising avenues of further study are highlighted, accompanied by unpublished preliminary results in some cases.

12.1 Reflection

One of the initial challenges at the dawn of this thesis was to identify the “radiation spreading” phenomenon (discussed in Ch. 4), which was limiting the minimum feature size attainable in focused x-ray patterning. The idea to add a development step was inspired through a literature search; development procedures optimized by the electron beam lithography community in the 1970s worked just as well for x-ray lithography (patterned mask method) in the 1980s and 1990s. To that end, a post-exposure development step was introduced in an early experiment. The many fine details revealed in a PMMA layer after development viewed with an optical microscope prompted the desire to investigate those details with the high spatial resolution of an AFM. Immediately feature sizes smaller than our previous best were observed. The first experiment was so successful that development and/or using AFM to image the x-ray irradiated areas were incorporated into almost every subsequent experiment. This directly led to the determination of the true mechanism of “radiation

spreading” i.e. the PSF, right to its ultimate source within the zone plate. Experimenting with development steps allowed us to excavate buried material patterned in a polymer bilayer. It also revealed an onset of cross-linking which was used to determine detector efficiency, and so on. The addition of the development step resulted in a paradigm shift that spurred many original experiments.

12.2 Original contributions of this thesis

The major original contributions contained in this thesis are,

- Demonstrated the smallest feature size ever created with direct write focused x-rays (33 ± 4 nm in PMMA at 1 keV, Ch. 5). This is also the smallest by a zone plate lens, in any orientation, at any wavelength. Furthermore, this ranks among the smallest feature sizes created using the direct write method and photons, if not the smallest.
- Determined the mechanism of the “radiation spreading” phenomenon observed in focused x-ray patterning and lithography is due to the PSF, while at the same time disproved the “migration of a damaging species” hypotheses (Ch. 4).
- Developed a method to create sealed nanofluidic channels (90 nm x 90 nm) in polymer bilayers with tunable x-rays, and determined the design rules which regulate their fabrication (Ch. 6).
- Systematically tested several variables which were speculated by some to affect the radiation sensitivity of polymers, including dose rate and pre-exposure thermal

treatments. Neither affected the radiation sensitivity of PMMA (Ch. 7) or PAN (Ch. 9).

- Developed a method to determine the detector efficiency of a soft x-ray transmission detector involving the onset of negative mode for PMMA, and carried out this measurement at all ALS 5.3.2 type STXMs in existence at the time of submission (Ch. 7).
- Determined that the mechanism by which carbon contamination forms on irradiated surfaces is by secondary electrons emitted from the surface, rather than direct photoabsorption by the precursor molecules themselves, with implications which favour new mitigation strategies (Ch. 8).
- Discovered a misapplication of sensitivity descriptors for radiation damage in the literature and attempted to clarify the situation (Ch. 9).
- Developed a method to determine the PSF of a STXM using lithography and an AFM (Ch. 10).
- Discovered asymmetry in the PSFs of all STXMs tested (Ch. 10).
- Fabricated a variable temperature sample holder and tested it in all ALS 5.3.2 type STXMs in existence at the time of submission (Ch. 11).
- Experimentally determined that the beam-induced temperature rise of the sample within the focal spot of a STXM is <1 °C for both typical and extreme imaging conditions (Ch. 11).

12.3 Future work

12.3.1 Further reduction of minimum feature size

Electrons and ions achieve smaller minimum feature size relative to x-rays because they can be focused to smaller spot sizes, currently on the order of nanometres to angstroms. Both electron and x-ray optics continue to advance, however it does not seem likely that x-rays will ever be able to achieve a spot size equal to electrons at the same point in time. However, there should come a time at which they are technically equivalent for patterning and lithography. It has been observed that the minimum feature size attainable in polymeric resists is around 5 nm, whereas the electron beams used to make these features have a spot size even smaller than that. The resists are thought to have an intrinsic resolution limit which may be due to exposure from secondary electrons produced by the ionizing radiation within the film [B88b, BHR96]. Therefore it would appear that a sub-5 nm focused x-ray beam should produce the same minimum feature size as a sub-angstrom focused electron beam. Sub-5 nm x-ray focusing is a goal of several synchrotron beamlines (the goal is in fact 1 nm focusing at the NSLS-II Hard X-ray Nanoprobe beamline which is under construction at the time of submission). It is probable that this will be achieved by the end of the decade with multilayer Laue lenses [KMS&06] and multi-keV (hard) x-rays. In the future, it would be worthwhile to attempt patterning and lithography on these beamlines.

Staying with current STXMs, perhaps the most obvious way to decrease the minimum feature size would be to pattern with improved zone plates.

Zone plates with 12 nm outer most zone widths have recently been fabricated [CKR&09]. Another possibility would be to use the third order focal point rather than the first order for patterning, which provides a three times smaller spot size in theory (Eqn. 2.6). The third order focal length is one third that of the first order (Eqn. 2.7), with a corresponding reduction in A_0 ; the experiment would have to be done at a higher photon energy such as 800 eV or greater to provide workable component distances in STXM using the CXRO 25 nm Δr zone plates. One brief attempt to establish third order focus was made at 11.0.2 at 800 eV but it was not successful in the limited amount of time dedicated to that goal.

PMMA was chosen as a resist for this study because it is consistently found to be the highest resolution organic resist using many different radiation sources and patterning techniques. However, the more recently developed inorganic resist HSQ is becoming increasingly popular because of its even higher resolution [GH09, YCD&09]. It would be worthwhile to experiment with this resist.

12.3.2 Patterning at wavelengths relevant to industry

The wavelengths used in industry for high volume lithography are standardized and have decreased stepwise over time (Fig. 12.1). This is known as “wavelength scaling”, and it continues to be a major reason why integrated circuits and the size of devices which employ them have steadily decreased.

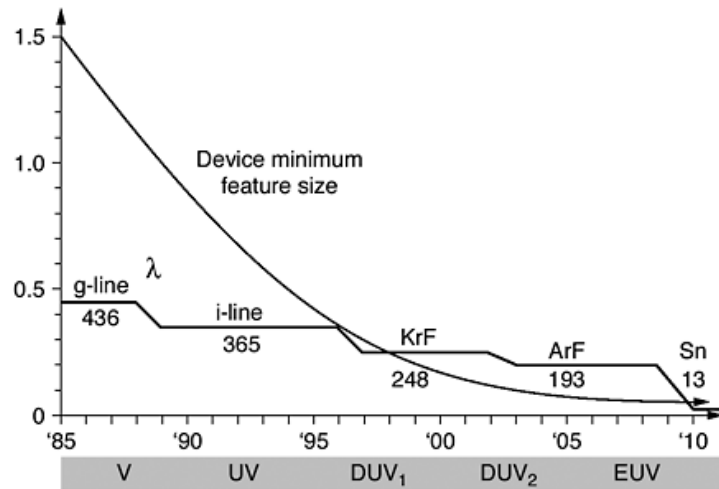


Figure 12.1: Plot depicting the stepwise decrease of the exposure wavelength used in industrial lithography systems over time, along with the decrease in device minimum feature size over the same period (from [WK09] Fig 1.3, © 2012 McGraw-Hill, used with permission).

Current state-of-the-art high volume lithography tools operate at 193 nm (6.4 eV) generated by ArF lasers. The next generation of tools is widely anticipated to operate at 13.5 nm (92 eV) generated by Xe or Sn plasmas. This technology is known as extreme ultraviolet lithography (EUVL). EUVL was expected to be introduced into the production lines of all major integrated circuit manufacturers by 2010 as depicted in Fig. 12.1. However this step has been repeatedly delayed; production with 193 nm ArF laser systems continues at present. Wavelength scaling is expected to continue beyond EUVL [TWP10, WH10]. The prime candidate wavelength after 13.5 nm is 6.7 nm (185 eV) possibly generated from Gd or Tb plasmas [OKW&10, MZL&12].

Both 92 eV and 185 eV are accessible with current STXMs. 11.0.2 has demonstrated operation at photon energies down to 80 eV [NTW&05], however it would be very challenging to pattern at 92 eV due to the very short distances

inside the STXM; with the CXRO 25 nm Δr zone plate operating at 92 eV, f is 445 μm , Δz is <100 nm, and the OSA must be mere tens of micrometres from the sample. 185 eV on the other hand can be reached at most STXMs used in this thesis, and is much more forgiving in terms of component distances. One attempt was made to demonstrate narrow lines in a 30 nm layer of PMMA patterned at 185 eV (Fig. 12.2).

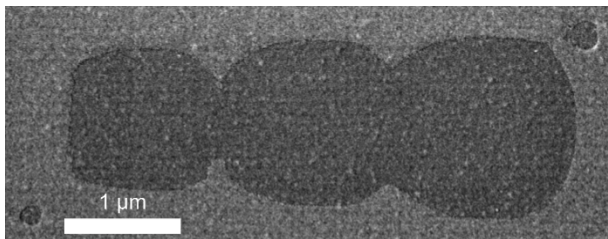


Figure 12.2: Scanning electron micrograph of developed PMMA patterned at 185 eV using 11.0.2.

Unfortunately the dose was too high and the pattern (three columns of 1 μm long lines) was over-exposed. The dose was unknown because the detector efficiency has not yet been determined at this photon energy for 11.0.2.

There are at the moment very few published works on 6.7 nm lithography, and there are currently few places to do such work. A possible project could involve testing new resists designed for high volume use at 6.7 nm provided by a collaborator in the lithography industry. Early identification of promising resist formulations will narrow the choices, and ultimately decrease the time necessary to develop and implement new high volume lithography technology.

12.3.3 Focused deep x-ray lithography

In deep x-ray (or deep etch) lithography a pattern on a mask is transferred into a thick (5 μm – 5 mm) layer of resist via keV x-ray exposure, which then undergoes a development procedure. The negligible scattering property of x-rays leads to very high aspect ratio features with almost perfectly vertical sidewalls. The patterned area then becomes a small metal part by electroplating in various metals. This process is known as LIGA (in German: Lithographische Galvanoformung Abformung) [EM91].

The potential exists for a direct write version of deep x-ray lithography, which would bypass the need to fabricate a mask. This would require a STXM with significant flux in the 1500 – 2500 eV range; the higher the photon energy the greater the penetration [HGØ80] and the thicker the resist layer that can be processed. As an added benefit, Δz for a given zone plate increases with increasing photon energy (Eqn. 2.9). Δz at 2500 eV is $\pm 2.5 \mu\text{m}$ for the CXRO 25 nm Δr zone plate. For a 40 nm Δr zone plate (another common size), Δz increases to $\pm 6.4 \mu\text{m}$. The central stop however becomes increasingly transmissive at these higher photon energies, which could reduce patterning contrast.

An initial attempt at focused deep x-ray lithography was made at 10ID-1. A 600 nm thick layer of PMMA on Si_3N_4 was fabricated by floating a 300 nm layer on top of another 300 nm layer, then annealing the sample at 150 °C for 1 h. Several 600 nm x 600 nm areas were patterned at various dwell times at 1 keV.

After patterning the samples were developed by a 30 s dip and stir in a 3:1 v/v IPA:MIBK solution, immediately followed by a 15 s dip and stir in IPA. A scanning electron micrograph of the developed structure is presented in Fig. 12.3.

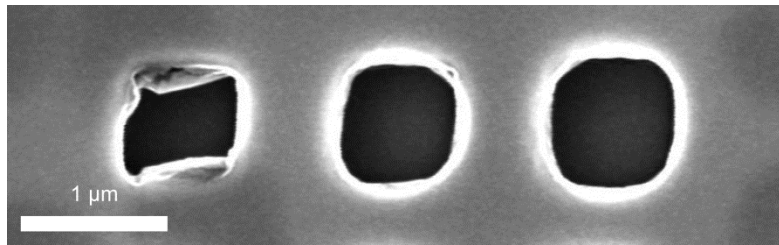


Figure 12.3: Scanning electron micrograph of 600 nm x 600 nm holes in a 600 nm layer of PMMA on Si₃N₄ patterned at 1 keV using 10ID-1.

The square areas were cleared down to the substrate. The dose for each square was unknown because the detector efficiency has not yet been determined at this photon energy for 10ID-1. SEM imaging caused a large amount of cracking and warping of the thick PMMA layer. The squares are rounded and misshapen, which was at least partly caused by SEM imaging. The SEM imaging conditions and the development conditions were those optimized for 30 – 100 nm layers of PMMA. Some immediate challenges of this project would be optimizing the thick resist sample preparation, adjusting the development conditions for thick resists [RKV&02], and finding acceptable SEM imaging conditions.

12.3.4 Towards a dedicated x-ray writer instrument

Advances in microscopy have become advances in lithography. The principles of immersion microscopy from the mid 1800s were applied to high

volume photolithography in the 2000s. The electron microscope of the 1930s became the electron beam writer by the 1970s. The atomic force microscope of the 1980s became the Dip Pen Nanolithography® system of the 2000s. History suggests the likelihood that the STXM is the starting point for a dedicated focused x-ray writer instrument of some sort. Until such an instrument arrives the following changes could be incorporated into existing or future STXMs that would facilitate existing patterning experiments and/or enable new ones.

12.3.4.1 Auto-focusing: Large areas, opaque substrates

Currently fine focus is achieved in STXM by scanning the zone plate to sample distance while observing transmission images of a thin opaque object amongst a transparent background. STXM samples must be thin enough to be transmissive at photon energies of interest (<300 nm for work at the C 1s edge) and positioned free standing or on x-ray transparent substrates such as Si₃N₄. These thin substrates are consequently extremely fragile. Current STXMs are also limited to patterning relatively small areas because they do not adapt the zone plate to sample distance to account for real non-flat substrates; currently the microscopes stay in reliable focus over approximately 80 µm x 80 µm using Si₃N₄ windows.

An auto-focusing system would enable both patterning on x-ray opaque substrates such as Si wafers, and in-focus patterning over larger areas. One simple idea would be to create four micrometre-sized holes in a Si wafer, possibly by

laser ablation, in the corners of a 2 cm x 1 cm rectangle (the approximate x - y stage travel limits of current STXMs). After mounting in the STXM, the tilt of the wafer could be determined by finding focus at each of the four holes, and noting the zone plate z positions. That information could be used to adjust the zone plate z motion during patterning so that the zone plate to sample distance would be constant over the area of the rectangle. The flatness of commercial Si wafers can be less than 50 nm across a 20 cm wafer, which is well within the ± 300 nm Δz of the STXM with CXRO 25 nm Δr zone plates at 300 eV. If the patterning does not have to be at the C 1s edge, it would be beneficial to pattern at a higher photon energy as the greater depth of focus (Eqn. 2.9) would be more forgiving. The holes could also be used as registration marks to enable several overlaid steps of processing and patterning as is often necessary in integrated circuit manufacture.

12.3.4.2 Throughput

Electrons or ions can be easily deflected and focused using electric or magnetic fields because they possess charge. During patterning the substrate is motionless while the beam is deflected above the substrate. The situation is different with x-rays as they do not possess charge. The substrate must be translated under the stationary beam for patterning and imaging, which is relatively slow in comparison. On the other hand, electrons and ions exhibit space charge. This repulsive force between like-charged particles limits the maximum

current that can be put into a narrow beam [B88b]. Patterning with charged particles can also lead to charge build up in certain resists and/or substrates such as quartz which can then deflect the incoming beam [ZFY&11, BSS&12]. These effects place a limit on ultimate patterning speed with charged particles. X-rays do not experience either of these effects which may one day result in an advantage for rapidly patterning extremely small feature sizes, but at the moment the motion of the stages from pixel to pixel is the rate limiting step.

The speed of patterning was in some cases limited by the minimum x-ray shutter speed. For example, the shortest period of time the shutter can go from closed to open to closed is about 1 ms [KT04]. In their current configurations, all of the STXM beamlines used in this thesis could provide more than enough dose in 1 ms to surpass the threshold necessary for positive mode development of PMMA while maintaining slit sizes necessary for diffraction limited focusing. A faster acting shutter could therefore provide some improvement in throughput.

12.3.4.3 Software

Several adjustments to the current PatternGen routine could lead to more efficient patterning experiments. Currently the PatternGen routine has a limitation on the maximum number of pixels it can write (20 000), and it takes a nearly a minute to offer the choice to save or discard the pattern generation header file after executing a pattern with many pixels. Also, PatternGen must be executed two or more times to do multiple patterns over the same area, such as for the

chemically selective patterning work in Ch. 6. It would be ideal if successive exposures at multiple photon energies could be input and executed with a single command.

Software additions could also increase patterning fidelity. In multi-bunch mode the storage ring current decreases over time at a predictable rate. Therefore the pixels which are the last to be patterned receive less dose than intended when the synchrotron is operating in this mode. This difference in dose was negligible for the patterns created in this thesis, which took no more than 10 min to complete, but it is expected to be large enough to cause fidelity issues for patterns with more pixels and/or longer exposure times. Adding an option to the PatternGen routine that would adjust each pixel's exposure time to correct for the predictable decaying ring current would increase pattern fidelity.

The PSF results in a dose overlap between adjacent pixels when patterning, which leads to non-uniform doses and decreased patterning fidelity especially at edges, corners or in densely patterned areas. This problem was noted during patterning experiments and is further discussed in Ch. 6.4.3. Several solutions, so called "proximity effect corrections", have been successfully implemented in electron beam lithography systems to counter this problem. The strategies include manipulating the shape of the patterned area, manipulating the dose, or equalizing the exposure background [MP89]. A PSF correction program has also been applied in a ZPAL system [MPG&05]. Incorporating a

PSF correction in the PatternGen routine would increase pattern fidelity. It would be most effective using PSF data obtained with the method developed in Ch. 10.

12.3.4.4 Is it practical?

It is probable that the minimum achievable feature size of focused x-ray lithography will be as good as electron beam lithography in 5 – 10 years (Ch. 12.3.1). But it is less likely that the throughput will be as good, and even less likely that the cost of the two systems will be remotely comparable. The very best commercially available electron beam writer systems today cost about four million Canadian dollars, which is about two orders of magnitude less than a STXM and an associated synchrotron (though it could be argued that synchrotrons can serve dozens of experiments simultaneously). The electron beam instrument can fit in a room of a few square metres, whereas a synchrotron usually requires its own hundreds-of-square-metre-sized building. At the moment, focused x-rays are not practical for patterning and lithography, for applications already covered by focused electron or ion beams.

Though the present performance doesn't exceed that of electron beam systems, it does rival them. If no such electron or ion instrument was available, the upgraded patterning ability of STXM would be advantageous. Other potential advantages which have yet to be explored are patterning samples that experience excessive charging with electrons or ions, and possibly focused deep x-ray lithography. The photon energy tunability remains the property which will enable

unique experiments, such as the work on nanofluidics (Ch. 6) and carbon contamination (Ch. 8); exploitation of the photon energy tunability will likely drive future applications of focused x-ray patterning and lithography.

12.3.5 Functional nanofluidic devices

Sealed sub-100 nm nanofluidic channels were created in a polymer bilayer using tunable focused x-rays in Ch. 6. This was largely a proof of concept experiment to demonstrate the formation of nanochannels by chemically selective lithography, and there was no clear goal as to what would be done with them afterwards. In a functional nanofluidic device the materials of the structure must ultimately be compatible with the solvent and analyte molecules. In addition, the device would have to be “plumbed” to control the flow into and out of the device. Our best idea at the moment is to align and bond a PDMS stamp with access holes on top of our devices. Other ideas are listed in Ch. 6.4. Going forward, the first step that would need to be settled upon is what the experiment(s) involving the fabricated nanochannels might be. Then hopefully compatible polymers with the right properties (criteria listed in Ch. 6.2.1) can be identified and finally methods of plumbing the devices could be attempted.

12.3.6 Deconvolution of the PSF from STXM images

The image of an object acquired using STXM (or any microscope) is a product of the object intensity convoluted with the PSF. If the PSF is known, then

it is possible to deconvolute the PSF from the image of an object to attain an image with enhanced spatial resolution [S87]. PSF deconvolution is commonly applied to certain methods of optical microscopy, and there are commercial software packages available for such work. PSF deconvolution was applied to STXM images using calculated PSFs in the early 1990s [JWA&91, JKW92], however this approach does not appear to have caught on within the STXM community. Since there is now a way to measure the real PSF in great detail (Ch. 10) it would be worthwhile to revisit PSF deconvolution experiments. These experiments would involve making the 100 pixel exposures in PMMA, followed by imaging the desired samples at the same photon energies. After the run, the PSF would be extracted from the exposures by the method outlined in Ch. 10. Conceivably the images acquired during the same run could then be deconvoluted by adapting the STXM data to a form acceptable to a commercial optical microscopy PSF deconvolution software package.

12.3.7 Variable temperature sample holder

The variable temperature sample holder was constructed to investigate beam heating in STXM (Ch. 11), but its utility is not limited to that experiment. The sample holder was also used to collect NEXAFS spectra of fatty acid molecules at elevated temperatures. The C 1s and O 1s NEXAFS spectra of stearic, palmitic, myristic and lauric acids showed no change with temperature until just above their respective melting points. The C 1s NEXAFS spectrum of

solid stearic acid collected at 25 °C is compared to the spectrum obtained of the liquid at 75 °C in Fig. 12.4.

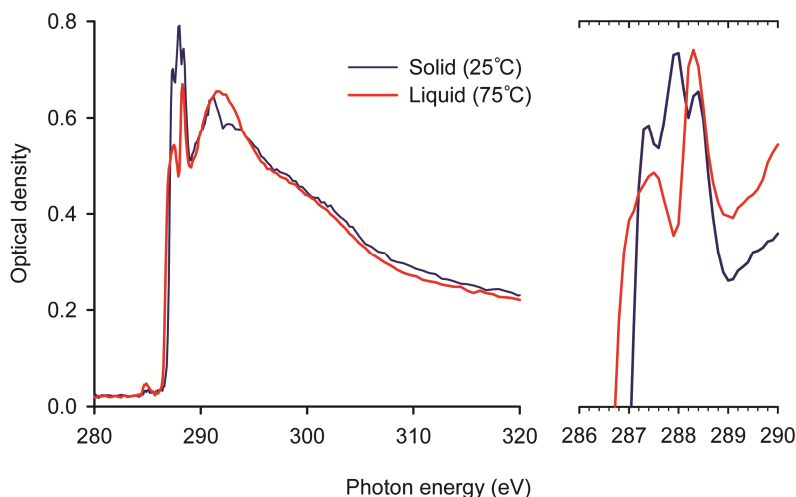


Figure 12.4: Comparison of the C 1s NEXAFS spectra of stearic acid in solid (blue) and liquid (red) phase, acquired at 11.0.2. The right plot has been rescaled to highlight the carbonyl peak shift.

The absorption peak in the spectrum of the solid at 288.4 eV is that of the carbonyl C atom, which was confirmed by comparing this spectrum to that of hexatriacontane ($C_{36}H_{74}$), a similar molecule with no carbonyl group that happens to have a similar melting point. This peak undergoes a slight but reproducible red shift to 288.3 eV in the liquid form. Our current hypothesis is that this is due to the conversion of the carboxylic acid from the hydrogen bonded dimer form in the solid phase [SO77] to the monomer form in the liquid phase. A similar shift was also observed at the O 1s edge (not shown).

Copies of the device have been made for collaborators and are enabling other science. Prof. Stephen Urquhart and Sahan Perera at the University of Saskatchewan are currently using a copy of the device to study the structure

dependence in the C 1s NEXAFS spectra of alkanes. Another copy is available for users at 10ID-1. The study of thermochromic materials would be an ideal fit for this device [WL99]. These materials are often heterogeneous mixtures of molecules including dyes and polymers, and sometimes polymer microcapsules. The thermally induced reactions occur on micrometre length scales, and many of the mechanisms of thermochromism are not yet known.

References

The reference code is formulated from the first letter of the last name of the first three authors, followed by the last two digits of the year of publication. If a reference has more than three authors, the initials are followed by an ampersand. If two references have the same author-year code, a sequence letter is added after the year for each publication.

- [A82] E. Abbe, *J. Royal Microscopical Soc.* **1882**, 2, 460-473.
- [A99] D. Attwood, *Soft X-rays and Extreme Ultraviolet Radiation*. Cambridge University Press: Cambridge, **1999**.
- [AGR&02] M.A. Avilés, J.M. Ginés, J.C.D. Rio, J. Pascual, J.L. Pérez-Rodríguez, P.J. Sánchez-Soto, *J. Thermal Anal. Calorim.* **2002**, 67, 177-188.
- [AH08] H. Ade, A.P. Hitchcock, *Polymer* **2008**, 49, 643-675.
- [AJZ&04] D. Amy, L. Jiang, R. Zheng, M. Feldman, F. Cerrina, S. Dhuey, Q. Leonard, D. Thielman, *J. Vac. Sci. Technol. B* **2004**, 22, 3570-3574.
- [ATM09] T.L. Andrew, H.Y. Tsai, R. Menon, *Science* **2009**, 324, 917-921.
- [AU02] H. Ade, S. Urquhart, *NEXAFS Spectroscopy and Microscopy of Natural and Synthetic Polymers*, pg. 290 In T.-K. Sham, ed., *Chemical Applications of Synchrotron Radiation, Part II: X-Ray Applications*. World Scientific Publishing Co.: Singapore, **2002**.
- [AZC&92] H. Ade, X. Zhang, S. Camerson, C. Costello, J. Kirz, S. Williams, *Science* **1992**, 258, 972-975.
- [B58] F.A. Bovey, *The Effects of Ionizing Radiation on Natural and Synthetic High Polymers*, Polymer Reviews, vol. 1. Interscience: New York-London, **1958**.
- [B80] G.R. Brewer, *Electron-Beam Technology in Microelectronic Fabrication*. Academic Press: New York, **1980**.
- [B82] J.H. Barrett, *Int. J. Appl. Radiat. Isot.* **1982**, 33, 1177-1187.
- [B88a] J.P. Blewett, *Nucl. Instrum. Meth. A* **1988**, 266, 1-9.
- [B88b] A.N. Broers, *IBM J. Res. Develop.* **1988**, 32, 502-513.
- [BAB&07] F. Bonfigli, S. Almaviva, G. Baldacchini, S. Bollanti, F. Flora, A. Lai, R.M. Montereali, E. Nichelatti, G. Tomassetti, A. Ritucci, L. Reale, A.Y. Faenov, T.A. Pikuz, R. Larciprete, L. Gregoratti, M. Kiskinova, *Spectrochimica Acta B* **2007**, 62, 631-635.
- [BBC87] R.E. Burge, M.T. Browne, P. Charalambous, *Microelectron. Eng.* **1987**, 6, 227-232.
- [BBC&10] M. Bei, M. Borland, Y. Cai, P. Elleaume, R. Gerig, K. Harkay, L. Emery, A. Hutton, R. Hettel, R. Nagaoka, D. Robin, C. Steier, *Nucl. Instrum. Meth. A* **2010**, 622, 518-535.

- [BCN&09] S. Bajt, H.N. Chapman, A.J. Nelson, R.W. Lee, S. Toleikis, P. Mirkarimi, J.B. Alameda, S.L. Baker, H. Vollmer, R.T. Graff, A. Aquila, E.M. Gullikson, J. Meyer Ilse, E.A. Spiller, J. Krzywinski, L. Juha, J. Chalupský, V. Hájková, J. Hajdu, T. Tschentscher, *Proc. SPIE* **2009**, 7361, 73610J.
- [BG03] D. Briggs, J.T. Grant, *Surface Analysis by Auger and X-Ray Photoelectron Spectroscopy*. IM Publications: West Sussex, **2003**. pg. 424.
- [BHR96] A.N. Broers, A.C.F. Hoole, J.M. Ryan, *Microelec. Eng.* **1996**, 32, 131-142.
- [BJ03] T. Beetz, C. Jacobsen, *J. Synchrotron Rad.* **2003**, 10, 280-283.
- [BSS&12] L.D. Bozano, R. Sooriyakumaran, L.K. Sundberg, M.I. Sanchez, E.M. Lofano, C.T. Rettner, T. Nagasawa, S. Watanabe, Y. Kawai, N. Palavesam, G.G. Montano, *Proc. SPIE* **2012**, 8325, 83250X.
- [BW99] M. Born, E. Wolf, *Principles of Optics*, 7th ed. Cambridge University Press: Cambridge, **1999**. Ch. 8.5.
- [C60] A. Charlesby, *Atomic Radiation and Polymers*, International Series of Monographs on Radiation Effects in Materials, Vol. 1. Pergamon: Oxford, **1960**.
- [C75] T.H.P. Chang, *J. Vac. Sci. Technol.* **1975**, 12, 1271-1275.
- [C04] J.A. Clarke, *The Science and Technology of Undulators and Wigglers*. Oxford University Press: New York, **2004**.
- [C12] Center for X-ray Optics (CXRO) website, **2012**, retrieved from http://henke.lbl.gov/optical_constants/
- [CCM66] P.P. Castrucci, R.H. Collins, W.R. Marzinsky, *Reprographics* **1966**, 4, 11-15, 26, 35.
- [CHW&06] C.-H. Chen, M.-L. Huang, S.-C. Wang, R. Klauser, A. Shaporenko, M. Zharnikov, *J. Phys. Chem. B* **2006**, 110, 17878-17883.
- [CKR96] S.Y. Chou, P.R. Krauss, P.J. Renstrom, *J. Vac. Sci. Technol. B* **1996**, 14, 4129-4133.
- [CKR&09] W. Chao, J. Kim, S. Rekawa, P. Fischer, E.H. Anderson, *Opt. Express* **2009**, 17, 17669-17677.
- [CKS&10] A.G. Caster, S. Kowarik, A.M. Schwartzberg, S.R. Leone, A. Tivanski, M.K. Gilles, *J. Vac. Sci. Technol. B* **2010**, 28, 1304-1313.
- [CLB07] B. Cord, J. Lutkenhaus, K.K. Berggren, *J. Vac. Sci. Technol. B* **2007**, 25, 2013-2016.
- [CMC&88] J.O. Choi, J.A. Moore, J.C. Corelli, J.P. Silverman, H. Bakhru, *J. Vac. Sci. Technol. B* **1988**, 6, 2286-2289.
- [CPB&05] D. Chao, A. Patel, T. Barwicz, H.I. Smith, R. Menon, *J. Vac. Sci. Technol. B* **2005**, 23, 2657-2661.
- [CUA02] T. Coffey, S.G. Urquhart, H. Ade, *J. Elec. Spectrosc. Relat. Phenom.* **2002**, 122, 65-78.
- [D72] M. Dole, ed. *The Radiation Chemistry of Macromolecules*. Academic Press: New York, **1972**.
- [D75] W.S. DeForest, *Photoresist: Materials and Processes*. McGraw Hill: New York, **1975**.
- [DD71] I.G. Draganić, Z.D. Draganić, *The Radiation Chemistry of Water*. Academic Press: New York, **1971**.

- [DGR&11] C. David, S. Gorelick, S. Rutishauser, J. Krzywinski, J. Vila-Comamala, V.A. Guzenko, O. Bunk, E. Färm, M. Ritala, M. Cammarata, D.M. Fritz, R. Barrett, L. Samoylova, J. Grünert, H. Sinn, *Nature Sci. Rep.* **2011**, *1*, 57.
- [DHC&08] W.F. van Dorp, C.W. Hagen, P.A. Crozier, P. Kruit, *Nanotechnology* **2008**, *19*, 225305.
- [DMS&98] D.C. Duffy, J.C. McDonald, O.J.A. Schueller, G.M. Whitesides, *Anal. Chem.* **1998**, *70*, 4974-4984.
- [E44] P. Eisler, *Manufacture of Electric Circuit Components*, **1944**, US Patent 2441960.
- [E47] W. Ehrenberg, *Nature* **1947**, *160*, 330-331.
- [EKL&09] G.G. Echner, W. Kilby, M. Lee, E. Earnst, S. Sayeh, A. Schlaefer, B. Rhein, J.R. Dooley, C. Lang, O. Blanck, E. Lessard, C.R. Maurer Jr., W. Schlegel, *Phys. Med. Biol.* **2009**, *54*, 5359-5380.
- [EM91] W. Ehrfeld, D. Münchmeyer, *Nucl. Instrum. Meth. A* **1991**, *303*, 523-531.
- [F10] J.T. Fourkas, *J. Phys. Chem. Lett.* **2010**, *1*, 1221-1227.
- [F50] E. Fermi, *Nuclear Physics: A Course Given by Enrico Fermi at the University of Chicago*. University of Chicago Press: Chicago, **1950**. Ch. 5, pg. 75.
- [FCJ&98] M. Feser, M. Carlucci-Dayton, C. Jacobsen, J. Kirz, U. Neuhäusler, G. Smith, B. Yu, *Proc. SPIE* **1998**, *3449*, 19-29.
- [FKT04] S. Fakra, A.L.D. Kilcoyne, T. Tyliczszak, *AIP Conf. Proc.* **2004**, *705*, 973-976.
- [FRW&10] U. Frommherz, J. Raabe, B. Watts, R. Stefani, U. Ellenberger, *AIP Conf. Proc.* **2010**, *1234*, 429-432.
- [FST&77] R. Feder, E. Spiller, J. Topalian, A.N. Broers, W. Gudat, B.J. Panessa, Z.A. Zadunaisky, J. Sedat, *Science* **1977**, *197*, 259-260.
- [FSW&10] R. Follath, J.S. Schmidt, M. Weigand, K. Fauth, *AIP Conf. Proc.* **2010**, *1234*, 323-326.
- [FU05] J. Fu, S.G. Urquhart, *J. Phys. Chem. A* **2005**, *109*, 11724-11732.
- [GG70] R. Glang, L.V. Gregor, "Generation of patterns in thin films". In, *Handbook of thin film technology*, L.I. Maissel, R. Glang, eds. McGraw-Hill: Toronto, **1970**. Ch. 7.3.
- [GH09] A.E. Grigorescu, C.W. Hagen, *Nanotechnology* **2009**, *20*, 292001.
- [GP75] I.S. Grant, W.R. Philips, *Electromagnetism*. Wiley: New York, **1975**. Ch. 10.
- [GSE&06] R. Gronheid, H.H. Solak, Y. Ekinci, A. Jouve, F.V. Roey, *Microelec. Eng.* **2006**, *83*, 1103-1106.
- [H12] A.P. Hitchcock, *Soft X-Ray Imaging and Spectromicroscopy*. In, *Handbook of Nanoscopy*, Vol. 2, Ch. 22., edited by Tendeloo, G. V., Dyck, D. V. & Pennycook, S. J. Wiley **2012**.
- [H59] J.A. Hoerni, *Method of Manufacturing Semiconductor Devices*, **1959**, US Patent 3025589.
- [H69] M. Hatzakis, *J. Electrochem. Soc.* **1969**, *116*, 1033-1037.
- [H70] M.A. Hayat, *Principles and Techniques of Electron Microscopy: Biological Applications*, Vol. 1. Van Nostrand Reinhold Co.: New York, **1970**. Ch. 1.
- [H77] H. Hiraoka, *IBM J. Res. Develop.* **1977**, *21*, 121-130.
- [H92] J.R. Helliwell, *Macromolecular Crystallography With Synchrotron Radiation*. Cambridge University Press: Cambridge, **1992**.
- [HBC&09] M.R. Howells, T. Beetz, H.N. Chapman, C. Cui, J.M. Holton, C.J. Jacobsen, J. Kirz, E. Lima, S. Marchesini, H. Miao, D. Sayre, D.A. Shapiro, J.C.H. Spence, D. Starodub, *J. Elec. Spectrosc. Relat. Phenom.* **2009**, *170*, 4-12.

- [HCH&07] W. Haske, V.W. Chen, J.M. Hales, W. Dong, S. Barlow, S.R. Marder, J.W. Perry, *Opt. Express* **2007**, *15*, 3426-3436.
- [HG06] E.J. Hall, A.J. Giaccia, *Radiobiology for the Radiobiologist*, 6th ed. Lippincott Williams & Wilkins: Philadelphia, **2006**.
- [HGD93] B.L. Henke, E.M. Gullikson, J.C. Davis, *Atomic Data and Nuclear Data Tables* **1993**, *54*, 181-342.
- [HGØ80] J.H. Hubbell, H.A. Gimm, I. Øverbø, *J. Phys. Chem. Ref. Data* **1980**, *9*, 1023–1147.
- [HHJ09] M.R. Howells, A.P. Hitchcock, C.J. Jacobsen, *J. Elec. Spectrosc. Relat. Phenom.* **2009**, *170*, 1-3.
- [HHS68] I. Haller, M. Hatzakis, R. Srinivasan, *IBM J. Res. Develop.* **1968**, *12*, 251-256.
- [HJA12] A. Hitchcock, “Gas phase core excitation database.” Retrieved from <http://unicorn.mcmaster.ca/corex/cedb-title.html>
C. Jacobsen, “X-1A x-ray absorption spectra.” Retrieved from <http://xray1.physics.sunysb.edu/~micros/xas/xas.html>
O. Dhez, H. Ade, S. Urquhart, “Polymers NEXAFS spectroscopy.” Retrieved from <http://www.physics.ncsu.edu/stxm/polymerspectro/>
- [HJW07] M. Howells, C. Jacobsen, T. Warwick, *Principles and applications of zone plate x-ray microscopes*. In P.W. Hawkes, J.C. Spence, eds. *Science of Microscopy*, Vol. 2, Ch. 13. New York: Springer Science+Business Media, **2007**.
- [HSL&04] W. Hu, K. Sarveswaran, M. Lieberman, G.H. Bernstein, *J. Vac. Sci. Technol. B* **2004**, *22*, 1711-1716.
- [I10] IBA Industrial, Inc. White paper – X-ray sterilization, March 2010. Edgewood, New York, **2010**.
- [IBP11] G.E. Ice, J.D. Budai, J.W.L. Pang, *Science* **2011**, *334*, 1234-1239.
- [J31] H.H. Johann, *Zeitschrift Für Physik* **1931**, *69*, 185-206.
- [J33] T. Johansson, *Zeitschrift Für Physik* **1933**, *82*, 507-528.
- [JFP&08] R.W. Johnstone, I.G. Foulds, M.V. Pallapa, A.M. Parameswaran, *J. Micro/Nanolithogr. MEMS MOEMS* **2008**, *7*, 043006.
- [JHK&90] C. Jacobsen, M. Howells, J. Kirz, S. Rothman, *J. Opt. Soc. Am. A* **1990**, *7*, 1847-1861.
- [JKW92] C. Jacobsen, J. Kirz, S. Williams, *Ultramicroscopy* **1992**, *47*, 55-79.
- [JVP&07] K. Jefimovs, J. Vila-Comamala, T. Pilvi, J. Raabe, M. Ritala, C. David, *Phys. Rev. Lett.* **2007**, *99*, 264801.
- [JWA&91] C. Jacobsen, S. Williams, E. Anderson, M.T. Browne, C.J. Buckley, D. Kern, J. Kirz, M. Rivers, X. Zhang, *Optics Comm.* **1991**, *86*, 351-364.
- [JWF&00] C. Jacobsen, S. Wirick, G. Flynn, C. Zimba, *J. Microscopy* **2000**, *197*, 173-184.
- [K74] J. Kirz, *J. Opt. Soc. Am.* **1974**, *64*, 301-309.
- [KCH&05] R. Klauser, C.-H. Chen, M.-L. Huang, S.-C. Wang, T.J. Chuang, M. Zharnikov, *J. Elec. Spectrosc. Relat. Phenom.* **2005**, *144-147*, 393-396.
- [KF96] M. Khoury, D.K. Ferry, *J. Vac. Sci. Technol. B* **1996**, *14*, 75-79.
- [KHW&03] R. Klauser, I.-H. Hong, S.-C. Wang, M. Zharnikov, A. Paul, A. Götzhäuser, A. Terfort, T.J. Chuang, *J. Phys. Chem. B* **2003**, *107*, 13133-13142.
- [KHW&04] R. Klauser, M.-L. Huang, S.-C. Wang, C.-H. Chen, T.J. Chuang, A. Terfort, M. Zharnikov, *Langmuir* **2004**, *20*, 2050-2053.

- [KJH95] J. Kirz, C. Jacobsen, M. Howells, *Q. Rev. Biophys.* **1995**, *28*, 33-130.
- [KKL&07] K.V. Kaznatcheev, Ch. Karunakaran, U.D. Lanke, S.G. Urquhart, M. Obst, A.P. Hitchcock, *Nucl. Inst. Meth. A* **2007**, *582*, 96-99.
- [KL84] M.C. King, K.J. Laidler, *Arch. Hist. Exact Sci.* **1984**, *30*, 45-86.
- [KMS&06] H.C. Kang, J. Maser, G.B. Stephenson, C. Liu, R. Conley, A.T. Macrander, S. Vogt, *Phys. Rev. Lett.* **2006**, *96*, 127401.
- [KPG09] M. Koechlin, G. Poberaj, P. Günter, *Rev. Sci. Instrum.* **2009**, *80*, 085105.
- [KR85] J. Kirz, H. Rarback, *Rev. Sci. Instrum.* **1985**, *56*, 1-13.
- [KT04] A.L.D. Kilcoyne, T. Tylliszczak, *AIP Conf. Proc.* **2004**, *705*, 605-607.
- [KTO&99] R.S. Kane, S. Takayama, E. Ostuni, D.E. Ingber, G.M. Whitesides, *Biomaterials* **1999**, *20*, 2363-2376.
- [KTS&03] A.L.D. Kilcoyne, T. Tylliszczak, W.F. Steele, S. Fakra, P. Hitchcock, K. Franck, E. Anderson, B. Harteneck, E.G. Rightor, G.E. Mitchell, A.P. Hitchcock, L. Yang, T. Warwick, H. Ade, *J. Synchrotron Rad.* **2003**, *10*, 125-136.
- [KTS&97] N. Kamijo, S. Tamura, Y. Suzuki, K. Handa, A. Takeuchi, S. Yamamoto, M. Ando, K. Ohsumi, H. Kihara, *Rev. Sci. Instrum.* **1997**, *68*, 14-16.
- [LCK&11] S.Y. Lee, I.H. Cho, J.M. Kim, H.C. Kang, D.Y. Noh, *J. Synchrotron Rad.* **2011**, *18*, 143-147.
- [LGD&02] R. Larciprete, L. Gregoratti, M. Danailov, R.M. Monteverde, F. Bonfigli, M. Kiskinova, *Appl. Phys. Lett.* **2002**, *80*, 3862-3864.
- [LGG&09] L. Li, R.R. Gattass, E. Gershgoren, H. Hwang, J.T. Fourkas, *Science* **2009**, *324*, 910-913.
- [LH11] A.F.G. Leontowich, A.P. Hitchcock, *Appl. Phys. A* **2011**, *103*, 1-11.
- [LH12a] A.F.G. Leontowich, A.P. Hitchcock, *Analyst* **2012**, *137*, 370-375.
- [LH12b] A.F.G. Leontowich, A.P. Hitchcock, *Proc. SPIE* **2012**, *8323*, 83231D.
- [LH12c] A.F.G. Leontowich, A.P. Hitchcock, *J. Vac. Sci. Technol. B* **2012**, *30*, 030601.
- [LHT&12] A.F.G. Leontowich, A.P. Hitchcock, T. Tylliszczak, M. Weigand, J. Wang, C. Karunakaran, *J. Synchrotron Rad.* **2012**, *19*, forthcoming.
- [LTH11] A.F.G. Leontowich, T. Tylliszczak, A.P. Hitchcock, *Proc. SPIE* **2011**, *8077*, 80770N.
- [M86] A.G. Michette, *Optical Systems for Soft X Rays*. Plenum: New York, **1986**. Ch. 8.
- [MBD&05] R.M. Monteverde, F. Bonfigli, G. Dietler, L. Gregoratti, M. Kiskinova, R. Larciprete, T. Marolo, S.K. Sekatskii, *Phys. Stat. Sol. C* **2005**, *2*, 298-301.
- [MC91] J.A. Moore, J.O. Choi, "Degradation of Poly(methyl methacrylate): Deep UV, x-ray, electron-beam, and proton-beam irradiation". In *Radiation effects on Polymers*, R.L. Clough, S.W. Shalaby, eds. ACS Symposium Series No. 475. American Chemical Society: Washington, DC, **1991**. Ch. 11, pg. 156-192.
- [MDD92] C.R.K. Marrian, E.A. Dobisz, J.A. Dagata, *J. Vac. Sci. Technol. B* **1992**, *10*, 2877-2881.
- [MHK&05] D.M. Mills, J.R. Helliwell, Å. Kvik, T. Ohta, I.A. Robinson, A. Authier, *J. Synchrotron Rad.* **2005**, *12*, 385.
- [MHK&10] H. Mimura, S. Handa, T. Kimura, H. Yumoto, D. Yamakawa, H. Yokoyama, S. Matsuyama, K. Inagaki, K. Yamamura, Y. Sano, K. Tamasaku, Y. Nishino, M. Yabashi, T. Ishikawa, K. Yamauchi, *Nature Phys.* **2010**, *6*, 122-125.
- [MI89] H. Makabe, K. Iwahashi, *Soft X-ray Lithographic System* **1989**, US Patent 4945551.

- [MP89] S.P. Murarka, M.C. Peckerar, *Electronic Materials: Science and Technology*. Academic Press: Boston, **1989**. Pg. 476-480.
- [MPG&05] R. Menon, A. Patel, D. Gil, H.I. Smith, *Materials Today* **2005**, *8*, 26-33.
- [MPK&05] L. Muntean, R. Planques, A.L.D. Kilcoyne, S.R. Leone, M.K. Gilles, W.D. Hinsberg, *J. Vac. Sci. Technol. B* **2005**, *23*, 1630-1636.
- [MS60] G. Möllenstedt, R. Speidel, *Physikalische Blätter* **1960**, *16*, 192-198.
- [MT10] B.W.J. McNeil, N.R. Thompson, *Nature Photon.* **2010**, *4*, 814-821.
- [MWK&08] N. Murphy-DuBay, L. Wang, E.C. Kinzel, S.M.V. Uppuluri, X. Xu, *Opt. Express* **2008**, *16*, 2584-2589.
- [MZL&12] I.A. Makhotkin, E. Zoethout, E. Louis, A.M. Yakunin, S. Müllender, F. Bijkerk, *Proc. SPIE* **2012**, *8322*, 832213.
- [NTW&05] H.J. Nilsson, T. Tyliczszak, R.E. Wilson, L. Werme, D.K. Shuh, *Anal. Bioanal. Chem.* **2005**, *383*, 41-47.
- [OHV&04] D.L. Olynick, B.D. Harteneck, E. Veklerov, M. Tendulkar, J.A. Liddle, A.L.D. Kilcoyne, T. Tyliczszak, *J. Vac. Sci. Technol. B* **2004**, *22*, 3186-3190.
- [OKW&10] T. Otsuka, D. Kilbane, J. White, T. Higashiguchi, N. Yugami, T. Yatagai, W. Jiang, A. Endo, P. Dunne, G. O'Sullivan, *Appl. Phys. Lett.* **2010**, *97*, 111503.
- [P01] M. Planck, *Ann. Phys.* **1901**, *309*, 553-563.
- [P83] H.C. Pollock, *Am. J. Phys.* **1983**, *51*, 278-280.
- [P99] M.N. Piancastelli, *J. Elec. Spectrosc. Relat. Phenom.* **1999**, *100*, 167-190.
- [PAM98] F.J. Pantenburg, S. Achenbach, J. Mohr, *Microsystem Tech.* **1998**, *4*, 89-93.
- [PDC00] A. Pépin, D. Decanini, Y. Chen, *J. Vac. Sci. Technol. B* **2000**, *18*, 2981-2985.
- [PHC&97] M. Park, C. Harrison, P.M. Chaikin, R.A. Register, D.H. Adamson, *Science* **1997**, *276*, 1401-1404.
- [PL05] C. Palmer, E. Loewen, *Diffraction Grating Handbook*, 6th ed. Newport Corp.: Rochester, **2005**.
- [PZX&99] R.D. Piner, J. Zhu, F. Xu, S. Hong, C.A. Mirkin, *Science* **1999**, *283*, 661-663.
- [R12] Registered Institution for Promoting Synchrotron Radiation Research, Japan Synchrotron Radiation Research Institute, *Spring-8 Detailed Brochure*. **2012**, Retrieved from http://www.spring8.or.jp/en/news_publications/publications/sp8_brochure/
- [R79] Lord Rayleigh, *Phil. Mag.* **1879**, *8*, 403-411.
- [R96] W.C. Röntgen, *Nature* **1896**, *53*, 274-276.
- [RKK&84] H. Rarback, J.M. Kenney, J. Kirz, M.R. Howells, P. Chang, P.J. Coane, R. Feder, P.J. Houzago, D.P. Kern, D. Sayre, "Recent results from the Stony Brook scanning microscope". In *X-ray Microscopy*, G. Schmahl, D. Rudolf, eds. Berlin: Springer, **1984**.
- [RKV&02] M.J. Rooks, E. Kratschmer, R. Viswanathan, J. Katine, R.E. Fontana, S.A. MacDonald, *J. Vac. Sci. Technol. B* **2002**, *20*, 2937-2941.
- [RLR86] R.A. Rosenberg, P.J. Love, V. Rehn, *Phys. Rev. B* **1986**, *33*, 4034-4037.
- [RMF&97] R.A. Rosenberg, Q. Ma, W. Farrell, M. Keefe, D.C. Mancini, *Rev. Sci. Instrum.* **1997**, *68*, 2550-2553.
- [RS80] D. Rudolph, G. Schmahl, *Ann. N Y Acad. Sci.* **1980**, *342*, 94-104.
- [RTF&08] J. Raabe, G. Tzvetkov, U. Flechsig, M. Böge, A. Jaggi, B. Sarafimov, M.G.C. Vernooij, T. Huthwelker, H. Ade, D. Kilcoyne, T. Tyliczszak, R.H. Fink, C. Quitmann, *Rev. Sci. Instrum.* **2008**, *79*, 113704.

- [RW09] W.H. Roos, G.J.L. Wuite, *Adv. Materials* **2009**, *21*, 1187-1192.
- [S10] D. Schwartz, *PNAS*, **2010**, *107*, 7190-7195.
- [S73] A.J. Swallow, *Radiation Chemistry: An Introduction*. Wiley: New York, **1973**.
- [S87] E.G. Steward, *Fourier Optics: An Introduction*. Ellis Horwood Ltd.: Chichester, **1987**.
- [S92] J. Stöhr, *NEXAFS Spectroscopy*. Springer: Berlin, **1992**.
- [S97a] H.I. Smith, *Maskless Lithography Using a Multiplexed Array of Fresnel Zone Plates* **1997**, US Patent 5900637.
- [S97b] S.J. Spector, *Diffraction Optics for Soft X Rays*, PhD thesis. State University of New York: Stony Brook, **1997**. Ch. 6.
- [SCL02] S. Sun, K.S.L. Chong, G.J. Leggett, *J. Am. Chem. Soc.* **2002**, *124*, 2414-2415.
- [SKO&79] R.L. Seliger, R.L. Kubena, R.D. Olney, J.W. Ward, V. Wang, *J. Vac. Sci. Technol.* **1979**, *16*, 1610-1612.
- [SL04] S. Sun, G.J. Leggett, *Nano Lett.* **2004**, *4*, 1381-1384.
- [SO77] K. Sato, M. Okada, *J. Crystal Growth* **1977**, *42*, 259-263.
- [SRS&10] I. Schmid, J. Raabe, B. Sarafimov, C. Quitmann, S. Vranjkovic, Y. Pellmont, H.J. Hug, *Ultramicroscopy*, **2010**, *110*, 1267-1272.
- [SS72] D.L. Spears, H.I. Smith, *Electronics Lett.* **1972**, *8*, 102-104.
- [SS00] I. Snigireva, A. Snigirev, *AIP Conf. Proc.* **2000**, *507*, 76-83.
- [T52] W.H.F. Talbot, "Improvements in the art of engraving", **1852**, British patent 565.
- [T88] J. Thieme, *Theoretical investigations of imaging properties of zone plates and zone plate systems using diffraction theory*, in: D. Sayre, M.R. Howells, J. Kirz, H. Rarback, eds. *X-ray Microscopy II*. Springer-Verlag: Berlin, **1988**. pg. 70-79.
- [TAG&09] A. Thompson, D. Attwood, E. Gullikson, M. Howells, K.-J. Kim, J. Kirz, J. Kortright, I. Lindau, Y. Liu, P. Pianetta, A. Robinson, J. Scofield, J. Underwood, G. Williams, H. Winick, eds. *Center for X-ray Optics and Advanced Light Source X-ray Data Booklet*, 3rd ed. Lawrence Berkeley National Laboratory: Berkeley, **2009**. Ch. 2.
- [TDH&02] A. Tarun, M.R.H. Daza, N. Hayazawa, Y. Inouye, S. Kawata, *Appl. Phys. Lett.* **2002**, *80*, 3400-3402.
- [TDM&08] P. Thibault, M. Dierolf, A. Menzel, O. Bunk, C. David, F. Pfeiffer, *Science*, **2008**, *321*, 379-382.
- [TWB83] L.F. Thompson, C.G. Wilson, M.J. Bowden, eds. *Introduction to Microlithography: Theory, Materials, and Processing*. Washington, D.C.: The American Chemical Society, **1983**.
- [TWK&04] T. Tylliszczak, T. Warwick, A.L.D. Kilcoyne, S. Fakra, D.K. Shuh, T.H. Yoon, G.E. Brown, S. Andrews, V. Chembrolu, J. Strachan, Y. Acremann, *AIP Conf. Proc.* **2004**, *705*, 1356-1359.
- [TWP10] G. Tallents, E. Wagenaars, G. Pert, *Nature Photon.* **2010**, *4*, 809-811.
- [UA02] S.G. Urquhart, H. Ade, *J. Phys. Chem. B* **2002**, *106*, 8531-8538.
- [VBB&07] G. Vaschenko, F. Brizuela, H. Bravo, C.S. Menoni, J.J. Rocca, O. Hemberg, B. Frazer, S. Bloom, W. Chao, E.H. Anderson, D.T. Attwood, "Soft X-Ray Laser Ablation of Nanometer-Scale Features", *X-ray Lasers 2006, Springer Proceeding in Physics* **2007**, *115*, 497-502.
- [VCJ&01] S. Vogt, H.N. Chapman, C. Jacobsen, R. Medenwaldt, *Ultramicroscopy* **2001**, *87*, 25-44.

- [VGF&11] J. Vila-Comamala, S. Gorelick, E. Färm, C.M. Kewish, A. Diaz, R. Barrett, V.A. Guzenko, M. Ritala, C. David, *Opt. Express* **2011**, *19*, 175-184.
- [W03] H. Wiedemann, *Synchrotron Radiation*. Springer-Verlag: Berlin, **2003**.
- [W08] J. Wang, *Radiation Chemistry by Soft X-ray Spectromicroscopy*, Ph.D. thesis. McMaster University: Hamilton, **2008**.
- [WAB&00] B. Winn, H. Ade, C. Buckley, M. Feser, M. Howells, S. Hulbert, C. Jacobsen, K. Kaznacheyev, J. Kirz, A. Osanna, J. Maser, I. McNulty, J. Miao, T. Oversluisen, S. Spector, B. Sullivan, Y. Wang, S. Wirick, H. Zhang, *J. Synchrotron Rad.* **2000**, *7*, 395-404.
- [WAK&02] T. Warwick, H. Ade, D. Kilcoyne, M. Kraitscher, T. Tyliszczak, S. Fakra, A. Hitchcock, P. Hitchcock, H. Padmore, *J. Synchrotron Rad.* **2002**, *9*, 254-257.
- [WBH01] D.M. Worrall, M. Birkinshaw, M.J. Hardcastle, *Mon. Not. R. Astron. Soc.* **2001**, *326*, L7-L12.
- [WBW&09] J. Wang, G.A. Botton, M.M. West, A.P. Hitchcock, *J. Phys. Chem. B* **2009**, *113*, 1869-1876.
- [WH10] C. Wagner, N. Harned, *Nature Photon.* **2010**, *4*, 24-26.
- [WK09] B. Wu, A. Kumar (eds.) *Extreme Ultraviolet Lithography*. New York: McGraw-Hill, **2009**.
- [WL99] M.A. White, M. LeBlanc, *J. Chem. Ed.* **1999**, *76*, 1201-1205.
- [WML&09] J. Wang, C. Morin, L. Li, A.P. Hitchcock, A. Scholl, A. Doran, *J. Elec. Spectrosc. Relat. Phenom.* **2009**, *170*, 25-36.
- [WRH92] A.T. Wen, E. Rühl, A.P. Hitchcock, *Organometallics* **1992**, *11*, 2559-2569.
- [WSH07] J. Wang, H.D.H. Stöver, A.P. Hitchcock, *J. Phys. Chem. C* **2007**, *111*, 16330-16338.
- [WSH&07] J. Wang, H.D.H. Stöver, A.P. Hitchcock, T. Tyliszczak, *J. Synchrotron Rad.* **2007**, *14*, 181-190.
- [WSK&93] M.N. Wilson, A.I.C. Smith, V.C. Kempson, M.C. Townsend, J.C. Schouten, R.J. Anderson, A.R. Jordan, V.P. Suller, M.W. Poole, *IBM J. Res. Develop.* **1993**, *37*, 351-371.
- [YCD&09] J.K.W. Yang, B. Cord, H. Duan, K.K. Berggren, J. Klingfus, S. Nam, K. Kim, M.J. Rooks, *J. Vac. Sci. Technol. B* **2009**, *27*, 2622-2627.
- [YHA01] S. Yasin, D.G. Hasko, H. Ahmed, *Appl. Phys. Lett.* **2001**, *78*, 2760-2762.
- [YJC&06] S. Yang, S.G. Jang, D. Choi, S. Kim, H.K. Yu, *Small* **2006**, *2*, 458-475.
- [ZFY&11] J. Zhang, M. Fouad, M. Yavuz, B. Cui, *Microelectronic Eng.* **2011**, *88*, 2196-2199.
- [ZJL&95] X. Zhang, C. Jacobsen, S. Lindaas, S. Williams, *J. Vac. Sci. Technol. B* **1995**, *13*, 1477-1483.

Appendix A

This appendix lists all public disseminations of the research contained in this thesis up to the time of submission. Only those presentations which were delivered by the author of this thesis in person are included.

A.1 Publications

A.1.1 Peer-reviewed publications

5. A.F.G. Leontowich, “Utility of the G value and the critical dose to soft x-ray radiation damage of polyacrylonitrile,” submitted June 1, **2012** to *J. Phys. Chem. B*.
4. A.F.G. Leontowich, A.P. Hitchcock, T. Tyliszczak, M. Weigand, J. Wang, C. Karunakaran, “Accurate dosimetry in scanning transmission X-ray microscopes via the cross-linking threshold dose of poly(methyl methacrylate),” *J. Synchrotron Rad.* **2012**, *19*, forthcoming.
3. A.F.G. Leontowich, A.P. Hitchcock, “Secondary electron deposition mechanism of carbon contamination,” *J. Vac. Sci. Technol. B* **2012**, *30*, 030601.
2. A.F.G. Leontowich, A.P. Hitchcock, “Experimental investigation of beam heating in a soft X-ray scanning transmission X-ray microscope,” *Analyst* **2012**, *137*, 370-375.
1. A.F.G. Leontowich, A.P. Hitchcock, “Zone plate focused soft X-ray lithography,” *Appl. Phys. A* **2011**, *103*, 1-11. (Invited)

A.1.2 Reviewed conference proceedings

2. A.F.G. Leontowich, A.P. Hitchcock, “Zone plate focused soft X-ray lithography for fabrication of nanofluidic devices,” *Proc. SPIE* **2012**, 8323, 83231D.
1. A.F.G. Leontowich, T. Tyliczszak, A.P. Hitchcock, “Measurement of the point spread function of a soft X-ray microscope by single pixel exposure of photoresists,” *Proc. SPIE* **2011**, 8077, 80770N.

A.2 Presentations

A.2.1 Invited presentations

2. A.F.G. Leontowich, A.P. Hitchcock, “Secondary electron deposition mechanism of carbon contamination” (Oral, 20 mins). Carbon contamination of optics: Causes, characterization and in-situ treatments. The 11th International Conference on Synchrotron Radiation Instrumentation Satellite Workshop. SOLEIL, St. Aubin, France. Jul 16-17, **2012**. (Abs. # IT-04)
1. A.F.G. Leontowich, A.P. Hitchcock, “Zone plate focused soft X-ray lithography” (Oral, 45 mins). FS-ML Seminar. Center for Free-Electron Laser Science, DESY, Hamburg, Germany. Nov 22, **2011**.

A.2.2 Contributed presentations

12. A.F.G. Leontowich, A.P. Hitchcock, “Secondary electron deposition mechanism of carbon contamination” (Poster). Canadian Light Source 15th Annual Users’ Meeting. Saskatoon, SK. May 3-4, **2012**. (Abs. # 1)
11. A.F.G. Leontowich, A.P. Hitchcock, “Zone plate focused soft X-ray lithography for fabrication of nanofluidic devices” (Oral, 20 mins). SPIE Advanced Lithography: Alternative Lithographic Technologies IV. San José, CA. Feb 12-16, **2012**. (Abs. # 8323-48)
10. A.F.G. Leontowich, A.P. Hitchcock, “Temperature dependent NEXAFS spectromicroscopy at the Canadian Light Source” (Poster). Canadian Light Source 14th Annual Users’ Meeting. Saskatoon, SK. Jun 24-25, **2011**. (Abs. # 45)
9. A.F.G. Leontowich, A.P. Hitchcock, “Temperature dependent NEXAFS spectromicroscopy at the Canadian Light Source” (Poster). 94th Canadian Society for Chemistry Conference. Montréal, QC. Jun 5-9, **2011**. (Abs. # 2142)
8. A.F.G. Leontowich, A.P. Hitchcock, “Three dimensional measurement of the point spread function of a soft X-ray zone plate via single pixel exposure of photoresists at focus” (Oral, 20 mins). SPIE Optics + Optoelectronics: Damage to VUV, EUV, and X-ray Optics (XDam3). Prague, Czech Republic. Apr 18-21, **2011**. (Abs. # 8077-24)

7. A.F.G. Leontowich, A.P. Hitchcock, “Approaching diffraction-limited resolution in zone plate-based soft X-ray lithography” (Poster). 10th International Conference on X-ray Microscopy. Chicago, IL. Aug 15-20, **2010**. (Abs. # Tues-P034)
6. A.F.G. Leontowich, A.P. Hitchcock, “Zone plate based soft X-ray lithography” (Poster). 37th International Conference on Vacuum Ultraviolet and X-ray Physics. Vancouver, BC. Jul 11-16, **2010**. (Abs. # 3P092)
5. A.F.G. Leontowich, A.P. Hitchcock, “Zone plate based soft X-ray lithography” (Poster). Canadian Light Source 13th Annual Users’ Meeting. Saskatoon, SK. Jun 17-18, **2010**. (Abs. # 29)
4. A.F.G. Leontowich, A.P. Hitchcock, “Approaching diffraction limited resolution in zone plate focused soft X-ray lithography” (Oral, 20 mins). 93rd Canadian Society for Chemistry Conference. Toronto, ON. May 29-Jun 2, **2010**. (Abs. # 1640)
3. A.F.G. Leontowich, A.P. Hitchcock, “Scanning transmission X-ray microscope as a lithographic tool” (Poster). 239th American Chemical Society National Meeting & Exposition. San Francisco, CA. Mar 21-25, **2010**. (Abs. # PMSE-438)
2. A.F.G. Leontowich, J. Wang, A.P. Hitchcock, “The scanning transmission X-ray microscope as a lithographic tool” (Poster). Advanced Light Source Users’ Meeting. Berkeley, CA. Oct 16-17, **2009**.

1. A.F.G. Leontowich, J. Wang, A.P. Hitchcock, “The scanning transmission X-ray microscope as a lithographic tool” (Oral, 20 mins). Synchrotron Radiation in Polymer Science 4. Kerkrade, The Netherlands. Sep 8-11, **2009**. (Abs. # O9)

Appendix B

This appendix lists all software packages used for this thesis.

B.1 Software packages used for this thesis

Adobe® Acrobat® X Pro

This .pdf file editing program was used to prepare written reports and figures for presentations and publications.

Adobe® Photoshop® CS v. 8.0

This powerful graphic design program was used to edit figures, and convert images from one file type to another.

aXis2000

aXis2000 is a freeware program written in Interactive Data Language (IDL) by Prof. Adam P. Hitchcock. This program was used for STXM data analysis, including imaging, stacks, NEXAFS spectra, and in creating patterns for the PatternGen routine in STXM_Control. Multiple versions of aXis2000 were used. However, version 21-Apr-2010 was preferred, operating within IDL Virtual Machine® v. 6.3.

Gwyddion v. 2.26

Gwyddion is a freeware scanning probe microscopy data visualization and analysis program. It was used to analyze acquired atomic force micrographs and prepare them for presentations and publications.

ImageJ v. 1.45s

This freeware graphics program was used to measure feature sizes in scanning electron micrographs.

Microsoft® Office v. 2003, 2007

The word processing program Word was used to write all computer generated reports and publications. The presentation program PowerPoint was used to prepare oral and poster presentations, and to prepare figures for presentations and publications. Excel is a spreadsheet application which was used for dose-damage data analysis, NEXAFS spectral analysis, regression analysis, and preparing graphical representations of data. Office v. 2007 was used from September 2011 onward.

Microsoft® Paint XP

This graphics program was used to create pattern generation files for the PatternGen routine in STXM_Control, and to prepare figures for presentations and publications.

NoteTab v. 6.2

NoteTab is a text editing program by Fookes Software Ltd. The freeware version of this program was used to manually edit the individual pixels of pattern generation files for the PatternGen routine in STXM_Control when necessary.

ScanAtomic® v. 4.05.7

ScanAtomic is a scanning probe microscopy control program from Quesant Instrument Corp. It was used to acquire and process atomic force micrographs obtained with the Quesant Q-Scope 350 AFM.

SigmaPlot 11

SigmaPlot is a plotting program by Systat Software, Inc. It was used to produce publication quality graphs and for regression analysis.

STXM_Control

This program controls the STXM microscope and was in use at all STXMs used in this thesis (Table 2.1). It also compiles the data acquired and controls many beamline functions, depending on the beamline. This program was written by Dr. Tolek Tyliszczak and Dr. Peter Hitchcock. Dr. Tyliszczak designed and wrote the PatternGen routine used extensively in this thesis. This program is under development thus several versions were used throughout this thesis. Additional details of this program have been reported elsewhere [KTS&03].